

Monte Carlo Calculations of the Intrinsic Detector Backgrounds
for the Karlsruhe Tritium Neutrino Experiment

Michelle L. Leber

A dissertation submitted in partial fulfillment
of the requirements for the degree of

Doctor of Philosophy

University of Washington

2010

Program Authorized to Offer Degree: Physics

University of Washington
Graduate School

This is to certify that I have examined this copy of a doctoral dissertation by

Michelle L. Leber

and have found that it is complete and satisfactory in all respects,
and that any and all revisions required by the final
examining committee have been made.

Chair of the Supervisory Committee:

John F. Wilkerson

Reading Committee:

John F. Wilkerson

R. G. Hamish Robertson

Ann E. Nelson

Date: _____

In presenting this dissertation in partial fulfillment of the requirements for the doctoral degree at the University of Washington, I agree that the Library shall make its copies freely available for inspection. I further agree that extensive copying of this dissertation is allowable only for scholarly purposes, consistent with "fair use" as prescribed in the U.S. Copyright Law. Requests for copying or reproduction of this dissertation may be referred to Proquest Information and Learning, 300 North Zeeb Road, Ann Arbor, MI 48106-1346, 1-800-521-0600, to whom the author has granted "the right to reproduce and sell (a) copies of the manuscript in microform and/or (b) printed copies of the manuscript made from microform."

Signature_____

Date_____

University of Washington

Abstract

Monte Carlo Calculations of the Intrinsic Detector Backgrounds
for the Karlsruhe Tritium Neutrino Experiment

Michelle L. Leber

Chair of the Supervisory Committee:

Professor John F. Wilkerson

Physics

The Karlsruhe Tritium Neutrino Experiment (KATRIN) aims to measure the absolute neutrino mass, an open question in neutrino physics. KATRIN exploits the fact that the beta-decay spectral shape near the endpoint depends on the neutrino mass. Using a gaseous tritium source and a precise electrostatic spectrometer, KATRIN will measure the integral beta-decay spectrum in a silicon detector. KATRIN strives for a sensitivity of 0.2 eV (90% CL) to the neutrino mass, ten times better than the current limit. A measurement at this level of sensitivity has broad implications for cosmology and particle physics.

To maximize sensitivity to the small beta-decay signal, the KATRIN silicon detector must have minimal intrinsic backgrounds. The background goal for the detector is less than 10^{-3} counts per second (1 mHz) in the region of interest near the 18.6 keV signal. In this dissertation, we present estimates of the detector background rate calculated with a custom Geant4-based Monte Carlo simulation. The simulation includes a detailed description of the detector system and attributes of the intrinsic background sources, natural radioactivity and cosmic rays.

We identified the largest background sources, optimized the detector region design to minimize the background rate, and performed measurements to confirm the simulation results. In particular, we have measured the radiation field from radioactivity in all objects in the detector laboratory using a germanium detector. The simulated germanium detec-

tor rate agrees within 5% of the measured rate. In addition, various calibration spectra measured with silicon and germanium detectors are within 7% of the simulated spectra.

The results from our simulations indicate that we should observe a background of $[2.54 \pm 0.11(\text{stat.}) \pm_{-0.35}^{+0.36}(\text{sys.})]\text{mHz}$ at the nominal magnetic field of 3 T and zero post acceleration. The largest background sources are radiation from the laboratory environment and cosmic-ray photons. Utilizing 20 kV of post-acceleration and the same magnetic field of 3 T, we should reduce the background rate to $[1.01 \pm 0.07(\text{stat.}) \pm_{-0.14}^{+0.13}(\text{sys.})]\text{mHz}$. A higher magnetic field may reduce the background rate further. These background studies indicate that the detector background rate is within the target limit and will not diminish KATRIN's expected neutrino-mass sensitivity.

TABLE OF CONTENTS

	Page
List of Figures	iv
List of Tables	viii
Glossary	xi
Chapter 1: Introduction	1
Chapter 2: Neutrino Properties and Open Questions	6
2.1 Neutrino Interactions	6
2.2 The Standard Model	9
2.3 Evidence for Neutrino Mass	12
2.4 Implications of Neutrino Mass	15
2.5 Open Questions	18
Chapter 3: Neutrino Mass Searches	21
3.1 Beta-Decay Spectral Analysis	21
3.2 Neutrino Mass in Cosmology	26
3.3 Neutrinoless Double-Beta Decay Searches	31
3.4 Summary of Neutrino Mass Searches	33
Chapter 4: The KATRIN Experiment	34
4.1 Overview	34
4.2 Systematic Uncertainties and Sensitivity	47
4.3 Backgrounds	54
4.4 Summary of the KATRIN Experiment	57
Chapter 5: The Detector and Data Acquisition System	58
5.1 Detector Region Design	58
5.2 Overview of the Data Acquisition System	66

5.3	Characterization of the Data Acquisition System	70
5.4	Summary of the Detector System	90
Chapter 6:	The Detector Background Model	91
6.1	Geant4 Simulation Overview	91
6.2	Sources of Backgrounds	103
6.3	Summary of the Background Model	121
Chapter 7:	Simulation Validation	122
7.1	Measurements with a Silicon Detector	122
7.2	Measurements in the Detector Laboratory at KIT	132
7.3	Measurements in the UW Commissioning Laboratory	172
7.4	Summary of the Validation	196
Chapter 8:	Background Estimates and Optimization of the Detector Design . . .	198
8.1	Background Contributions From Each Source	199
8.2	Background Reductions	212
8.3	Uncertainty Estimates and Discussion	219
8.4	Summary	222
Chapter 9:	Conclusion	224
	Bibliography	227
Appendix A:	IPE DAQ Characteristics	235
A.1	Hardware	235
A.2	Data Acquisition Modes	238
A.3	User Controls	244
A.4	Recursive Trapezoidal Filter	246
A.5	Upgrades for Mark IV	247
Appendix B:	Radioactivity in the Detector Components	249
B.1	Component Masses and Activities	249
B.2	Background Rates from Radioactivity in the Components	255
B.3	Cosmogenic Activities	258

Appendix C: Comparison With Previous Simulations	260
C.1 Detector Geometry and Response	261
C.2 Natural Radioactivity in the Ceramic Mount	262
C.3 Cosmic-Ray Muons	265

LIST OF FIGURES

Figure Number	Page
2.1 Mass hierarchy	20
3.1 Beta-decay spectrum	22
3.2 Allowed region of neutrino mass	25
3.3 Energy density of the universe	27
3.4 Neutrino mass effect on the power spectrum	29
3.5 Neutrinoless-double-beta-decay spectrum	31
3.6 Effective Majorana mass	33
4.1 Major components of the KATRIN experiment	35
4.2 Scattering cross-section of e^- off T_2	36
4.3 Excited states of the $(^3HeT)^+$ molecule	38
4.4 MAC-E filter	40
4.5 Detector signal	44
4.6 Integral β spectrum	46
4.7 KATRIN statistical uncertainty	48
4.8 Ultimate KATRIN sensitivity	51
4.9 KATRIN sensitivity over time	53
4.10 Optimization of the ROI	57
5.1 Detector region design	59
5.2 Detector cross section	61
5.3 Detector pixel pattern	62
5.4 Feed through flange	65
5.5 Active and passive shields	66
5.6 Digitally-shaped pulses	69
5.7 Trapezoidal filtering	71
5.8 Effect of the gap on peak-height shape	72
5.9 Pile-up in the trapezoidal filter	73
5.10 Impulse response for the trapezoidal filters	75

5.11	Simple-filter response to a 10 μ s-fall-time pulse	76
5.12	Pole-zero-corrected-filter response to a 10 μ s-fall-time pulse	76
5.13	Peak heights with pole-zero correction	77
5.14	ADC non-linearity	79
5.15	Electronics chain for measuring counting efficiency	81
5.16	The two signal pulses used to test counting efficiency	82
5.17	Time separation of random events	83
5.18	The various pulses in the electronics chain.	85
5.19	Counting efficiency in histogram mode	87
5.20	Counting efficiency in event mode	88
5.21	Blocks of events lost in event mode	89
6.1	Simulation scheme	92
6.2	Detector geometry in the simulation	94
6.3	Close-up of the silicon detector in the simulation	95
6.4	Photon interaction cross section in silicon	96
6.5	Neutron pulse-height defect	99
6.6	Cosmic-ray differential intensities and zenith angle dependence	105
6.7	Muon intensity measurements compared with the theoretical function	107
6.8	Diagram of the <code>CosmicRayGun</code>	110
6.9	The uranium and thorium decay chains	112
6.10	Photons emitted in the uranium and thorium chains	115
6.11	Environmental radioactivity energy spectrum	118
7.1	Hamamatsu silicon detector and simulation geometry	124
7.2	^{241}Am spectrum measured with a silicon detector	126
7.3	^{109}Cd spectrum measured with a silicon detector	128
7.4	Muon spectrum measured with a silicon detector	131
7.5	15 cm shield with funnel opening and germanium detector	135
7.6	Germanium detector simulation geometry at KIT	136
7.7	KIT germanium detector energy resolution	137
7.8	KIT germanium detector ^{60}Co calibration	139
7.9	Effect of scattering in the concrete on the spectrum of photons	142
7.10	Unshielded-germanium-detector spectrum at KIT	143
7.11	Angular regions of the environmental radiation simulation	144
7.12	Fit to ^{212}Pb peak in the shielded spectrum	153

7.13	Fit to ^{214}Bi peak in the shielded spectrum	155
7.14	Fit to ^{40}K peak in the shielded spectrum	156
7.15	Shielded-germanium-detector spectrum at KIT (0–1.4 MeV)	157
7.16	Shielded-germanium-detector spectrum at KIT (1.4–2.8 MeV)	158
7.17	Difference of two measured shielded-germanium-detector spectra	159
7.18	Intensity from each peak at KIT	165
7.19	Fits to ^{214}Pb and ^{212}Pb peaks in the unshielded spectrum	166
7.20	Fit to the ^{40}K peak in the unshielded spectrum	166
7.21	Unshielded-germanium-detector spectrum at KIT (0–1.4 MeV)	167
7.22	Unshielded-germanium-detector spectrum at KIT (1.4–2.8 MeV)	168
7.23	B037 germanium detector simulation geometry	174
7.24	B037 germanium detector energy resolution	175
7.25	B037 germanium detector ^{60}Co calibration	176
7.26	Difference in KATRIN-shield spectra with and without cover	182
7.27	Intensity from each peak in B037	186
7.28	Unshielded measurement in B037	187
7.29	Contributions to the spectra inside the KATRIN shield	188
7.30	Measurements with the KATRIN shield in B037	189
7.31	Cosmic-ray spectrum inside the KATRIN shield	190
7.32	Measurement and simulation inside the KATRIN shield	191
7.33	Effect of the angular distribution inside the KATRIN shield	192
7.34	Comparison of 15 cm-shield measurements in B037 and KIT	194
8.1	Scintillator spectrum from cosmic-ray muons	201
8.2	Background spectrum from cosmic-ray muons	202
8.3	Veto cut effect on the cosmic-muon background spectra	203
8.4	Scintillator spectrum from cosmic-ray photons	205
8.5	Background spectrum from cosmic-ray photons	205
8.6	Veto cut effect on the cosmic-photon spectra	206
8.7	Background spectrum from cosmic neutrons and nucleons	207
8.8	Background spectrum from natural radioactivity in the detector components	209
8.9	Background spectrum from environmental radiation	211
8.10	Total background spectrum	213
8.11	Photon interaction cross section in lead	217
8.12	Veto cut with 100% efficiency	218

A.1	Flow of signals through the IPE DAQ	236
A.2	Flow of signals through the Mark IV IPE DAQ	248
C.1	Schwamm's simulation geometry	261
C.2	Thorium background spectrum from Schwamm's detector mount	264
C.3	Uranium background spectrum from Schwamm's detector mount	264
C.4	Schwamm's muon spectrum after veto	266

LIST OF TABLES

Table Number	Page
4.1 Endpoints of various atomic- and molecular-tritium decays	39
4.2 KATRIN systematics	50
5.1 Detector region design parameters	58
5.2 Detector dimensions and design parameters	63
6.1 Physics processes defined in the simulation	103
6.2 Cosmic-ray intensities	105
6.3 Constants used in the cosmic-ray photon spectrum	108
6.4 Constants used in the cosmic-ray neutron spectrum	109
6.5 Intensity of environmental radioactivity	119
7.1 Features in the ^{241}Am spectrum	127
7.2 Features in the ^{109}Cd spectrum	128
7.3 Average measured rates from cosmic-ray muons	130
7.4 Measured and simulated rates from cosmic-ray muons	132
7.5 KIT germanium detector ^{60}Co calibration	140
7.6 Thorium chain peaks in the KIT shielded measurements	148
7.7 Uranium chain peaks in the KIT shielded measurements	148
7.8 Potassium and other peaks in the KIT shielded measurements	149
7.9 Requirements for including peaks from the shielded spectrum	150
7.10 KIT intensity of thorium through the shield openings	152
7.11 KIT intensity of uranium through the shield openings	152
7.12 KIT intensity of potassium through the shield openings	154
7.13 Requirements for including unshielded peaks	160
7.14 KIT intensity of thorium incident on the shield walls	161
7.15 KIT intensity of uranium incident on the shield walls	162
7.16 KIT intensity of potassium incident on the shield walls	162
7.17 Time duration of the UW measurements	174
7.18 B037 germanium detector ^{60}Co calibration	177

7.19	B037 intensity of thorium through the shield openings	180
7.20	B037 intensity of uranium through the shield openings	181
7.21	B037 intensity of uranium and potassium through the shield openings	181
7.22	Comparison of KIT and B037 intensity through the shield openings	183
7.23	B037 intensity of thorium incident on the shield walls	184
7.24	B037 intensity of uranium incident on the shield walls	185
7.25	B037 intensity of potassium incident on the shield walls	185
7.26	Comparison of KIT and B037 intensity incident on the shield walls	187
8.1	Regions of interest at 3 T	200
8.2	Veto cut effect on the cosmic-muon background rates	204
8.3	Veto cut effect on the cosmic-photon background rates	206
8.4	Cosmic neutron background rates	208
8.5	GRDM background rates	210
8.6	<code>CalibrationGenerator</code> background rates	210
8.7	KIT environmental radiation background rates	211
8.8	B037 environmental radiation background rates	212
8.9	Total background rates at 3 T	213
8.10	Regions of interest at 5 T	214
8.11	Total background rates at 5 T	215
8.12	Transmission of various-energy photons through 3 cm of lead	216
8.13	Veto cuts with 100% efficiency	219
8.14	Total systematic and statistical uncertainty	223
A.1	Channel groups for each FPGA	237
A.2	Structure of an ADC record for Mark III	239
A.3	Waveform mode data structure	240
A.4	Event mode data structure	241
A.5	Histogram mode data structure	242
A.6	Readout times	243
A.7	Peak height maximums for various shaping lengths	246
B.1	Mass of each component in the simulation	250
B.2	Measured and estimated uranium impurities	251
B.3	Measured and estimated thorium impurities	252
B.4	Measured and estimated potassium impurities	253
B.5	Uranium background rates from the GRDM	255

B.6	Thorium background rates from the GRDM	255
B.7	Potassium background rates from the GRDM	256
B.8	Uranium background rates from the CalibrationGenerator	256
B.9	Thorium background rates from the CalibrationGenerator	257
B.10	Potassium background rates from the CalibrationGenerator	257
B.11	Cosmogenic activity for copper and steel	258
B.12	Cosmogenic activity for silicon and ceramic	259
C.1	Thorium background rates from Schwamm's detector mount	262
C.2	Uranium background rates from Schwamm's detector mount	263
C.3	Schwamm's muon rates before veto	265
C.4	Schwamm's muon rates after veto	266

GLOSSARY

B037: Laboratory at the University of Washington where the detector system will be commissioned

CALIBRATION GENERATOR: Custom particle generator used to simulate photons produced in radioactive decay

CAMAC: Computer Automated Measurement And Control; type of data acquisition crate used for many of the measurements

CKM: Cabbibo-Kobayashi-Maskawa matrix; describes the rotation from the quark mass eigenstates to the weak interaction eigenstates

CENPA: Center for Experimental Nuclear Physics and Astrophysics

COUNT: Individual detector signal, as opposed to a Geant4 Event

DAQ: Data acquisition

EVENT: All interactions caused by a primary particle (Geant4 definition)

FEB: Front End Board; part of the IPE DAQ

FLT: First-Level Trigger; part of the IPE DAQ

FPGA: Field-Programmable Gate Array; used by the IPE DAQ

FWHM: Full-width-half-max

GEANT4: Geometry and Tracking simulation toolkit

GPS: General Particle Source

GRDM: Geant4 Radioactive Decay Model, used to simulate radioactive decay including beta electrons

IPE: Institut für Prozessdatenverarbeitung und Elektronik or Institute of Data Processing and Electronics; institute which designed the data acquisition hardware for KATRIN

KATRIN: Karlsruhe Tritium Neutrino Experiment

KIT: Karlsruhe Institute of Technology, location of the KATRIN experiment

MHV: Medium High Vacuum; 10^{-7} mTorr

ORCA: Object-oriented Realtime Control and Acquisition; software which controls the DAQ

ORTEC: Oak Ridge Technical Enterprise Company

PMNS: Ponetecorvo, Maki, Nakagawa, and Sakata mixing matrix; describes the rotation of the neutrino mass eigenstates to neutrino weak eigenstates and is analogous to the CKM matrix

PMT: Photo-multiplier Tube

ROI: Region of Interest

ROOT: Object-oriented analysis framework

SIB: Second-Level Trigger Interface Board; part of the IPE DAQ

SIPM: Silicon Photo-multiplier; used by the scintillator veto

SLT: Second-Level Trigger; part of the IPE DAQ

TORI: Table of Radioactive Isotopes

VME: The VERSAmodule Eurocard bus; type of data acquisition crate used for some of the measurements

WLS: Wavelength-shifting; refers to the fibers embedded in the plastic scintillator veto

X RAY: Photons emitted by atomic electrons

XHV: Extremely High Vacuum: 10^{-10} mTorr

ACKNOWLEDGMENTS

As I worked on this research over the last six years, I was always amazed that I have the opportunity to do what I love and am so grateful for that. Although I really enjoyed it, graduate school was often challenging and frustrating, and I couldn't have finished this dissertation without the guidance, advice, and support of a large network of people. I have learned so much more than just physics during this process, and am grateful to many people for the experiences, lessons, and support they have shared with me.

In particular, I am proud to be a part of the KATRIN collaboration. Working and learning with all of you was a pleasure. I am amazed at the dedication of the collaboration and hope we can celebrate a neutrino mass measurement together.

I have been very fortunate to have John Wilkerson as an advisor. I am grateful for the endless supply of questions and comments, and the last-minute reviews of my talks and abstracts. John's admirable dedication to his students creates a great group to work with. With his advice, I feel I have grown into a confident scientist. I also appreciate the windsurfing lessons.

I would like to thank Hamish Robertson for all the thoughtful comments and for being right all the time. Peter Doe, for teaching me, among other things, to laugh at both good and bad news. I'd like to acknowledge Joe Formaggio, Nikolai Tolich, and Ferenc Gluck for all the advice and conversations about physics.

I could not have been as successful or happy in graduate school without the advice and insight of my fellow graduate students. I am greatly indebted to Laura Stonehill, Minesh Bacrania, Claire Cramer, Sky Sjue, Ruth Van de Water, Thomas Gadfort, Rob Johnson, Chris Spitzer, Brian Smigelski, Wan Chan Tseung, Laura Bodine, Alexis Schubert, Mike Marino, and Florian Habermehl. Brent VanDevendar, Mike

Miller, Kazumi Tolich, Jason Detwiler, and Jessica Dunmore also shared valuable advice with me.

Much appreciation to the CENPA staff for being so knowledgeable, helpful, and such wonderful people to work with. Thanks to Doug Will, Greg Harper, Tom Burritt, Kate Higgins, Mark Howe, Dick Seymour, and Victoria Clarkson.

Fay, thank you for your creativity and zeal, and thank you for inviting me to your Agraphia group. Without the help of Fay, Nils, Kevin, and Susumu, this dissertation would have fewer semicolons and certainly would not have any em dashes.

To all my climbing partners: thanks for the great experiences, conversations, and for saving my life. A great climbing trip with a great partner never fails to rejuvenate and inspire me. Melissa and Jacquie, thanks for tearing me away from my computer so much this summer. Mia, Eric, Frank, Kevin, Katie and Matt, Glenn, and Kim: can't wait to climb with you all again. Cory and Matt, thanks for making me laugh for a year. Matt, I miss you and aspire to carry your adventurous and caring spirit with me.

My parents have my deepest gratitude, for years of support and encouragement. Thank you for accepting my decision to pursue physics as a career. My sister never fails to make me laugh and lighten the most serious situation, and I appreciate her unfailing optimism.

Lastly, Susumu, thank you for everything. I don't know where I would be without your patience, high expectations, company, and support. Arigato gozaimasu.

DEDICATION

To you, for reading.

Chapter 1

INTRODUCTION

Today, neutrino physicists are commonly asked to explain what exactly a neutrino is. Before 1930, no one was asking this question. At that time, scientists were only aware of a few fundamental particles and were investigating radioactive decays. Beta decay was particularly puzzling; the observed final state of the decay seemed to involve only two particles: the daughter nucleus and a beta particle, or electron. The total energy of the two particles did not equal the expected energy. If beta decay was really a two-body decay, the energy of the electron should have been a single value, but a continuous distribution was observed.

In 1930 Wolfgang Pauli predicted that a new particle—now called a neutrino—must also be emitted in this decay and must carry the missing energy [1, 2]. Pauli realized the spin-statistics of certain beta-decay nuclei could also be explained by a neutrino, so he postulated the neutrino to be a spin-1/2 particle, a fermion. This new particle he proposed was very difficult to detect: it was neutral, had a very small or zero mass, and had a very small probability of interacting with other particles. These properties helped to explain why the neutrino had not been previously observed.

In 1934 Enrico Fermi developed a theory of the interaction that produces the neutrino and coined the name neutrino [3]. In beta decay, a neutron n turns into a proton p , and an antineutrino $\bar{\nu}_e$ and an electron e are created:

$$n \rightarrow p + \bar{\nu}_e + e^- . \tag{1.1}$$

The electron and antineutrino are created at the time of the decay and do not reside in the nucleus. This theory lays the foundation for our current understanding of the weak inter-

action. Fermi also predicted inverse beta decay, where a proton p absorbs an antineutrino $\bar{\nu}_e$, turning into a neutron n and creating a positron e^+ :

$$\bar{\nu}_e + p \rightarrow n + e^+. \quad (1.2)$$

If a bright source of antineutrinos is placed close to a detector filled with protons, this process provides a method of observing the antineutrino, since the final state neutron and positron are relatively easy to detect.

Because neutrinos have very small interaction rates, a very bright source is necessary. The cross section for a proton to absorb an antineutrino is incredibly small, 10^{-44} cm^2 . With this cross section, antineutrinos can pass through light-years of lead before an appreciable number are absorbed by protons. Fission reactors create a large number of neutron-rich nuclei; based on Fermi's theory, neutron-rich nuclei will beta decay as in Eq. 1.1, producing antineutrinos.

The antineutrino was observed by Reines and Cowan in 1956 [4], finally confirming Pauli's conjecture. Reines and Cowan used the fission reactor at the Savannah River Plant as a bright source of antineutrinos. They detected both final state particles, a positron and a neutron, and correlated the signal rate with the reactor, conclusively showing that antineutrinos interact in their detector.

Shortly after, Ray Davis attempted to observe neutrinos from the same reactor via a different process [5]:

$$\nu_e + n \rightarrow p + e^-. \quad (1.3)$$

In this process, a neutrino is absorbed, changing a neutron into a proton and creating an electron. In Davis' detector, the neutron resides in a $^{37}_{17}\text{Cl}$ nucleus, so he was looking for the production of $^{37}_{18}\text{Ar}$, not a proton. Instead of observing the reaction, Davis placed an upper limit on the rate twenty times lower than Reines and Cowan. An antineutrino $\bar{\nu}_e$, released by a reactor with a proton as in Eq. 1.1, appears to be the same as an antineutrino $\bar{\nu}_e$ absorbed by a proton in Reines and Cowan's experiment, as in Eq. 1.2. Conversely, a neutrino

ν_e , which participates in the reaction in Eq. 1.3, must be different from an antineutrino $\bar{\nu}_e$ released by a reactor since Davis did not observe the reaction. From this and similar experiments, it appears that for weak interactions a neutrino, denoted as ν_e , is distinct in some way from an antineutrino, denoted as $\bar{\nu}_e$.

A neutrino is the particle created when a proton is converted into a neutron. An antineutrino is the particle created when a neutron is converted into a proton. Since protons and neutrons transform into each other in many places in the universe, neutrinos and antineutrinos have many sources. In the following discussion, we use the term neutrinos to refer to both neutrinos and antineutrinos. Our sun and all stars, supernovae, the big bang, and even the core of the earth are all natural sources of neutrinos. Humans create neutrinos in nuclear reactors, nuclear bombs, accelerators, and even themselves through the beta decay of ^{40}K .

Although neutrinos are pervasive, they only interact weakly and are difficult to detect. The neutrino's weak interaction rates are a challenge to neutrino physics, but also are a useful characteristic. Some sources of neutrinos are not directly observable through other means—for example the interior of the sun, the interior of the earth, and the interior of nuclear reactors. Neutrinos will stream out of these sources without scattering, and if detected, provide insight into these sources.

The neutrino is very different from all other fundamental particles. Neutrinos have the smallest mass of all known particles, less than $2.3\text{eV}/c^2$, but the neutrino mass is still unknown. What is the actual neutrino mass? Is there a reason the mass is so small compared to other known leptons and quarks? Neutrinos are the only neutral, fundamental spin-1/2 particle. Most particles are easily distinguished from their antiparticle by the electric charge; for example, an electron is negative and its antiparticle is the positively charged positron. Without an electric charge, a neutrino does not need to be distinct from an antineutrino. Is it possible for a neutrino to change into an antineutrino? What are the implications of this unique feature? Like the other fundamental particles, quarks and charged leptons, neutrinos come in three flavors. The flavors of quarks and leptons mix, or change into each other. But unlike quarks, which only have a small mixing of flavors, some neutrino flavors are maximally mixed. Is there a reason the mixing patterns of neutrinos are different from

quarks? Chapter 2 reviews the known neutrino properties and explores these open questions in more detail.

Measuring the neutrino properties precisely will constrain models that attempt to explain the neutrino behavior and will eventually extend our knowledge beyond the Standard Model of fundamental interaction. Chapter 3 discusses multiple methods to measure neutrino mass and the complementarity of the methods.

In Chapter 4 we give an overview of the Karlsruhe Tritium Neutrino Experiment (KATRIN), which is designed to directly measure the neutrino mass. Just as Pauli inferred the existence of the neutrino based on the electron-energy spectrum from beta decay, KATRIN uses the electron-energy spectrum and energy conservation to measure the neutrino mass. To accurately measure the beta-decay spectrum of tritium near the maximal electron energy, 18.6 keV, KATRIN uses a high-resolution magnetic-electrostatic spectrometer and a silicon detector, a high-efficiency electron detector. Situated in Karlsruhe, Germany, the experiment is in the construction phase and expects to start taking data in 2011. After three years of data, KATRIN should be capable of reaching a sensitivity to the neutrino mass of $0.2 \text{ eV}/c^2$ (90%CL), ten times lower than the current limit.

Chapter 5 focuses on the KATRIN detector region and data acquisition system, which are being commissioned at the University of Washington and will be delivered to Karlsruhe in 2010. To achieve the projected neutrino-mass sensitivity, the beta-decay signal must be efficiently detected and the signal rate must be larger than the rate of other interactions, or backgrounds, in the detector. In this dissertation, we predicted the background rate in the KATRIN silicon detector and optimized the design of the KATRIN detector region to reduce the background rate. Also, we have developed tests of the data acquisition system which are discussed in Chapter 5.

Chapter 6 outlines the Geant4-based Monte Carlo simulation we used to estimate the background rate and describes other processes that can cause counts in the detector: cosmic rays and natural radioactivity.

Any simulation requires a comparison to real-world measurements to confirm the results. In Chapter 7, we present measurements with a silicon detector to validate the simulation. We also measured, using germanium detectors, the radiation from natural radioactivity orig-

inating in the collective laboratory environment. These measurements help customize the simulation to the KATRIN laboratory and double as a validation of the natural radioactivity simulations.

Chapter 8 presents the results of the simulations. We identified the largest background sources, and with this knowledge, we optimized the detector region design to minimize the background rate. In particular, we investigated the effects of radioactivity in the detector components, a scintillator veto for cosmic rays, and a passive lead and copper shield and recommended an optimized design. Also, we considered the effects of changing the electric and magnetic field configuration to reduce the backgrounds.

This thesis is only a portion of all the work by the KATRIN collaboration towards the goal of precisely measuring neutrino mass. When KATRIN reaches its sensitivity goal, the neutrino mass limit or measurement will have exciting consequences for the Standard Model. The consequences of neutrino mass are explored in the next chapter.

Chapter 2

NEUTRINO PROPERTIES AND OPEN QUESTIONS

Since the detection of the antineutrino in 1956, many additional experiments have revealed neutrino properties. Currently, we know there are three weak interaction flavors of neutrinos, with each flavor particle distinct from its antiparticle. As the only neutral fermion, the neutrino is unique, and many of its properties are still not known.

2.1 Neutrino Interactions

Neutrinos only interact through what we now call the weak interaction. Early experiments uncovered the structure of the weak interaction and provided surprising results.

2.1.1 Parity Violation

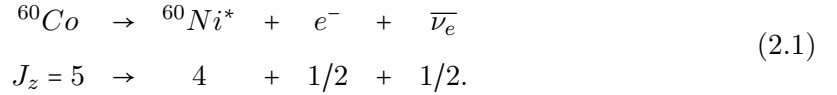
Weak interactions violate one of the long-held beliefs of physics: that parity, or spatial inversion, is a conserved symmetry of nature. Hints of parity violation were seen in the mid-1950s in the decay of kaons. Motivated by the kaon decays, Tsung-Dao Lee and Chen Ning Yang suggested in 1956 that the weak interaction violates parity [6]. Chien-Shiung Wu and her collaborators definitively demonstrated parity violation in their 1957 polarized ^{60}Co experiment [7].

Wu and her collaborators aligned ^{60}Co nuclei, which are spin-5 states, with a magnetic field and observed emission of the beta electrons preferentially in the hemisphere opposite the spin. The spin of the nucleus is unchanged under parity inversion, but the momentum of the electron does change sign under parity. To conserve parity, the electrons must be emitted equally in the directions parallel and antiparallel to the nuclear spin. Within experimental uncertainty, Wu observed a maximal violation of parity.

Inspired by this large parity violation in the weak interaction, Lee and Yang suggested neutrinos might exist in only one helicity state [8]. Helicity is defined as the spin of a particle

dotted into the momentum ($\frac{\mathbf{s}\cdot\mathbf{p}}{|\mathbf{p}|}$). All other known particles come in both states.

Using our current understanding of the ^{60}Co decay, we can see the neutrinos are produced in one helicity state. The decay products and spins J_z as:

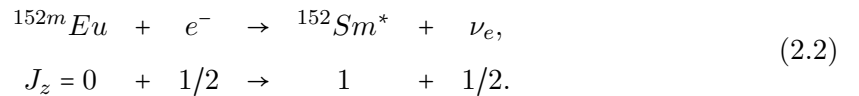


This is predominantly an allowed Gamow-Teller decay, so the electron and neutrino usually carry no orbital angular momentum and their spins must align with the nuclear spin. The electron momentum was observed most often in the hemisphere opposite the polarization. Therefore, the electron was preferentially emitted in the left-helicity state. By conservation of momentum, the antineutrino was preferentially emitted in the right-helicity state, with spin and momentum aligned.

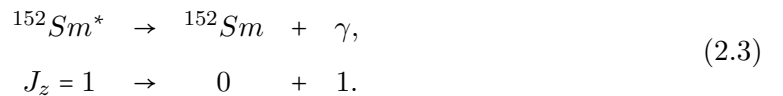
2.1.2 Neutrino Helicity

Within a year of Lee and Yang's two-component neutrino conjecture, Maurice Goldhaber, Lee Grodzins, and Andrew Sunyar measured the helicity of neutrinos [9]. By cleverly choosing a decay nucleus, the authors relied on spin conservation to produce a neutrino and photon in the same helicity state, reducing the problem to measuring the photon helicity.

The chosen decay was the electron capture of ^{152m}Eu , a spin-0 nuclear state. This proceeds through an excited spin-1 state of $^{152}\text{Sm}^*$:



Then it emits a photon to reach the spin-0 ground state:



Since the initial electron capture occurs almost entirely with zero orbital angular momentum, the intermediate neutrino-samarium state must have antiparallel spins. The electron-

capture decay is a two body decay; the momenta are also antiparallel, and the neutrino and samarium have the same helicity. In the special case that the excited samarium emits a photon parallel to the samarium recoil momentum, the photon will have the same helicity as the samarium and the neutrino. The experimental challenge was to identify photons emitted parallel to the recoil and measure their helicity.

The photons emitted parallel to the samarium recoil momentum received an energy-boost; the boost was enough energy to cause resonant scattering in a Sm_2O_3 target. Photons scattered by the target were counted in a scintillator counter. To measure the helicity, magnetized iron was added between the source and target to preferentially absorb photons of a single helicity. By reversing the direction of the magnetic field, an asymmetry in the detector rate would develop if the photons are all in one helicity state. Within the experimental uncertainty, all photons—and therefore all neutrinos—were in the left-helicity state, with the spin and momenta antiparallel. Lee and Yang’s two component neutrino conjecture was correct; the neutrino created by the weak interaction only exists in one helicity state, the left-helicity state.

2.1.3 Argument for Massless Neutrinos

Goldhaber and collaborators showed the neutrino is preferentially emitted in one helicity state. Helicity is conserved, but is only Lorentz invariant for massless particles. For massive particles, an observer can travel faster than the particle, switching the sign of the momentum but not the spin, and observe the second helicity state. For the neutrino to only exist as a left-helicity particle, it must be massless.

Instead of including all possible components of neutrinos, physicists first assumed that neutrinos were massless. This is the simplest model, but not required. Adding a neutrino mass would add the right-handed particle, but the interaction picks out the left-handed particle. In the Standard Model, only massless left-handed neutrinos and right-handed antineutrinos exist.

2.2 The Standard Model

The Standard Model, based on quantum field theory, explains the interaction of the fundamental fermions via exchange of gauge bosons. Fermions appear as both particle and antiparticle states and have two spin projections. Therefore they have four-components and are represented by field operators ψ which obey the Dirac equation.

The Standard Model includes the strong, weak, and electromagnetic interactions, but we focus on the electroweak theory developed independently by Glashow, Weinberg, and Salam [10, 11, 12]. In this theory, the weak isospin and hypercharge group symmetries, $SU(2)_L \times U(1)$, are spontaneously broken because the Higgs obtains a non-zero vacuum expectation value. The gauge coupling constants are g for weak isospin and g' for hypercharge. After symmetry breaking, the W^\pm and Z^0 gauge bosons obtain a mass from the Higgs mechanism, explaining the short range of the weak interactions.

The Lagrangian describes the particle interactions. The field operator for each fermion ψ_i can either destroy a particle or create an antiparticle. The hermitian conjugate of a field operator $\bar{\psi}_i$ can either destroy an antiparticle or create a particle. A parity violating interaction can be written as:

$$\bar{\psi}_i \gamma^\mu (1 - \gamma^5) \psi_i, \quad (2.4)$$

where γ^μ and γ^5 are Dirac matrices and μ is the index of a four-vector. This violates parity because γ^μ transforms as a vector but $\gamma^\mu \gamma^5$ transforms as an axial vector, so a relative minus sign is picked up under parity. The interpretation of the term is that a fermion field is destroyed by ψ_i and a fermion is created by $\bar{\psi}_i$, with the $(1 - \gamma^5)$ picking out spin states to violate parity.

The electroweak Lagrangian density for the three fermion families and a single complex

Higgs doublet [13] is:

$$\begin{aligned}
\mathcal{L}_F = & \sum_i \bar{\psi}_i \left(i\not{\partial} - m_i - \frac{gm_i H}{2M_W} \right) \psi_i \\
& - \frac{g}{2\sqrt{2}} \sum_i \bar{\psi}_i \gamma^\mu (1 - \gamma^5) (T^+ W_\mu^+ + T^- W_\mu^-) \psi_i \\
& - e \sum_i q_i \bar{\psi}_i \gamma^\mu \psi_i A_\mu \\
& - \frac{g}{2 \cos \theta_W} \sum_i \bar{\psi}_i \gamma^\mu (g_V^i - g_A^i \gamma^5) \psi_i Z_\mu.
\end{aligned} \tag{2.5}$$

The first term contains the kinetic term, the mass terms m_i , and the interaction with the neutral Higgs scalar, H . M_W is the mass of the W boson. The second term represents the charged-current weak interaction mediated by the W^\pm with the isospin coupling constant g . The weak isospin raising and lowering operators are T^\pm . The third term is the electromagnetic interaction mediated by the photon A and coupling to the electric charge e . The last term is the neutral-current weak interaction mediated by the Z^0 . The coupling constant for the Z^0 is $g/\cos\theta_W$, where θ_W is the weak angle and g is the isospin coupling. The hypercharge coupling g' and the electromagnetic coupling e are not independent; they are related by the weak angle: $\cos\theta_W = e/g'$. The neutral-current vector and axial couplings, g_V and g_A , are different for each fermion; they depend on the weak angle and the fermion's isospin and charge. For neutrinos, g_V and g_A are $1/2$, ensuring that parity is maximally violated in neutrino interactions.

2.2.1 Chiral Theory

Since the weak interaction violates parity and only left-handed neutrinos have been observed, it is useful to represent them as two-component chirality eigenstates, instead of four-component Dirac spinors. Chirality is a Lorentz-invariant quantity related to helicity; for massless particles, helicity and chirality are identical. Therefore, massless neutrinos only exist in the left helicity and left chirality state.

In general, for massive particles chirality and helicity are not the same. The chirality

operator is γ^5 , and the left and right projection operators are:

$$\begin{aligned} P_L &\equiv \frac{1-\gamma^5}{2}; & P_L\psi &= \psi_L, \\ P_R &\equiv \frac{1+\gamma^5}{2}; & P_R\psi &= \psi_R. \end{aligned} \quad (2.6)$$

The subscripts L and R refer to the chirality state. Chirality is not conserved, but helicity is conserved. Chirality is frame-independent, but helicity depends on the observer. Massive particles will have both chirality states and therefore have all four components.

The left handed particles occur as doublets of isospin, the components of which transform between each other with the exchange of an W^\pm . These particles have both weak isospin and weak hypercharge:

$$\begin{pmatrix} \nu_e \\ e \end{pmatrix}_L, \begin{pmatrix} \nu_\mu \\ \mu \end{pmatrix}_L, \begin{pmatrix} \nu_\tau \\ \tau \end{pmatrix}_L \quad \text{and} \quad \begin{pmatrix} u \\ d' \end{pmatrix}_L, \begin{pmatrix} c \\ s' \end{pmatrix}_L, \begin{pmatrix} t \\ b' \end{pmatrix}_L. \quad (2.7)$$

The mass eigenstates of the down-type quarks are different than the weak-interaction states d', s', b' , which are doublet partners of the up-type quarks. Therefore, the quark weak-interaction states d'_i are connected to the mass states d_j via a matrix: $d'_i = \sum_j V_{ij} d_j$. This matrix, V_{ij} , is the Cabibbo-Kobayashi-Maskawa (CKM) matrix [14,15]. A single observable phase in the CKM matrix causes CP violation in the quark sector.

The right handed particles do not have weak isospin and therefore do not interact with the W^\pm . These do have weak hypercharge and couple to the Z^0 .

$$e_R, \mu_R, \tau_R \quad \text{and} \quad u_R, d_R, c_R, s_R, t_R, b_R. \quad (2.8)$$

Notice there is no right-handed neutrino.

The electroweak Lagrangian terms can be rewritten in this notation. The coupling to the W^+ becomes:

$$\bar{\nu}_L \gamma_\mu e_L W^{-\mu}. \quad (2.9)$$

The parity-violating $(1 - \gamma^5)$ is part of the projection operator P_L and picks out only the

left-handed components. The coupling to the Z^0 can be written as:

$$\bar{\nu}_L \gamma_\mu \nu_L Z^{0\mu} + (\sin^2 \theta_W - 1/2) \bar{e}_L \gamma_\mu e_L Z^{0\mu} + \bar{e}_R \gamma_\mu e_R Z^{0\mu} \quad (2.10)$$

The mass terms show that chirality is not conserved:

$$m_e \bar{e}_R e_L. \quad (2.11)$$

The left-handed electron field e_L can either destroy a left-chirality electron or create a right-chirality positron. The hermitian conjugate of a right-handed electron field \bar{e}_R can either destroy a left-chirality positron or create a right-chirality electron. In the Standard Model, the neutrino is massless because this type of mass term can convert a left-handed neutrino ν_L into a right-handed ν_R , but right-handed neutrinos are not included in the Standard Model.

The Standard Model also includes antiparticles, which are charge conjugates of the particles with the opposite quantum numbers. Particles with negative electric charge have antiparticles with positive electric charge. For neutrinos, which have no electric charge, only the chirality changes for antiparticles. Therefore, the left-handed neutrino and right-handed antineutrino are described by the fields ν_L and $(\nu_L)^c$, where c represents charge conjugation. The field ν_L can either destroy left-handed neutrinos or create right-handed antineutrinos, and the field $(\nu_L)^c$ can either destroy right-handed antineutrinos or create left-handed neutrinos. The right-handed neutrinos and left-handed antineutrinos ν_R and $(\nu_R)^c$ do not appear.

2.3 Evidence for Neutrino Mass

Despite the power of the Standard Model for predicting particle interactions, it is not complete. In the last decade, oscillation experiments have definitely shown neutrinos have mass and oscillate between flavors.

2.3.1 Neutrino Oscillations

The first hint that neutrinos might have mass came from a solar neutrino experiment underground in the Homestake mine [16]. Ray Davis, Don Harmer, and Kenneth Hoffman measured fewer ν_e 's coming from the sun than predicted by solar models. Although Pontecorvo and Gribov noted as early as 1969 that the solar neutrino deficit could be explained by neutrino oscillations [17], the deficit was not convincing evidence of neutrino mass.

Neutrino oscillations occur if the flavor and mass states are different. Recall the CKM matrix connects the quark mass basis with the quark weak-isospin basis. A similar matrix could exist for neutrinos, causing ν_e 's coming from the sun to oscillate to other flavors and escape detection. For oscillations to occur, the three mass eigenvalues cannot all be the same; therefore, the three neutrino mass eigenvalues cannot all be zero.

Consider two flavor states and two mass states. A mixing matrix can relate the mass eigenstates ν_1 and ν_2 to the flavor eigenstates ν_α and ν_β :

$$\begin{pmatrix} \nu_\alpha \\ \nu_\beta \end{pmatrix} = \begin{pmatrix} \cos \theta & \sin \theta \\ -\sin \theta & \cos \theta \end{pmatrix} \begin{pmatrix} \nu_1 \\ \nu_2 \end{pmatrix} \quad (2.12)$$

If the neutrino is created in the weak eigenstate α , it will propagate in the mass eigenstates and the relative phase will change:

$$|\nu_\alpha(t)\rangle = e^{-iE_1 t/\hbar} \sin \theta |\nu_1\rangle + e^{-iE_2 t/\hbar} \cos \theta |\nu_2\rangle. \quad (2.13)$$

The probability of detecting the neutrino in weak eigenstate β is:

$$P(\nu_\alpha \rightarrow \nu_\beta) = |\langle \nu_\beta | \nu_\alpha(t) \rangle|^2 = \sin^2(2\theta) \sin^2(1.27 \Delta m_{21}^2 L/E_\nu). \quad (2.14)$$

Here, the distance the neutrino travels in km is L , the neutrino energy in GeV is E , the factor of 1.27 accounts for \hbar and c , and $\Delta m_{21}^2 \equiv m_2^2 - m_1^2$ is measured in eV^2 . The maximum probability of oscillation is given by θ and the wavelength of the oscillation is determined by Δm_{21}^2 .

To observe neutrino oscillations, a detector is placed a distance L from a source that is

known to produce a certain flavor neutrino. Either the detector observes a disappearance of the original flavor or an appearance of a new flavor. The range of mass splittings Δm^2 to which an experiment is sensitive is determined by L/E , the distance to the neutrino source and the neutrino energy. Neutrino oscillation experiments at different values of L/E have found evidence of two different mass splittings, the maximum possible for three flavors of neutrinos.

2.3.2 Atmospheric Neutrino Experiments

Cosmic rays produce neutrinos of a known flavor; mesons and muons decay in the upper atmosphere creating high-energy atmospheric neutrinos. One pion decay produces a muon neutrino, a muon antineutrino, and one electron neutrino: $\pi^+ \rightarrow \nu_\mu + \mu^+$ and $\mu^+ \rightarrow \bar{\nu}_\mu + \nu_e + e^+$. If a detector can distinguish between flavors, the ratio of muon to electron neutrinos should be about two.

SuperK is a large, underground Cherenkov detector that can distinguish ν_e from ν_μ . In 1998, SuperK observed a zenith-angle dependence of the ratio $\frac{\nu_\mu}{\nu_e}$ and a deficit of ν_μ coming up through the earth [18]. These up-going neutrinos travel farther than down-going neutrinos, giving the ν_μ time to oscillate to ν_τ and thus avoid detection. This is convincing evidence of oscillations because, although the neutrinos simply disappear, the fraction that disappears was shown to depend on L/E as expected.

Combined with oscillation results from the K2K accelerator experiment, the data indicate two flavor oscillations: $\nu_\mu \rightarrow \nu_\tau$. The best fit parameters are $\theta_{atm} \approx 45^\circ$ (maximal mixing) and $\Delta m_{atm}^2 \approx 2.5 \times 10^{-3} \text{ eV}^2$ [19]. The sign of Δm_{atm}^2 is unknown.

2.3.3 Solar Neutrino Experiments

In 2001, the Sudbury Neutrino Observatory (SNO) solved the solar neutrino problem [20,21] by measuring the appearance of ν_μ and ν_τ in solar neutrinos. SNO is unique because it is filled with heavy water. Electron neutrinos can break up the deuterium via exchange of a W^- , producing two protons in the final state. All neutrinos can break up the deuterium via the exchange of a Z^0 , producing a proton and neutron in the final state. All neutrinos

can also elastically scatter off electrons in the detector, but this happens with a higher probability for electron neutrinos due to the additional W exchange. SNO observed the familiar deficit of ν_e 's in the elastic scattering and charged current channels, but the neutral current measurements agreed with the theoretical flux predictions, showing that 2/3 of the electron neutrinos emitted by the sun were changing into ν_μ and ν_τ .

Combing results from all solar neutrino experiments with the KamLAND reactor experiment, the two-neutrino oscillation best fit values are $\Delta m_{solar}^2 \approx 8 \times 10^{-5} \text{ eV}^2$ and $\theta_{solar} \approx 34^\circ$ [22]. Because solar neutrinos undergo matter enhanced oscillations [23, 24] as they exit the sun, the sign of Δm_{solar}^2 is known to be positive. The solar mass splitting is much smaller than the atmospheric mass splitting, but the mixing angle is still quite large.

2.4 Implications of Neutrino Mass

Oscillation experiments have conclusively shown neutrinos have mass, but only massless neutrinos are included in the Standard Model. Not only are right-handed neutrinos unobserved, but there is doubt that neutrinos acquire mass through the same mechanism as other particles. Currently, neutrino masses are 10^5 times smaller than the electron mass, the next-to-lightest particle. Understanding what unconventional mechanism gives neutrinos mass may set the scale for new physics.

2.4.1 See-saw Mechanism

One explanation for the smallness of neutrino mass is the “see-saw” mechanism, suggested by Murray Gell-Mann, Pierre Ramond, Richard Slansky [25] and Tsutomu Yanagida [26]. Here we discuss the type I see-saw mechanism for a single flavor, following the notation of Kai Zuber [27], but this can be generalized to three flavors.

Recall the mass terms for electrons, which is a Dirac mass term:

$$\mathcal{L}_D = -\frac{m_e}{2} (\bar{e}_L e_R + \bar{e}_R e_L + \bar{e}_R^c e_L^c + \bar{e}_L^c e_R^c). \quad (2.15)$$

This expression contains all four components of the electron. In the first term, the right-handed electron field e_R can either destroy a right-handed electron or create a left-handed

positron (anti-electron). The hermitian conjugate of the left-handed electron field \bar{e}_L can either create a left-handed electron or destroy a right-handed positron. The first term is identical to the third, and the second term is identical to the fourth. It is called a Dirac mass term because the particles are distinct from antiparticles; it cannot destroy a particle and create an antiparticle, or destroy an antiparticle and create a particle.

A Dirac mass term conserves lepton number and helicity, but does not conserve chirality since it can change a particle or antiparticle from right to left handed. It also does not conserve weak isospin or hypercharge; it converts a component of a weak isospin doublet e_L into a right-handed electron, a weak isospin singlet. The Higgs mechanism gives the electron mass and breaks the weak symmetry. The mass, m_e , is determined by the vacuum expectation value of the Higgs $\langle v \rangle$ and a Yukawa coupling Y_e ,

$$m_e = \frac{Y_e \langle v \rangle}{\sqrt{2}}. \quad (2.16)$$

If we simply add one right-handed neutrino to the Standard Model for every flavor, neutrinos can have a Dirac mass term just like other fermions. We denote the right-handed neutrino, which does not have weak isospin or hypercharge and will be very heavy, as N_R and reserve the notation ν_L for standard, weakly-interacting neutrinos. The neutrino Dirac mass is:

$$\mathcal{L}_D = -\frac{m_D}{2} (\bar{\nu}_L N_R + \bar{N}_R \nu_L + \bar{N}_R^c \nu_L^c + \bar{\nu}_L^c N_R^c). \quad (2.17)$$

In the first term, the right-handed heavy neutrino field can either destroy a heavy right-handed neutrino or create a heavy left-handed antineutrino. The hermitian conjugate of the left-handed neutrino field can either create a left-handed, weakly-interacting neutrino, or destroy a right-handed, weakly interacting antineutrino. Again, the first and third terms and the second and fourth terms are the same. If this is the neutrino mass term, unobserved right-handed neutrinos must be added to the Standard Model and the Yukawa coupling to the Higgs vacuum expectation value must be 10^5 times smaller than other particles.

Another mass term is possible if the new right-handed neutrinos obtain a large Majorana

mass:

$$\mathcal{L}_M = -\frac{M}{2} (\overline{N_R^c} N_R + \overline{N_R} N_R^c). \quad (2.18)$$

In the first term, the right-handed heavy neutrino field N_R can either destroy a right-handed heavy neutrino or create a left-handed heavy antineutrino. The hermitian conjugate of the charge-conjugated left-handed heavy neutrino $\overline{N_R^c}$ can either create a left-handed heavy antineutrino or destroy a right-handed heavy neutrino. The second term can destroy a left-handed heavy antineutrino and create a right-handed heavy neutrino. This is called a Majorana mass term because it has the new feature of changing a particle into an antiparticle. It does not conserve lepton number. Majorana particles are self-conjugate, or are their own antiparticle.

Combing the Majorana and Dirac terms and writing this in matrix form:

$$(\overline{\nu_L}, \overline{N_R^c}) \begin{pmatrix} 0 & m_D \\ m_D & M \end{pmatrix} \begin{pmatrix} \nu_L^c \\ N_R \end{pmatrix} + h.c. \quad (2.19)$$

If M is very heavy and the Dirac mass m_D is the same order of other leptons and quarks, the matrix is approximately diagonal. In this case, a small rotation will diagonalize the matrix.

Rotating and finding the mass eigenvectors and eigenvalues, the lightest eigenstate is:

$$\begin{aligned} \nu_{\text{light}} &= [\nu_L - \nu_L^c] + \frac{m_D}{M} [N_R - N_R^c], \\ m_{\text{light}} &\approx \frac{m_D^2}{M}. \end{aligned} \quad (2.20)$$

Because m_D/M is very small, the lightest eigenstate is mostly ν and has an eigenvalue much lighter than the other fermions. The heavy state is:

$$\begin{aligned} \nu_{\text{heavy}} &= [N_R + N_R^c] + \frac{m_D}{M} [\nu_L + \nu_L^c], \\ m_{\text{heavy}} &\approx M \left(1 + \frac{m_D^2}{M}\right), \end{aligned} \quad (2.21)$$

and is mostly the right-handed neutrino N . If we measure the mass of ν_L , we will mostly measure the lightest eigenvalue. The observable neutrinos ν_L are now Majorana particles. There is a probability proportional to m_{light} that a weakly-interacting neutrino ν_L will oscillate into a weakly-interacting antineutrino.

The see-saw mechanism can explain the light observable neutrino mass by adding a heavy Majorana particle. The Yukawa coupling for the Dirac mass may be the same order as other particles. This can be extended to three flavors by adding three heavy neutrinos.

Many grand unified theories, which predict that the electroweak and strong forces can be combined into one theory above 10^{14} GeV, contain neutrinos of both handedness. Giving the right-handed neutrino a very large mass helps to explain why it has never been observed. If the see-saw mechanism is correct, the light observable neutrino's mass is related to this very heavy partner. Measuring the light neutrino's mass will yield information about the heavy neutrino, which resides at an energy scale that cannot be explored with other means. Even if the see-saw mechanism is not correct, measuring the light neutrino's mass will restrict theories beyond the Standard Model.

2.5 Open Questions

In the Standard Model extended to include neutrino mass, neutrinos are described by three flavor eigenstates and three mass eigenstates. The flavor content of each mass eigenstate is determined by the PMNS mixing matrix of Pontecorvo, Maki, Nakagawa, and Sakata [28, 29, 30]. The matrix is sometimes represented as three separate two-dimensional rotations, as in Equation 2.22, with $c_{12} \equiv \cos \theta_{12}$ and $s_{12} \equiv \sin \theta_{12}$.

$$\begin{aligned} \begin{pmatrix} \nu_e \\ \nu_\mu \\ \nu_\tau \end{pmatrix} &= \begin{pmatrix} 1 & 0 & 0 \\ 0 & c_{23} & s_{23} \\ 0 & -s_{23} & c_{23} \end{pmatrix} \begin{pmatrix} c_{13} & 0 & s_{13}e^{-i\delta} \\ 0 & 1 & 0 \\ -s_{13}e^{i\delta} & 0 & c_{13} \end{pmatrix} \begin{pmatrix} c_{12} & s_{12} & 0 \\ -s_{12} & c_{12} & 0 \\ 0 & 0 & 1 \end{pmatrix} \begin{pmatrix} e^{i\alpha_1/2}\nu_1 \\ e^{i\alpha_2/2}\nu_2 \\ \nu_3 \end{pmatrix} \quad (2.22) \\ &= \begin{pmatrix} c_{12}c_{13} & s_{12}c_{13} & s_{13}e^{-i\delta} \\ -s_{12}c_{23} - c_{12}s_{23}s_{13}e^{i\delta} & c_{12}c_{23} - s_{12}s_{23}s_{13}e^{i\delta} & s_{23}c_{13} \\ s_{12}s_{23} - c_{12}c_{23}s_{13}e^{i\delta} & -c_{12}s_{23} - s_{12}c_{23}s_{13}e^{i\delta} & c_{23}c_{13} \end{pmatrix} \begin{pmatrix} e^{i\alpha_1/2}\nu_1 \\ e^{i\alpha_2/2}\nu_2 \\ \nu_3 \end{pmatrix} \end{aligned}$$

Unlike quarks, the mixing angles $\theta_{12} \approx 34^\circ$ and $\theta_{23} \approx 45^\circ$ are large angles, or near-maximal. Oscillation experiments also require the upper limit $\theta_{13} < 10^\circ$. Just like the CKM matrix of the quarks, the rotation includes one CP-violating phase δ . If the neutrinos are Majorana particles, the mass eigenstates will also have Majorana phases, α_1 and α_2 .

In addition to these parameters, the three mass eigenvalues, m_{1-3} , describe the neutrinos. The masses have an upper limit of 2.3 eV, but the eigenvalues are unknown. Oscillations measure the mass-squared splittings. The solar-pair mass difference corresponds to $\Delta m_{21}^2 \approx 8 \times 10^{-5} \text{ eV}^2$. The sign of the atmospheric mass difference is unknown; ν_3 may be heavier or lighter than the solar pair, but is separated by $\Delta m_{32}^2 \approx 2.5 \times 10^{-3}$. Figure 2.1 shows the two possibilities for the sign of Δm_{32}^2 ; either m_1 is the lightest mass, called the normal hierarchy, or m_3 is the lightest mass, called the inverted hierarchy. If the mass splittings are small compared to the absolute masses, the eigenvalues are called quasi-degenerate. The normal hierarchy has the closest analogy to the quarks, with largest mass states having the largest tau and muon components. Compared to the charged lepton or quark mass splittings, a quasi-degenerate or inverted hierarchy would seem quite strange. Variations on the see-saw mechanism, discussed in Section 2.4.1, can predict quasi-degenerate masses or hierarchical masses.

Assuming the Standard Model is correct, some remaining experimental questions are:

- What is the neutrino mass scale? In addition, what is the pattern of mass splittings, quasi-degenerate, normal hierarchy, or the inverted hierarchy?
- Are neutrinos Majorana particles, and if so, what are the Majorana phases?
- What are the remaining parameters in the mixing matrix, θ_{13} and the CP-violating phase δ ?

In addition, experiments should be open to the possibility of surprises beyond the Standard Model.

This dissertation is focused on the absolute masses of the neutrinos. In the next chapter, we give an overview of methods designed to measure the neutrino mass scale. The methods are complementary, and together could answer the first two questions.

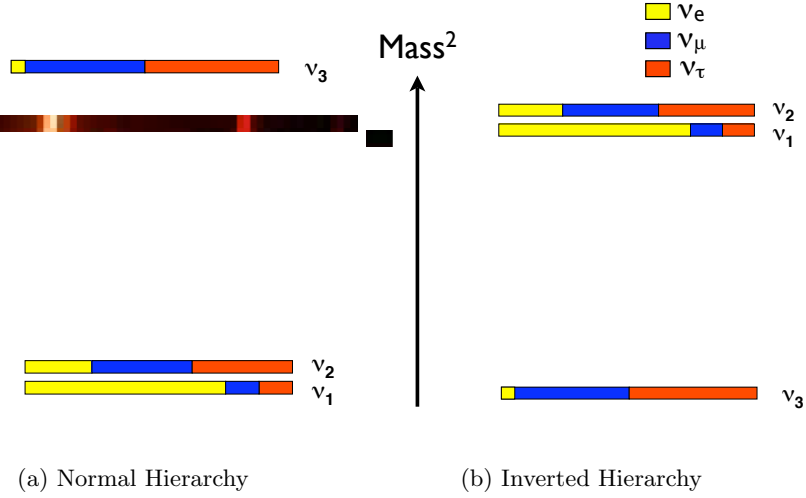


Figure 2.1: Due to the ambiguity of the mass difference measured in atmospheric oscillations, the mass eigenstates have two possible interpretations; either m_1 is the lightest mass, or m_3 is the lightest mass. The mass splittings are not to scale. The absolute masses are not known, with only an upper limit of 2.3 eV. The colors represent the flavor content of each mass eigenstate.

Chapter 3

NEUTRINO MASS SEARCHES

Since neutrinos are abundant in the universe and are emitted in radioactive decay, there are multiple methods to search for the neutrino mass. Indirect searches rely on models or unknown neutrino properties. A direct search relies on particle kinematics: for example the energy of the electron released in beta decay is inherently tied to the value of the neutrino mass. A direct measurement or limit can be compared to indirect measurements to test the underlying model assumptions of the indirect methods. We discuss beta-decay experiments, cosmological limits, and neutrinoless-double-beta decay searches. The different methods are complimentary; combining results of all searches improves our knowledge of the neutrino.

3.1 *Beta-Decay Spectral Analysis*

In beta decay, the weak interaction transforms a neutron into a proton and releases an electron, an electron antineutrino, and energy Q .



Since this is a three-body decay, all particles have continuous energy distributions depending on the relative angles between the particles. Based on energy and momentum conservation, the kinetic energy of the electron must depend on the neutrino mass.

The energy released in the decay is called the Q-value and is defined as the nuclear mass differences of the decay products, corrected for the electron mass:

$$Q = [m_N({}^A_Z X) - m_N({}^A_{Z+1} X') - m_e]c^2 \quad (3.2)$$

Historically, the Q-value is not corrected for the neutrino mass. Therefore, the energy of the Q-value is shared between the total energy of the neutrino and the kinetic energy of the

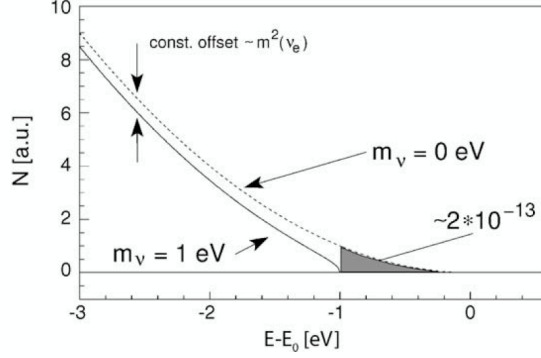


Figure 3.1: The differential beta-decay spectrum near the endpoint is modified by the neutrino mass. For tritium, only 2×10^{-13} of all decays occur within 1 eV of E_0 . Figure from Otten, Bonn, and Weinheimer [31].

electron and recoil-nucleus:

$$Q = T_e + T_{recoil} + E_{\nu_{Tot}}. \quad (3.3)$$

The more useful quantity, the energy shared between the electron and the neutrino, is

$$E_0 = Q - T_{recoil}.$$

The differential beta-decay spectrum is the number of electrons emerging with a given kinetic energy E . Since the neutrino has mass, the minimum energy it carries from the decay is its rest mass. Conversely, the maximal electron energy depends on neutrino mass. Figure 3.1 shows the electron energy spectrum near the maximal energy E_0 . The spectrum falls to zero at the endpoint energy, which is $E_0 - m_\nu$. A non-zero neutrino mass causes a lower endpoint and a different shape near the endpoint.

The differential beta-decay spectrum is:

$$\frac{dN}{dE} = \frac{G_f^2}{2\pi^3 \hbar^7 c^5} \cos^2(\Theta_c) |M|^2 F(Z+1, E) E_{e_{Tot}} p_e E_{\nu_{Tot}} p_\nu. \quad (3.4)$$

The spectrum is the product of the interaction matrix element and the density of final states.

The first constants in Eq. 3.4 describe the interaction; G_f is the Fermi coupling constant,

Θ_c is the Cabibbo angle from the CKM matrix, and M is the nuclear matrix element. The nuclear matrix element can be a function of the electron and neutrino momentum, but is a constant for allowed decays in which the electron and neutrino carry no orbital angular momentum. The Fermi function, $F(Z + 1, E)$, accounts for the electron's attraction to the daughter nucleus and has the largest effect at low electron energy. The density of final states contains the product of the momentum and total energy E_{Tot} of the electron and neutrino. Other than the nuclear matrix element and the Fermi function, the density of final states provides all the dependence on electron energy. The neutrino mass appears in the neutrino momentum. Collecting all the constants—including M for an allowed decay—we define K :

$$K \equiv \frac{G_f^2}{2\pi^3 \hbar^7 c^5} \cos^2(\Theta_c) |M|^2. \quad (3.5)$$

The electron neutrino is actually a super-position of the three mass eigenstates, with the rotation from mass basis to flavor basis determined by the mixing matrix in Eq. 2.22. Therefore, the measured spectrum is a sum of three spectra for each mass eigenstate, weighted by the probability $|U_{ej}|^2$ of an electron neutrino being in the mass-eigenstate j . Writing Eq. 3.4 in terms of the electron kinetic energy E and including all neutrino-mass eigenstates, the form is:

$$\frac{dN}{dE} = KF(Z + 1, E)(E + m_e c^2)p \sum_j (E_0 - E) |U_{ej}|^2 \sqrt{(E_0 - E)^2 - m_{\nu_j}^2}. \quad (3.6)$$

The electron mass is m_e and p is the electron momentum. The three endpoints for these spectra occur when the neutrino momentum is zero, at $E = E_0 - m_{\nu_j}$.

For nearly degenerate neutrino masses, the sum over eigenstates simplifies and we define the observable m_ν^2 .

$$m_\nu^2 = \sum_j |U_{ej}|^2 m_{\nu_j}^2 \quad (3.7)$$

In this case, the spectrum has the simplified form:

$$\frac{dN}{dE} = KF(Z + 1, E)(E + m_e c^2)p(E_0 - E)\sqrt{(E_0 - E)^2 - m_\nu^2} \quad (3.8)$$

Beta-decay spectral-analysis experiments are challenging as the effect of neutrino mass is only apparent in a very small portion of the spectrum near the endpoint. Isotopes with lower endpoints have a larger fraction of decays affected by neutrino mass. Historically, tritium is the most common isotope used to search for neutrino mass due to its beneficial characteristics.

Tritium is an ideal choice for a neutrino mass search for multiple reasons. Tritium has one of the lowest endpoints of all beta emitters, near 18.6 keV. Tritium beta decay is super-allowed, meaning the comparative half-life or ft -value is relatively large and beta decay is highly probable for this nucleus. The half life is a favorable 12.3 years. Also, since it is super-allowed, the nuclear matrix element is independent of the momentum of the electron and neutrino and is easy to calculate. In addition, hydrogen and its daughter have simple atomic structures, making calculations of atomic or molecular final states manageable. The low nuclear charge of hydrogen reduces scattering of the beta electrons within the source.

There is a long history of tritium-beta-decay experiments. The two most recent are the Mainz experiment [32] and the Troitsk experiment [33]. Both relied on an electrostatic spectrometer, based on the Magnetic Adiabatic Collimation combined with Electrostatic Filter, or MAC-E Filter. This method of integrating the beta spectrum is explained in Section 4.1.3.

The Mainz experiment used a solid source, a thin film of tritium quench-condensed onto graphite. This solid source presented challenging systematic uncertainties. After minimizing the source-related systematic uncertainty, the Mainz experiment reached a limit of:

$$m_\nu < 2.3 \text{ eV (Mainz 95\%CL)}. \quad (3.9)$$

In contrast, the Troitsk experiment utilized a gaseous molecular tritium source. Gaseous tritium sources were first used by the LANL experiment [34]. The Troitsk experiment

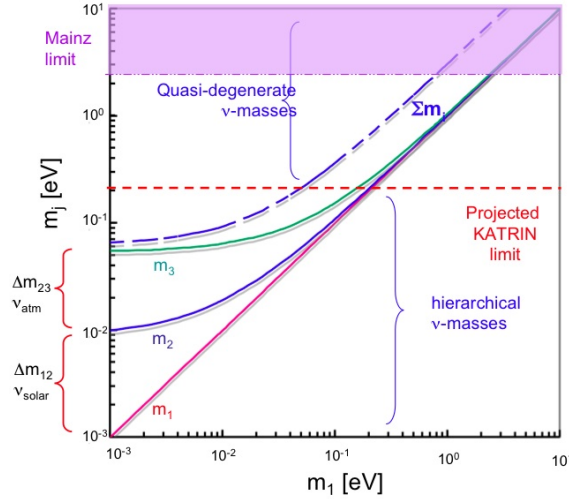


Figure 3.2: The neutrino mass eigenstates as a function of the lowest mass eigenstate. The shaded region is excluded by the Mainz experiment. The dotted red line shows the projected sensitivity of the KATRIN experiment, which is only sensitive to the quasi-degenerate region. Figure from R. G. H. Robertson.

observed an unexplained sharp step in the count rate a few eV below the endpoint, which was not seen in the final Mainz spectrum. Fitting the beta-spectrum to a function including this anomaly, the final Troitsk limit is:

$$m_\nu < 2.5 \text{ eV (Troitsk 95\%CL)}. \quad (3.10)$$

The origin of the step was never explained.

The atmospheric and solar oscillation experiments, discussed in Section 2.3.1, place lower limits on two neutrino masses. Figure 3.2 shows the three mass eigenstates as a function of the lowest mass eigenstate for the normal hierarchy. In the inverted hierarchy, there are two closely-spaced states at a larger mass. The Mainz limit excludes the shaded region. The KATRIN experiment aims for an order-of-magnitude better sensitivity than the Mainz experiment. If KATRIN does not observe a neutrino mass, the quasi-degenerate region will be ruled out.

3.2 Neutrino Mass in Cosmology

Neutrinos are abundant particles in the universe; there are 339 neutrinos and antineutrinos in every cubic centimeter of the universe, slightly less than the number of photons. Although neutrinos do not make up a significant portion of the energy density today, a neutrino mass has an observable signature in large-scale structure and the cosmic microwave background.

The standard cosmological model is the Λ CDM universe, which usually has eleven parameters [35]. Neglecting curvature—which is consistent with observations—the expansion of the universe is governed by the Friedmann equation:

$$H^2 = \left(\frac{\dot{a}}{a}\right)^2 = \frac{8\pi G}{3}(\rho_\gamma + \rho_{cdm} + \rho_b + \rho_\nu + \rho_\Lambda). \quad (3.11)$$

All of these parameters are time-dependent: the Hubble parameter H , the scale factor a , and the energy density ρ_i of the various matter species. It is useful to introduce the scaled Hubble parameter h , which is dimensionless but also time-dependent:

$$h = \frac{H}{100 \text{ km s}^{-1} \text{ Mpc}^{-1}}. \quad (3.12)$$

Often, the energy density is quoted relative to the critical density ρ_c , the density for zero curvature at zero cosmological constant:

$$\rho_c \equiv \frac{3H^2}{8\pi G} = 1.88 \times 10^{-26} h^2 \text{ kg m}^{-3}. \quad (3.13)$$

The fractional energy density for each matter species is $\Omega_i \equiv \rho_i/\rho_c$. Today, the universe is mostly made up of a cosmological constant or dark energy with density $\Omega_\Lambda = 0.742$ and cold dark matter with density $\Omega_{cdm} = 0.213$ [36]. The remainder of the fractional energy density is divided between photons, neutrinos, and baryons (which includes the charged leptons). The fractional energy density was not always distributed in this way.

As shown in the Friedmann equation, the energy density and the rate of expansion of the universe are related. The energy density of radiation decreases like a^{-4} and the density of matter decrease like a^{-3} as the universe expands. Figure 3.3a shows the fourth-root of the

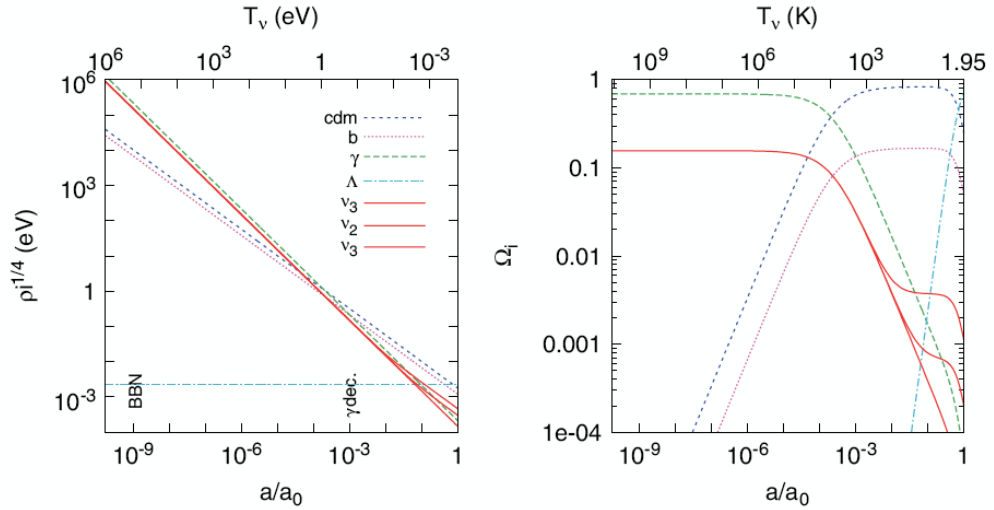


Figure 3.3: Evolution of the energy density of the constituents of the Λ CDM universe: cold dark matter, baryons, photons, cosmological constant, and neutrinos, assuming the normal hierarchy and the lowest mass is zero. On the left, the density of each to the 1/4 power as a function of the scale factor. On the right, the fractional density. The time of big-bang nucleosynthesis and photon decoupling are shown in the left plot. Neutrinos transition from radiation-like to matter-like as they become non-relativistic. Figure from Lesgourgues and Pastor [37].

density for each component as a function of the scale factor a . The cosmological-constant density is time-independent. The neutrino density decreases like radiation when relativistic, and like other matter when non-relativistic.

Figure 3.3b shows the evolution of the fractional energy density of each component Ω_i as a function of the scale factor a . The evolution of the fractional energy density affects large-scale-structure formation. The early universe was radiation dominated, followed by a matter-dominated phase, and the current universe is dark-energy dominated. Neutrinos are different than the other components of the universe, since they convert from radiation-like to matter-like during the phase of structure formation.

To understand large-scale structure, a short history of the universe is necessary. The very early universe was homogeneous with small perturbations. All particles were in thermal equilibrium. A particle species would decouple when the reaction rate per particle

decreased below the Hubble expansion rate. Neutrinos decoupled around a temperature of 1 MeV, shortly before big-bang nucleosynthesis. Photons remained in thermal equilibrium with baryons until recombination. After recombination, both photons and neutrinos were collision-less. The cosmic microwave background (CMB) still retains the signature of the density perturbations at the time of recombination. Near the same time, dark matter began to dominate the energy density. Unlike radiation, the non-relativistic dark matter is pressure-free, so the small initial density fluctuations grew into structures of matter. For a while, both photons and neutrinos free-streamed out of density perturbations. Eventually, during the matter-dominated phase, neutrinos became non-relativistic and converted to a matter component.

Free streaming suppresses the growth of perturbations on scales smaller than the particle travels. For a relativistic neutrino, the free-streaming length is the Hubble radius. Once non-relativistic, the comoving free-streaming length decreases due to the expansion of the universe. Therefore, the comoving free-streaming wave number goes through a minimum, which depends on the neutrino mass [37]:

$$k_{nr} = 0.018 \Omega_m^{1/2} \left(\frac{m}{1 \text{ eV}} \right)^{1/2} h \text{ Mpc}^{-1}. \quad (3.14)$$

Once non-relativistic, the neutrino perturbations start to follow those of cold dark matter.

Large-scale structure is measured with the matter power spectrum. Figure 3.4 shows the ratio of the power spectrum for massive neutrinos to massless neutrinos. The minimum free-streaming wave number increases with mass as in Eq. 3.14, but the larger observable effect of neutrino mass is a suppression of the power spectrum. The suppression occurs at larger wave number—or smaller scales—and is a greater suppression for larger neutrino mass. This is because the non-relativistic neutrinos have a larger energy density with larger mass. When relativistic, neutrino energy density is proportional to the neutrino temperature to the fourth, T_ν^4 . When non-relativistic, the neutrino energy density depends on neutrino mass.

$$\Omega_\nu = \frac{\sum_j m_{\nu_j}}{93 \text{ eV} h^2} \quad (3.15)$$

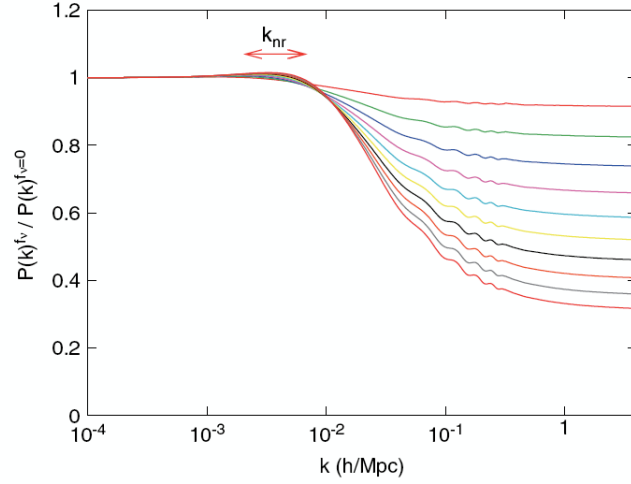


Figure 3.4: Ratio of the power spectrum with three degenerate neutrinos $P(k)^{f_\nu}$ to the three-massless-neutrino power spectrum $P(k)^{f_\nu=0}$. The cosmological constant density and the total matter density are kept fixed at $\Omega_m h^2 = [\Omega_{cdm} + \Omega_b + \Omega_\nu] h^2 = 0.147$ and $\Omega_\Lambda = 0.70$. The minimum free-streaming wave number k_{nr} occurs when neutrinos transition to non-relativistic. The curves correspond to $f_\nu = \frac{\Omega_\nu}{\Omega_m} = 0.01, 0.02, 0.03, \dots, 0.10$, or individual degenerate neutrino mass of 0.046 to 0.46 eV, from top to bottom. Figure from Lesgourgues and Pastor [37].

The non-relativistic neutrino energy density contributed to the expansion of the universe, smearing out perturbations on scales smaller than the free-streaming length.

A larger contribution of Ω_ν today due to a larger neutrino mass reduces the contribution of Ω_{cdm} at matter-radiation equality, since Ω_{cdm} is determined today as $\Omega_m - \Omega_\nu - \Omega_b$. The time of radiation-matter equality depends on Ω_{cdm} , and a smaller value of Ω_{cdm} shifts the start of structure formation to larger scale factor and later times. The time of matter-radiation equality affects the CMB temperature anisotropy spectrum.

Large-scale structure can be characterized in multiple ways. The temperature fluctuations of the CMB shows the power spectrum on large scales at the time of recombination. Recombination occurred before the neutrinos became non-relativistic, so the neutrino-mass signature appears in the evolution of the CMB. The power spectrum at any time τ can be decomposed into the primordial power spectrum, $P_0(k)$, and a transfer function for each wave number, $T(k, \tau)$.

$$P(k, \tau) = P_0(k)T(k, \tau) \quad (3.16)$$

The galaxy power spectrum at the present time can be traced with galaxy surveys, and the luminous matter is mapped to dark matter with a bias parameter.

Limits on neutrino mass from cosmology depend on the complex cosmological model and the number of free parameters. Degeneracies exist between parameters. The limits also depend on which data sets are included, and each type of measurement has different, sometimes large, systematic uncertainties. The current limits from the CMB alone (WMAP) and combined with Type IA Supernovae (SN) and Baryon Acoustic Oscillations are:

$$\begin{aligned} \sum m_{\nu_j} &< 1.3 \text{ eV} (95\% \text{CL WMAP [36]}), \\ \sum m_{\nu_j} &< 0.67 \text{ eV} (95\% \text{CL WMAP + BAO + SN [38]}). \end{aligned} \quad (3.17)$$

These limits are stricter than the Mainz neutrino mass limit. As cosmological observations becomes more precise, the sensitivity of cosmological limits are expected to improve.

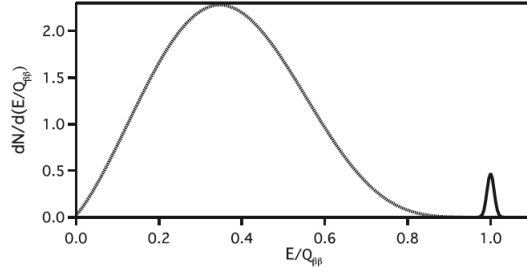


Figure 3.5: The double-beta-decay spectrum. The peak at $Q_{\beta\beta}$ occurs for $0\nu\beta\beta$. Figure from Avignone, Elliot, and Engel [39].

3.3 Neutrinoless Double-Beta Decay Searches

In some unstable isotopes, single-beta decay is forbidden or improbable due to energy or angular-momentum conservation. In these cases, two neutrons can decay simultaneously, releasing two electrons and two electron antineutrinos, denoted as $2\nu\beta\beta$. If the neutrino is its own antiparticle, a Majorana particle, the two neutrinos can annihilate and only two electrons are emitted, denoted as $0\nu\beta\beta$. If observed, neutrinos are Majorana particles and lepton number is violated. Figure 3.5 shows the energy spectrum of the two electrons for $2\nu\beta\beta$ and $0\nu\beta\beta$. For $2\nu\beta\beta$, the spectrum is continuous since the energy is shared between the pair of neutrinos and the pair of electrons. The peak at $Q_{\beta\beta}$, the Q-value, occurs for neutrinoless double-beta decay.

Multiple underlying processes can cause neutrinoless double-beta decay. In the simplest model, the exchange of a light Majorana neutrino, the rate for $0\nu\beta\beta$ depends on an effective Majorana mass $\langle m_{\beta\beta} \rangle$. Similar to single-beta decay, it also depends on the phase space factor for two electrons $G_{0\nu}(Q_{\beta\beta,Z})$, and the nuclear matrix element $M_{0\nu}$.

$$(T_{1/2}^{0\nu})^{-1} = G_{0\nu}(Q_{\beta\beta,Z}) |M_{0\nu}|^2 \langle m_{\beta\beta} \rangle^2 \quad (3.18)$$

The rate for such a process is extremely small since it scales like neutrino-mass squared. The nuclear matrix element is difficult to calculate and introduces an uncertainty on $\langle m_{\beta\beta} \rangle$

of around a factor of two. The effective Majorana mass is a combination of neutrino mass eigenstates and mixing parameters:

$$\langle m_{\beta\beta} \rangle = \left| \sum_j m_{\nu_j} U_{ej}^2 \right|. \quad (3.19)$$

This is a coherent sum, so the Majorana phases in Eq. 2.22 do not cancel. The Majorana phases are completely unknown; the only observable appearance of the Majorana phases may be in $\langle m_{\beta\beta} \rangle$.

Figure 3.6 shows the $0\nu\beta\beta$ observable as a function of the smallest mass eigenstate for both hierarchies. The dark filled areas represent the possible ranges due to the Majorana phases. The lighter filled areas represent the uncertainties in the mixing parameters. The effective mass was calculated from best-fit mixing parameters from the 2006 Particle Data Group evaluation, except for θ_{13} , which is assumed to be the upper limit of 10° . In the normal hierarchy, there is a region where the Majorana phases cancel, making $\langle m_{\beta\beta} \rangle$ much smaller than the lightest mass, even if the neutrino is a Majorana particle. The size of this region depends on the value of θ_{13} . If the neutrino mass is measured by other means but $0\nu\beta\beta$ is not observed, neutrinos could either be Dirac particles or the Majorana phases are canceling in the normal hierarchy. Comparing observations or limits of $0\nu\beta\beta$ to limits from beta decay or cosmology potentially increases our knowledge of the Majorana phases and the processes underlying $0\nu\beta\beta$.

Due to the complications of the nuclear matrix elements and rare nature of $0\nu\beta\beta$, observations should be made in multiple isotopes to create a convincing case. The CUORE experiment will use ^{130}Te -enriched bolometers as a source and detector. They aim for an order of magnitude improvement over the current CUORICINO limits of $\langle m_{\beta\beta} \rangle < 0.19\text{--}0.68\text{ eV}$ [41]. The EXO collaboration will use a liquid time-projection chamber enriched with ^{136}Xe . A prototype of 200 kg of xenon is expected to reach $\langle m_{\beta\beta} \rangle < 0.13\text{--}0.19\text{ eV}$ [42]. The Majorana demonstrator will use 60 kg of germanium, half of it enriched to 86% ^{76}Ge . The collaboration aims for a sensitivity of 0.15 eV [39]. Eventually, Majorana may combine with Gerda for a one-tonne experiment with the goal of 25–50 meV. These experiments are sensitive to the region of degenerate masses and the inverted hierarchy. The smallest values

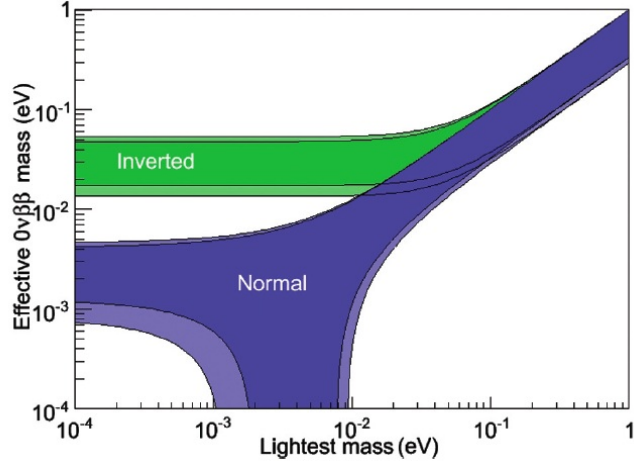


Figure 3.6: The effective Majorana mass as a function of the lowest mass eigenstate in both hierarchies. Figure from the Frontiers of Nuclear Science [40].

of $\langle m_{\beta\beta} \rangle$ in the normal hierarchy remain out of reach.

3.4 Summary of Neutrino Mass Searches

The multiple methods to measure neutrino mass are complementary; direct measurements from beta-decay spectral analysis can be used as an input to cosmological models to break the parameter dependencies. Comparing a direct measurement with a $0\nu\beta\beta$ measurement or limit, we either learn about the Majorana phases or the nature of the neutrino. The challenges of tritium beta decay—increasing the sensitivity and controlling systematic uncertainties—are addressed by the KATRIN experiment.

Chapter 4

THE KATRIN EXPERIMENT

KATRIN is a next-generation tritium-beta-decay experiment. Similar to past experiments, it employs a highly-luminous gaseous tritium source and an extremely precise electrostatic retarding spectrometer as an energy filter. Only a small fraction of the tritium-beta-decay electrons are affected by the neutrino mass, making the experiment challenging. All sections of the experiment must work together to achieve sensitivity to neutrino mass at the sub-eV level.

4.1 Overview

The KATRIN experiment is larger, longer, and more luminous than past experiments. Figure 4.1 shows the major components: the source, the electron transport section, the pre- and main spectrometers, the detector, and the rear calibration section. The experiment is 70 m long, much longer than the 6 m Mainz experiment. Every second, almost 10^{11} neutrinos and electrons are emitted in the gaseous source, an order of magnitude more than in the Troitsk gaseous source. The neutrinos freely stream away, while the electrons are guided by a chain of about forty super-conducting magnets from the source to the detector. In between, the main spectrometer provides an electrostatic retarding potential, which only allows electrons very close to the endpoint—within 30 eV—to pass through to the detector. The detector counts the electrons that overcome the spectrometer’s potential barrier, which arrive at a rate of less than one every second. KATRIN aims for an order-of-magnitude greater sensitivity than the Mainz and Troitsk experiments, down to 0.2 eV (90% CL) [43].

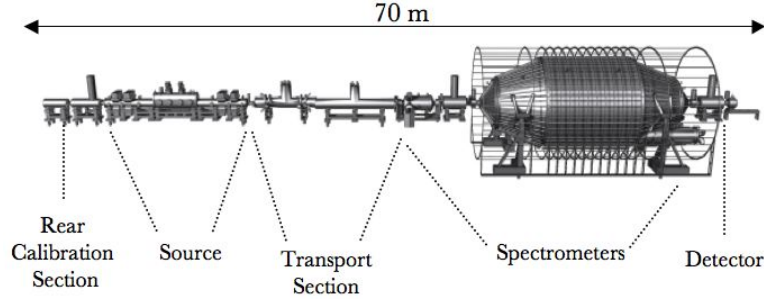


Figure 4.1: Major components of the KATRIN experiment.

4.1.1 Gaseous Tritium Source

The gaseous tritium source is windowless; there is no barrier between the gas and the main spectrometer. Although tritium gas is continuously injected and circulated through the KATRIN source, the source activity must remain extremely stable to control the associated systematic uncertainties. The total source activity is defined by the area of the source and the column density ρd , the number density ρ times the length of the source d . The probability of an electron scattering grows with the column density. Therefore, the amount of un-scattered electrons that can exit the source, represented by an effective column density ρd_{eff} , will not increase for all values of ρd . Alternatively, expanding the source area will continue to boost the source activity. The KATRIN source area is three times larger than the Troitsk source area.

Scattering affects ρd_{eff} and is one factor defining the response function of the experiment, f_{res} . Figure 4.2 shows the scattering cross section of electrons in molecular hydrogen gas. Near the tritium endpoint, the dominant scattering processes are ionization and excitation. The minimum energy loss is about 10 eV for these processes. The beta-decay spectrum is only affected by the neutrino mass within a few eV of the endpoint, so electrons that inelastically scatter in the source are removed from the sensitive energy region.

Elastic scattering, conversely, is much less probable than inelastic scattering, but the average energy loss is only 16 meV per scatter. Therefore, an electron can elastic scatter but remain in the energy region near the endpoint most sensitive to neutrino mass. Although

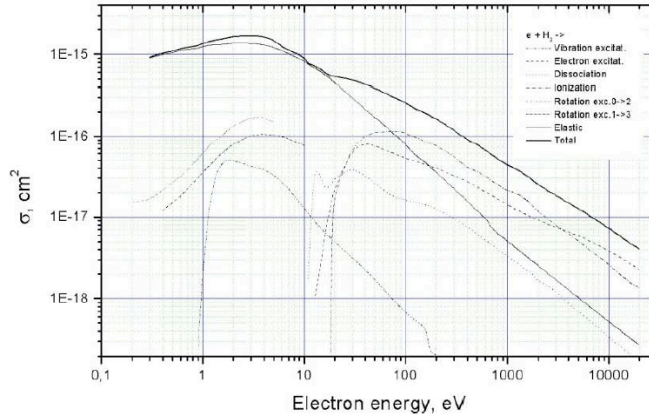


Figure 4.2: Scattering cross-section of e^- off H_2 . Figure adapted from Janev et al. [44].

less probable, the beta-decay spectrum must be corrected for elastic scattering.

The amount of electrons that exit the source without scattering can be attributed to a virtual source, defined by values ρd_{eff} , in which no scattering occurs. The physical source's column density ρd will always be larger than ρd_{eff} due to scattering. Electrons with the longest path length are most likely to scatter. Therefore, the probability for scattering depends on the starting position within the source and the starting angle with respect to the magnetic field lines. Taking the physical source length d to infinity and averaging over all starting positions and angle, we find the maximal virtual source $\rho d_{\text{eff}}^{\text{max}} = 1/2\sigma = 1.6 \times 10^{17}$ molecules/cm², where σ is total inelastic cross section at 18.6 keV. This is the column density produced by a virtual source of length $d_{\text{eff}} = l/2 = 1/2\rho\sigma$, half of the mean free path. The KATRIN will use a column density ρd of 5×10^{17} molecules/cm², which corresponds to an effective column density ρd_{eff} that is 90% of the maximal $d_{\text{eff}}^{\text{max}}$. With these design parameters, 41% of electrons near the endpoint reach the spectrometer without scattering [43].

The column density must be stable to 0.1% to minimize systematic shifts in scattering probability and effective activity. The isotopic purity of the gas, the temperature, and the injection and recirculation rates affect the column density. The tritium purity design goal is 0.95%. The source temperature is kept as low as possible, at 27 K, to achieve the

highest gas density and reduce the pressure, doppler broadening, and space-charge effects. At temperatures much lower than 27 K, tritium molecules would form clusters, creating systematic uncertainties. The column density must be continuously monitored throughout the experiment.

In addition to the macroscopic requirements on the total source stability, the molecular structure and molecular purity of the source can introduce two complications. First, the daughter molecule has electronic, rotational, and vibrational states that can be excited in the decay. Second, the source gas will contain molecules other than pure T₂. Both of these effects introduce multiple beta-decay spectra with different endpoints.

The electronic, rotational and vibrational excitations of the daughter molecule will change the beta-decay spectrum from Eq. 3.8. The actual spectrum is a sum over all possible final states. It depends on the probability of a given final state P_i and the endpoint is lowered by the excitation energy V_i :

$$\begin{aligned} \frac{dN}{dE} = & KF(Z + 1, E)(E + m_e c^2)p \\ & \times \sum_i P_i(E_0 - V_i - E) \sqrt{(E_0 - V_i - E)^2 - m_\nu^2}. \end{aligned} \quad (4.1)$$

Figure 4.3 shows the probability of exciting a given state of the daughter molecule. The atomic excitations have a minimum energy of 20 eV, large enough to remove the electron from the energy region near the endpoint. However, the rotational and vibration excitations of the electronic ground state have smaller excitation energies. Therefore, the excitation energy and probability of the rotational and vibrational states present a potentially large systematic uncertainty and must be well understood.

The second complication is the molecular purity of the source; it will contain molecules and ions other than (³H₂), all of which have different endpoints. Beta-decay of ³H₂ creates an ions, and electrons ionize the source molecules or occasionally cause dissociation. Table 4.1 lists the endpoint energies for various tritium molecules and ions. Since the endpoint for the atomic-tritium ion ³H⁻ is above molecular tritium, a small contamination in the source by atomic-tritium ions can cause decays in the standard ³H₂ analysis window. A small contamination of other molecules or atomic tritium will produce decays below the analysis

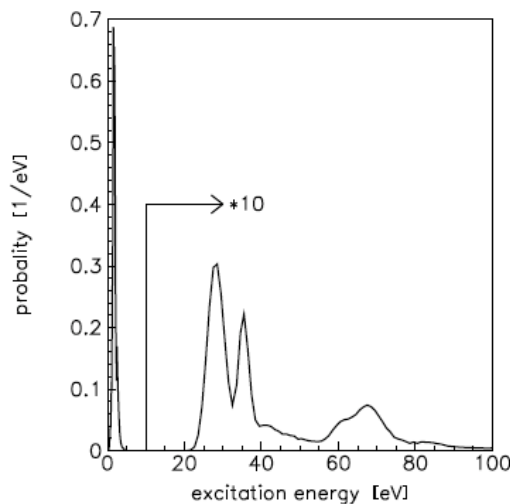


Figure 4.3: Excited states of the $({}^3\text{HeT})^+$ molecule, daughter of T_2 beta decay. The probability of atomic excitations, above 20 eV, have been scaled up by ten for visibility. The rotational and vibrational excitations are below 5 eV. Figure from Saenz, Jonsell, and Froehlich [45].

window. Therefore, the atomic tritium contamination of the source must be minimized, but reducing the contamination of other molecules is not crucial due to the lower endpoints.

An atomic tritium source would avoid complications due to the rotational and vibrational final states, but an atomic tritium gas is technically challenging. Atomic tritium would spontaneously form molecules with hydrogen or tritium. As listed in Tab. 4.1, the endpoint of molecular tritium is higher than atomic tritium. A small contamination of molecular tritium in an atomic source would be difficult to prevent and would cause complications to the atomic spectrum.

4.1.2 Transport Section

The transport section isolates the relatively high-pressure source gas from the rest of the experiment. It reduces the flow of tritium into the main spectrometer by a factor of 10^{11} . If neutral tritium passed through the transport section, it could partially climb the potential barrier of the main spectrometer then decay, creating a background. A combination of

Table 4.1: Endpoints of various tritium decays in relation to the atomic mass difference. Molecular tritium, ${}^3\text{H}_2$, has the second-highest endpoint, second only to the atomic-tritium ion, ${}^3\text{H}^-$. Therefore, the atomic-tritium ion contamination must be reduced. Table from the KATRIN Design Report [43].

Decay Process (with $\bar{\nu}_e$)	$\tilde{Q} = E_0 - \Delta({}^3\text{He}, {}^3\text{H})$	comment
${}^3\text{H} \rightarrow {}^3\text{He}^+ + e^-$	-24.6 eV	atomic decays
${}^3\text{H}^- \rightarrow {}^3\text{He} + e^-$	-0.75 eV	
${}^3\text{H}^+ + e^- \rightarrow {}^3\text{He}^{++} + 2e^-$	-65.4 eV	
${}^3\text{H}_2 \rightarrow ({}^3\text{He}{}^3\text{H})^+ + e^-$	-16.5 eV	molecular decays
${}^3\text{H}_2^+ + e^- \rightarrow ({}^3\text{He}{}^3\text{H})^{++} + 2e^-$	-48.9 eV	
${}^3\text{H}_3^+ + {}^3\text{H} + e^- \rightarrow ({}^3\text{He}{}^3\text{H}_2)^{++} + 2e^-$	-35.1 eV	

differential and cryogenic pumping sections will achieve the necessary reduction in tritium gas. More details on the transport section can be found in the KATRIN Design Report [43].

4.1.3 Spectrometers and MAC-E Filters

The purpose of the main spectrometer is to evaluate the energy of the beta-decay electrons. The main-spectrometer can achieve excellent energy resolution of 0.93 eV at 18.6 keV by implementing a Magnetic Adiabatic Collimation combined with Electrostatic (MAC-E) Filter. These filters were first proposed by Beamson *et al.* [46] and were used for the Mainz [47] and Troitsk [48, 49] experiments. It is a high-pass filter, allowing electrons that have energy greater than qU , the charge times the retarding electric potential, to pass. The spectrometer's electric potential is fixed to some value near the tritium endpoint, and the source potential is scanned to map out the beta spectrum. Therefore, the retarding potential is the difference between these two voltages: $U = U_{\text{Spec}} - U_{\text{Source}}$.

Figure 4.4 illustrates how a MAC-E filter works. Two solenoidal magnets, shown in blue, produce a magnetic field, B_S within the solenoid. The magnetic field lines, represented by blue lines, connect the two solenoids. The region at the half-way point between the two magnets has the minimum magnetic field, B_{min} , and is called the analyzing plane. If a tritium source is placed in the left solenoid, electrons emitted in the forward direction will

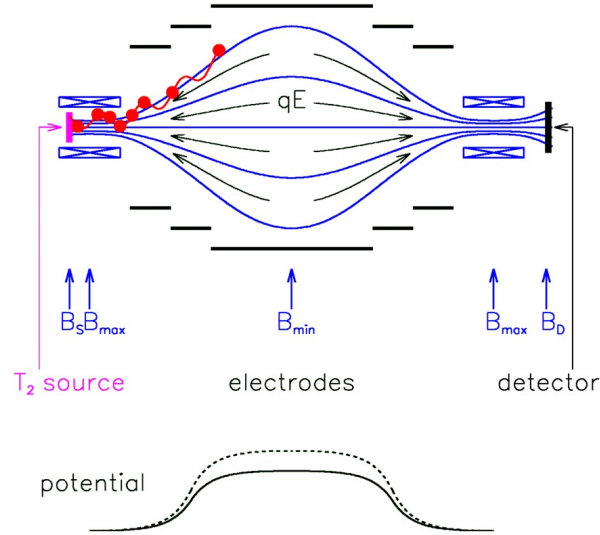


Figure 4.4: Magnetic Adiabatic Collimation with Electrostatic Filter. Figure from C. Weinheimer.

spiral around the magnetic field lines toward the right solenoid. To evaluate the electron's energy, high-voltage electrodes, shown in black, are added outside the guided magnetic field region. The electrodes create an electric field parallel to the magnetic field.

The tritium source emits electrons isotropically. The angular distribution complicates the energy analysis, as the requirement for an electron to pass through the spectrometer depends on the electron energy and initial angle. Defining the parallel energy $E_{||}$ as the energy calculated from the momentum parallel to the electromagnetic fields, the requirement for passing the spectrometer is:

$$E_{||} \equiv \frac{p_{||}^2}{2m} > qU. \quad (4.2)$$

Without collimation, $E_{||}$ is strongly dependent on the initial angle of the electrons with respect to the axes of the solenoids. The MAC-E filter collimates the electrons as they move into a lower magnetic field region, resulting in an electron beam parallel to the electric and

magnetic fields. The electron's cyclotron energy is adiabatically converted into longitudinal energy because the magnetic field is slowly decreasing, and the magnetic moment μ is conserved [46]:

$$\mu = \frac{p_{\perp}^2}{2mB} = \frac{E_{\perp}}{B} = \text{const} \quad (4.3)$$

As can be seen in Eq. 4.3, the smaller the magnetic field in the analyzing plane, the smaller E_{\perp} in the analyzing plane. The electron's momentum is transferred parallel to the electric fields for high-resolution energy analysis. The sharpness of the filter depends on the initial angular distribution of the electrons and the ratio of the magnetic fields. For an isotropic source, it is:

$$\Delta E = \frac{B_A E}{B_S}. \quad (4.4)$$

KATRIN achieves even better energy resolution by using a 6 T pinch magnet after the main spectrometer as a magnetic mirror. A magnetic mirror is the opposite of Magnetic Adiabatic Collimation; as electrons travel into higher field regions, parallel energy is converted into cyclotron motion and the high-angle electrons are reflected. The maximum angle an electron can have in the KATRIN source and pass through the mirror depends on the ratio of the magnetic fields.

$$\sin \theta_S^{\max} = \sqrt{\frac{B_S}{B_{\max}}} \quad (4.5)$$

For KATRIN, with a source field of 3.6 T, the maximum source-angle transmitted is 51° . By limiting the transmitted angles, the pinch magnet improves the energy resolution of the MAC-E filter. Using the analyzing plane magnetic field of 0.3 mT and the pinch magnetic field of 6 T, the energy resolution at 18.6 keV is:

$$\Delta E = \frac{B_A E}{B_{\max}} = 0.93 \text{ eV} \quad (4.6)$$

This is the width of the transmission function, $T(E, qU)$, the probability of an electron

of energy E passing through the main spectrometer. Including the pinch, the transmission function is:

$$T(E, qU) = \begin{cases} 0 & \text{if } E - qU < 0 \\ \frac{1 - \sqrt{1 - \frac{(E - qU)}{E} \frac{B_S}{B_{\min}}}}{1 - \sqrt{1 - \frac{\Delta E}{E} \frac{B_S}{B_{\min}}}} & \text{if } 0 \leq E - qU \leq \Delta E \\ 1 & \text{if } E - qU > \Delta E \end{cases} \quad (4.7)$$

The transmission function, along with the probability of scattering, defines the response function f_{res} of the experiment.

Additionally, the pinch magnet limits the path length of electrons in the source. Large-angle electrons spiral around the field lines many more times, and have a longer path length in the source. Limiting the path length is desirable because it reduces the fraction of electrons reaching the detector that have scattered in the source.

An unfortunate requirement of a MAC-E filter is the size. As the magnetic fields decrease near the analyzing plane, the electron beam spreads out spatially because the magnetic flux is conserved. Assuming a homogeneous magnetic field over a cross section A , the magnetic flux is:

$$\Phi = B_S A_S = B_{\min} A_A \quad (4.8)$$

Since B_{\min} must be much smaller than B_S for a sharp filter, the area of the analyzing plane A_A must be much larger than the area of the source A_S . Re-writing the magnetic fields in terms of the energy resolution and maximum transmitted angle, we find the area of the analyzing plane:

$$A_A = A_S \frac{E}{\Delta E} \sin^2 \theta_S^{\max} \quad (4.9)$$

The main-spectrometer diameter must be 10 m, ten times larger than the Mainz [32] spectrometer.

The conservation of magnetic flux holds for the entire length of the experiment. The

magnetic flux of 191 Tcm^2 in the source is transported through the entire experiment. Therefore, we refer to the guided electrons as the flux tube. At any point in the experiment, the area of the flux tube can be calculated from the value of the magnetic field. Just as electrons do not escape the flux tube, external charged particles of the same energy cannot enter the flux tube.

KATRIN actually employs two spectrometers. The smaller pre-spectrometer performs an initial rejection of low-energy electrons, greatly reducing the flow of electrons into the main spectrometer. The main spectrometer is much larger to achieve the required energy resolution.

4.1.4 *Detector Section*

Electrons that pass through the main spectrometer are counted by the detector. KATRIN uses a highly-segmented silicon detector to achieve high detection efficiency and low background contamination. Figure 4.5 shows the simulated response of the silicon detector to 18.6 keV electrons. The detector energy resolution determines the width of the peak. In the dead layer, or inactive surface region of the detector, electrons lose a small amount of energy that is not included in the signal. As a result, the dead layer causes the low-energy tail.

In addition to the signal peak shown, detector backgrounds create counts at all energies in the real data. To determine the number of signal counts, the spectrum is integrated in the Region of Interest (ROI) around the peak. Therefore, it is important to reduce the background in the ROI. Normally, the ROI is a few keV around 18.6 keV, shifted to slightly lower energy to include the tail. An electric field in the detector section can accelerate electrons toward the detector, increasing the detected energy. This post-acceleration can move the signal and ROI to a region of lower background and also increase the detection efficiency. Post-acceleration decreases the angle of incidence of the electron, decreasing the probability of backscattering off the dead layer. It also decreases the energy loss in the dead layer, as a smaller angle of incidence leads to a shorter path length, and the differential energy loss per step is smaller at higher energy. The detector section is described in greater

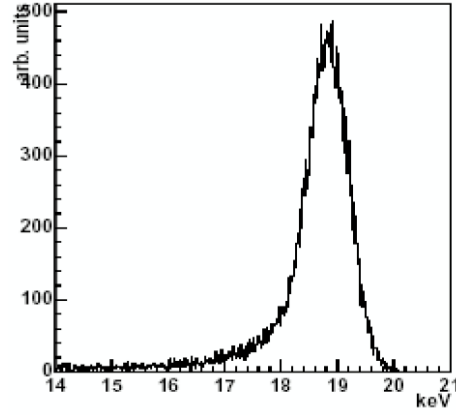


Figure 4.5: Simulated signal of electrons in the silicon detector assuming 800 eV electronic resolution and 50 nm dead layer. Figure from Doe et al. [50].

detail in Section 5.1.

4.1.5 Rear Calibration and Monitoring Section and Other Calibrations

Calibration and monitoring are necessary to understand systematic uncertainties. The rear calibration and monitoring system consists of an electron gun and a monitor detector. The monitor detector will continuously measure the activity of the source. The rear system is covered by a conducting plate which defines the electric potential in the gaseous source.

The rear electron gun is used to measure the response function f_{res} of the experiment. It shines electrons through the tritium gas in the source, measuring the scattering off the source molecules and the transmission function of the spectrometer. Since the electrons follow field lines, all electrons from the gun will strike a single pixel in the detector. This creates a challenge for the data acquisition system (DAQ), as the rate from the rear electron gun will be 100 kHz focused into one pixel. After an initial measurement of the response function f_{res} , the column density can be monitored every two hours by shining the same electron gun through the source and measuring the scattering of electrons.

The source gas is not necessarily neutral; beta-decay electrons ionize the gas. The space charge in the source gas can be monitored by adding gaseous ^{83m}Kr . The ^{83m}Kr

decay produces conversion electrons with well-defined energies. Three conversion lines are of importance for KATRIN: the K-32 conversion line at 17.8 keV, the L₃-32 line at 30.4 keV, and N-32 line at 32.1 keV. Space-charge potentials in the tritium can shift or smear the conversion lines. The potential shift due to the space-charge effect can be determined by comparing the positions of the lines when the source is filled with only krypton gas with the line positions when the source has both tritium and krypton gas.

The main-spectrometer retarding potential is calibrated into absolute energy with a ^{83m}Kr source. The K-32 line is well-defined and only 800 eV below the tritium endpoint. Mapping the position of this peak with respect to the main-spectrometer retarding potential calibrates the retarding potential into energy. If tritium and krypton are combined in the source and the retarding potential is below the K-32 line, the rate at the detector will be 1.2 MHz spread through all pixels. This is also a very challenging calibration for the DAQ.

4.1.6 Expected signal and analysis

KATRIN will measure the integrated tritium-beta-decay rate by counting the electrons that pass through the main spectrometer at multiple retarding potentials. The number of events in the detector peak, as in Fig. 4.5, includes the potential-dependent signal and a background rate, b , assumed to be independent of the retarding potential. The total number of counts, N_{Tot} , is the integral of Eq. 4.1 multiplied by the number of tritium molecules, N_{T_2} , in the source, the measuring time, t , the response function of the experiment, $f_{res}(E, qU)$, and the detector efficiency, $\epsilon(E)$:

$$N_{Tot}(qU, m_\nu, E_0, b) = bt + N_{T_2}t \int_{qU}^{E_0 - m_\nu} f_{res}(E, qU)\epsilon(E) \frac{dN}{dE} dE. \quad (4.10)$$

The response function is a convolution of the spectrometer transmission function and energy loss in the source, including multiple scattering. The detector efficiency is largely independent of energy over the 30 eV integration range, qU to $E_0 - m_\nu$. Post-acceleration of the electrons can increase the detected energy by up to 30 keV and increase the detection efficiency. Using multiple retarding potentials, we measure the integral spectrum as a function of the potential.

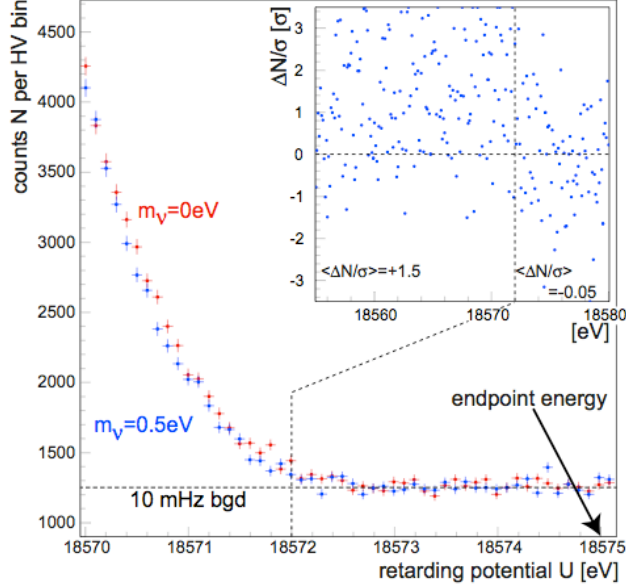


Figure 4.6: Simulated integral β spectrum including a constant background of 10 mHz per measurement point for two values of neutrino mass, $m_\nu = 0$ eV (red; upper dots) and $m_\nu = 0.5$ eV (blue; lower dots). The inset shows the relative difference between the points. Figure from the KATRIN Design Report [43].

Figure 4.6 shows simulations of multiple retarding potentials for two values of the neutrino mass. Each point is the number of detected counts for a given retarding potential, including the target background of 10 mHz. The simulation assumes one year of measuring time uniformly distributed between each point within the interval $[E_0 - 20 \text{ eV}, E_0 + 5 \text{ eV}]$. The inset shows the relative difference of the points $\Delta N/\sigma$. There is a clear difference between the points in the beta-spectrum region and the difference is compatible with zero in the background region.

A spectrum like the one shown in Fig. 4.6 will be fit to determine the parameters m_ν , E_0 , and b . The background is measured by setting the retarding potential above the endpoint. With a retarding potential much lower than the endpoint, the high signal rate enables an accurate determination of the endpoint. A single measurement is most sensitive to neutrino mass a few eV below the endpoint. Therefore, to decrease the statistical uncertainties on

the points with the most sensitivity to neutrino mass, more time will be spent measuring a few eV below the endpoint. Since the spectrum actually depends on m_ν^2 , an increase of 100 in the signal rate near the endpoint would only improve the measurement of m_ν by 10.

We can gain some insight to the signal by integrating Eq. 4.10. For simplicity, we approximate the response function and detection efficiency as a constant. In Eq. 4.1, we neglect the final states. Near the endpoint the Fermi function, $F(Z+1, E)$, and the electron total energy and momentum approach constants. With these approximations, the integrand becomes:

$$N_{T_2} t \frac{dN}{dE} = 3rt(E_0 - E)[(E_0 - E)^2 - m_\nu^2]^{1/2} \quad (4.11)$$

where all the constants have been absorbed into three constants, 3, r , and t . Integrating over electron energy from the retarding potential to the endpoint and Taylor expanding about $m_\nu^2/(E_0 - qU)^2$, we find the number of signal electrons:

$$N_s \approx rt(E_0 - qU)^3 \left[1 - \frac{3}{2} \frac{m_\nu^2}{(E_0 - qU)^2} \right]. \quad (4.12)$$

Neglecting neutrino mass, we see that the signal rate increases as $(E_0 - qU)^3$. Using the KATRIN design parameters for the source area, column density and the response function of the experiment, $r \approx 1.1 \text{ mHz/eV}^3$. As discussed below, the retarding potential will vary between $E_0 - 30 \text{ eV}$ and $E_0 + 5 \text{ eV}$ for neutrino-mass measurements. Therefore, the signal rate at the detector will vary between 0 and 100 Hz. For retarding potentials most sensitive to neutrino mass, the signal rate will be close to 20 mHz, twice the target background rate.

4.2 Systematic Uncertainties and Sensitivity

To achieve the optimal sensitivity to neutrino mass, the statistics must be maximized and the systematic uncertainties must be well-understood and minimized. The statistical uncertainty was investigated with simulations of a KATRIN-like signal for four experimental configurations [43]. Figure 4.7 shows the statistical uncertainty in each configuration as a function of retarding potential interval. The largest statistical uncertainties, curve (a), use

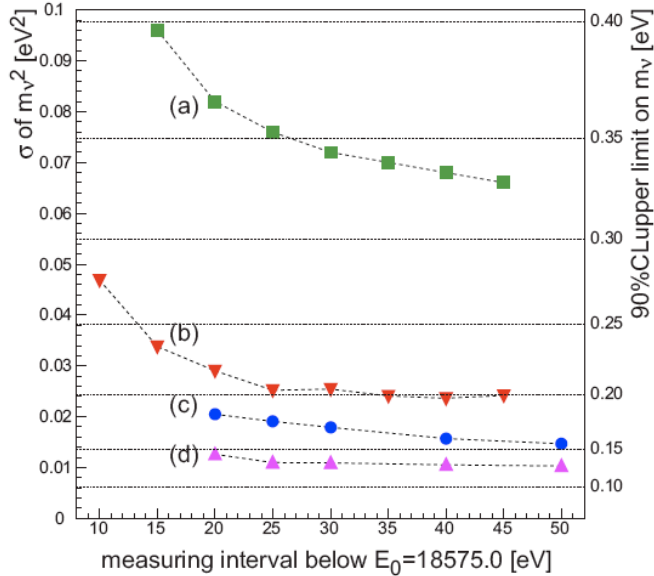


Figure 4.7: Statistical uncertainty on m_ν^2 as calculated from simulated KATRIN-like spectra. This assumes three years of live time and is shown as a function of the analysis interval for four experimental configurations: (a) using design parameters from the letter of intent, including a 7 m-diameter main spectrometer, (b) 10 m-diameter spectrometer and uniform measuring time for each retarding potential, (c) the standard design, a 10 m-diameter spectrometer and optimized measuring times, and (d) reducing the total background from 10 mHz to 1 mHz. The right vertical axis is the corresponding 90%CL upper limit on m_ν assuming zero systematic uncertainty. Figure from the KATRIN Design Report [43].

the design values from the KATRIN Letter of Intent [51]. This includes a smaller-diameter spectrometer of 7 m, a smaller-diameter source, and a background rate of 10 mHz. Curve (b) uses the current design parameters, including a 10 m-diameter spectrometer and a background rate of 10 mHz. The improvement to curve (c) is achieved by optimizing the time at each retarding potential, such that the points most sensitive to neutrino mass have the longest measuring time. Curve (d) is for a reduced background of 1 mHz total. For each configuration, the statistical uncertainty decreases at larger analysis intervals. Systematic uncertainties, especially from energy loss in the source, will increase for larger intervals. The minimum total uncertainty is expected over the interval $[E_0 - 30 \text{ eV}, E_0 + 5 \text{ eV}]$. From

curve (c), the projected statistical uncertainty over this interval is:

$$\sigma_{stat}(m_\nu^2) = 0.018 \text{ eV}^2. \quad (4.13)$$

To keep the systematic uncertainties as small as the statistical uncertainty, KATRIN aims to limit each systematic effect to less than 0.0075 eV^2 shift in m_ν^2 . Each identified systematic effect has been investigated, and the expected uncertainties are listed in Tab. 4.2. The three largest systematic effects are the stability of the source column density, the description of the final states, and the energy loss in the source. High-voltage variations in the main spectrometer and elastic scattering in the source are also large systematic effects. Smaller systematic uncertainties arise if the background is dependent on the retarding potential, and from potential and magnetic field variations in the source. A varying source magnetic field changes the maximum angle of electrons that pass through the pinch magnet. The estimated individual systematic uncertainties are all lower than the target maximal shift. As a conservative estimate for the total systematic uncertainty, KATRIN assumes five contributions of maximal shift 0.0075 eV^2 , larger than the estimated total in the table.

$$\sigma_{\text{sys, tot}}(m_\nu^2) \leq 0.017 \text{ eV}^2 \quad (4.14)$$

With the KATRIN design parameters and expected three-year live time, the systematic and statistical uncertainties are approximately equal: $\sigma_{\text{sys}}(m_\nu^2) \leq 0.017 \text{ eV}^2$ and $\sigma_{\text{stat}}(m_\nu^2) = 0.018 \text{ eV}^2$. Using these assumptions, Fig. 4.8 shows the KATRIN sensitivity to m_ν . Since the actual observable is m_ν^2 , the discovery potential is defined as $m_\nu = \sqrt{5\sigma_{\text{tot}}(m_\nu^2)} = 0.35 \text{ eV}$. Assuming the measured m_ν is zero, the 90% CL upper limit is $m_\nu = \sqrt{1.64\sigma_{\text{tot}}(m_\nu^2)} = 0.20 \text{ eV}$, since negative neutrino mass is unphysical.

To achieve a better understanding of the statistical uncertainty, it can also be estimated analytically by differentiating Eq. 4.12 with respect to m_ν^2 and assuming Poisson statistics

Table 4.2: All of the identified systematic shifts are estimated to be less than the target of 0.0075 eV^2 . The estimates are made on the retarding potential interval $[E_0 - 30 \text{ eV}, E_0 + 5 \text{ eV}]$ except the column density, as noted. As a conservative estimate, the total systematic uncertainty is assumed to contribute $\sigma_{sys}(m_\nu^2) \leq 0.017 \text{ eV}^2$. Table from the KATRIN Design Report [43].

Source of Systematic Shift	Achievable/Projected Accuracy	Systematic Shift $\sigma_{sys}(m_\nu^2)[10^{-3}\text{eV}^2]$
description of final states	$f < 1.01$	< 6
T^- ion concentration $n(T^-)/n(T_2)$	$< 2 \times 10^{-8}$	< 0.1
unfolding of the energy loss function (determination of f_{res})		< 2
		< 6 (including a more realistic e-gun model)
monitoring of ρd [$E_0 - 40 \text{ eV}, E_0 + 5 \text{ eV}$]	$\Delta\epsilon_T/\epsilon_T < 2 \times 10^{-3}$ $\Delta T/T < 2 \times 10^{-3}$ $\Delta\Gamma/\Gamma < 2 \times 10^{-3}$ $\Delta p_{inj}/p_{inj} < 2 \times 10^{-3}$ $\Delta p_{ex}/p_{ex} < 0.06$	$< \frac{\sqrt{5 \times 6 \times 5}}{10}$
background slope	$< 0.5 \text{ mHz/keV}$ (Troitsk)	< 1.2
HV variations	$\Delta\text{HV}/\text{HV} < 3 \text{ ppm}$	< 5
potential variations in the WGTS	$\Delta U < 10 \text{ meV}$	< 0.2
magnetic field variations in the WGTS	$\Delta B_S/B_S < 2 \times 10^{-3}$	< 2
elastic $e^- - T_2$ scattering		< 5
Total identified syst. uncertainties		$\sigma_{syst,tot} = \sqrt{\sum \sigma_{syst}^2} \approx 0.01 \text{ eV}^2$

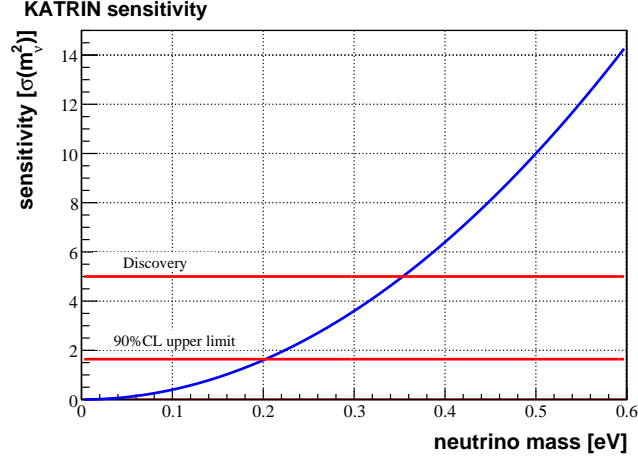


Figure 4.8: KATRIN sensitivity assuming $\sigma_{tot}(m_\nu^2) = 0.025 \text{ eV}^2$, which could be reached after three years of live time. The discovery potential for m_ν is 0.35 eV at 5σ or a mass limit of 0.2 eV (90% CL).

for the total number of counts [52]:

$$\sigma_{stat}(m_\nu^2) = \frac{2}{3rt(E_0 - qU)} \sqrt{N_S + N_b}. \quad (4.15)$$

Both the statistical uncertainty and the number of signal counts, N_S , are functions of the retarding potential. Minimizing the uncertainty with respect to $E_0 - qU$ determines the optimal retarding potential:

$$\frac{\partial \sigma(m_\nu^2)}{\partial (E_0 - qU)} = 0 \text{ for } 2N_b = N_S = rt(E_0 - qU)^3. \quad (4.16)$$

Therefore, the statistical uncertainties are at a minimum when the signal is twice the background. The optimal retarding potential is:

$$(E_0 - qU) = \left(\frac{2b}{r}\right)^{1/3} = 2.6 \text{ eV}. \quad (4.17)$$

The minimum statistical uncertainty occurs at the optimal retarding potential:

$$\sigma(m_\nu^2) = \left(\frac{16}{27}\right)^{1/6} \frac{b^{1/6}}{r^{2/3}t^{1/2}}. \quad (4.18)$$

This analytic minimum statistical uncertainty illuminates the statistical dependence on the signal rate r , the background rate b , and the measuring time t , but is not the actual statistical uncertainty. Correlations between parameters require measurements at many retarding potentials to fix all of the parameters. The projected statistical uncertainty was estimated with full simulations of a KATRIN-like experiment.

From Eq. 4.18, we see the statistical uncertainty on m_ν^2 decreases as $t^{-1/2}$. Figure 4.9a shows this evolution for the first year of live time, assuming $\sigma_{stat}(m_\nu^2) = 0.018 \text{ eV}^2$ is reached in three years of live time. The statistical uncertainty on m_ν is the square root of $\sigma_{stat}(m_\nu^2)$, and will be proportional to $t^{-1/4}$. The 90% CL upper limit on m_ν depends on the systematic uncertainties as well as the statistical uncertainty. Figure 4.9b shows the 90% CL upper limit on m_ν assuming the systematic uncertainty has been accurately determined. Within a few weeks of operation, the KATRIN experiment will exceed the Mainz and Troitsk limits.

We can also investigate correlations of the neutrino mass with E_0 analytically by differentiating Eq. 4.12 with respect to E_0 :

$$\begin{aligned} \delta N_s = 0 &= \delta m_\nu^2 + \delta E_0, \\ \delta m_\nu^2 &\approx 2(E_0 - qU)\delta E_0. \end{aligned} \quad (4.19)$$

Again, we see the importance of measuring the spectrum close to the endpoint to minimize $(E_0 - qU)$. Because of this correlation, external measurements of E_0 are currently not accurate enough to improve the m_ν sensitivity and E_0 must be a free parameter in the fit. The most recent Penning trap measurement of the mass difference of the neutral mother and daughter atoms, $\Delta M(\text{T}, {}^3\text{He}) = 18589.8 \pm 1.2 \text{ eV}$ [53], corresponds to a relative uncertainty of 4×10^{-10} on the actual T and ${}^3\text{He}$ masses. Taking into account the molecular bonds of the tritium molecule, $E_0(T_2)$ is calculated from the mass difference and is $18571.8 \pm$

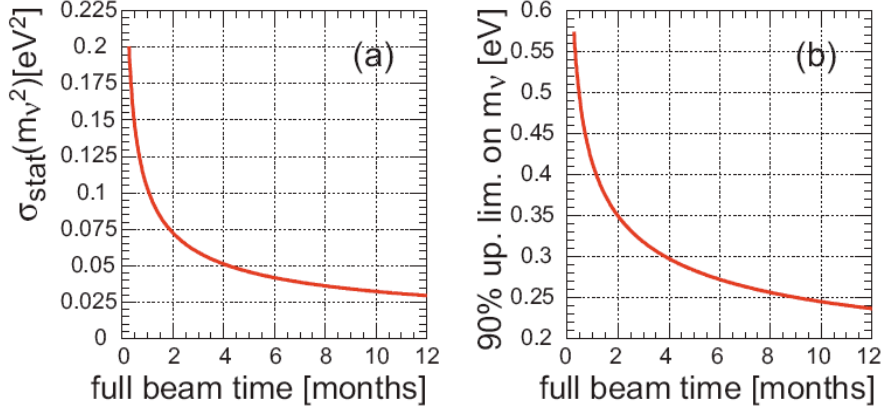


Figure 4.9: (a) KATRIN statistical uncertainty on m_ν^2 as a function of live time, where $\sigma_{stat}(m_\nu^2) = 0.018 \text{ eV}^2$ after three years of live time. (b) Once the systematic uncertainties are determined, the sensitivity to m_ν will exceed the Mainz limit of 2.3 eV [32] within a few weeks. Figure from the KATRIN Design Report [43].

1.2 eV [54]. Using this measurement of E_0 instead of a fit, the uncertainty on m_ν^2 at the optimal retarding potential would be above 6 eV, higher than the uncertainty achieved by letting E_0 float in the fit. To improve the measurement of m_ν^2 with an external measurement of E_0 , the uncertainty on E_0 needs to be less than 0.005 eV [31]. This corresponds to a relative uncertainty of 2×10^{-12} on the T and ^3He masses, two orders of magnitude better than the current value. In contrast, determining E_0 from a fit to the KATRIN data is sensitive to the relatively small potential differences in measurement points.

Even if Penning traps cannot achieve this accuracy on E_0 , external measurements can be compared with KATRIN's best-fit to check for unidentified systematic shifts on m_ν^2 due to high voltage shifts or space-charge effects in the source gas. A gaussian variation on the high voltage with width σ will cause a systematic shift on m_ν^2 of order $2\sigma^2$ [55]. As listed in Tab. 4.2, the high voltage must be stable to 3 ppm, or 50 mV.

4.3 Backgrounds

For an experiment with vanishingly small signal, reducing the background is an important goal. From Eq. 4.18, we see the statistical uncertainty at the optimal retarding potential rises as the 6th root of background. This is a weaker dependence than the standard Poisson square root as in Eq. 4.15 because it includes an optimization of the retarding potential, and a higher background pushes the optimal retarding potential to a lower value. The systematic uncertainties increase at lower retarding potentials. For our goal of a 10 mHz background rate, the systematic and statistical uncertainties are projected to be equal.

The actual dependence of the statistical uncertainty on the background can be discerned from the full simulation of a KATRIN spectrum, as in Fig. 4.7, which includes correlations between all parameters. Comparing the points of curve (c) and (d), the simulation shows $\sigma_{stat}(m_\nu^2) \propto b^{1/4}$.

A longer measuring time can compensate for a larger background as shown by M. Steidl [56]. Using sensitivity estimates from the full KATRIN spectrum simulation, Steidl found an increase of the live time by 1.5 months or of the real time by 2.5 months compensated for an increase in the background rate from 10 mHz to 11 mHz.

These results apply to all KATRIN backgrounds, regardless of the source of the events. There are two very different sources of background for KATRIN. The peak in Fig. 4.5 includes both the signal electrons and any background electrons coming from the main spectrometer. A second source of background is intrinsic to the detector and appears as a continuum under the peak.

4.3.1 Spectrometer-Related Backgrounds

The spectrometer-related background is defined as any electrons that reach the detector from the spectrometer. This is the anticipated major background source and the target limit is 9 mHz. These background events are identical to the signal events, and so the production rates must be minimized. There are multiple production mechanisms and multiple techniques for reducing them.

Any electrons within the flux tube that can climb the spectrometer's retarding potential

reach the detector. In addition to the signal electrons, ionization of the residual gas in the large-volume main spectrometer can produce a background of electrons. The ionization cross section of electrons in hydrogen gas peaks at 100 eV, as shown in Fig. 4.2. Therefore, the low-energy electrons in the analyzing plane of the main spectrometer can easily create many more electrons in the residual gas, which are a background for KATRIN. The main spectrometer must adhere to extremely strict vacuum requirements to prevent ionization of the residual gas. Also, great care has been taken in the design of the spectrometers to prevent penning traps for electrons. When electrons are trapped, they have extremely long path lengths and ionization is much more likely, resulting in large backgrounds.

There is a small probability that electrons can enter the flux tube from the spectrometer walls. These electrons will also follow the field lines to the detector. Cosmic rays or natural radioactivity create a large number of electrons through ionization in the vessel walls. By applying a more negative potential to a low-mass wire electrode inside the vessel, the number of background electrons entering the flux tube is minimized.

Tritium decay in the spectrometer is also considered a spectrometer-related background. The long transport section reduces the flow of tritium to an acceptable level.

4.3.2 *Detector-Related Backgrounds*

In addition to the spectrometer background, the detector inevitably contributes to the background. These backgrounds can be from cosmic rays or natural radioactivity in the detector region and are not correlated with the beam of signal electrons. With a careful detector-region design, we may reach the target limit of 1 mHz.

Early estimates of the detector-related backgrounds were made by F. Schwamm [57] using a preliminary design for the KATRIN detector region. These first simulations showed lines from X-ray photons in the nominal Region of Interest (ROI) near the endpoint, and a large number of electrons in the continuum. Using a 3.5 keV wide ROI, between 15.9–19.4 keV, Schwamm estimated a total detector-related background rate of 15.4 mHz (99% CL). With 30 kV of post-acceleration, Schwamm estimated a reduced background of 5.5 mHz (99% CL). The three largest sources of background were the ^{210}Pb in the electronics solder

and ^{232}U and ^{232}Th in the ceramic detector mount and signal traces. These components lie within a few mm of the detector, behind the detector and inside the magnetic flux tube.

Clearly, the detector backgrounds can be significantly higher than the target if the detector region is not carefully designed. In this work, we estimate the detector-related backgrounds, building on the early estimates of Schwamm. The connection scheme to the detector has been redesigned eliminating the largest background sources identified by Schwamm. In addition to sources investigated by Schwamm, we include cosmic rays and radiation from the detector environment. The latest background estimates and the achievable reductions are discussed in Chapter 8.

4.3.3 Region of Interest Effect on Sensitivity

The two types of backgrounds have a different dependence on the width ΔE of the region of interest. The signal and spectrometer-related backgrounds appear as a gaussian peak with a long low-energy tail. The fraction of electrons detected, $f(\Delta E)$, will be the same for the signal and spectrometer background. The fraction detected depends on the detector response function, which is a function of detector energy resolution, detector dead layer, and the energy and angle of incidence of the electron. Assuming the detector background is a flat continuum, the detector background will depend linearly on ΔE . Therefore, we can modify the analytic statistical uncertainty at the optimal retarding potential with a Figure of Merit, F [50]. We assume the statistical uncertainty has a $b^{1/4}$ dependence as suggested by simulations.

$$\sigma_{stat}(m_\nu^2) = \left(\frac{16}{27}\right)^{1/6} \frac{b^{1/4}}{r^{2/3}t^{1/2}} F \quad (4.20)$$

$$F = \frac{[f(\Delta E) + \alpha\Delta E]^{1/4}}{f(\Delta E)^{2/3}}$$

The statistical uncertainty increases with F , so we minimize F with respect to ΔE .

Using the detector response function shown in Fig. 4.5, the Figure of Merit has been investigated as a function of dead layer, detector energy resolution, and background, assuming no post-acceleration. Post-acceleration up to 30 kV will affect the response function. Fig-

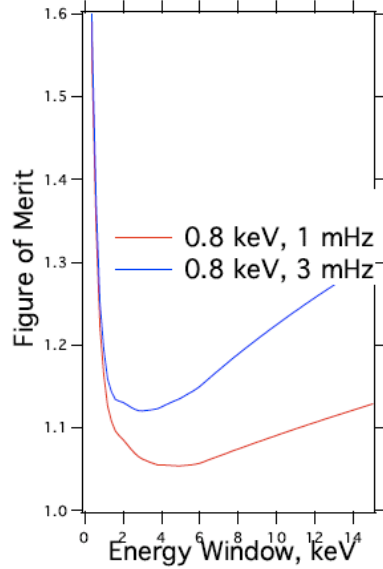


Figure 4.10: Figure of Merit F as a function of ROI width assuming the statistical uncertainty $\sigma_{stat}(m_\nu^2) \propto b^{1/4}$. Two values of detector background are shown for a detector energy resolution of 0.8 keV FWHM and a dead layer of 50 nm. Figure from Doe et al. [50].

Figure 4.10 shows the dependence on the width of the energy window, ΔE , for two values of detector background per 2.4 keV window. The spectrometer-related background is assumed to be 10 mHz, higher than the design goal of 9 mHz. There is a clear increase in the Figure of Merit for larger values of detector background—and therefore an increase in the statistical uncertainty. The optimal ROI may be wider than the assumed 2.4 keV width, and wider than the 3.5 keV width assumed by Schwamm. Clearly, reducing the detector backgrounds will help reduce the statistical uncertainty on m_ν .

4.4 Summary of the KATRIN Experiment

The KATRIN experiment faces a number of challenges in pushing the neutrino mass sensitivity down an order of magnitude. With a more luminous source, more accurate analyzing potential, and high-efficiency, low-background detector, KATRIN should reach the projected sensitivity.

Chapter 5

THE DETECTOR AND DATA ACQUISITION SYSTEM

Electrons emerging from the KATRIN main spectrometer enter the detector system. Magnetic fields guide the electrons to a silicon detector which counts them with high efficiency. This detector must have good energy and position resolution and have low intrinsic backgrounds. Post-acceleration, an active veto, a passive shield, and the magnetic field setting help reduce the detector backgrounds. The signals from the detector must be accurately recorded by the data acquisition system. Since the detector system is open to the main spectrometer, it must adhere to strict vacuum requirements to preserve the vacuum in the main spectrometer.

5.1 Detector Region Design

Within the detector system, shown in Fig. 5.1, electrons are guided by two magnets: the pinch and detector magnets. The flux tube of electrons, shown in green in Fig. 5.1, expands and contracts in the changing magnetic field. The flux tube diameter must be smaller than all the vacuum tubes and the silicon detector to avoid scattering and count all the electrons. The detector is positioned within the detector magnet, offset 16 cm toward the readout direction. Table 5.1 shows the design parameters for the detector region.

Table 5.1: Detector region design parameters.

Feature	Design goal
Detector Background	1 mHz
Detector-magnet Field	3.6–6 T
Post-acceleration Voltage	up to 30 kV
Extreme-High Vacuum	10^{-11} mbar

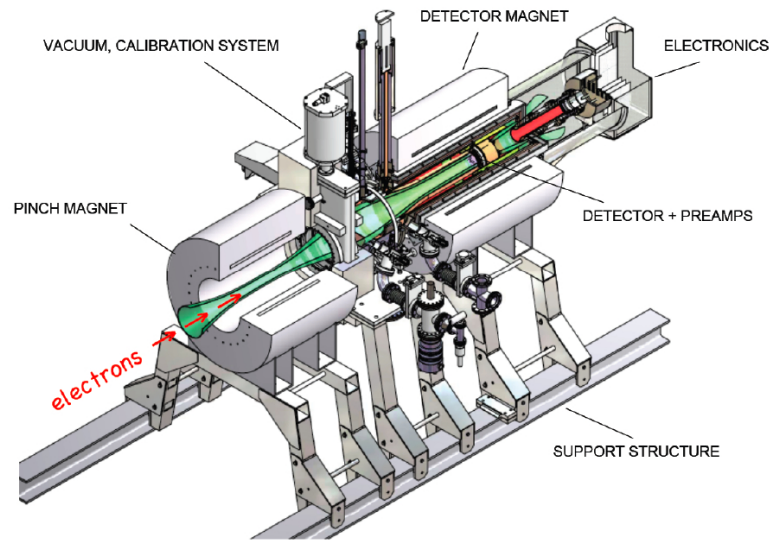


Figure 5.1: Detector region design. Figure from T. Burritt.

At 6 Tesla, the pinch magnet has the highest magnetic field of any magnet in the KA-TRIN experiment. As discussed in Section 4.1.3, it limits the angle of electrons that reach the detector and determines the energy resolution of the main spectrometer.

The detector magnet can be varied between magnetic fields of 3.6 to 6 T to optimize the backgrounds and detection efficiency. The area of the flux tube at the detector depends on the magnetic field at the detector. At the minimum field setting of 3.6 T, the field at the detector is 3.3 T, setting the required detector radius at more than 4.3 cm. If the field at the detector increases to 5 T, the flux tube radius decreases to 3.5 cm. Assuming the total detector background does not change with magnetic field, using a smaller section of the detector will reduce the background. Therefore, the detector must be segmented to allow use of only the inner 3.5 cm. Unfortunately, a higher magnetic field decreases the detection efficiency. Since the magnetic moment is conserved as in Eq. 4.3, the angle of incidence with the detector increases with magnetic field. The higher angle increases the probability that an electron will backscatter off the detector.

The detector region design includes a post-acceleration electrode, which accelerates elec-

trons to higher energy. This can move the signal of electrons to a region of lower background. Post-acceleration also improves the detector efficiency in two ways. At higher energy, the differential energy loss of electrons is smaller, so the electrons lose less energy in the detector dead layer. Since post-acceleration increases the electron's longitudinal momentum, it decreases the angle of incidence with the detector. Fewer electrons backscatter off the detector at low angles. Also, the electron path length in the dead layer is shorter for low-angle electrons.

Post-acceleration requires a large number of insulators which are not visible in Fig. 5.1. Three quartz tubes of various diameters separate the post-acceleration electrode and elevated readout tube from the grounded medium-high vacuum (MHV) tube. Between the magnets, a large ceramic insulator connects the post-acceleration electrode to the grounded gate valve. Another small ceramic insulator is on the readout side.

The post-acceleration electrode doubles as the vacuum tube inside the detector magnet. The electrons travel through extreme-high vacuum (XHV) of 10^{-11} mbar. Vacuum pumps, a gate valve, and the calibration system are between the two magnets. A retractable electron gun and radioactive ^{241}Am source can be used to calibrate the detector.

The preamps are close to the detector, but are not compatible with XHV. Instead, they are mounted behind the detector in a medium-high vacuum (MHV) region of 10^{-8} mbar. The detector and preamps are cooled to reduce thermal noise. A pulse-tube cooler mounted between the magnets is connected to the post-acceleration electrode. This cools the entire electrode, detector, and preamp housing. The detector operates at -100°C and the electronics at -40°C . Further downstream of the preamps are the distribution and cable electronics boards.

5.1.1 Silicon Detector

Electrons are detected in a segmented silicon detector. Due to its doping profile shown in Fig. 5.2, the detector is called a *p-i-n* diode. The bulk material is *n*-type intrinsic silicon. The front side has uniform shallow *n*++ doping. The rear surface is *p*-type doped and contains the segmentation pattern shown in Fig. 5.3a. There are twelve rings on the detector and

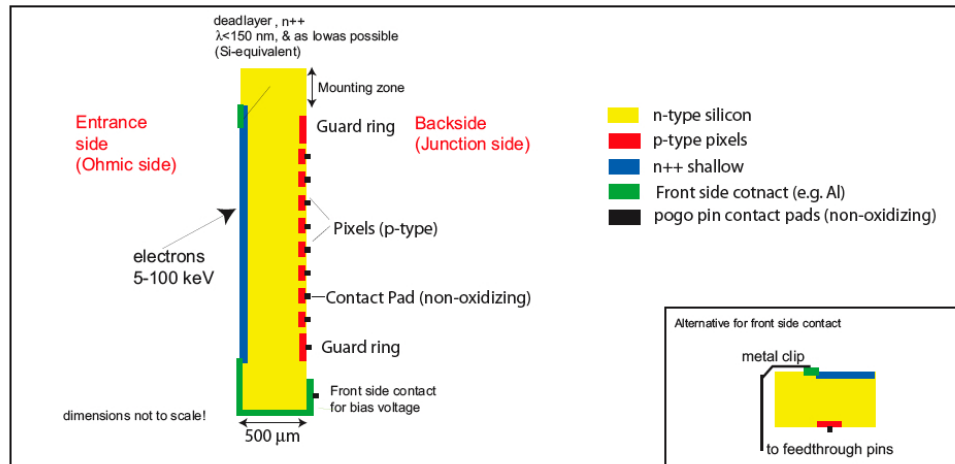


Figure 5.2: Cross section and doping scheme of the silicon detector. Figure from M. Steidl et al. [58].

four inner pixels.

This segmentation pattern has multiple benefits. First, every pixel has the same area and capacitance and therefore should have the same noise. Second, the radial segmentation allows the use of only the inner section of the detector with a higher magnetic field, possibly reducing the backgrounds. For a magnetic field at the detector of 5 T, the signal electrons will impact only the inner eight rings of pixels. Third, the radial width of each pixel decreases with radius, compensating for the inhomogeneities of the magnetic and electric fields in the main spectrometer. The transmission function defined in Eq. 4.7 assumes constant electric and magnetic fields across the radius of the main spectrometer. In reality, the field variations increase the width of the transmission function. With radial segmentation, the field variation across a pixel is limited, and the width of the transmission function is the same for each pixel [59].

The wafer has a radius of 5.7 cm, but the radius of the sensitive area is only 4.5 cm.

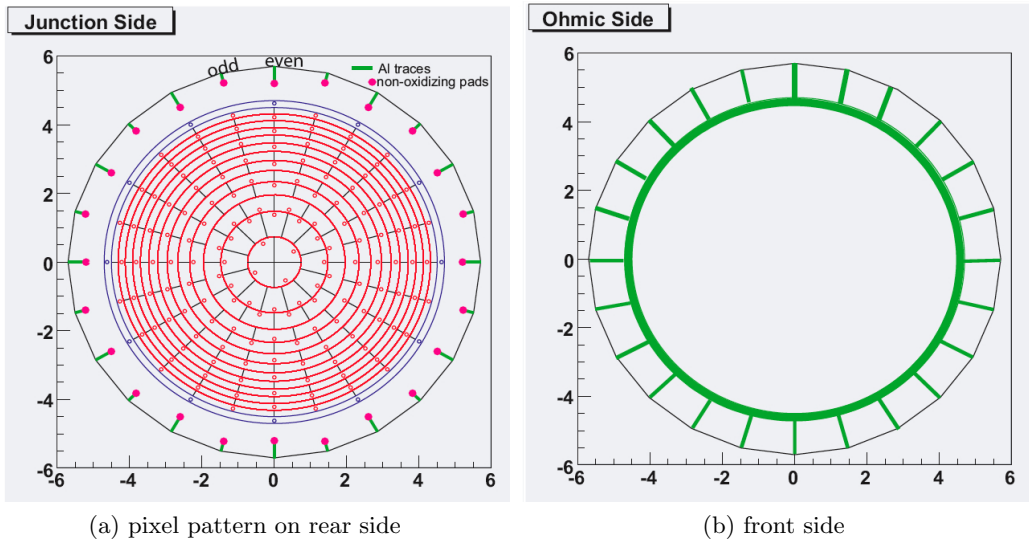


Figure 5.3: Detector segmentation pattern. Figure from M. Steidl et al. [58].

Figure 5.3a shows the sensitive pixels on the rear surface in red, surrounded by a grounded guard ring. All connections are made on the rear side, and metal traces bring the bias voltage to the front side. Figure 5.3b shows the front side of the detector with bias voltage ring in green. The pixels, guard ring, bias traces and bias ring are all covered in titanium nitride (TiN). Other than the bias ring, the front surface is unmetallized.

When a particle interacts in the detector, it creates electron–hole pairs through ionization and phonon excitations of the crystal. In this detector the phonons are not observed, but the reverse bias voltage moves the charges to the contacts within a few nanoseconds. The electronics amplify the charge signal and determine the time constants of the pulse shape. By cooling the detector, the number of thermally produced electron–hole pairs and the leakage currents are reduced, improving the energy resolution.

The front surface of the detector contains a dead layer of silicon. Electrons can lose energy in this region where the electron–hole pairs will not be collected. We expect a dead layer on the front surface to be approximately 100 nm. Table 5.2 summarizes the detector dimensions and design goals.

Table 5.2: Detector dimensions and design parameters.

Feature	Design goal
Sensitive area	$\pi \times (4.5 \text{ cm})^2$
Number of pixels	148
Number of rings	12
Azimuthal Sensitivity	30°
Radial Position Sensitivity	1.9–7.4 mm
Thickness	$500 \mu\text{m}$
Dead layer	$\sim 100 \text{ nm}$
Energy resolution	$\sim 600 \text{ eV FWHM}$
Detection Efficiency	90%

The detection efficiency goal is 90%, which depends on the electron energy and angle of incidence. The magnetic fields and post-acceleration affect the detection efficiency as discussed above. A significant fraction of electrons backscatter off the detector. To reach 90% detection efficiency, we rely on backscattered electrons returning to the detector; either the pinch magnet reflects high-angle electrons or the main-spectrometer voltage reflects the scattered electrons. To effectively count the reflected electrons, the time-of-flight of the electrons must be short compared to the detector response time.

Novel Connection Scheme

Silicon wafers are usually mounted on ceramic substrates. As discussed in Section 4.3.2, a ceramic substrate causes unacceptable backgrounds for the KATRIN experiment. Therefore, we replace the ceramic substrate with the novel connection scheme shown in Fig. 5.4.

A copper standoff and hold-down ring attach the detector to the Conflat flange. The detector wafer is unsupported inside the radius of the copper ring at 4.95 cm. The pixels are directly contacted by spring-loaded “pogo pins,” which are 0.5 mm diameter copper-beryllium electrical contacts. The pogo pins slide over niobium pins fixed in the Conflat flange with sapphire insulators. On the MHV side, the niobium pins connect to the preamps. There are a total of 184 pins: 148 to read out the pixels, twenty-four to bias the detector,

and twelve to contact the guard ring.

The performance of this novel detection scheme has been tested [60]. The stress placed on the silicon from the pogo pins does not degrade the performance of the detector or increase the leakage current.

5.1.2 Passive and Active Shield

Both the passive and active shields are designed to reduce backgrounds at the KATRIN detector. The shields fit inside the magnet bore, surrounding the detector but constrained in thickness by the size of the bore. The passive shield is a dense material that attenuates photon backgrounds originating outside the shield. We choose to use an inner copper shield of 1 cm and an outer lead shield of 3 cm. Copper can be more radio-pure than lead, so the inner lining may absorb lead X rays and reduce backgrounds from the lead shield itself. The shield is a cylinder, 105 cm long. It has two openings: one for the beam and one for the readout electronics.

The active shield is designed to tag cosmic rays, namely muons, with greater than 90% efficiency [61]. We are using a Bicron-408 plastic scintillator as the active veto. Organic scintillating molecules are suspended in the plastic and release light after a particle ionizes the molecules. The plastic was formed into a cylindrical shape to fit around the passive shield. Four panels of plastic surround the lead shield as shown in Fig. 5.5. The plastic is covered by reflective Tyvek for maximum light collection. Wavelength-shifting (WLS) fibers are embedded in the surface of the plastic. The Bicron-408 scintillator emits light at 425 nm. The WLS fibers shift the light up to 493 nm. Twelve WLS fibers are embedded in the four panels, and four more fibers are in the end-cap. At the end of the shield, the WLS fibers are coupled to clear fiber optics.

The fiber optics transport the signals to silicon photomultiplier (SiPM) tubes. Unlike conventional photomultiplier tubes, SiPMs work in magnetic fields, making them ideal for this application. Unfortunately, SiPMs have a large amount of dark noise.

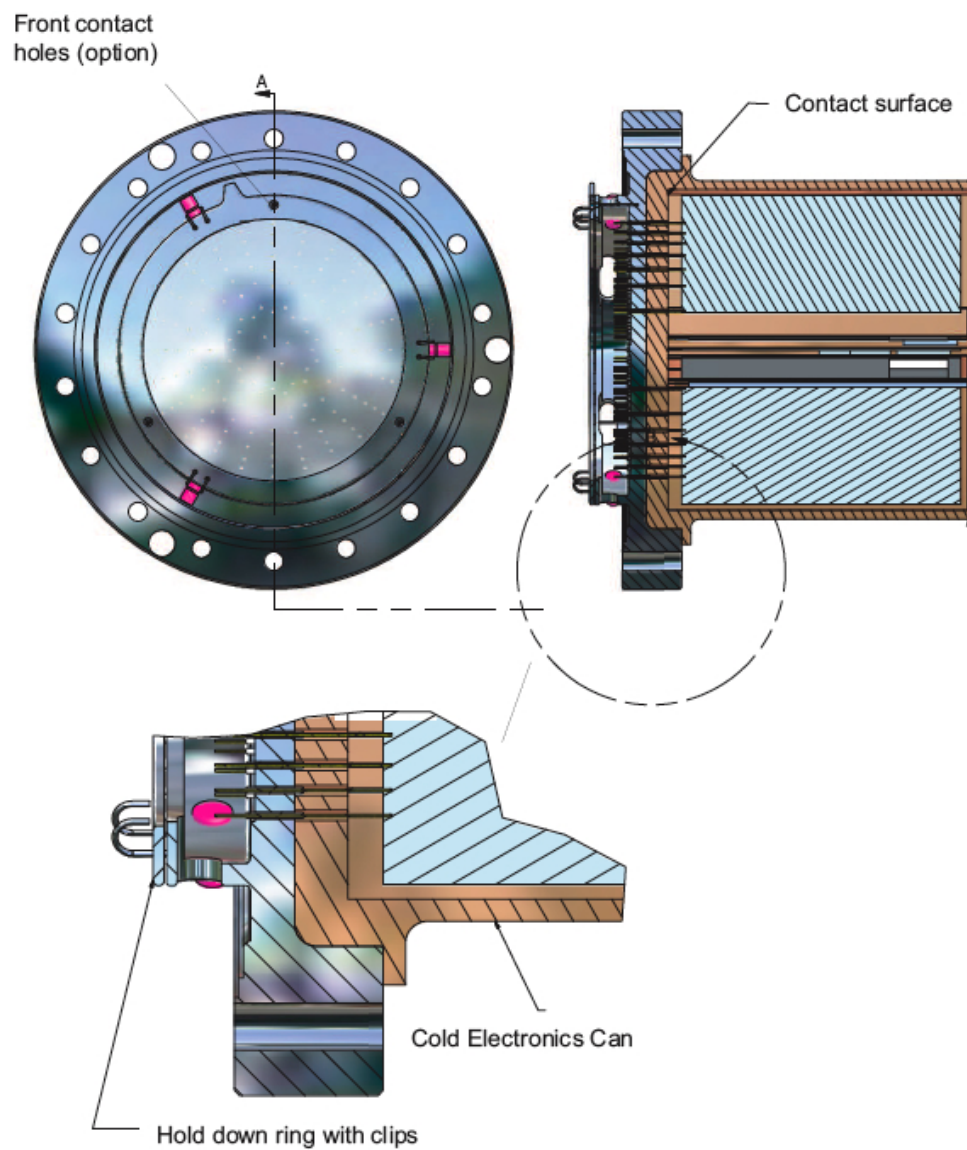


Figure 5.4: Silicon detector mounted on the feed through flange with contact pins. The detector is held in place by a copper ring. Pogo pins (not shown) contact the back of the detector and slide over niobium pins fixed in the Conflat flange. The preamps mount in a copper holder on the back of the Conflat flange and connect to the niobium pins. Figure from M. Steidl et al. [58].

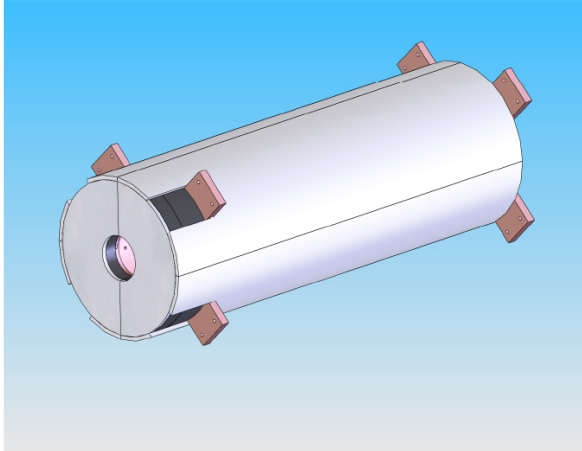


Figure 5.5: Active and passive shields. The plastic scintillator is shown in light grey on the outside of the lead shield. The shields attach to the detector magnet by the eight copper tabs. Therefore, the shield sticks out of the magnet by 14 cm on the readout side. Figure from M. Steidl et al. [58].

5.2 Overview of the Data Acquisition System

The data acquisition (DAQ) system records data from the KATRIN experiment. It must process signals from 148 channels from the silicon detector and thirty-two channels from the scintillator veto. The silicon detector signals have a fast rise of about 20 ns and a slow fall with a time constant of 1 ms. The scintillator veto and SiPMs create fast pulses, only tens of nanoseconds long. The two different types of signals require different trigger algorithms. The scintillator trigger will also require a coincidence between both ends of a scintillator-veto fiber to prevent the large dark-noise rates of the SiPMs from increasing the dead time.

For neutrino-mass data, we expect rates up to 140 Hz, but various calibrations lead to very high rates that the DAQ must accommodate. Calibrations with both tritium and krypton gases in the source will create rates up to 1.2 MHz spread through all the detector pixels. The rear electron gun is a point source and is used to measure the complete response

function of the KATRIN experiment. It can shoot electrons into a single pixel with rates up to 100 kHz. Section 4.1.5 explains these calibrations.

Finally, data from the KATRIN detectors must seamlessly merge with other information about the status of the experiment. The Slow Control system monitors and records the status of other subsystems, including the high voltage, vacuum, and magnets. The DAQ must associate a time stamp with each event to allow merging of the two data streams.

The requirements on KATRIN’s data acquisition system include:

- Process signals from 148 channels from the silicon detector and thirty-two channels from the scintillator veto
- Implement the veto logic requiring a coincidence between both ends of a scintillator’s fiber to reduce noise
- Time-stamp events and tag coincidences between the scintillator veto and the silicon detector
- Handle the high rates required for calibrations: up to 100 kHz per channel and 1.2 MHz total

To fulfill these requirements, we are using a custom data acquisition system first developed for the Pierre Auger Southern Observatory. KATRIN collaborators at the Institut für Prozessdatenverarbeitung und Elektronik (IPE)—translated as the Institute of Data Processing and Electronics—currently develop the system [62]. Therefore, we refer to the custom data acquisition system as the IPE DAQ. Data from the IPE DAQ is read out through the Object-oriented Real time Control and Acquisition (ORCA) [63] software, developed at the University of North Carolina.

This chapter discusses the capabilities and characterization of the Version III or Mark III IPE DAQ. A more detailed description of the Mark III hardware, data format, data transfer rates, and user controls can be found in Appendix A. To ensure the integrity of the data, we have designed tests for the system with silicon detectors and pulse generators. Characterization of the Mark III system has led to design changes in the Mark IV system.

Upgrades to the DAQ system to a Mark IV version will take place in 2009 and are discussed in Appendix A.5.

The IPE DAQ receives analog signals from the silicon detector and scintillator veto. It digitizes and records the signals and digitally filters them to determine the pulse height. Digital signals are more versatile to work with than analog signals. The filtering is carried out by field-programmable gate arrays (FPGAs), so filter values can be changed with a click of a button instead of changing resistors and capacitors. With FPGAs, we can program different readout modes for neutrino data and for calibration data and easily switch between them.

The IPE DAQ can acquire data via three modes; histogram, event, and waveform. At high calibration rates, we will use histogram mode, where histograms of pulse heights are built on-board and only the histogram is read out. For neutrino-mass data, we will use either the event or waveform mode. In event mode, the pulse heights and time stamps are read out. In waveform mode, the entire digitized pulse is also read out.

5.2.1 Pixel-trigger Algorithm: Trapezoidal Filter

The IPE DAQ pixel trigger for silicon detector pulses is based on a trapezoidal filter [64]. Silicon detectors create step pulses with step height proportional to the energy deposited in the detector. The IPE DAQ estimates the step height with a trapezoidal filter. Due to the fast charge-collection time of silicon detectors, the pulse-step height is usually the only information about the interaction that can be extracted from the pulse shape. Both the rise time and fall time are determined by the electronics, so pulse-shape analysis will not be useful.

A trapezoidal filter shapes a step pulse—like a silicon detector pulse—into a trapezoid. The height of the trapezoid is also proportional to the energy deposited in the detector, but should have less variation than the initial pulse since filtering averages over the noise in the input pulse. The IPE DAQ finds the height of the trapezoidal pulse, which we call the peak height, instead of finding the input-pulse step height.

The first plot in Fig. 5.6 shows an input pulse from a pulse generator digitized by the

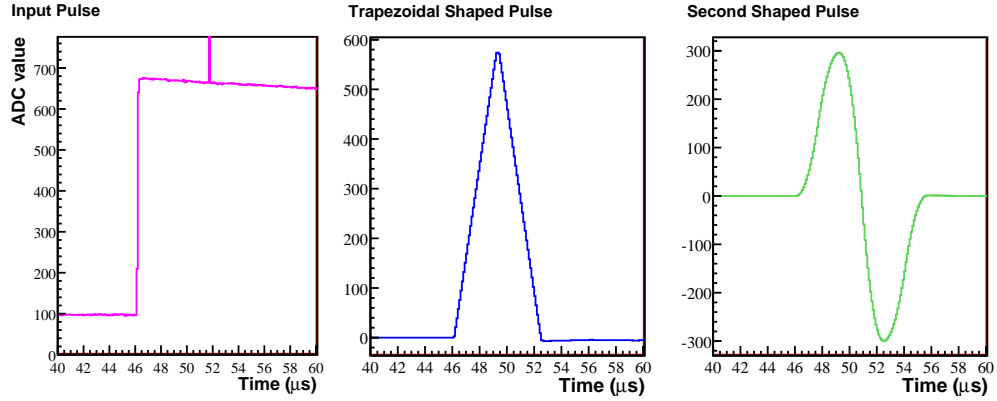


Figure 5.6: An example step input pulse and shaped pulses.

IPE DAQ. The signal shape is intentionally similar to a silicon detector pulse. The value of each bin is called an ADC value. The high-value bin is the trigger bit, set by the DAQ to indicate a trigger.

The second plot in Fig. 5.6 is the trapezoid or shaped pulse. For every time bin i , the trapezoidal pulse value T_i is calculated from a moving sum of the previous $2L$ ADC values:

$$T_i = \sum_{k=0}^{L-G} ADC_{i-k} - \sum_{k=L+G}^{2L} ADC_{i-k}. \quad (5.1)$$

The most recent $L - G$ bins of ADC values are summed up, and earlier $L - G$ bins are subtracted. The trapezoid maximum occurs one shaping length L after the input-pulse step, when $L - G$ high-value bins are summed and the earlier $L - G$ baseline bins are subtracted. The shaping length L determines the length of the trapezoidal pulse, which is $2L$. A longer shaping length sums up more bins, averaging out the noise and increasing the value of T_i . The trapezoid has a flat top of length $2G$, so G is called the gap setting. If the gap is zero, the filter is called a triangle filter since the resulting pulse has no flat top.

To find the peak height of the trapezoidal pulse, the IPE DAQ filters the trapezoidal pulse a second time. The second shaped pulse is the last plot in Fig. 5.6. The second filter has a shaping length of $L/2$ —half of the first filter—and no gap G . The second shaped

pulse crosses zero from positive to negative $L/2$ bins after the peak of the trapezoidal pulse. At this point, $L/2$ bins on the rising edge of the trapezoid are subtracted from $L/2$ bins on the falling edge, so the value of the second shaped pulse is zero. The FPGAs can more easily find the zero crossing of the second shaped pulse than detect the highest point of the trapezoidal pulse. The trapezoidal pulse value $L/2$ bins before the zero crossing is extracted as the peak-height value. This may not be the actual maximum of the trapezoidal pulse due to the finite decay of the input pulse described in Section 5.3.3. The zero crossing of the second shaped pulse also determines the time of the event; it is $3L/2$ bins after the step rise in the ADC values.

We refer to the extracted trapezoidal height as the peak height, which is $L - G$ times the input step height for a perfect step. The peak height must not be confused with ADC values; the ADC values are merely the digitized input-pulse values, but the peak height is the result of the trapezoidal filter.

In summary, the IPE-DAQ pixel-trigger algorithm has two requirements to read out a silicon detector event. First, the trapezoidal pulse must be above a programmable threshold. Once it is above threshold, an analysis window, delayed by $L/2$ bins, opens to look for the zero crossing of the second shaped pulse. Second, the second shaped pulse must cross zero from positive to negative while the analysis window is open. Figure 5.7 shows the input pulse, the trapezoidal pulse, the delayed analysis window, and second shaped pulse as calculated by an offline software filter. None of the shaped pulses shown are read out of the IPE DAQ; only the ADC waveform of the input pulse, the peak height, and the time stamp can be read out. In the FPGAs, the filtering is done recursively, as described in Appendix A.4.

5.3 Characterization of the Data Acquisition System

Using the Mark III crate, we have developed tests to characterize the data acquisition system. Mark IV will be tested with the same methods. What we learn from these tests can be used to improve the Mark IV operation. We optimized the trapezoidal filter gap, investigated pile-up and pole-zero corrections in the trapezoidal filter, tested the ADC linearity, and measured the counting efficiency in two modes.

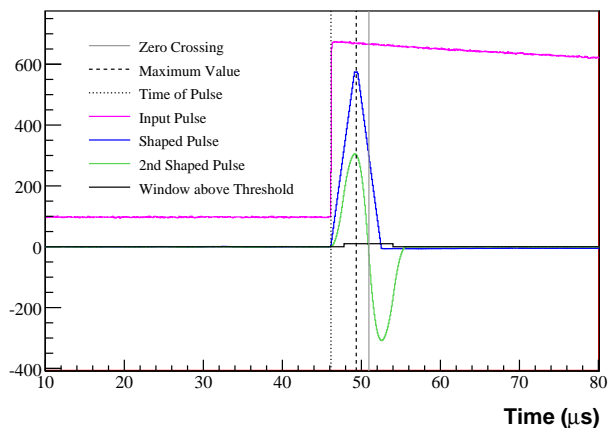


Figure 5.7: An example input pulse and shaped pulses showing the delays between pulses. The shaped pulses are normalized by the shaping length for easy viewing, but the IPE DAQ does not normalize this way.

5.3.1 Optimizing the Trapezoidal-Filter Gap

Early versions of the Mark III crate did not give the user control over the gap length; it was fixed at a total width of 1 bin. With this total gap, the peak heights calculated by the IPE DAQ did not have a gaussian shape, as shown in black in Fig. 5.8a.

To optimize the IPE-DAQ trapezoidal filter, we wrote a software replica based on a preliminary code by Jessica Dunmore. Using the waveforms read out from the DAQ, we optimized the filter offline. The gaussian peak-height spectrum shown in Fig. 5.8a was produced by increasing the total gap in the software filter to three bins. Increasing the gap fixes the peak-height spectrum because the gap must be longer than the input-pulse rise time.

Figure 5.8b, shows the digitized-waveform rise time of two to three bins. The digitized rise time is longer than the input-pulse rise time because the IPE DAQ analog filtering affects the digitized-pulse. When the gap is shorter than the rise time, bins in the rise are included in the filter's high-ADC sum and the baseline sum, decreasing the calculated peak height. This is also known as ballistic deficit. Therefore, using a total gap longer than the

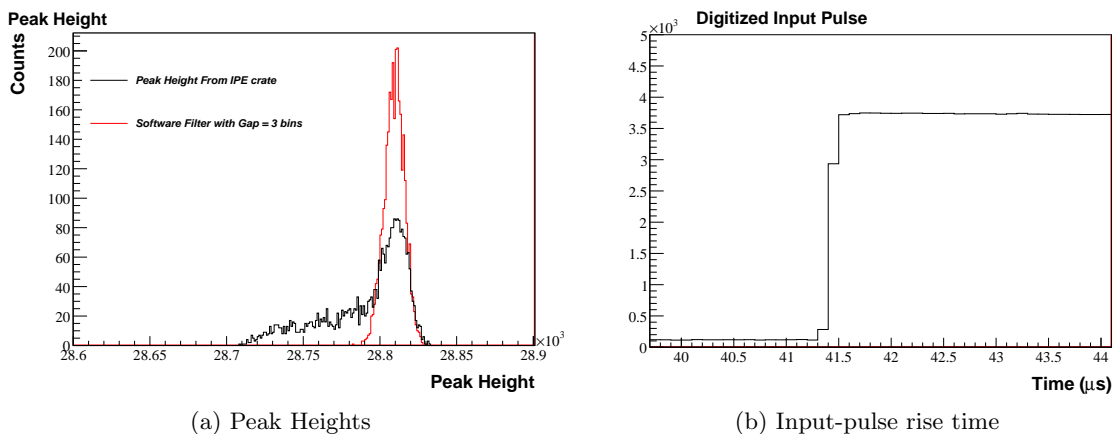


Figure 5.8: The peak height calculated with 1 bin gap in the IPE DAQ was non-gaussian. Using a software filter, we determined the total gap should be at least as long as the rise time. This input pulse has a fall time of 10 ms.

pulse rise time corrects the tail on the peak-height distribution.

We optimized the gap setting with an input pulse from a pulse generator, not the KATRIN preamps. We recommend checking that the gap is longer than the rise time of the digitized KATRIN-preamp pulses. The trapezoidal filter currently implemented in the FPGAs, described in Section 5.2.1, has a total gap twice the gap setting. Therefore, we recommend a setting of at least two bins so the total gap is wider than the rise time.

5.3.2 Pile-up in a Trapezoidal Filter

The IPE DAQ must be able to handle rates as large as 100 kHz for calibrations. High rates combined with the long fall time of the KATRIN-preamp pulses can cause pile-up of the input pulses. For preamps with 1 ms fall time, a significant number of the pulses overlap at a rate of $\frac{1}{1\text{ms}}$, or 1 kHz, much lower than the maximum rate of 100 kHz. The data acquisition system must be able to distinguish overlapping pulses.

If the pulses occur too close in time, the data acquisition system incorrectly identifies two pulses as one count with higher energy. Therefore, the energy spectrum and the number of counts will be incorrect. The probability of pile-up distorting the measured spectrum is

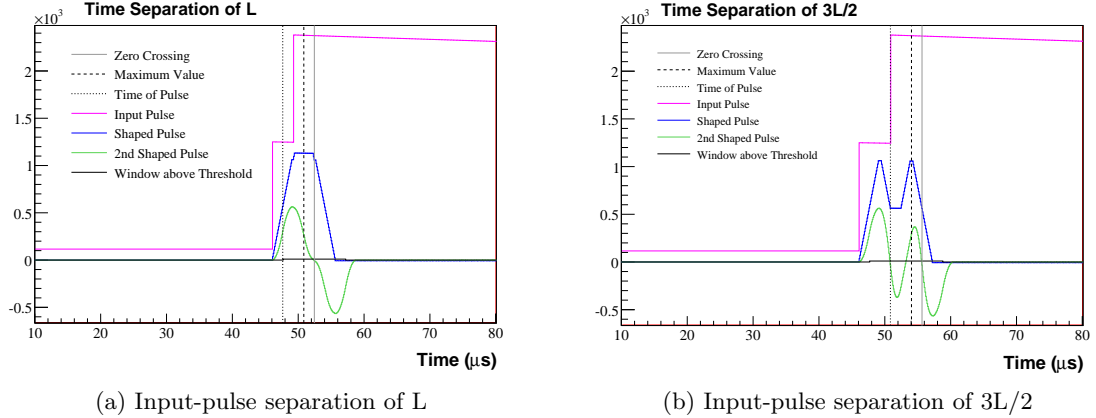


Figure 5.9: Pileup in the trapezoidal filter. Input pulses must be separated by $3L/2$ or more for the IPE trigger algorithm to identify both pulses. On the left, pulses are only separated by L , and the second-shaped pulse has a single zero-crossing. On the right, pulses are separated by $3L/2$, so the second-shaped pulse has two zero-crossings and identifies two events.

$1 - e^{-R_T \Delta T}$, where R_T is the true rate and ΔT is time separation required by the DAQ to distinguish two events.

To find the time separation required by the IPE DAQ to distinguish two events, we simulate overlapping input pulses with variable separation and filter them in the software filter. Figure 5.9 shows two different time separation filtered with a shaping length of $3.2 \mu\text{s}$. If the input pulses are separated by less than $3L/2$ as in Fig. 5.9a, only one count is identified and stamped with a time in between the two pulses. With a separation of $3L/2$ or more as in Fig. 5.9b, two peaks are distinguished, both with the correct time stamp. Therefore, the IPE-DAQ pixel-trigger algorithm can distinguish pulses which are separated by more than $3L/2$, although the input pulses overlap.

Using this necessary time separation ΔT , we calculate the probability of pile-up. For a 100 kHz signal and a shaping length of $3.2 \mu\text{s}$, the probability is 38%. A shorter shaping length, which is easily changed in a digital filter, will reduce the pile-up.

Although the peaks can be distinguished with this separation, the peak heights may be incorrect. First, there is the danger of exceeding the ADC range when input pulses are on

top of each other, causing incorrect peak heights. In event and histogram modes, there is no indication that the ADC range has been exceeded, and therefore no way to identify these events. Second, the slow decay of the first pulse can affect the shape of the second pulse. A pole-zero correction, discussed in the next section, can correct for this.

5.3.3 Pole-zero Corrections for a Trapezoidal Filter

Signals from the KATRIN silicon detector are not true steps. The high values slowly decay back to the baseline with a fall time of 1 ms. If the shaping time is comparable to the decay time of the pulse, the calculated peak height can be underestimated and distorted because of the finite decay. A filter with pole-zero correction suggested by Jordanov and Knoll [64] can account for the pulse decay time.

The simple trapezoidal filter discussed in Section 5.2.1 can be expressed more generally by introducing weighting factors W_k . Then the filter response is:

$$T_i = \sum_{k=0}^{2L} W_k \times ADC_{i-k}. \quad (5.2)$$

The weighting factors are also called the impulse response, which is the output of the filter when presented with a impulse signal or delta function input. For example, replace the ADC_{i-k} with a Kronecker delta, δ_{ik} , and the output equals the impulse response, $T_i = W_i$. For the simple trapezoidal filter discussed above, the weighting factors are ± 1 or zero.

The pole-zero correction accounts for the exponential fall of the input pulse. Therefore, the bins close to the step should be weighted more than bins farther from the step where the pulse has decayed. Figure 5.10 shows the impulse response for both the simple filter and a filter with a pole-zero correction. The simple filter's impulse response is flat; it has a slope of zero. The impulse response for the pole-zero-corrected filter does not have a flat top; it has a slope of one to correct for the fall time.

The corrected filter has a variable length L and gap G just like the simple filter. It also depends on the expected fall time τ of the input pulse, in units of time bins. When the shaping length is much shorter than the fall time, the pole-zero-corrected impulse response approaches the simple filter impulse response; it has approximately a flat top with height

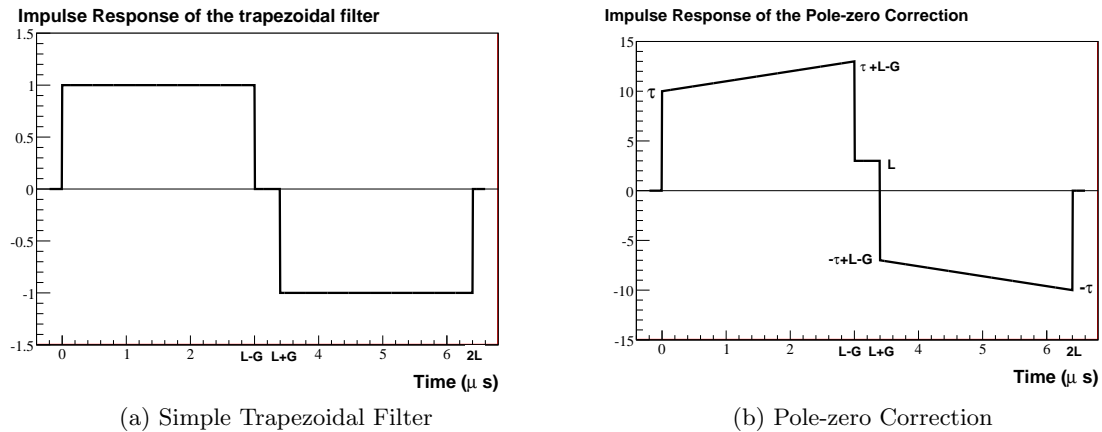


Figure 5.10: The impulse response for the trapezoidal filters assuming a shaping time of $3.2 \mu\text{s}$ and a gap of $0.2 \mu\text{s}$. The pole-zero correction is shown for an input-pulse fall-time constant of $10 \mu\text{s}$. The KATRIN-pulse fall time is 1 ms .

$\pm\tau$ bins instead of ± 1 . In this case, the input pulse looks like a true step to the filter. When the shaping length is comparable to the fall time, the pole-zero-corrected impulse response has sloped tops, as in Fig. 5.10b.

We implemented the pole-zero correction into the software filter using code from Mike Marino. To amplify the distortion, we tested the two filters with an input pulse with a fast fall time of $10 \mu\text{s}$. Both filters used a shaping length of $3.2 \mu\text{s}$ and a gap of $0.4 \mu\text{s}$, preventing distortion due to the rise time. The pole-zero-corrected filter was programmed with the fall time of $10 \mu\text{s}$.

Figure 5.11 shows the simple filter response. The trapezoidal pulse is not symmetric and undershoots past zero due to the fast fall time. The peak-height value extracted by the filter is not the maximum because the trapezoidal pulse is not symmetric.

Figure 5.12 shows the same input pulse filtered with a pole-zero correction. The trapezoidal pulse is much more symmetric and does not undershoot as far past zero. The slight undershoot is because the digitized pulse has a slightly faster fall time than the input pulse due to the AC-coupling of the analog filtering. If we fit the digitized pulse to find the fall time instead of using the fall time of the input pulse, the pole-zero correction could be even

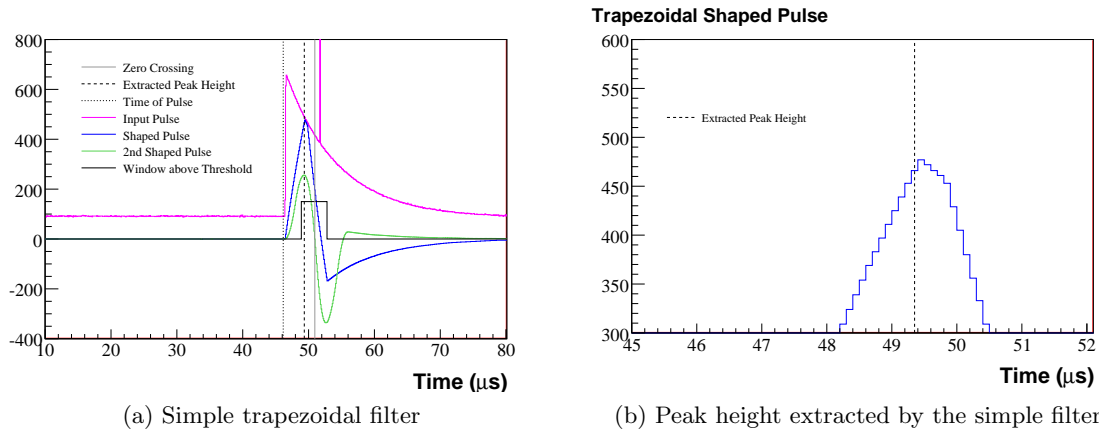


Figure 5.11: The response of the simple trapezoidal filter to a pulse with $10 \mu\text{s}$ fall time.

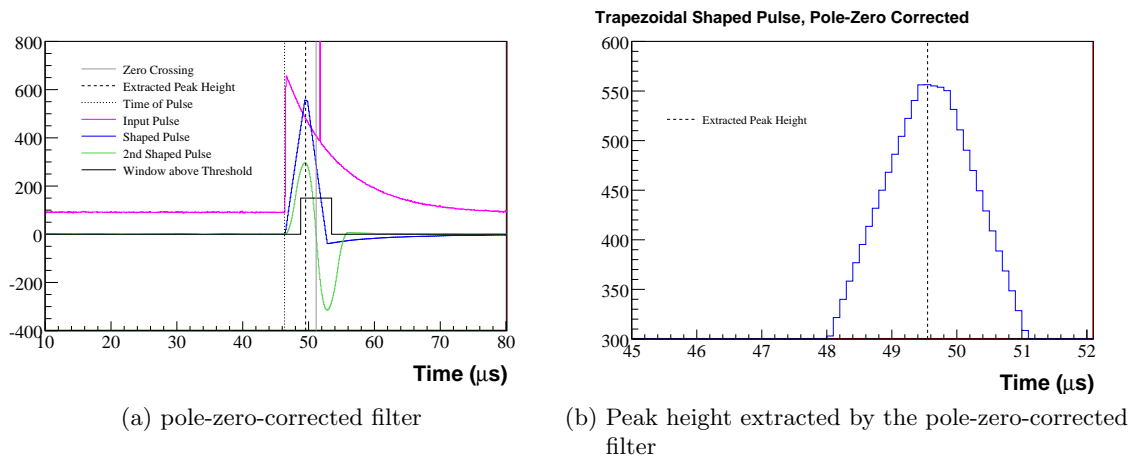


Figure 5.12: The response of the trapezoidal filter with pole-zero correction to a pulse with $10 \mu\text{s}$ fall time.

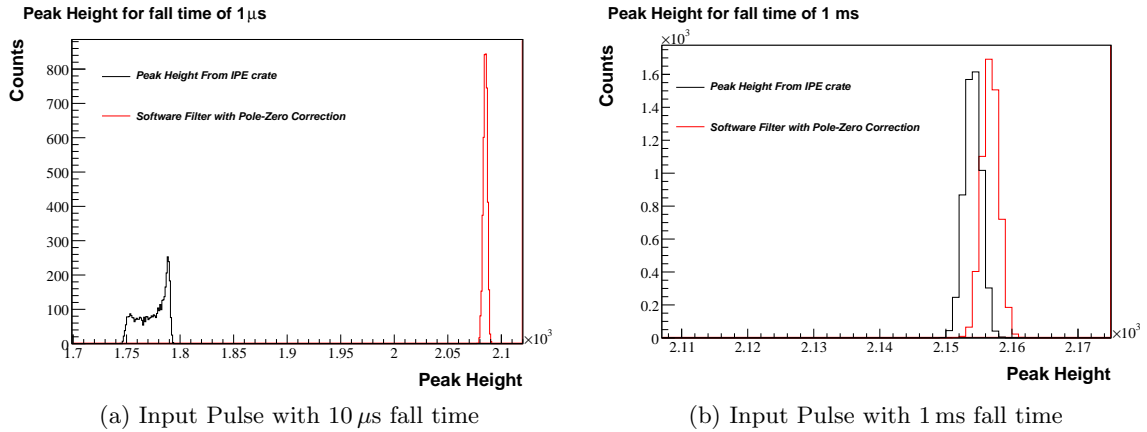


Figure 5.13: Peak heights from an input pulse with 10 μ s and 1 ms fall time with and without pole-zero correction. The pole-zero correction is more important for fall times short compared to the shaping length.

better. With a pole-zero correction, the extracted peak-height value is the maximum of the trapezoidal pulse.

Figure 5.13a compares the peak heights calculated by the two filters for a 10 μ s fall time. Without a pole-zero correction, the peak height is clearly underestimated and distorted. This would be unacceptable for KATRIN, but the magnitude of the effect depends on the input-pulse fall time.

Figure 5.13b compares the two filters for an input pulse with a 1 ms fall time, like the KATRIN-preamp pulses. The effects of a pole-zero correction are much smaller. The peak height is shifted down 0.14% without pole-zero correction, and the peak is 0.05% wider. Therefore, with the current fall time, the KATRIN signals do not require a pole-zero correction.

5.3.4 Integral Non-Linearity

To measure the energy of a particle interacting in our detector, we assume the calculated peak height is linearly proportional to the input pulse and the energy deposited in the detector. Three variables affect the conversion from peak height to energy since all three affect

the calculated peak heights: gain, shaping length, and the ADC linearity. We convert from peak height to energy by measuring the spectrum from a well-known calibration source. The energy calibration can be measured for each gain or shaping length setting used, correcting for any non-linearity in these variables. But the ADC linearity must be measured since it depends on the input-pulse voltage. We measure the ADC linearity by changing the input-pulse voltage at a fixed gain and shaping length.

We tested the system using an Agilent 33220 pulse generator creating a “PIN-diode” pulse with fall time constant of 1 ms. We varied the pulse-generator voltage from 10 to 250 mV in steps of 24 mV, covering the range of the ADC for this gain setting. With a pulse-generator burst rate of 99 Hz, the recording time for each voltage setting need only be 30 s. We tested two channels on card KAT03, channels 0 and 5. Since we expect to use a shaping length of $3.2 \mu\text{s}$ or $6.4 \mu\text{s}$, we made a set of measurements at both settings. We chose a gain of 100, which is in the middle of the range of gains. The data was taken in event mode using a threshold of 40 and gap setting of 2.

For each input voltage, the measured peak-height spectrum includes a gaussian peak. Using a code by Brent VanDevender, we fit each peak to a gaussian, extracting the mean M and uncertainty σ_M . Next, we plot the gaussian mean as a function of the pulse-generator voltage setting as shown in Fig. 5.14. We fit this plot to a line, assuming no uncertainty on the pulse-generator voltage. The residuals or deviations of the gaussian mean from the linear fit are also shown in Fig. 5.14. The residuals are in units of peak-height bins. The uncertainty on the mean is less than one bin, but the residuals can be as large as 100 bins. Integral non-linearity is defined as the maximum deviation from the linear fit divided by the peak-height range. Both shaping lengths give an integral non-linearity of 0.3% for an input range of 0 to 250 mV. Typically ADCs can attain an integral non-linearity of better than 0.1% [65]. For the KATRIN experiment, we require linearity over an energy range of 0–100 keV, which is a small portion of the range tested. The IPE DAQ should be linear within our specifications.

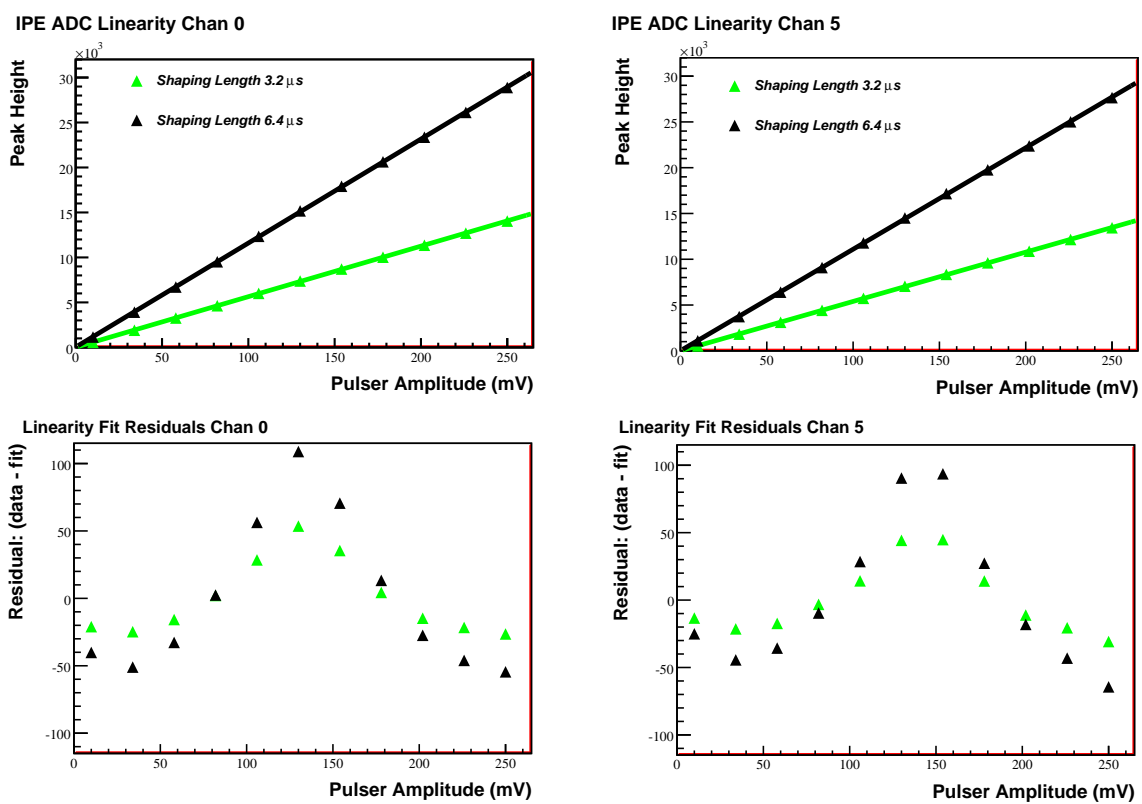


Figure 5.14: ADC non-linearity. The top plots show the linear fits to the peak heights, and the bottom plots show the fit residuals.

5.3.5 Counting Efficiency

The DAQ must handle a maximum of 1.2 MHz total and 100 kHz per channel for separate calibrations. We expect to use histogram mode for these calibrations. Neutrino data rates should not exceed 140 Hz total. Event mode or possibly waveform mode will be used to record neutrino-mass data. In event and histogram modes, the IPE DAQ should read out 100% of events as long as the rate stays below the maximum rate for that mode. In this section, we measure the counting efficiency in both modes.

Appendix A.2 explains the readout schemes for the different data acquisition modes and estimates the maximum recordable rate in each mode. Since the detector has 148 pixels, a total rate of 1.2 MHz is equivalent to 8 kHz per channel, or 195 kHz per 24-channel card. In histogram mode, a histogram is made for each channel, so the counting efficiency depends on the rate in the individual channels. Histograms are read out every second but only require 0.8 ms for the data transfer. Therefore, the maximum rate of 16.8 MHz is set by the size of the histogram bins.

In event mode, a single circular buffer per card stores up to 512 events for the entire card. No events will be lost at low rates, but if the total rate per 24-channel card is high enough to fill the buffer, events will be lost from all channels. The maximum rate is estimated in Appendix A.2.4 to be 7.7 kHz for the entire card.

A single channel has been tested with an input pulse that does not exhibit pile-up at rates up to 50 kHz. We have not tested multiple channels or a single channel up to 100 kHz. We have not confirmed the pile-up predictions of Section 5.3.2. For event and waveform modes in Mark III, we expect the counting efficiency to depend on the total rate in a card; in histogram mode, we expect the counting efficiency to depend on the rate per channel. All modes should be tested with multiple channels, especially histogram mode with rates up to 195 kHz per card.

Method for Measuring Counting Efficiency

The counting efficiency, ϵ , is the number of counts recorded by the IPE DAQ, C_{IPE} , divided by the number of true counts, C_{true} . With a large number of true counts, the uncertainty

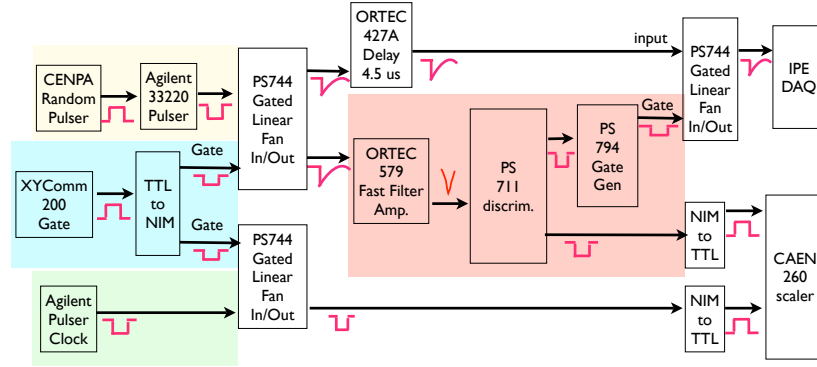


Figure 5.15: Electronics chain for measuring counting efficiency. The random signal is highlighted in yellow, shown here as the Agilent pulse generator externally triggered by the CENPA random pulse generator, but could also be a detector signal or a combination of both. The run gate and the start of data taking are controlled by the XYCOM 200 card, highlighted in blue. The discriminator, highlighted in orange, creates the event gate and ensures the thresholds are the same for the IPE DAQ and scaler counter. The periodic pulse-generator clock determines the live time and is highlighted in green.

depends on the number of lost counts, $C_{\text{true}} - C_{\text{IPE}}$. The efficiency and uncertainty on the efficiency σ_ϵ are:

$$\epsilon = \frac{C_{\text{IPE}}}{C_{\text{true}}} \quad \sigma_\epsilon = \sqrt{\frac{C_{\text{true}} - C_{\text{IPE}}}{C_{\text{true}}^2}}. \quad (5.3)$$

To measure the efficiency, we need a random signal and a method of accurately determining the true number of events and the true rate. Figure 5.15 shows the electronics chain that provides these capabilities.

We have a choice between two random signals: a square pulse from a pulse generator, and signals from a detector and radioactive source, usually ^{241}Am . Figure 5.16 contrasts the two pulse shapes. We generate the square pulse with a programmable Agilent 33220

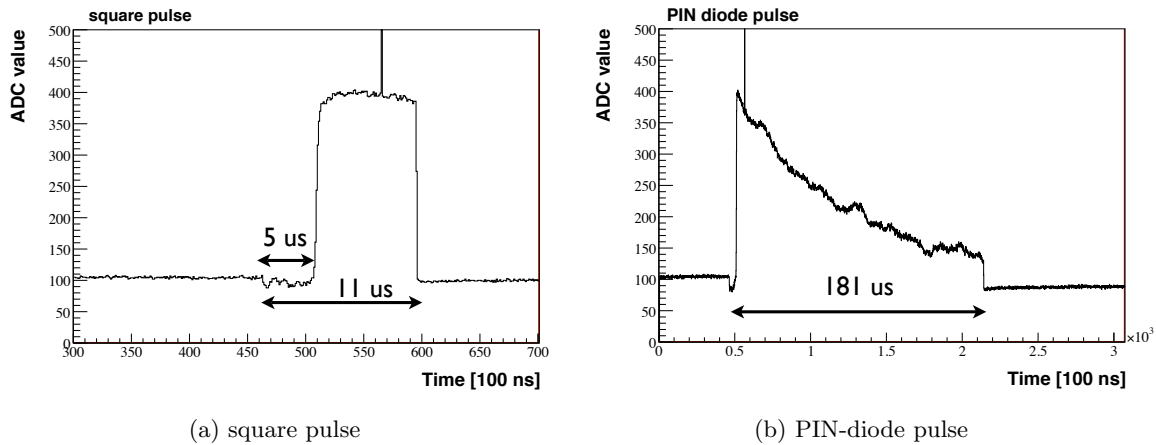


Figure 5.16: The two signal pulses used to test counting efficiency. Both plots are waveforms recorded by the IPE DAQ, which have been inverted and digitized. The pulses are gated, as discussed in the text.

pulse generator, which is periodic but gives us control over the pulse shape. The Agilent pulse generator is externally triggered by a random pulse generator designed at the Center for Experimental Nuclear Physics and Astrophysics (CENPA), making the square pulse random. The radioactive source is inherently random.

The two signals, square pulse and detector pulse, have different benefits and drawbacks. The detector signals are closer to the real KATRIN-pulse shape but have more noise. The ^{241}Am detector spectrum has multiple peaks near the noise threshold, making it hard to recognize problems in the peak-height spectrum. The rate from the radioactive source can be varied by changing the source position, but it is more cumbersome than changing the pulser rate. The maximum detector rate is limited by source activity and detector size. A pulse generator creates a single gaussian peak in the peak-height spectrum; therefore problems are easy to identify. The pulse-generator square-pulse shape does not match the real KATRIN-pulse shape and therefore does not exhibit pileup. The pulse-generator rate can be easily varied, but is not completely random, as discussed below.

The Agilent pulse generator will not generate piled-up pulses even if triggered by the CENPA random pulser, which introduces a minimum time-separation between pulses. Fig-

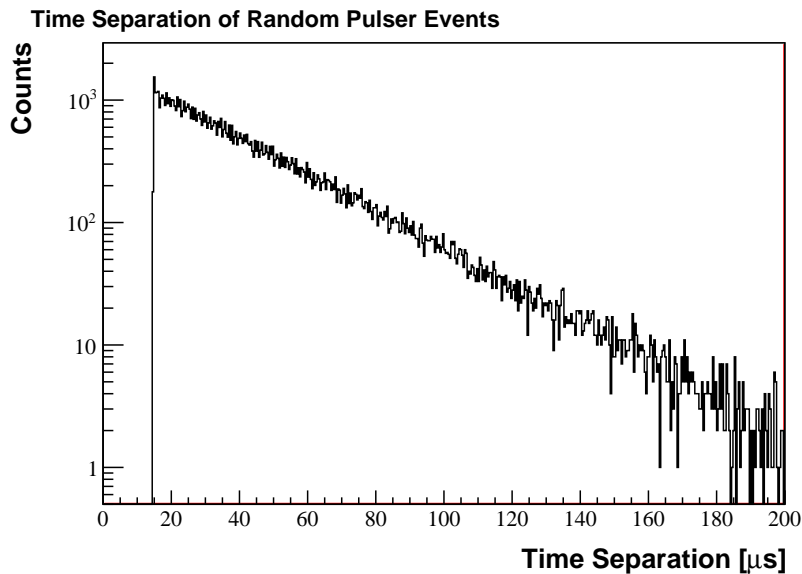


Figure 5.17: The CENPA random pulse generator is truly generating random events. The sharp drop in rate occurs at $14.5 \mu\text{s}$ separation and is due to the inherent minimum separation of events in the Agilent pulse generator. No pulses are closer than this minimum. This data was taken in event mode with an average rate of 22.8 kHz.

Figure 5.17 shows the time distribution of events from the externally triggered Agilent pulse generator, which are random except for the minimum time separation of $14.3 \mu\text{s}$. This minimum separation causes two problems; the signals are no longer random and the signals do not pile-up. Pile-up is discussed in Section 5.3.2.

Since this is a non-paralyzable system, the probability for the Agilent pulse generator to produce a pulse when triggered is $1 - R_P \Delta T$, where R_P is the produced rate and ΔT is the minimum separation between pulses. When the Agilent pulse generator is producing 14 kHz, 20% of events have already been lost due to this minimum separation. Therefore, above 14 kHz the signals are no longer truly random since an appreciable number of events are excluded by the minimum time separation.

The true number of counts, C_{true} , is measured by a VME-based fast scaler counter, CAEN model V260. The thresholds and duration of counting must be the same between this scaler counter and the IPE DAQ. To synchronize the thresholds and run duration,

we use gated fan outs. At the start of a run, a XYCOM 200 card opens the gate on the input signal fan out. We refer to this as the run gate since it controls the run duration. No signals are counted until the XYCOM card opens the run gate or after it closes the run gate. To ensure the same threshold for the IPE DAQ and scaler counter, we use a discriminator as the threshold for both. First, the input pulse is shaped by an ORTEC Fast Filter Amplifier to reduce noise. Then the shaped pulse is compared with a discriminator threshold. When the shaped pulse is above threshold, the discriminator sends a logic pulse to the scaler counter and opens another gate on the input to the IPE DAQ. We refer to this as the event gate, since it determines which events are counted. The event gate is most important for detector signals since the spectrum is continuous and requires a synchronized threshold.

We delay the input signal to the IPE DAQ so it arrives after the event gate opens. The delay must be longer than the shaping length of the IPE DAQ for the filter to accurately sample the baseline. The delay is $4.5 \mu\text{s}$, longer than the shaping time of $3.2 \mu\text{s}$. The length of the input square wave must be longer than $3L/2$, or $4.8 \mu\text{s}$, to accurately sample the pulse step. We use a square pulse $12 \mu\text{s}$ long.

Figure 5.18 shows the pulses from the various components in the electronics chain. In this case the square pulse input is shown. The fast filter amplifier shapes the long square pulse to a short pulse and averages over noise. The event gate is $11.1 \mu\text{s}$ long. The delayed input pulse is delayed by $4.5 \mu\text{s}$. The event gate closes before the delayed input pulse returns to baseline, shortening the actual input square pulse as seen by the IPE DAQ. The reason for this is discussed below, but both the baseline and high values of the gated input pulse are longer than the shaping length, so the peak heights are correctly calculated.

The Phillips Scientific 794 gate generator does not produce a second event gate if a second pulse comes within a few μs of the event gate closing. Therefore, to prevent missing pulses due to a closed gate, the event gate closes at $11.1 \mu\text{s}$, even before the end of the square pulse. The Agilent pulse generator has an inherent constraint that pulses must be completely separated; for a square pulse length of $12 \mu\text{s}$, the separation must at least $14.3 \mu\text{s}$. With these settings, the pulse generator will never produce a second pulse before the gate generator has recovered from the last event gate.

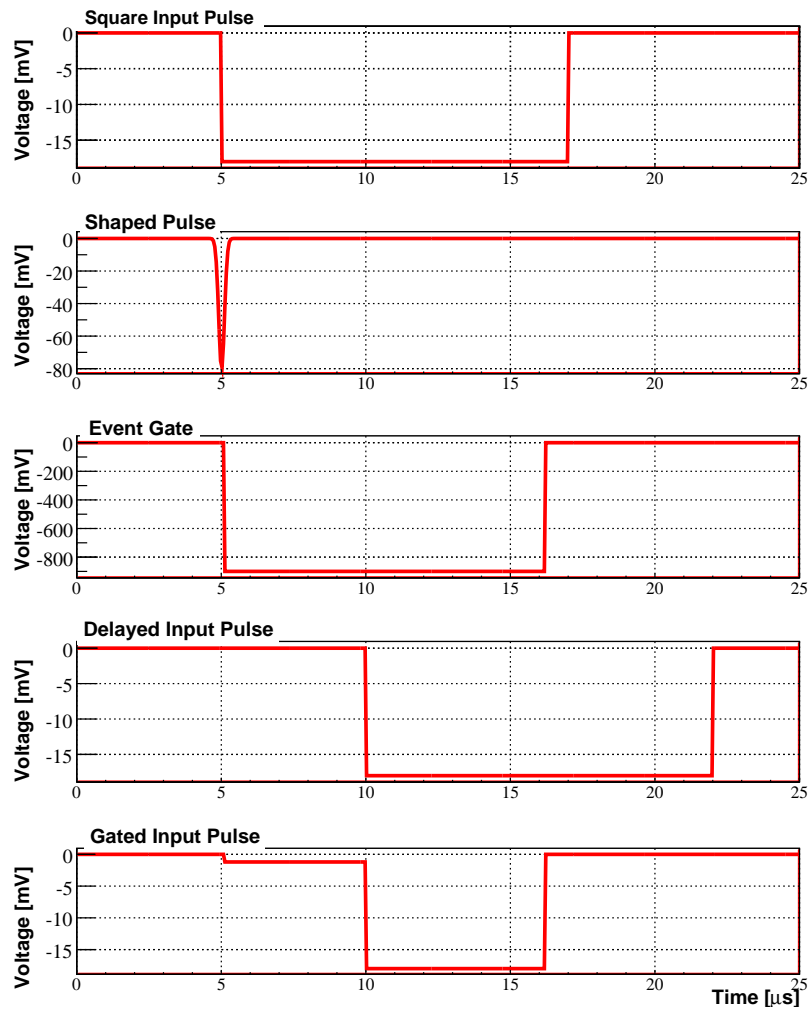


Figure 5.18: The various pulses in the electronics chain.

For the detector signals, there are additional considerations due to the long fall times. The event gate must be open for the entire pulse. If the gate opens before the signal has returned to baseline, the IPE DAQ will trigger on the gate opening, creating false events in the IPE crate count. If the IPE DAQ triggers on both the gate opening and the input pulse, a peak appears in the time-separation plot at $4.5 \mu\text{s}$ for a delay on the input of $4.5 \mu\text{s}$. As shown in Fig. 5.17, there is no peak at a separation of $4.5 \mu\text{s}$ in the pulse-generator data, so the IPE crate does not trigger on the gate opening when testing with the pulse generator.

An ORCA script controls the runs. Within the script, the ORCA run starts but the run gate remains closed for eight seconds to ensure all data takers are initialized. Then the XYCOM 200 card opens the run gate, and data taking begins. Eight seconds before the run ends, the XYCOM 200 card closes the run gate. A periodic pulse generator—Agilent model 33120—is also controlled by the run gate. It sends clock ticks at 1 kHz to an independent channel on the scaler counter to determine the counting time. The pulse-generator clock rate R_{clock} divided by the scaler-clock counts C_{clock} is the run duration in seconds.

$$t = \frac{R_{\text{clock}}}{C_{\text{clock}}} \quad (5.4)$$

The ORCA script also controls the run durations. For low rates, we set the run duration to 45 s. At higher rates, we set the run duration to 15 s, but the actual duration as determined by the pulse-generator clock varied between 14.5 to 16.8 s. In between runs, the script can automatically change the rate on the random CENPA pulse generator, or the user can move the source position.

Counting Efficiency Results

For each run, we calculate the counting efficiency as in Eq. 5.3. The number of counts recorded by the IPE DAQ is C_{IPE} . The true number of counts C_{true} is the counts recorded by the scaler. We plot the counting efficiency as a function of the true rate, or C_{true} divided by the time.

Figure 5.19 shows the counting efficiency in histogram mode and the peak heights. The peak heights fall into a single peak and do not indicate any problems with the readout,

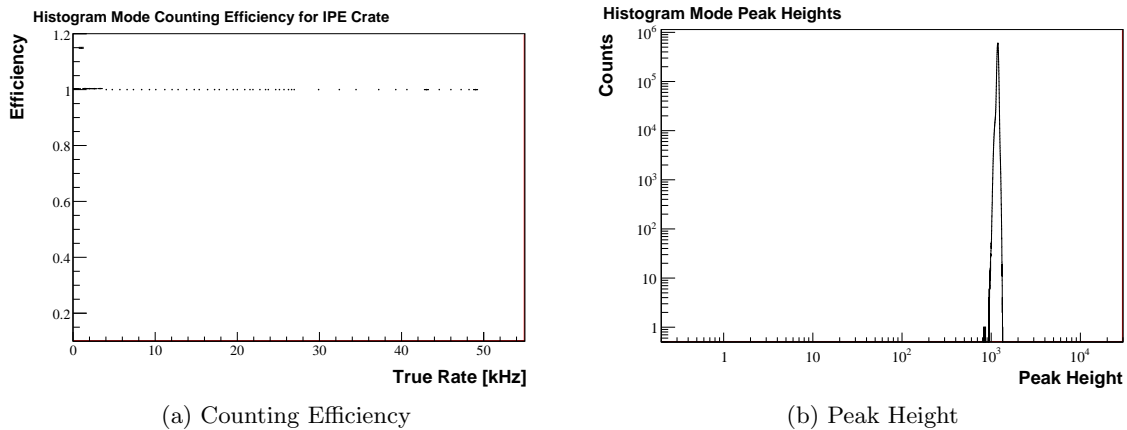


Figure 5.19: The counting efficiency (left) and peak heights (right) in histogram mode. The efficiency for one run is greater than 100% because the buffers are not cleared at the end of every run, so some histograms can be read out twice.

but one run has an efficiency of greater than 100%. A bug prevents all histograms from clearing at the end of a run, so histograms can be read out twice in two different runs. These twice-counted events cannot be removed with a cut and cause the efficiency to be greater than 100%.

Figure 5.20 shows the counting efficiency in event mode and the peak heights. A large fraction of events are lost above 7 kHz due to the readout scheme, discussed below. A smaller fraction of events are affected by three bugs, which have been found by inspecting the peak heights and scanning the time stamps. The bugs cause events to be read out twice, events to occur below threshold, and events to occur above the maximum possible peak height as discussed in Appendix A.3.2. We remove events related to these bugs from C_{IPE} in event mode. The requirements for a real IPE count are: event time stamps must be later than the previous events, peak height must be above the threshold of 800, and the peak height must be less than 14,000. A maximum of 1.8% of events are removed per run with the repeated events cut. A maximum of 0.035% of events are removed per run for being below threshold or above the maximum peak height.

In event mode, events are lost in blocks. Figure 5.21a shows the time separation between

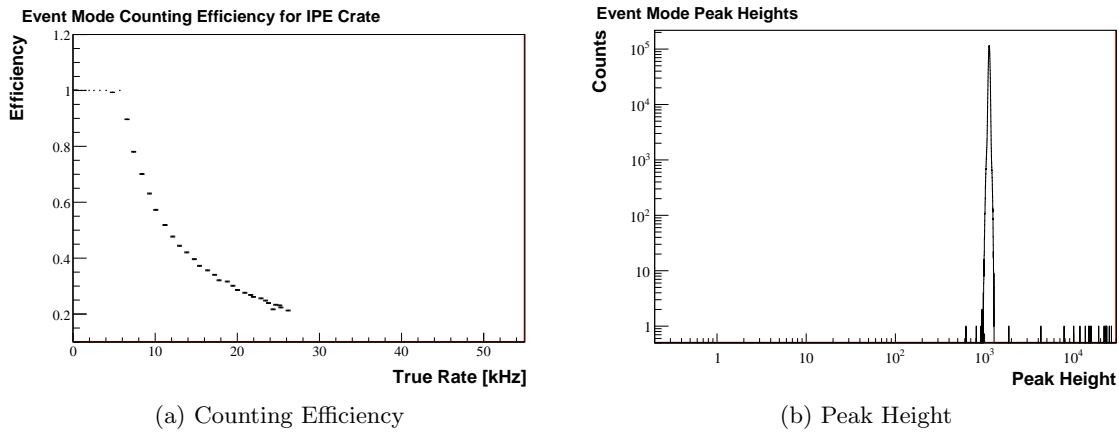


Figure 5.20: The counting efficiency for event mode (left) and peak-height spectrum (right). As expected, the counting efficiency is 100% below 7 kHz. Above 7 kHz, the efficiency is surprisingly low because events are lost in blocks instead of as single events.

events when the rate is 22.8 kHz. There is a peak in the time separation at 22.5 ms. Figure 5.21b shows the time stamps of events in this run. There are holes 22.5 ms long in the time stamps. For a rate of 22.8 kHz, a 22.5 ms hole corresponds to about $22.8 \text{ kHz} \times 22.5 \text{ ms} = 513$ events. By inspecting the event IDs, we verified the blocks correspond to 512 missing events, which is the capacity of the circular buffer. This pattern of missing events indicates that when the buffer fills up, the first event is overwritten with the last event. Pointers to the start of the buffer and the end of the buffer point to the same place and buffer appears empty. Therefore, although only one event was overwritten, all events in the buffer are lost. This is not the most efficient way to store events.

The counting efficiency for event and histogram modes have been tested up to 50 kHz for a single channel. Due to the minimum time separation of pulse-generator events, the events are not truly random above 14 kHz. At a measured rate of 50 kHz, the actual CENPA random pulse-generator output was almost 175 kHz, with 71% of the external triggers rejected by the Agilent pulse generator. The rate is no longer random at this point, it is approaching a 50 kHz periodic signal. Even without a truly random signal, these tests clearly show the histogram mode handles the high rates better than the event mode. The findings are:

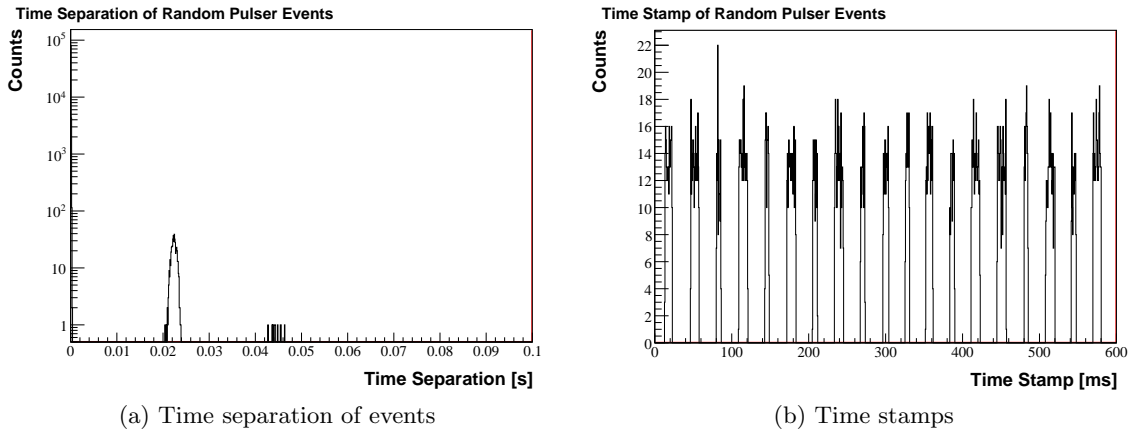


Figure 5.21: For this event mode run with a rate of 22.8 kHz, blocks of events instead of single events are lost. On the left, the time separation between events has a peak near 22.5 ms. On the right, the time stamps of recorded events show 22.5 ms holes where no events are recorded. At lower rates, the holes are longer in time as it takes more time to record 512 events, but the frequency of the holes is also reduced.

- In event mode, we observe 100% counting efficiency below 7 kHz in a single channel, consistent with the estimate in Appendix A.2.4. Above this rate, entire blocks of 512 events are lost instead of single events. This design makes the efficiency plummet above 7 kHz. The maximum rate of 7 kHz per card is much higher than the expected neutrino-mass data rates of 140 Hz total and meets our requirements. We expect the maximum recordable rate for the entire card is 7 kHz, but this has not been tested.
- In histogram mode, we observe 100% efficiency with non-random input signals up to 50 kHz. We expect every channel can handle random signals up to 100 kHz, but this should be tested.
- Bugs observed in histogram mode prevent the histograms from being cleared at the end of a run, so some histograms are read out twice. This causes an apparent efficiency of over 100%.
- Bugs observed in event mode include repeated events, events below threshold, and

events above the maximum possible ADC values. These bugs affect a small fraction of events.

5.4 Summary of the Detector System

All components in the detector system work together to maximize the efficiency with which the detector counts the signal electrons. We understand the detector signals and process them with a trapezoidal filter to find the electron energy. The data acquisition system accurately records information from the detector with minimal dead time. In addition to maximizing the signal, the detector system must be designed to reduce the background, a topic covered in the next chapter.

Chapter 6

THE DETECTOR BACKGROUND MODEL

To minimize the detector backgrounds, we must understand their sources and interaction mechanisms. Cosmic rays and natural radioactivity are well-known sources of background, but the actual rates detected by KATRIN will depend on the components surrounding the detector and the design of the cosmic-ray veto and shield. We model all the sources with extensive Geant4-based Monte Carlo simulations to identify the largest backgrounds and their signatures. With this information, we can optimize the detector-region design, concentrating on reducing the largest backgrounds. Once the detector is built, if it exhibits an unexpected large background the simulations can be used to identify the problem by comparing the signatures of the simulated sources to the measurements. This chapter presents the assumptions in the KATRIN background model.

6.1 *Geant4 Simulation Overview*

The GEometry ANd Tracking (Geant4) [66, 67] simulation toolkit models the passage of particles through matter and electromagnetic fields. It is freely available and widely used for many applications, ranging from collider physics to medical physics. Each user must customize Geant4 for their application: defining the initial particles which are simulated; the geometry and materials which the initial particle traverses; choosing the Geant4 models to calculate the interaction of the particles; and defining how to access, manipulate, and store information about particles as they propagate.

The major components of the KATRIN simulation, shown in Fig. 6.1, include the geometry, physics processes, primary generators, and the user interface. The Geant4 Run Manager accepts information from the user and stores information requested by the user. For the KATRIN simulation, the geometry is a simplification of the KATRIN design and is discussed in Section 6.1.1. We choose the Geant4 models to simulate physics processes

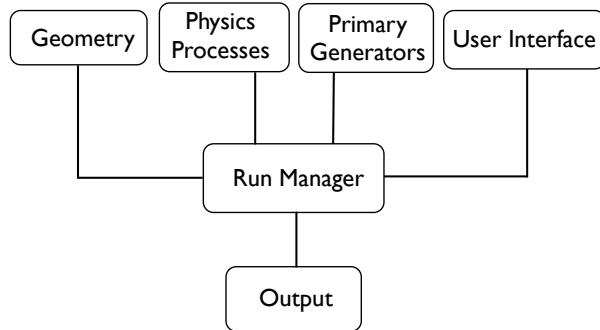


Figure 6.1: Simplified flow of information in the KATRIN simulation.

which are appropriate for the energy region of our background sources and include them in the physics list. Section 6.1.3 gives an overview of these models and processes. The primary generators are programmed with information about the sources of background for KATRIN and produce the initial particles for a simulation. The energy and angular dependence of each background source, which is implemented in the Primary Generators, has been found in the literature or we have measured it. These are discussed in more detail in Section 6.2. As the simulation runs, we can make changes to the geometry and control which particles to simulate through the user interface. The output of the simulation, which is stored in ROOT [68] files, is used to calculate a background rate, as described in Section 6.1.2. All simulations use Geant4 version 9.2 patch 01 and run on the University of Washington’s 140 node Athena cluster, which has 64-bit AMD processors.

Mistakes in any of the user-defined structures or in the physics models included by Geant4 can adversely affect results. The Geant4 collaboration systematically verifies the models and users often report problems, but each application requires a dedicated validation to ensure the results are correct. We have carefully reviewed the inputs to the KATRIN simulation described in this chapter. The simulation output and results are verified with measurements, discussed in Chapter 7.

6.1.1 *Geometry and Materials*

The simulation geometry must be a close approximation of the actual physical design to correctly model particle interactions in the detector regions. In order to have the correct absorption and production of secondary particles, the simulation geometry should include as much of the surrounding materials as possible. The silicon detector itself needs to have accurate dimensions and segmentation pattern to produce the correct detector response. The components must be positioned correctly with respect to the detector because the background from radioactivity depends on the distance between the detector and the components. We first present information on components surrounding the detectors, then discuss the silicon detector and scintillator in more detail later in this section. Finally, we list the limitations of the current geometry.

Figure 6.2 shows the entire simulated detector region. The simulation geometry does not contain all components of the actual detector region, discussed in Section 5.1, only those closest to the detector. It includes all components out to the detector-magnet cryostat, at a radius of 46 cm, but does not include the support structure for the magnet. The length of the entire system is 1.89 m. Inside the stainless steel magnet cryostat are the superconducting coils and aluminum coil banding. The veto scintillator and passive shield are positioned inside the magnet’s cryostat. All of the ceramics, which isolate the high voltage electrode, are included because ceramics are expected to be high in radioactivity. The detector itself is not at the center of the magnet, being offset by 16 cm toward the readout direction. The connections to the detector are made with “pogo pins”. The pogo pins, insulators for the readout pins, and twenty-four preamps are behind the detector on the readout side. The preamps are on ceramic boards, but for the simulation no electronic components are placed on the preamp boards. On the beam side, the calibration ports are included, as well as the gamma calibration source. The electron gun has not been added to the simulation geometry.

The real KATRIN experiment is much more than just the detector section. It contains a chain of magnets 70 m long, which create a magnetic field aligned along the axis of the experiment, called the beam direction. We do not simulate anything past the calibration

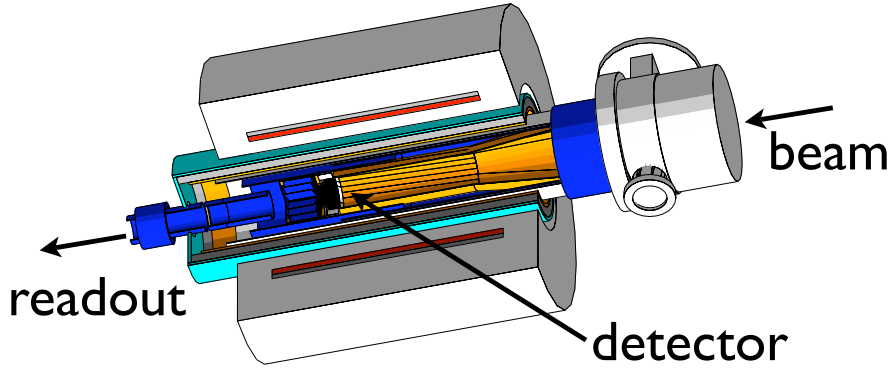


Figure 6.2: Detector region, including the magnet cryostat (grey) surrounding the magnet coils (red). The scintillator (cyan) and lead (dark grey) and copper (orange) shield are inside the magnet. The high-voltage insulators (blue), and high-voltage electrode (orange) are also visible. The calibration region (grey) is on the beam side.

region under the assumption that it will not affect the detector backgrounds. Like the true KATRIN field, the simulation magnetic field is aligned with the beam axis. But, for simplicity, the simulation field is constant at 3 T along the beam direction and neither expands nor contracts. All regions inside the magnet cryostat, up to a radius of 22 cm, have the constant field. The simulation magnetic field is 1.38 m long; it encloses all components on the readout side, but it stops before the calibration region. The constant magnetic field should be an adequate approximation of the real field since neither the KATRIN guided magnetic flux nor the simulation field connect the walls of the vacuum chamber to the detector. We did not simulate electric fields even though the post-acceleration electrode is in the geometry. The post-acceleration voltage could be any value between 0 and 30 kV. This low voltage should not affect high-energy cosmic rays or neutral particles, but the effect on beta-decay electrons should be investigated.

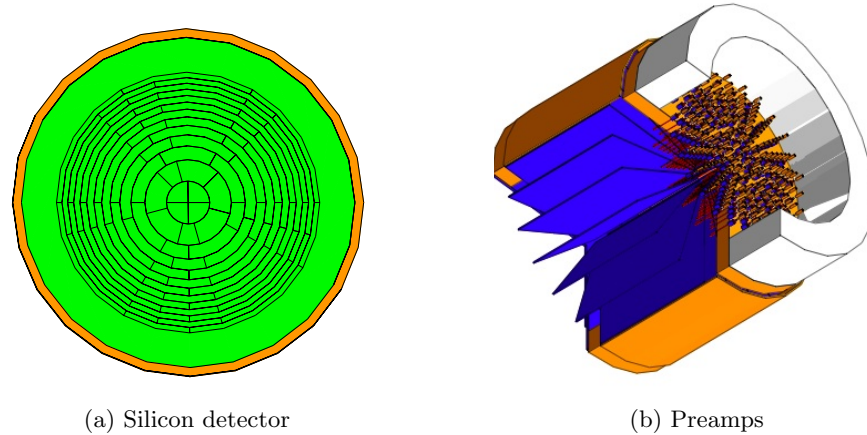


Figure 6.3: (a) Close-up of the silicon detector (green) showing the pixel pattern. (b) With the detector removed, the Conflat flange (grey) is cut away to reveal the 148 readout pins and insulators. Behind the flange are the twenty-four preamps (blue) in a copper carousel (orange).

Silicon Detector

Figure 6.3 shows the segmented silicon detector and a close-up of the Conflat flange including the readout pins and insulators and the preamps. The detector front surface includes a 50 nm dead layer, where the signal electrons lose some energy. This deadlayer is more optimistic than the design goal of 100 nm. The rear surface does not have any dead layer or coating. The flange and readout pins are the most complicated sections of the geometry. Because the detector is most sensitive to radioactivity in these components, it is important to model them in detail. The readout pins and insulator sleeves in the Conflat flange are niobium—which can produce an 18.6 keV X ray in our region of interest. Therefore, all niobium parts are included.

This type of detector was chosen because it efficiently detects KATRIN’s 18.6 keV signal electrons. In contrast, higher-energy electrons and muons at normal incidence are not fully absorbed by the detector; electrons and muons above 120 keV completely pass through the thin detector, which is only $500\ \mu\text{m}$ thick. These particles leave a fraction of their energy in the detector proportional to their path length, creating a broad bump in the spectrum

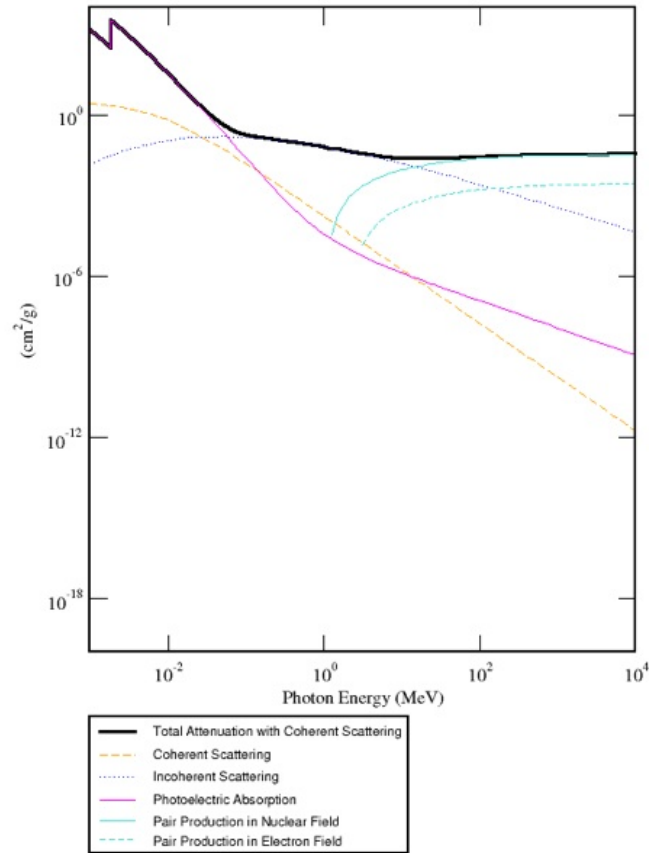


Figure 6.4: Photon interaction cross section in silicon. Figure from XCOM: The photon cross sections database [69].

starting around 120 keV.

A detector this thin is also not an efficient photon detector. Figure 6.4 shows the photon cross section for interactions in silicon. Around 60 keV the Compton-scattering cross section—labeled incoherent scattering—equals the photoelectric absorption cross section. Through the photoelectric effect, the total photon energy can be deposited in the detector in one interaction. But in Compton scattering, photons transfer only part of their energy. Therefore, for photons above 60 keV, collecting the total photon energy is unlikely.

The KATRIN signal will be a peak somewhere between 15–50 keV, depending on the voltage of the post-acceleration electrode. Photons with energy higher than our region of

interest (ROI) can still cause background events in the ROI by leaving only part of their energy. For these interactions, the detected energy is the energy transferred to an electron in the detector. The energy depends on scattering angle, with a maximum energy occurring for head-on collisions. Equation 6.1 shows the maximum electron energy, E_e , as a function of incident photon energy, E_γ .

$$E_e = E_\gamma \frac{2E_\gamma/m_e c^2}{1 + 2E_\gamma/m_e c^2} \quad (6.1)$$

Photons of energy 79 keV or above could create electrons with energy up to 18.6 keV in our detector; photons of energy 141 keV or above could create electrons with energy up to 50 keV. Therefore, we must reduce the high-energy photon backgrounds even though the photon energy is above our ROI.

In a real silicon detector, particles interact creating electron–hole pairs and phonon excitations in the crystal. The charge is collected, creating a voltage signal that is proportional to the energy deposited by the particle interaction, as discussed in Section 5.2.1. In the simulation, we also assume this proportionality holds and do not model the collection of electron–hole pairs. This is a good approximation for electrons and photons. Conversely, incident neutrons transfer energy to silicon nuclei. The recoiling silicon nucleus does not create as much ionization as an electron, so the deposited energy will not be proportional to the final voltage signal. A correction is applied for incident neutrons in the analysis, as addressed later in this section.

Both active detectors in the simulation, the silicon detector and the plastic scintillator, are implemented as Geant4 Sensitive Detectors. The silicon detector is divided into 148 individual pixel detectors. We use the Geant4 methods `GetTotalEnergyDeposit` and `GetNonIonizingEnergyDeposit` to get the energy deposited in the active regions by all particles at the end of every step. In Geant4, only neutrons or nuclei deposit non-ionizing energy through nuclear recoils. We compare the non-ionizing energy calculated by Geant4 to the correction for neutrons discussed later in the section.

For all particle types, the energy deposited within a 100 ns time window is added up to be one count. The 100 ns window starts with the first interaction. If a second particle

interacts after 100 ns, the energy deposited by the second particle is added up into a second count.

In this simple scheme, pile-up of counts is not correctly modeled. The signal from the KATRIN detector and preamps will have a charge collection and rise time faster than 100 ns, but a very slow fall time constant of 1 ms. In reality, if two counts are within 1 ms, these long pulses will overlap. In the KATRIN data acquisition system, pile-up will affect events that come within $4.8 \mu\text{s}$ as discussed in Section 5.3.2. For neutrino-mass data, we expect rates under 200 Hz, so less than 0.1% of events should be affected by pile-up. Therefore, we can neglect pile-up in the simulation.

Electronic and statistical noise are added as a Gaussian smearing to the energy. The gaussian width of the total noise should be slightly energy dependent as shown in Eq. 6.2.

$$\sigma^2 = \frac{\Delta^2}{2.35^2} + E F \epsilon \quad (6.2)$$

Here $F=0.14$ [70] is the Fano factor, $\epsilon=3.76 \text{ eV}$ [65] is the energy per electron-hole pair and E is the deposited energy. Since the noise cannot yet be measured, we assume the total noise is exactly the design goal of 600 eV full-width at half-maximum (FWHM) at 18 keV. Using these values, we solve for the electronic noise Δ , and find $\Delta=550 \text{ eV}$ FWHM. We assume the electronic noise is constant at all energies.

Neutron Pulse-Height Defect

Neutrons under 10 MeV, for example neutrons produced by cosmic rays, interact in the silicon detector predominantly by elastic scattering. The energy transferred to the recoiling silicon atom depends on the scattering angle, with the maximum being about 13% of the incident neutron's energy. Recoiling atoms are different from recoiling electrons; both lose some energy to ionization and some to phonon excitations of the crystal, but recoiling atoms lose more to phonon excitations than for electrons. The deficit of ionization for nuclear recoils is often called a pulse-height defect or quenching.

As discussed above, the Geant4 simulation computes the total energy deposited and the non-ionizing-energy deposited. Rather than depend on Geant4's non-ionizing energy as a

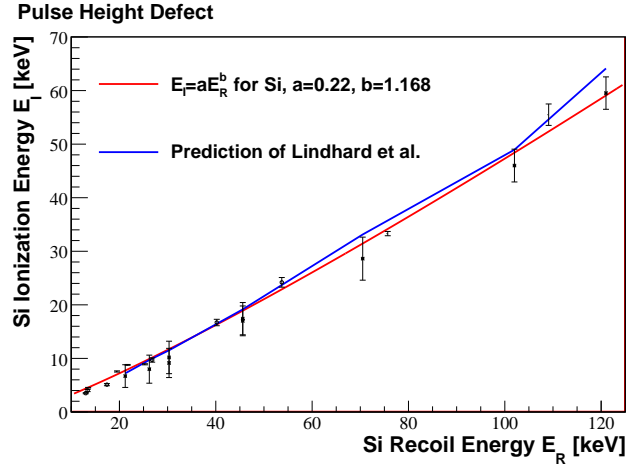


Figure 6.5: Measurements [72, 73, 74, 75] of visible ionization energy versus Si recoil energy and the fit we use to correct the neutron pulse-height defect.

correction to the total energy, we correct the total energy deposited based on measurements. Lindhard, Nielsen, Scharff and Thomsen [71] numerically calculated the ratio of the recoil energy to ionization, and it has been measured in silicon by bombarding silicon detectors with neutrons of energies up to 24 MeV [72]. More recent measurements have explored recoil energies down to 4 keV with greater precision [73, 74, 75]. For KATRIN, we are interested in the ionization energy range of 15–50 keV, which corresponds to a recoil energy up to 100 keV.

We fit the neutron recoil data to find the visible ionization energy, E_I , as a function of simulated recoil energy, E_R . Figure 6.5 shows the data and the fit along with the predictions of Lindhard et al. The best-fit parameters for the fit function $E_I = aE_R^b$ are $a = 0.219 \pm 0.006$ and $b = 1.168 \pm 0.008$. For the cosmic-ray neutrons, we correct the energy of all counts caused by neutrons. Although the correction may only be valid in the region of the fit, we apply the correction at all energies. Since neutron interactions at high energy are rare, and the correction is valid in our region of interest, this is not expected to affect the background estimates.

Plastic Scintillator

The purpose of the plastic scintillator is to tag silicon detector counts in coincidence with cosmic rays. It is divided into four panels and an end-cap. Each panel is separated by 0.25 cm. We assume the scintillation light signal is proportional to the energy deposited inside the plastic within 100 ns. No optical photons are produced or propagated through the optical fibers. We do not add electronic noise to the energy since we are not interested in the energy spectrum. The scintillator is 1 cm thick plastic, so a through-going minimum-ionizing particle such as a cosmic-ray muon will deposit greater than 1.2 MeV of energy in one panel. To veto a count, greater than 1.2 MeV must be deposited in one scintillator panel within $1 \mu\text{s}$ of the silicon detector event. The goal for the scintillator is at least 90% efficiency, so we assume the veto efficiency is 90%.

Implementation and Limitations of the Geometry

Defining the geometry in Geant4 has three steps; a Solid is created with the desired shape, the material is associated with the Solid as a Logical Volume, and the Logical Volume is positioned with respect to the rest of the geometry by placing the Physical Volume. We defined the detector region by hand using simple Constructive Solid Geometry (CSG) shapes and combining them with boolean operations. Multiple copies of a volume with the same shape can be placed with a different copy number. Using this method, we added 184 identical readout pins and insulators to the geometry. The detector pixels are a different shape in each ring, so we define the pixels as Parameterized Volumes. Geant4 provides a database of common materials that the user can access through the G4NistManager. We define more complicated materials by hand, after looking up chemical formulas and densities.

As the KATRIN design progressed, we often experimented with variations in the simulation. Changing the geometry from the standard design and changing the geometry between simulation runs was useful. But as the components of the detector region are built and the dimensions are determined by the physical objects, it will be necessary to have a geometry that matches the detector region as-built. A few tools for importing CAD drawings into the Geant4 Geometry Description Markup Language (GDML) exist, for example the

FASTRAD software (www.fastrad.net). This option should be explored.

In addition, some components may need to be added for other purposes. Simulations of the KATRIN beam or electron guns will need an accurate magnetic field. After the front-surface dead layer of the detector is measured, the value should be updated. Including the fibers in the scintillator will improve its response. Therefore, this simulation geometry is not considered the final KATRIN geometry.

Geant4 provides tools to check for overlapping volumes—`/geometry/test/grid.test true`—but it is the user’s responsibility to check that dimensions and materials match the design. The masses of all components as computed by the Geant4 simulation are listed in Appendix B.1 and were compared with the design as an additional test.

6.1.2 *Simulation Output*

We use the Geant4 toolkit to understand what happens to particles as they interact in the detector region. In the Geant4 structure, a run contains a group of events with the same geometry, physics list, and generator settings. Each event starts with a primary particle (or particles) which can create secondary particles. Every particle is tracked through the geometry, and its energy loss is computed for each step. We use the Geant4 definitions of these terms—a run contains events, an event contains tracks, and a track contains steps. We save information about what type of particle enters the detector, what interaction created the particle, where it was created, and more. This information is useful in understanding how a source of background creates counts in our detector. But the ultimate goal of the simulation is to calculate the background rate in the silicon detector.

As described above, the energy deposited in the detector within a 100 ns window is a count. Therefore, for a single Geant4 event, we may have no detector counts or we may have multiple detector counts. We calculate the number of counts in our detector as a function of energy. To get the number of counts in our region of interest, N_{ROI} , we integrate over the ROI energy range. The position and width of the ROI will depend on post-acceleration and the detector magnetic field. To convert to a rate and compare to our design goal, we must normalize N_{ROI} by a time duration T that depends on the background source. The

definition of the time duration is different for each source, and is discussed for each of the sources later in this chapter. The statistical uncertainty is calculated assuming Poisson statistics.

$$R_{\text{ROI}} = \frac{N_{\text{ROI}}}{T} \quad \sigma_R = \frac{\sqrt{N_{\text{ROI}}}}{T} \quad (6.3)$$

The rate from each source is calculated separately and added together:

$$\begin{aligned} R_{\text{Tot}} &= R_1 + R_2 + \dots \\ \sigma_{\text{Tot}}^2 &= \sigma_1^2 + \sigma_2^2 + \dots \end{aligned} \quad (6.4)$$

The background spectra must also be normalized and added together in this way. An additional uncertainty arises from the simulation time duration, T , which depends on the background source and is presented in Section 8.3.

6.1.3 Physics Processes

Particles interact with matter through various processes. Geant4 provides codes which are models of the physical process. The user decides which model to use and includes it in the physics list. For each process, there may be multiple models to choose from. To make it easier for the user, each Geant4 code release contains realistic examples of simulation applications for various physics experiments. The “underground_physics” example application is a simulation of a low-background dark matter experiment, which has background mechanisms and an energy range of interest similar to KATRIN. We use the physics list from the “underground_physics” example to simulate backgrounds for KATRIN.

Our region of interest is 18.6 keV or higher with post-acceleration, so we require that the simulation is accurate for energies at least as low as 18.6 keV. The detector’s energy resolution is 600 eV FWHM, so simulation errors of 600 eV or below will not affect the spectrum. Reaching this accuracy can be challenging since the initial particles cover a wide range of energy, from 100 GeV for muons down to a few keV for X rays. The “underground_physics” example’s physics list is therefore appropriate for use in the KATRIN simulation since it

Table 6.1: Physics processes defined for each particle in the KATRIN simulation.

Particle	Allowed Processes
Photons	photoelectric effect, Compton scattering Rayleigh scattering, pair-production
Muon	ionization, bremsstrahlung pair-production, multiple scattering μ^- -capture, decay
Electrons	ionization, bremsstrahlung multiple scattering
Neutron	elastic scattering, inelastic scattering neutron capture, neutron decay
Positrons	ionization, bremsstrahlung annihilation, multiple scattering
Alphas	ionization, elastic scattering inelastic scattering, multiple scattering

was built for a similar problem.

Table 6.1 shows a partial list of particles included in the KATRIN simulation and the processes allowed for each. The models we use to simulate these processes include: the Low Energy Electromagnetic model which is valid down to 250 eV for electrons and down to 1 keV for photons, protons and ions [66]; the Standard Electromagnetic model for positrons; the High Precision Neutron model for neutrons; the Low and High Energy Parameterized Hadronic model for hadrons; and the Radioactive Decay model to calculate decay products. In Geant4, all particles are tracked down to zero range, but are only produced and tracked if the initial energy is greater than the production cuts. For electrons and positrons the production cut is set to a range of 800 nm; for photons the range cut is 5 μm . In silicon, this translates to a production energy of 600 eV for electrons and 250 eV for photons.

6.2 Sources of Backgrounds

Two well-known sources of background are cosmic rays and natural radioactivity. Each generate different particles with different energy ranges, creating counts in the detector

in different ways. The initial positions and angular distribution of the various particles depend on the production mechanisms. We review the production mechanisms and present the initial positions, energy distributions, and angular dependence of each source in the next sections.

6.2.1 Cosmic Rays

Cosmic rays, produced in many astrophysical sources in our Universe, continuously bombard the Earth's atmosphere, creating showers of particles that reach the Earth's surface. The composition of the shower changes as particles interact and decay while propagating through the atmosphere. At the surface of the Earth where the KATRIN experiment will operate, the composition of particles includes neutrinos, photons, muons, electrons, neutrons, protons, and pions in order of abundance. Historically, cosmic rays have been divided into the "hard component" that can penetrate 15 cm of lead and the "soft component" which cannot. The KATRIN shield is only 3 cm of lead, so we must simulate some of the soft component in addition to the most penetrating. Photons, muons, neutrons, and protons have been investigated as background sources for KATRIN. Neutrinos, electrons, and pions are expected to make negligible contributions and are not generated as initial particles.

Cosmic rays have been studied in detail since Victor Hess's discovery in 1912, so the characteristics of the cosmic-ray types are well known. Due to different production mechanisms, each type of particle has a different angular and energy distribution. Typically, the angular distribution has only a weak azimuthal dependence and a strong dependence on zenith angle θ . Therefore, we denote the directional intensity by $I(E, \theta)$ indicating the zenith angle dependence but neglecting the weak azimuthal dependence. For each particle type, we found the directional intensity in the literature. Fig 6.6 summarizes the vertical intensities $I(E, 0)$ and zenith angle dependence we used for the different cosmic-ray types. Each type is discussed in detail below.

To find the total number of particles passing through a horizontal area per unit time,

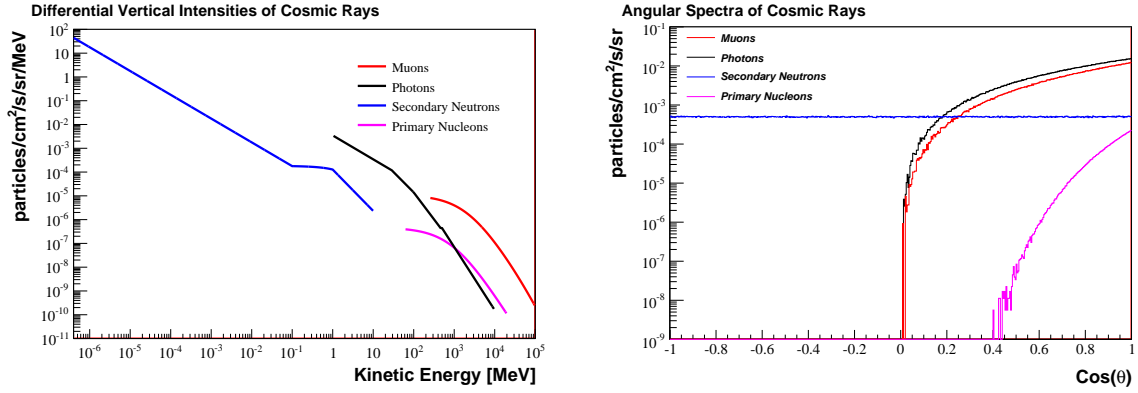


Figure 6.6: Differential vertical intensities and zenith angle dependence at sea level of all particles as implemented in the simulation. For each source, the intensity is taken from the literature, as discussed in the text.

Table 6.2: Energy range and total intensity of the simulated cosmic rays.

Particles	Kinetic Energy Range MeV	Intensity $J(>E)$ particles/cm ² /s
Photons	1 – 10 ⁴	0.0324
Muons	250 – 10 ⁵	0.0231
Neutrons	4×10 ⁻⁷ – 10	0.00626
Nucleons	61 – 2×10 ⁴	0.000141

we integrate the directional intensity over energy and solid angle [76] as in Eq. 6.5.

$$I(E, \theta) = \frac{dN}{dA dt d\Omega dE} \frac{\text{particles}}{\text{cm}^2 \text{ s sr MeV}} \quad (6.5)$$

$$J(> E) = \int_E^\infty \int_\Omega I(\theta, E) d\Omega dE \frac{\text{particles}}{\text{cm}^2 \text{ s}}$$

Table 6.2 shows the simulated total intensities $J(> E)$, after integrating the directional intensity over the energy range and solid angle as in Eq. 6.5.

The intensity of cosmic rays depends on altitude and latitude and varies with the solar cycle. Karlsruhe, Germany is close to sea level at an altitude of 110 m or an atmospheric depth of 1020 g/cm² [77], so we use the sea level intensities when possible. Geomagnetic

effects cause an increase in the intensity with latitude and a decrease the minimum energy. The latitude of Karlsruhe is 49.00° N. Since we do not correct the intensities for latitude or solar cycle, we introduce an uncertainty in the intensities. This will be discussed in more detail for each particle.

Cosmic-Ray Muons

Cosmic-ray muons are produced in the atmosphere by the decay of charged mesons—mostly pions. At the Earth’s surface the average muon energy is 4 GeV [78]. The angular distribution changes with energy. At low energy, large angles are suppressed due to the longer path length in the atmosphere and the distribution is $\cos^2 \theta$. Around 100 GeV the angular distribution approaches $\sec^2 \theta$. We use an empirical form of the muon directional intensity [79] that includes these angular features:

$$I(E, \theta) = \frac{372}{E \cos \theta + 80} (5E + 10 \sec \theta)^{-2.57} \frac{E + 15}{E + 15 \sec \theta} \frac{\mu's}{\text{cm}^2 \text{ s sr GeV}}. \quad (6.6)$$

Here, E is the total muon energy in GeV and θ is the zenith angle.

This empirical form used for the simulation agrees well with more recent measurements compiled by the Particle Data Group [78] as shown in Fig. 6.7. In addition, this spectrum is also in agreement with newer numerical calculations [80] over the energy range that we simulate. Solar activity and geomagnetic effects can influence the intensity of muons near 1 GeV at the 10% level [78], but we do not correct the intensity for these effects, so this introduces an uncertainty. In 1995, Wentz et al. [89] measured the vertical intensity in Karlsruhe, Germany above 0.5 GeV to be $(85.4 \pm 3.4) \times 10^{-4} \mu/\text{cm}^2/\text{s}/\text{sr}$. The intensity used in the simulation gives $100 \times 10^{-4} \mu/\text{cm}^2/\text{s}/\text{sr}$ above 0.5 GeV, 15% higher than Wentz’s measurement. Therefore, we estimate the uncertainty on the intensity to be $^{+10\%}_{-15\%}$ from the Wentz measurement and the expected variation from geomagnetic and solar effects.

A larger number of positive muons reach the surface of the Earth compared to negative muons due to the large number of protons in the primary cosmic-ray flux. For the simulation, we use a constant ratio of 1.2 between positive and negative muons, although the actual ratio increases to 1.3 at 100 GeV [86], the edge of the simulated energy. Positive and negative

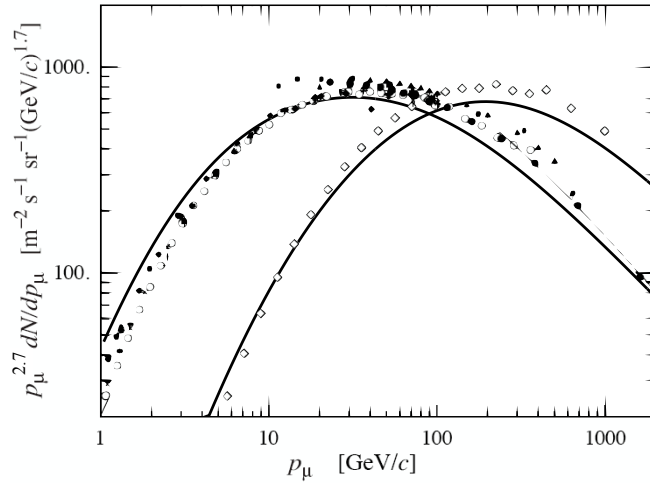


Figure 6.7: Comparison of the simulated differential intensity of muons (Eq. 6.6) to sea level measurements at $\theta = 0^\circ$ (\blacklozenge [81], \blacksquare [82], \blacktriangledown [83], \blacktriangle [84], \times , $+$ [85], \circ [86], \bullet [87]) and $\theta = 75^\circ$ (\diamond [88]). The differential intensity is plotted as a function of momentum p and has been normalized by a factor of $p^{2.7}$ for ease of viewing. Figure modified from the Particle Data Group [78].

muons interact differently at low energies; positive muons decay and negative muons can be captured by surrounding atoms. The simulation includes both types of interaction.

Cosmic-Ray Photons

Cosmic-ray photons are produced in the atmosphere through neutral pion decay and bremsstrahlung of charged particles and are part of the soft electromagnetic component, which—unlike muons—cannot penetrate 15 cm of lead. Historically, separating photons from electrons and positrons in measurements has been challenging. Daniel and Stephens [90] calculated the photon differential energy spectrum from measurements including electrons, positrons and photons. We fit the sea level calculation plot of Daniel and Stephens to a power law with a different exponent in four energy regions:

$$I(E, \theta) = A E^\alpha \cos^2 \theta \frac{\gamma' s}{\text{cm}^2 \text{ s sr MeV}}. \quad (6.7)$$

Table 6.3: Constants used in the photon differential energy spectrum, Eq. 6.7, where E is the total energy in MeV.

Energy Range MeV	A	α
1 – 30	0.00347	-1.01
30 – 10	0.0378	-1.72
100 – 500	0.455	-2.26
500 – 10^4	6.33	-2.65

Table 6.3 shows the constants in each energy region. This function describes the cosmic-ray photons from 1 MeV to 10 GeV, with an average of 40 MeV.

Primary Nucleons

The degraded remnants of the primary cosmic-ray nucleons reach the Earth's surface as protons and neutrons. These nucleons represent the smallest fraction of the total cosmic ray spectrum at the Earth's surface that we simulate. About 2/3 of the flux is protons, while the other 1/3 is neutrons. All nucleons are attenuated by strong interactions with the nuclei of air molecules in the atmosphere. The directional intensity [78] which describes nucleons is:

$$I(E, \theta) = 1.8 E^{-\alpha} e^{-X/\Lambda \cos \theta} \frac{\text{nucleons}}{\text{cm}^2 \text{ s sr GeV}} \quad (6.8)$$

Here, $\alpha = 2.7$ is the differential spectral index of the primary cosmic rays, E is the total energy in GeV, $X = 1020 \text{ g/cm}^2$ is the atmospheric depth, and $\Lambda = 121 \text{ g/cm}^2$ is the attenuation length of nucleons in air. As seen in Fig. 6.6, nucleons have a steeper zenith angle dependence than a $\cos^2 \theta$ distribution. Therefore, the primary nucleons are only generated with zenith angles up to 70° .

Table 6.4: Constants used in the neutron differential energy spectrum power law function.

Energy Range MeV	Variable	Value
4×10^{-7} –0.1	C_1	0.000223
0.1–1	C_3	0.0023
	C_4	-0.0007
1–10	C_2	0.0016
	n	1.74

Secondary Neutrons

The energy spectrum of secondary neutrons near the air–ground boundary is different than in the atmosphere due to the ground’s effect on neutron production and deceleration. At the boundary, neutrons are produced after high-energy nucleons interact, through evaporation from excited nuclei and high-energy nuclear interactions. Yamashita [91] plots the calculated differential intensity for various altitudes and gives the form of the differential intensity:

$$\begin{aligned}
 4\pi I(E, \theta) &= C_1/E & 0.4 \text{ eV} < E < 0.1 \text{ MeV} & \quad (6.9) \\
 &= C_3 + C_4 E & 0.1 \text{ MeV} < E < 1 \text{ MeV} & \\
 &= C_2 E^{-n} & 1 \text{ MeV} < E < 10 \text{ MeV}. &
 \end{aligned}$$

In this equation, E is kinetic energy in MeV and n is the spectral index. We fit Yamashita’s plot of the calculated differential intensity with Eq. 6.9. Table 6.4 shows the results of the fit. The measured angular distribution is approximately isotropic, with some results showing a slight increase from the downward direction. This simulation assumes the distribution is isotropic.

In addition to these secondary neutrons, a large number of thermal neutrons are produced with an average energy of 0.025 eV. The flux of thermal neutrons is 1.07 n/cm²/s [91], about one sixth of the total secondary neutrons. We have not simulated thermal neutrons, but estimated the background from photons produced by neutron capture in the copper

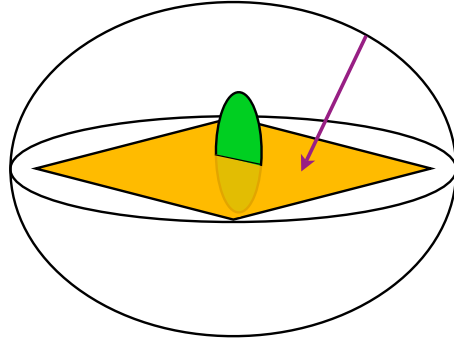


Figure 6.8: Diagram of the `CosmicRayGun`. The silicon detector is shown in green in the center. The orange plane intersects the detector and represents the random positions that can be chosen. A direction is chosen, and a cosmic ray aimed in that direction, like the purple arrow, toward a position on the orange plane.

shield to be negligible.

Cosmic Ray Generator

Cosmic rays come from the atmosphere, so their starting positions are external to the detector geometry. To simulate cosmic rays, we wrote the primary generator called the `CosmicRayGun`. It creates particles with the energy and angular dependence of cosmic rays. This algorithm saves computation time by starting the cosmic rays outside the detector geometry and aiming them toward a region around the detector. Figure 6.8 is a simplified diagram of how the gun works.

First, we randomly choose a position on a plane centered around the detector, as shown in orange. The plane is perpendicular to the zenith. Next, we choose an energy and angular direction from the intensity distributions defined for each cosmic-ray type. Using this angular direction, the particle is moved to a position on a sphere outside the detector geometry. This is the initial position of the particle. It is shot toward the position on the plane with the chosen energy, as shown by the purple arrow.

For the KATRIN geometry, we use a plane which is 60 cm by 60 cm. This plane surrounds the detector, saving computation time by aiming the particles toward the detector, but

allows the cosmic rays to interact in the shield and magnet. We use a sphere of radius 100 cm for the initial positions of the cosmic rays. This positions them outside the simulation geometry, except in the calibration region on the beam side. Here, they start within the calibration vacuum which is not in a magnetic field due to simplifications in the simulation as described in Section 6.1.1. In reality these cosmic rays must pass through the main spectrometer to enter the detector region from this angle.

For cosmic rays, the simulation time duration—which normalizes the rate—equals the number of simulated cosmic rays, N , divided by the area of the plane, A , and the intensity, $J(> E)$.

$$T = \frac{N}{J(> E)A} \text{ s} \quad (6.10)$$

Only the intensity $J(> E)$ has an uncertainty associated with it. Although the uncertainty can be different for each cosmic-ray type, we assume each has the same uncertainty as muons. For muons, we assume an uncertainty of ${}^{+10\%}_{-15\%}$ based on variations due to solar and geomagnetic effects and the difference between a measurement in Karlsruhe of Wentz et al. [89] and the assumed muon intensity.

6.2.2 *Natural Radioactivity*

Primordial radionuclides, created in supernovae at some point in the universe’s history, now permeate all materials. The most common, ${}^{238}\text{U}$, ${}^{232}\text{Th}$ and ${}^{40}\text{K}$, have half-lives of billions of years; therefore a large fraction of the initial concentration remains. Cosmic rays interact with nuclei to produce other unstable isotopes, called cosmogenic radioactivity. These radioactive isotopes usually have short half-lives. Without the continuous activation from cosmic rays, they would decay away.

All radioactive isotopes decay emitting radiation. Uranium and thorium both feed chains of alpha and beta decays that progress through unstable daughter isotopes. The decay chains emit low-energy X rays near our region of interest and gammas with energy up to 2.6 MeV. Figure 6.9 shows the daughters in the chains with their half-lives. Even though the daughter isotopes have shorter half-lives, the entire chain’s activity is solely determined by the parent’s activity, assuming equilibrium.

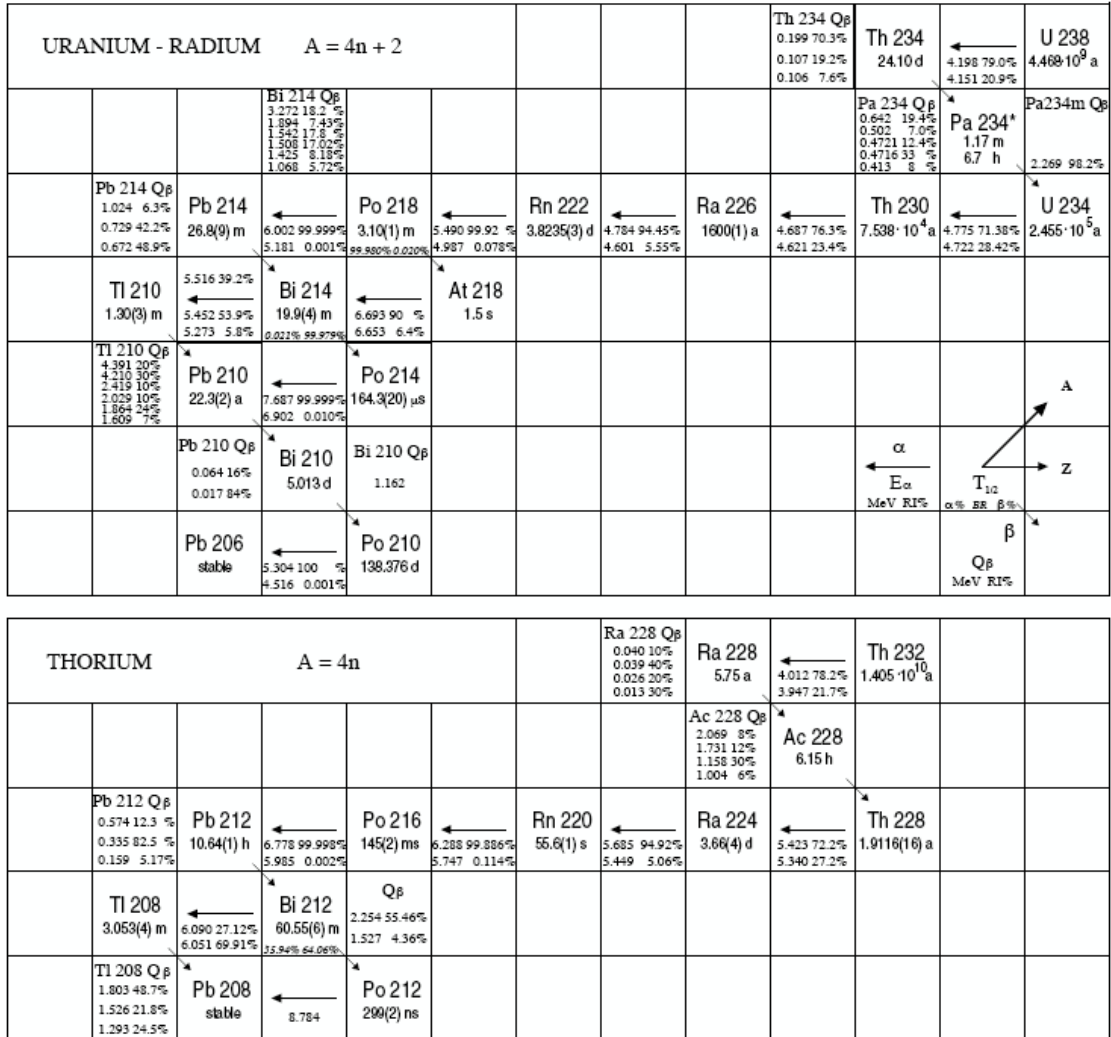


Figure 6.9: The uranium and thorium decay chains. Figure from Farine [92].

All substances contain some amount of primordial radionuclides and all materials have radioactive isotopes activated by cosmic rays. Therefore, we simulate primordial and cosmogenic activity in the detector components. Since primordial radionuclides emit high-energy photons, we also simulate primordial radioactivity from the KATRIN detector laboratory outside the detector components. This radiation can penetrate the KATRIN shield and create a background. We first discuss primordial radionuclides in the detector components and the environment, then we discuss cosmogenic radioactivity produced in the detector components.

Primordial Radioactivity in the Detector Components

Although all substances contain some amount of radionuclides, a careful assessment of materials can reveal some more radio-pure choices. On average, soil contains 400 Bq/kg ^{40}K , 37 Bq/kg ^{232}Th and 66 Bq/kg ^{238}U [93]. Materials used in the KATRIN detector region must be much more radio-pure. Reducing the radioactivity very close to the detector is mandatory since beta-electrons and low-energy photons are easily detected. Even though the detector is less efficient for high-energy photons, radiation far from the detector must be included since photons with 1 MeV of energy can penetrate the KATRIN shield. Therefore, we simulate natural radioactivity in all the detector components to determine the allowable activity for materials used in the construction.

We estimate the effects of uranium, thorium and potassium in the detector components by assuming the impurities are uniformly distributed throughout a material. Alan Smith at LBNL [94] assayed samples of most materials, measuring the specific activity in Bq/kg. Using the measured specific activity or one taken from the literature, we calculate the total activity of a component by multiplying by the total mass of the component. The specific activities are listed in Appendix B.1, along with the mass of each component as computed by the Geant4 simulation. In total, we investigate the impact of radioactivity in twenty components. Unless otherwise noted, all chains are assumed to be in equilibrium.

Primordial Radioactivity Generators

To simulate the radioactive decay of uranium, thorium, and potassium in the detector components we use two different primary generators; one released with Geant4, the other written for the KATRIN simulation. Both define the energy and type of radiation released, but do not set the particle's position. To uniformly spread the isotopes throughout a material, we use Geant4's General Particle Source (GPS). Given coordinates and the shape of a volume, this utility picks homogeneous random starting positions within the volume. For complicated shapes, like the 148 readout pins, we use the `/gps/pos/confine name` command to choose positions only in physical volumes with the specified name.

Geant4 Radioactive Decay Module

The Geant4 Radioactive Decay Module (GRDM) is a particle generator released by Geant4. It will calculate all products of a radioactive decay including radioactive daughters. It is easy to use and generates the required betas, Auger electrons, gammas, X rays, alphas, neutrinos, and recoil nuclei. The particles are simultaneously released with an energy and angular distribution based on the Evaluated Nuclear Structure Data File (ENSDF) [95]. Summation of particles can occur if two or more particles from one decay enter the detector.

Since uranium and thorium have such long half-lives, each isotope in the chain must be simulated separately to prevent physically impossible summation of counts while maintaining a precision on the detector's readout time. The `/grdm/nucleusLimits A A Z Z` command instructs the GRDM to decay only one isotope per event, preventing physically impossible summations. The GRDM generates ions from the ground state by default. ^{234m}Pa in the uranium chain decays from an excited state. Using the `/grdm/ion Z A E` command, the user can specify the excited state of energy 73.92 keV.

Unfortunately, many problems with the GRDM exist. For KATRIN, the major concerns are the under-production of X rays and low-energy gammas from the uranium and thorium chains with energy in our region of interest. The GRDM also has the incorrect intensities for photons from ^{241}Am , one of our calibration sources. The GRDM's low-energy photon intensities change with each release of Geant4. Figure 6.10 shows the low-energy photons

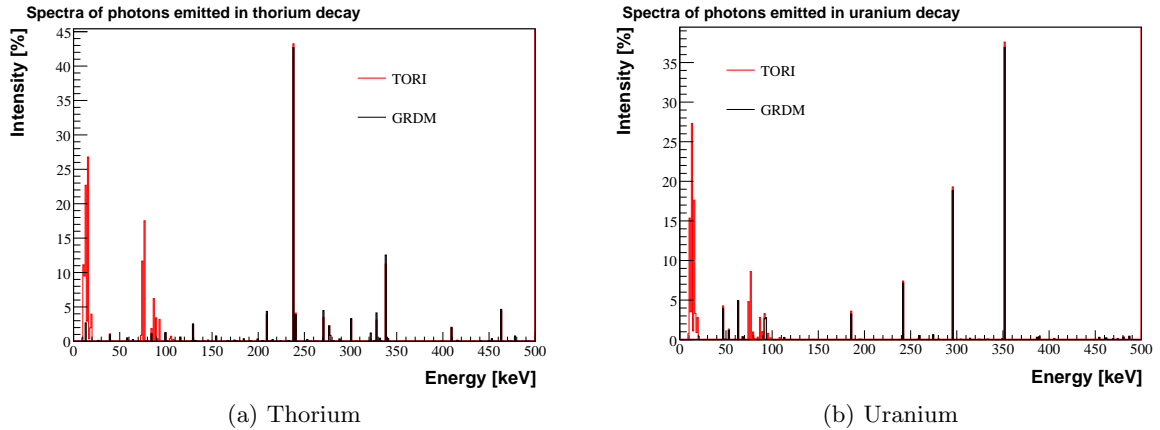


Figure 6.10: Photons emitted in the uranium and thorium chains. The Y-axis is the probability in percent of producing a photon per uranium or thorium decay. The GRDM underproduces X rays in the KATRIN region of interest.

generated by the GRDM version 9.2 patch 01 compared with those listed in the Table of Radioactive Isotopes (TORI) [96]. The underproduction of photons under 100 keV is obvious.

Despite its drawbacks, the GRDM is useful for producing particles other than photons. Both the beta-electrons and the X rays in our region of interest are important for KATRIN, so the GRDM must be fixed. A simple solution is to stop all GRDM photons under 100 keV during their first step, so they cannot contribute to the background. Then we run a second simulation which includes only photons under 100 keV and add it to the GRDM results. This method puts the photons into a new event, so no summation can occur between photons and electrons—but this should be a small correction.

For the GRDM, the simulation time duration in seconds equals the number of parent isotopes generated, N , divided by the specific activity, A , and the mass of the component, M :

$$T = \frac{N}{AM} \text{ s.} \quad (6.11)$$

The specific activities and masses are listed in Appendix B.1. For materials that have been assayed, the measurement includes a small uncertainty on the specific activity. Not all

materials have been assayed, so there are larger uncertainties on the assumed activities.

Calibration Generator

The second primordial radioactivity generator we use was written specifically for KATRIN. Photons are the only particle released in radioactive decay that can penetrate the KATRIN shield and reach the detector from far away. Rather than simulating all particles with the GRDM when only photons contribute to the background, it is computationally faster to generate only the photons. We wrote the custom `CalibrationGenerator` to correct the GRDM simulations and to generate only the photons.

The energy and intensity of photons released in radioactive decays are listed in the Table of Radioactive Isotopes [96]. Photons from the uranium and thorium chains with intensities greater than 0.05% have been added to the `CalibrationGenerator`. For the uranium chain, we have added 212 photons. For thorium, 229 photons have been added. Potassium has not been implemented in the `CalibrationGenerator` because it releases a single photon and is therefore easy to simulate directly with the General Particle Source.

In addition to photons released in decays, the highest-energy beta-decay electrons can have energies of a few MeV, enough to release bremsstrahlung radiation. Since we do not simulate the electrons, the bremsstrahlung photons are not produced. These make up a small fraction of all photons and should not affect the background estimates.

The `CalibrationGenerator` relies upon the GPS to uniformly spread the photons throughout a material and to isotropically choose directions for the photons. In this method a single photon is generated per event, without angular or time correlations between the photons.

We use the `CalibrationGenerator` for all components that do not have a direct line of sight to the detector since everything except photons has short ranges. The `CalibrationGenerator` simulation time duration in seconds equals the number of photons generated, N , divided by the specific activity, A , the mass of the component, M , and the average number of photons emitted per decay, F :

$$T = \frac{N}{AMF} \text{ s.} \quad (6.12)$$

For potassium, 10% of decays release a 1.46 MeV photon, so F is 0.1. For ^{238}U , after summing up the whole chain, an average of 3.16 photons are emitted per uranium decay. For ^{232}Th , F is 3.82. Again, the only uncertainty we consider is the uncertainty on the activity.

Environmental Radioactivity

Radiation from uranium, thorium, and potassium originates in materials outside the KATRIN detector construction as well as the detector components. Soil has an especially high level of contamination compared to the materials chosen for the detector region. At sea level, the environmental radiation outdoors is typically 10 photons/cm²/s above 50 keV and 1 m above the ground [97]. The walls and roof of the building and other objects around the detector are other potential sources or shields for radiation. Depending on housing structures and construction materials, the ratio of human exposure from terrestrial radiation indoors compared to outdoors can be 0.8 to 1.2 [93]. Instead of assaying all construction materials and simulating decays in all possible sources, we have made a series of measurements in the detector laboratory in the Karlsruhe Institute of Technology (KIT) using a germanium detector. The measurements, described in detail in Section 7.2, were designed to determine the energy spectrum and angular distribution of the incident radiation.

Although the sources of radiation are believed to be uranium, thorium, and potassium mostly in the ground, we cannot assume the energy spectrum of environmental photons to be the same as the initial energy of photons emitted in these decays. Compton scattering of the photons occurs within the source, creating a larger number of low-energy photons. Furthermore, we cannot calculate the initial spectrum by normalizing the measured spectrum with the efficiency of the germanium detector. The full-energy-peak efficiency of the detector cannot correct the measured energy spectrum for photons that Compton scatter in the detector and do not leave their full energy in the detector. Therefore, to determine the initial energy spectrum, we simulate photons spread through concrete to cause Compton scattering in the source and allow Compton scattering in the detector. Section 7.2 discusses this calculation. Figure 6.11 shows the photons emitted by potassium and the uranium

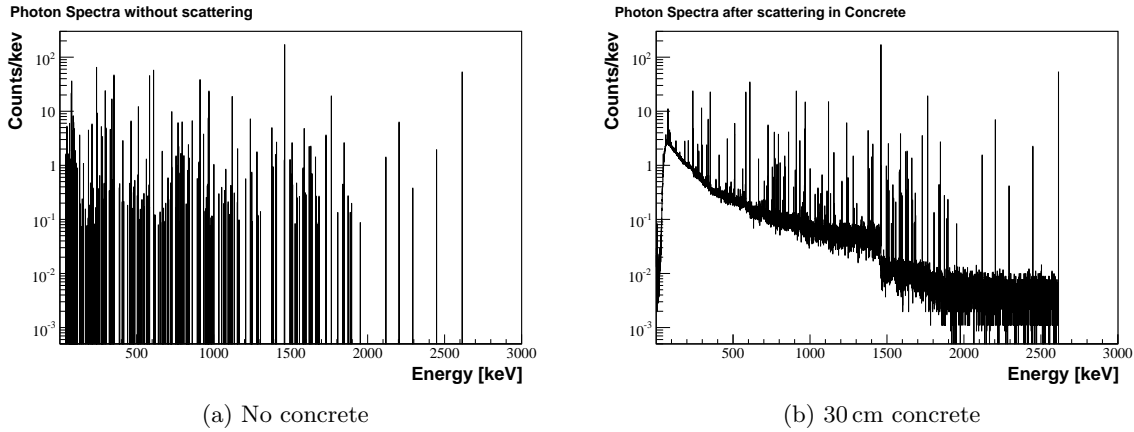


Figure 6.11: Effect of scattering in the concrete on the spectrum of photons. The photon spectrum emitted by potassium and the uranium and thorium chains as implemented in the `CalibrationGenerator` is shown in (a). The spectrum of photons emerging from 30 cm of concrete after scattering as implemented in the `RoomRadiationGun` is shown in (b).

and thorium chains; it also shows the energy spectrum we calculated for the environmental radiation including scattering.

The environmental radiation may come predominantly from the ground, but some fraction may come from other sources of radiation or scattering off other objects. The KATRIN detector is most sensitive to radiation coming through the openings of the KATRIN shield. Therefore, we do not assume the radiation comes from the ground. Instead, we measured the amount of radiation coming through the shield openings and assume the rest is isotropic. These measurements are discussed in Section 7.2. Since the KATRIN shield is a cylinder with two openings for the beam and readout, we made two measurements with a germanium detector inside a shield that has an opening like the KATRIN shield. In the first measurement, the opening of the shield faced the beam direction, and in the second measurement, the opening faced the readout direction.

To model the angular distribution, we divide the simulation into three angular regions: photons from the beam direction, photons incident on the walls of the shield, and photons coming from the readout direction. The first angular region contains photons with starting angle less than 26° with respect to the axis of the shield, for a total angle of 52° . This is

Table 6.5: Intensity of environmental radioactivity through both the shield openings and incident on the walls of the shield in the KIT laboratory.

Source	Beam Side I_B $10^{-3}\gamma/\text{cm}^2/\text{s}$ $\theta < 26^\circ$	Incident on Walls I_W $10^{-3}\gamma/\text{cm}^2/\text{s}$ $26^\circ < \theta < 164^\circ$	Readout Side I_{RO} $10^{-3}\gamma/\text{cm}^2/\text{s}$ $\theta > 164^\circ$
^{232}Th	1.37 ± 0.19	335 ± 3	1.39 ± 0.20
^{238}U	1.53 ± 0.13	252 ± 2	1.54 ± 0.15
^{40}K	0.63 ± 0.06	266 ± 2	0.64 ± 0.10

much larger than the shield opening to properly include the photons entering through the opening. The second region is angles between 26° and 164° , including photons which will impact the shield walls. The third region is photons making an angle greater than 164° with the shield axis.

The intensity of the environmental radiation in these three regions as determined in Section 7.2 is summarized in Tab. 6.5. If the radiation were isotropic, the intensity through each shield opening would be 5% of the total, since both angular regions are 5% of the total solid angle. Comparing the intensities in Tab. 6.5, it is clear that less than 5% of the radiation comes through the shield openings and the radiation is not isotropic.

The total intensity for the uranium and thorium chains or potassium is the sum of the intensity from each region. For example, the total potassium intensity is: $I_{K,Tot} = I_{K,B} + I_{K,W} + I_{K,RO}$. Summing up each chain and potassium, the total intensity from the environmental radiation is $0.860 \gamma'/\text{cm}^2\text{s}$ in the KIT laboratory. Similar measurements made in the commissioning laboratory yield a total intensity of $1.10 \gamma'/\text{cm}^2\text{s}$. This is 27 times more radiation than cosmic-ray photons, but the average energy is much lower. This is also lower than the estimate of $10 \gamma'/\text{cm}^2\text{s}$ at 1 m above ground outdoors [97]. The walls of the building and the spectrometer may be shielding some of the radiation.

Environmental Radioactivity Generator

We simulate environmental radioactivity with the `RoomRadiationGun` custom primary generator. The photon energy is chosen from the spectrum including scattering in concrete. We aim the photons at the detector with the same method as the `CosmicRayGun`; we choose a position on a plane surrounding the detector, then choose an isotropic direction, then move the photon out to a position on a sphere. The photon is shot into the position on the plane. The radius of the sphere is 100 cm, outside the KATRIN geometry. The plane dimensions are 60 cm by 60 cm, the same as for cosmic rays.

Photons with angle less than 26° are simulated with a lower intensity than photons with an angle greater than 26° . Unlike cosmic rays, this angle is defined with respect to the axis of the shield, not the zenith, although both are denoted by θ .

The simulation time duration in seconds equals the number of photons generated, N , divided by the area of the plane, A , and the intensity, I :

$$T = \frac{N}{AI} \text{ s.} \quad (6.13)$$

Each angular region (beam side, incident on shield wall, and readout side) is simulated separately and normalized by the proper intensity. In addition, we apply a correction to each region for the angular distribution as discussed in Section 7.3.5. Although the statistical uncertainty on the intensity is given in Tab. 6.5, we assume the systematic uncertainty is larger. The variance of the intensity incident on the walls of the shield for all peaks in the uranium and thorium chain is 15%, so we take this as the uncertainty on the intensity.

Cosmogenic Radioactivity in the Detector Components

We estimate the activity of isotopes produced by cosmic ray spallation in materials surrounding the detector using the COSMO code [98]. Given the target’s chemical formula and the exposure time, COSMO will compute the produced isotopes using the cosmic-ray spectrum within the code. No part of the KATRIN experiment will be built or be moved underground, so the materials are continuously exposed to cosmic rays and do not “cool down.” We calculated the isotopes produced in copper, steel, silicon and ceramic since

these are the materials closest to the detector. Isotopes of cobalt, silicon, iron, vanadium and more are created. Appendix B.1 lists the calculated activities assuming a five year exposure and no cool down. The cosmogenic activity is much lower than the primordial radioactivity in the detector components. Because of the lower activity and the early estimates of F. Schwamm [57] indicate cosmogenics are not a major background for KATRIN, we do not include cosmogenics in the background model.

6.3 Summary of the Background Model

In this chapter we have presented the geometry, physics processes, and source of backgrounds used in the KATRIN background model. The geometry is based on the KATRIN detector region. The sources of background range from 100 GeV cosmic-ray muons to photons of a few keV. Each source has been implemented into a primary generator to simulate the background. The physics processes describe the interactions of the particles in the geometry. The next step is to verify this model and confirm the simulation results.

Chapter 7

SIMULATION VALIDATION

The last chapter outlined all the sources of background for KATRIN. In this chapter, we measure the interaction of the background particles in a silicon detector, validating the initial spectra of these particles and the detector response. By confirming the results, we can confidently use the simulation predictions to estimate the KATRIN background and optimize the detector design. In addition, we measure the environmental radiation in the KATRIN detector laboratory using a germanium detector. Due to the superior energy resolution and efficiency of germanium, this is a stringent test of the assumptions we make about the spectrum of natural radioactivity. We use the measured intensity of radiation to customize the simulation to the detector environment.

7.1 Measurements with a Silicon Detector

Measurements with a silicon detector are crucial to understanding the validity of KATRIN's background model. Since the KATRIN detector was not operational, we made a series of measurements with a small commercial silicon detector. The goals of these measurements were to verify the response of the detector to photons and measure backgrounds from cosmic ray muons. We mounted a Hamamatsu Photonics windowless silicon *p-i-n* photodiode detector—model S3590-09—directly on a preamplifier inside a light-tight aluminum box. The active volume of the detector—1 cm by 1 cm by 300 μm —is smaller and thinner than the KATRIN detector. Spectra were measured from two calibration sources, ^{241}Am and ^{109}Cd . The KATRIN detector will be calibrated with both these isotopes, so their decay products and spectra must be understood. In addition, we used two small plastic scintillator paddles to isolate the cosmic-ray muon background in the silicon detector. Each scintillator paddle is attached to a single conventional PMT. Using a simple Geant4 geometry, these sources were simulated and compared with the measurements.

7.1.1 *Simulation Geometry and Response*

Figure 7.1a shows the detector used for the measurements. A very simple simulation geometry is shown in 7.1b, with the active silicon detector in purple. In general, the geometry definition is based on data sheets from the manufacturer or on measurements of a component’s dimensions. Close inspection of the detector response to calibration sources reveal X-ray lines from silver. This indicates that the detector package itself contains silver, which fluoresces when illuminated with photons. Although silver is not listed in the data sheets, it is a common material to use in silicon detectors [99]. Since we do not know the exact location or amount of silver, we assumed a thin layer is between the silicon and ceramic mounting structure. We simulated various thicknesses of silver, resulting in varying silver fluorescence line strengths. A silver backing of $10\ \mu\text{m}$ was consistent with the measurements, and is a reasonable amount for a contact. The thickness of the silver is the only free parameter in the simulation.

The silicon detector response is similar to the KATRIN detector response, but the electronic noise is larger in this detector— $2.75\ \text{keV}$ FWHM instead of $600\ \text{eV}$. Because of this large electronic noise, we neglected the energy-dependent statistical noise. Rielage [100] measured the dead layer of this type of detector to be $107 \pm 10\ \text{nm}$; the simulation uses this value.

Although the scintillator veto used for this measurement is different than the KATRIN scintillator veto, we use the same scintillator response described in Section 6.1.1, except we assume these scintillators have 100% efficiency. For these measurements, the plastic scintillator is attached to a conventional PMT instead of using fiber optics and SiPMs. The plastic scintillator paddles are the same thickness as the KATRIN plastic scintillators, 1 cm, but are only 17 cm long and 12 cm wide. For the measurements, we centered the paddles over the aluminum box, not the detector, with one PMT sticking out on each side. Accurately placing the scintillators in the same position was not attempted. The height of the aluminum box sets the minimum separation between the two paddles, but the separation could be a few centimeters larger after moving the paddles. The simulation assumed the minimum separation, introducing an error in the scintillator efficiency. No PMTs are in

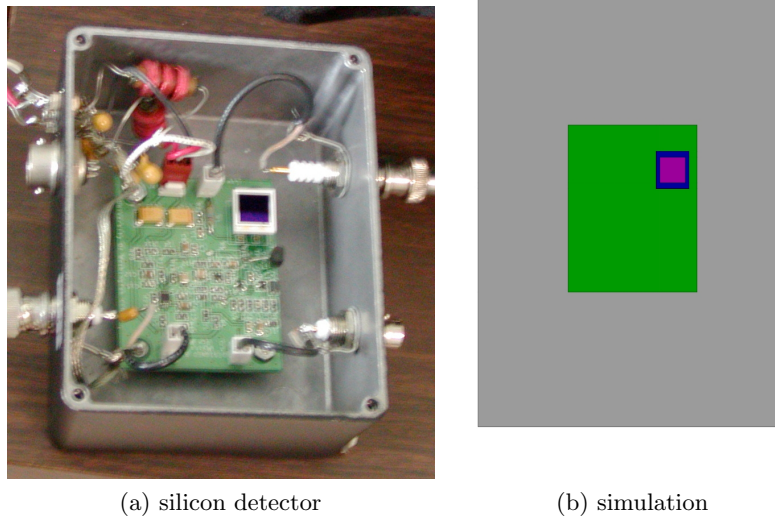


Figure 7.1: Small Hamamatsu $p-i-n$ diode used for validation measurements mounted on a preamp (green) inside the aluminum box (grey).

the simulation. To tag a muon, both paddles require energy depositions of 1.2 MeV within 100 ns.

7.1.2 Calibration Sources

Commercial calibration sources are essentially point sources with well-defined energy and minimal self-absorption, making them ideal for validation. For this investigation, we used sealed ^{109}Cd and ^{241}Am sources because they emit photons under 88 keV. Full-energy peaks are detected with high efficiency for photons below about 40 keV. The higher-energy photons can also Compton scatter in the detector and in other objects, backscattering to the detector and creating edges in the spectra. We placed the sources both inside and outside the aluminum box to observe attenuation by the aluminum. The measurements were taken in October of 2007 in the University of Washington's Center for Experimental Nuclear Physics and Astrophysics (CENPA) room 165.

The ^{109}Cd photon's energy and intensity listed in TORI [96] are implemented in the

`CalibrationGenerator`, described in Section 6.2.2. All cadmium photons are generated; the average number of photons emitted per decay is 1.148. Unlike the other isotopes in the `CalibrationGenerator`, the ^{241}Am intensities are taken from the newer measurements of M. C. Lepy et al. [101], which are not included in the compilation of TORI. For americium, only photons under 60 keV are generated, so the average number of photons per decay is 0.760.

The activity of the source normalizes the simulation. Amersham manufactured the americium source with an activity of $12.15\ \mu\text{Curies}$ in 1982. Since it has a long half-life, it still had an activity of $11.5\ \mu\text{Curies}$ in 2007. Isotope Products Labs manufactured the cadmium source with an activity of $105.7\ \mu\text{Curies}$ in October 2007—just before these measurements were made. We cannot obtain detailed drawings of the sources; therefore we make assumptions about what materials are inside the sources. Self-absorption within the simulated sources should be accurate since the masses of the simulated sources match the physical sources.

Depending on the location of the sources and the rates, the duration of a source run was a half hour to two hours each. The background was negligible in these short runs. The spectra were recorded with VME-based fast shapers and peak-detect ADCs originally designed for the emiT experiment. The Object-oriented Real-time Control and Acquisition (ORCA) software reads out the spectra. The detector is biased to +60 V. For each source run, the silicon detector's ADC value is converted to energy using a single peak in the spectrum and assuming the zero ADC value corresponds to zero energy. For americium, we fit the 60 keV peak to a gaussian; for cadmium, we fit the 88 keV peak. All peaks have a width of 2.75 keV FWHM. This electronic noise is added to the simulation.

Figure 7.2 shows the comparison between the measurements and simulation of the americium source, and the major features are explained in Tab. 7.1. The attenuation by aluminum causes the obvious difference in the measured spectra taken in the two locations, and is reproduced well by the simulation. With the source inside the box, peaks 2 and 3 are somewhat stronger in the simulation than the measurement. With the source outside the box, conversely, peak 3 is weaker in the simulation. This may indicate there is too much attenuation in the aluminum. Since the silver fluorescence line—peak 4—is most prominent when the

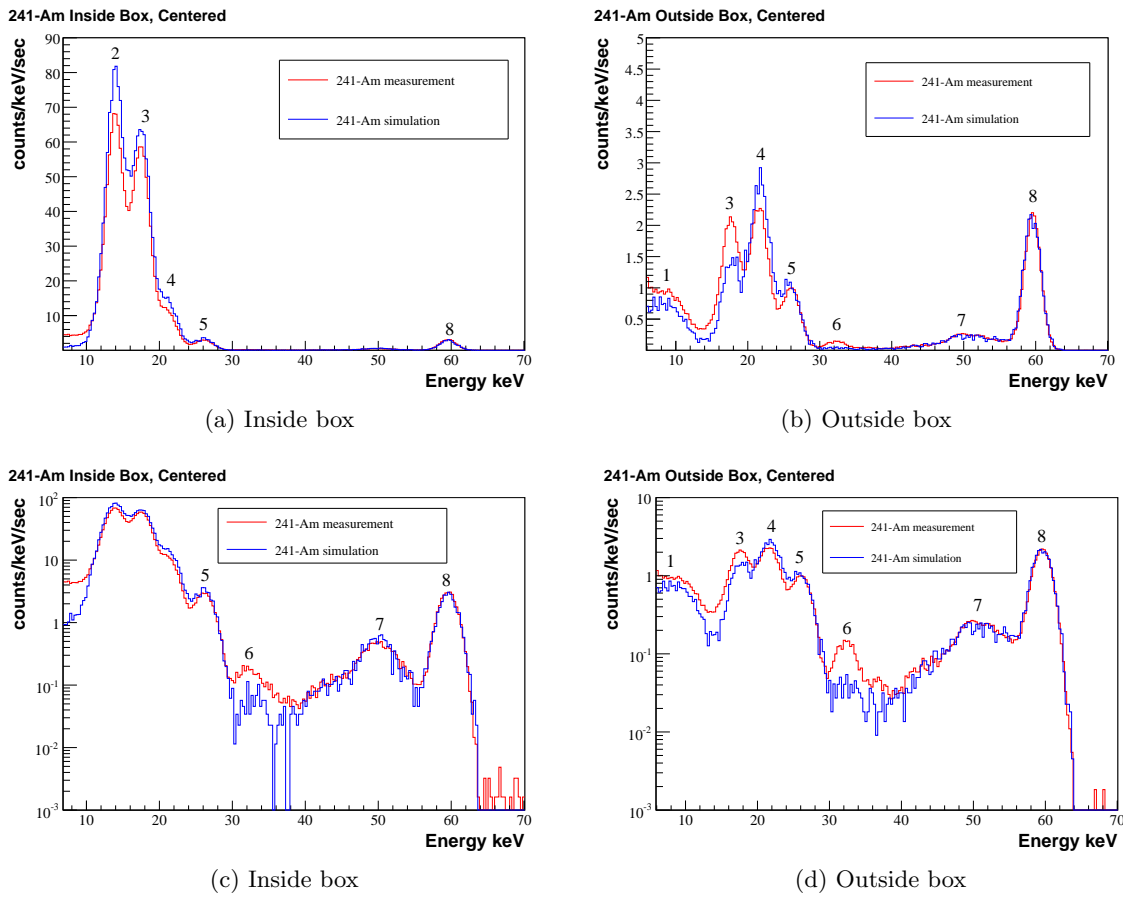


Figure 7.2: Measured and simulated spectra from the ^{241}Am source placed inside and outside the aluminum box. The spectra are shown on a log scale in (c) and (d) to make the backscattering edge visible.

Table 7.1: Largest features in the ^{241}Am spectrum.

Label	Approximate Energy	Am Feature	Ag Feature
1	0–11 keV	Compton scattering	
2	14 keV	Np L_α X rays	
3	18 keV	Np L_β X rays	
4	21–22 keV	Np L_γ X rays	Ag κ_α X rays
5	25–26 keV	Am γ	Ag κ_β X rays
6	33 keV	Am γ	
7	49–60 keV	backscattering	
8	59.5 keV	Am γ	

source is outside the box, we determined the silver thickness from this measurement. Consequently, this feature should be equivalent in the simulation and the measurement outside the box. The simulation's peak 6 is smaller than the measurement. The initial intensity of this peak may be too weak or some other mechanism may add counts to the feature. For example, none of the preamp components or connectors are in the simulation; this line may be a weak fluorescence of another material. Feature 1 is only visible with the source outside the box and is caused by the 60 keV photons Compton scattering in the detector. The measurement has more counts in this energy region in both locations. Feature 7, the backscattering edge, and peak 8 agree in both locations. Since Compton scattering in the detector and in other materials causes a large fraction of our backgrounds, the agreement is reassuring.

The cadmium source has a very high activity; therefore the measured spectra can be distorted by pile-up at the highest rates. The simulation does not model pile-up and will not match this measurement. For this reason, we placed the cadmium source outside the aluminum box, offset from directly above the detector to lower the rates. Figure 7.3 shows the comparison between the measurements and simulation of the cadmium source. Table 7.2 lists the major features in the cadmium spectrum. Silver is the daughter of ^{109}Cd ; the silver X rays are produced by fluorescence in the detector as well as being released in the decay. The silver X-ray lines are under-produced in the simulation, possibly due to too

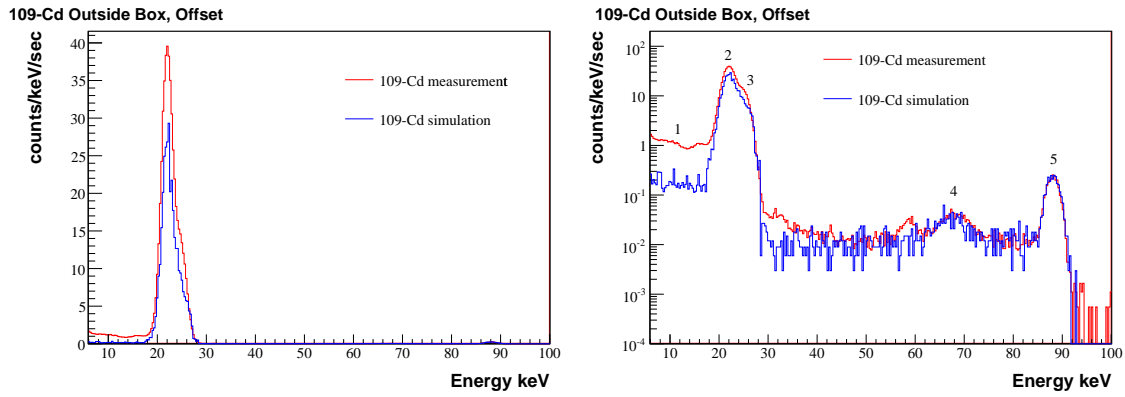


Figure 7.3: Measured and simulated spectra from the ^{109}Cd source placed outside the box, offset from directly above the detector to reduce the rate.

Table 7.2: Largest features in the ^{109}Cd spectrum.

Label	Approximate Energy	Cd Feature	Ag Feature
1	0–22 keV	Compton scattering	
2	21–22 keV	Ag κ_{α} X rays	Ag κ_{α} X rays
3	25–26 keV	Ag κ_{β} X rays	Ag κ_{β} X rays
4	65–88 keV	backscattering	
5	88 keV	Cd γ	

much attenuation in the aluminum, incorrect initial probability of production in the decay, or too little fluorescence. The 88 keV line, which causes silver fluorescence, is emitted in only 3.6% of decays, so we do not expect much fluorescence. In the simulation, only 1.3% of the counts in the silver peaks are from fluorescence. Just like the ^{241}Am , the higher-energy line—88 keV—and the backscattering edge agree with the measurements. The measurement includes more counts below 20 keV.

All major features appear in the simulation and are within 60% of the measurements. Above the silver fluorescence, the agreement is within 7%. Two discrepancies seen with both sources are the attenuation in aluminum and the low-energy counts. The interaction cross section for photoelectric absorption in aluminum is exponentially increasing at 20 keV. A small uncertainty in the aluminum thickness could cause a large change in the attenuation; we may be simulating an aluminum box that is too thick by a fraction of a millimeter. Overall, the agreement is good, especially in the higher-energy peaks and backscattering edges, which is an important background mechanism for KATRIN. Measuring the spectra from these calibration sources increases our confidence in the KATRIN background model, especially the detector’s response to photons.

7.1.3 *Cosmic-Ray Muons*

The cosmic-ray muon backgrounds must be directly measured to validate the simulation, but are a small part of the total background in the Hamamatsu detector. To isolate cosmic-ray muons from other backgrounds, we surrounded the aluminum box with small plastic scintillator paddles. Interactions are required in both scintillators and the silicon detector to read out a count, ensuring that the interaction is from cosmic-ray muons, as no other type of radiation would cause so many counts in coincidence. The measurements were taken in room 108 of CENPA. The laboratory is in a single-story building, but behind the laboratory is a large hill which could possibly alter the cosmic-ray spectrum. Using the muon spectrum given in Section 6.2.1, muons shower the simulation geometry and the resulting background is compared to the measurements. Just as for the KATRIN background estimate, we did not correct the initial muon spectrum for latitude or overburden. Seattle’s latitude—47.62° N—

Table 7.3: Average measured rates from cosmic-ray muons. The “dual PMT rate” is the rate of coincidences between the two PMTs. The “Si Det coincidence” rate is the rate of coincidences between the silicon detector and two PMTs.

Type	Dual PMT Rate Hz	Si Det Coincidence mHz
Run 1	1.18	12.8
Run 2	0.99	14.0
Measurement Average	1.09	13.4

is close to that of Karlsruhe.

When both scintillator PMT signals are above a discriminator threshold within a 25 ns window, a coincidence logic unit opens the gate on the silicon detector’s ADC. For these measurements, we used CAMAC-based ADC modules and the ORCA software. A LeCroy 3512 ADC in coincidence mode recorded the silicon detector ADC values within a 15 μ s gate. The PMTs must be biased to -1.8 kV and the silicon detector biased to $+60$ V.

Measurements of cosmic-ray muons were made in two runs in September 2006, each run 24 hours long. In between the runs, the scintillator paddles were moved to allow recording of a ^{241}Am spectrum to calibrate the detector’s energy scale. After the calibration, placing the paddles around the detector in the same position was difficult, so some variation between the runs is expected. Table 7.3 shows the rate measured in each run and the average.

The energy calibration is the same as for the calibration sources. Assuming zero ADC offset, the 60 keV peak can be fit to a gaussian to calculate the calibration. For the cosmic-ray muon runs, the FWHM was again 2.75 keV.

We combined both runs and compare the spectra to the simulation in Fig. 7.4. The minimum ionizing particle bump has a larger number of counts in the simulation, but below 60 keV the number of measured counts may be higher than the simulation. The counts at low energy can be caused by two mechanisms: by muons which have a short path length in the detector because they graze the corner; or by photons created by muon interactions in other objects. Since the simulation does not include all objects around the detector, for

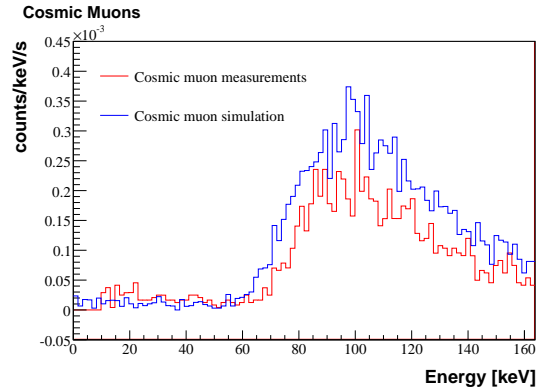


Figure 7.4: Muon spectrum measured and simulated in a small Hamamatsu silicon $p-i-n$ diode detector.

example the PMTs, the photon production may be incorrect.

Table 7.4 shows the average measured rate compared to the simulation. The ADC has both a lower and upper level discriminator, so the measured rates are integrated over the range from 10 keV to 162 keV. Compare the measurement average the “simulation coincidences” rate, which requires a coincidence with both PMTs and is integrated over the same energy range. The simulated silicon detector rate is 30% higher than the measured rate, possibly by overestimating the assumed initial intensity, the simulated scintillator efficiency, or the silicon detector efficiency. The simulated “dual PMT rate” is also higher than the measurement, consistent with an overestimate of the initial intensity or veto efficiency. Comparing the simulation singles to the simulation coincidences in the silicon detector shows the veto tags 69% of events between the lower and upper level discriminator. The veto tags 86.8% of counts over the entire energy range in the silicon detector simulation.

The measurements indicate we may have overestimated the initial intensity of muons and the efficiency for tagging them with a veto by 30%. Overestimating the initial intensity will increase the KATRIN background estimate; overestimating the veto efficiency will decrease it. The simulated veto efficiency can be improved by propagating the optical photons and measuring the KATRIN scintillator efficiency. Although the simulation is 30% higher than the measurement, the shape of the spectrum is correct and we are confident the muon

Table 7.4: Comparison of coincidence rates in the measurement and simulation of cosmic-ray muons. The “dual PMT rate” is the rate of coincidences between the two PMTs. The “Si Det coincidence” rate is the rate of coincidences between the silicon detector and two PMTs. In contrast, the simulation singles row shows the total rates in the PMTs and silicon detector without requiring any coincidences.

Type	Dual PMT Rate Hz	Si Det Coincidence mHz
Measurement Average	1.09	13.4
Simulation Coincidences	2.87	19.5
Simulation Singles	5.0	28.3

background estimate is reasonable.

7.2 Measurements in the Detector Laboratory at KIT

Measurements in the detector laboratory at the Karlsruhe Institute of Technology (KIT) are necessary to understand the backgrounds specific to that area. As discussed in Section 6.2.2, the environmental radiation can be a large source of background and depends on location. Cosmic rays also depend on location; latitude and altitude affect the initial spectrum and a large overburden can attenuate some of the particles.

Germanium detectors are ideal photon detectors; they have high efficiency and excellent energy resolution. Using a germanium detector, we measured the total intensity of environmental photons in the detector laboratory at KIT. The intensity is used to estimate the background from environmental radiation in the KATRIN detector. Unlike a silicon detector, all of the photon peaks in the uranium and thorium chains are visible in a germanium detector. This measurement doubles as a validation of the simulated decays of potassium and the uranium and thorium chains.

Without a shield, the background in the germanium detector is dominated by the environmental radioactivity and shows lines from uranium, thorium, and potassium. Adding a 15 cm shield reduces the total rate across the entire spectrum by a factor of fifty-seven. Such a large reduction indicates the majority of the background in the unshielded measurements

comes from sources external to the shield. In the shielded spectrum, conversely, other backgrounds become visible. In particular, neutron interactions cause nuclear recoils and photon peaks in the shielded spectrum, which are discussed in more detail in Section 7.3.6.

For the environmental radiation, the KATRIN detector is most sensitive to radiation coming from the beam or readout directions due to the openings in the KATRIN shield. The KATRIN shield is relatively thin—3 cm of lead and 1 cm of copper—but only about 15% of the highest-energy environmental radiation passes through the shield. Since the radiation through the shield openings is not attenuated, it could be a large background and must be measured. To measure the amount of environmental radiation coming from the directions of the shield openings, we put a germanium detector inside a 15 cm thick lead shield with a funnel-shaped opening in one of these directions. The 15 cm of lead blocks 99.94% of the highest-energy environmental radiation from other directions, but there is still a large background from other sources; we measured these other backgrounds by blocking the funnel opening and completely enclosing the germanium detector inside the shield. The measurements were made in five configurations:

Unshielded, facing the beam direction: Measurements with the unshielded germanium detector facing the beam direction to measure the total environmental radiation.

Unshielded, facing the readout direction: Measurements with the unshielded germanium detector facing the readout direction to measure the total environmental radiation and look for a directional asymmetry.

Shielded, funnel opening facing the beam direction: Measurements with the germanium detector inside the 15 cm shield with a funnel opening. The shield's funnel and the detector faced the beam direction to measure the amount of environmental radiation coming from the beam direction.

Shielded, funnel opening facing the readout direction: Measurements with the germanium detector inside the 15 cm shield with a funnel opening. The shield's funnel

and the detector faced the readout direction to measure the amount of environmental radiation coming from the readout direction.

Closed shield: Measurements with the germanium detector inside the 15 cm shield. The shield's funnel opening was blocked by more lead to measure the "background" to the previous two measurements. The shielded measurements also ensure the radiation measured without a shield predominantly comes from sources external to the shield. Cosmic neutron peaks are visible in this spectrum. The detector faced the beam direction.

Our colleagues in Germany designed and built the 15 cm lead shield with a machined funnel opening for these measurements. Figure 7.5 shows the lead shield with germanium detector inside. The detector is first surrounded by a low-radioactivity lead pipe. Lead bricks are stacked outside of the pipe up to a total thickness of 15 cm. The total funnel opening is 25° , the same as the KATRIN shield's beam-direction opening, but larger than the readout-direction total opening of 14° .

The system was built at KIT in the detector laboratory, near the planned position of the KATRIN detector. For both the shielded and unshielded measurements, the germanium detector was positioned 1.2 m above the detector platform, close to the KATRIN detector's location at 1.3 m. The germanium detector had to be placed 3 m from the main spectrometer flange, farther than the 2.3 m separation of the KATRIN detector. Even with these small changes, the germanium detector's field of view was similar to the KATRIN detector; it faced the main spectrometer in one direction and the rear door in the other direction.

All measurements were taken in June and July 2008 using a Canberra GX3018 p-type coaxial germanium detector with 0.5 mm aluminum window. The cryostat for this detector was a Canberra 7935SL-7 portable two-day cryostat. The shield did not completely cover the cryostat, but a rear wall of lead blocked the line of sight of external sources to the detector, as shown in Fig. 7.5. Unfortunately, we have no information on the detector bias or the type of data acquisition system used by our colleagues. Unshielded detector measurements were 60,000 seconds long. Shielded detector measurements were longer, 500,000 seconds, due to the lower rate.

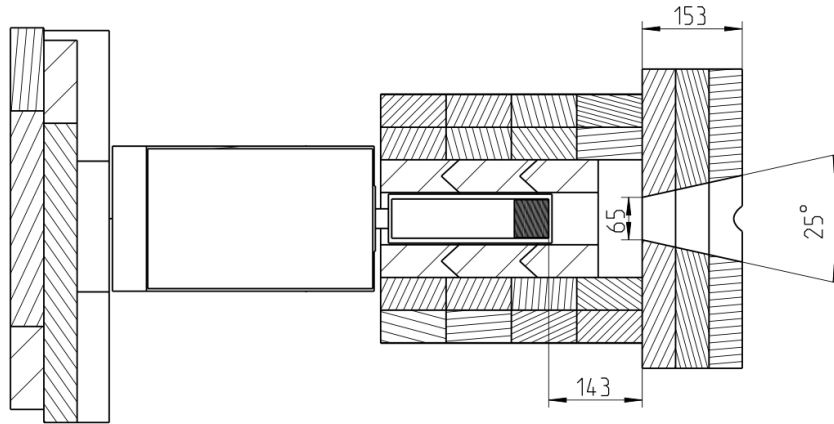


Figure 7.5: Drawing of the 15 cm lead shield with funnel opening used in the KATRIN detector laboratory. The germanium detector is the darkest cross hatching shown at the end of the cryostat. Dimensions are in millimeters. Figure from S. Kage.

7.2.1 Simulation Geometry and Response

Figure 7.6 shows the simple detector and shield in the simulation. The coaxial detector is surrounded by vacuum and a 3 mm thick aluminum cryostat. The front window is 0.5 mm aluminum. The dewar is not included in the simulation; the only material behind the detector is 3 mm of aluminum.

We do not know the exact dimensions of the inner bore of the detector or the dead layer. Therefore, we estimated the detector's dimensions with a ^{60}Co calibration, described in Section 7.2.2, to get a total active volume of 125.6 cm^3 . We assume this detector has typical dead layers of $750\ \mu\text{m}$ on the outer contact and $0.3\ \mu\text{m}$ on the inner contact [65]. The Canberra Extended Range (XtRa) detectors have a thinner dead layer on the front surface; we assume it is $0.3\ \mu\text{m}$.

Electronic and statistical noise are added to this germanium detector the same way they are added to a silicon detector:

$$\sigma^2 = \frac{\Delta^2}{2.35^2} + E F \epsilon. \quad (7.1)$$

For germanium, the typical energy per electron hole pair ϵ is 2.96 eV [65] and the typical

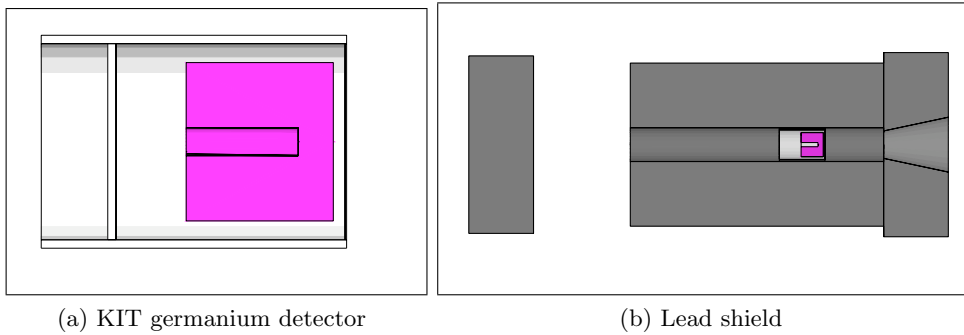


Figure 7.6: Simulation geometry for the germanium detector measurements in the KIT detector laboratory. The germanium crystal, shown in purple, is surrounded by aluminum on all sides. The lead shield is shown in dark grey.

Fano factor F is 0.129 [102]. We fit a single peak in the measured spectrum to find the electronic noise Δ , which is 846 eV FWHM.

Although we use the energy resolution in Eq. 7.1, we investigate other forms. For large detectors, variations in the efficiency of charge collection can also affect the resolution. This adds a term to the width that is linearly dependent on energy, represented by the coefficient C :

$$\sigma^2 = \frac{\Delta^2}{2.35^2} + E F \epsilon + E^2 C. \quad (7.2)$$

By fitting all peak widths as a function of energy, the parameters Δ , ϵF , and C can be determined from the data instead of using external measurements.

To test this form of the energy resolution, we fit thirty peaks in the unshielded measurements to gaussians to find the peak width. As discussed in Section 7.2.3, these peaks are chosen because they pass the requirements listed in Tab. 7.13. The thirty peaks and the fit p-values are discussed later and are listed in bold in Tab. 7.14, 7.15, and 7.16.

Figure 7.7 shows the simulated width, along with a fit of the peak widths to Eq. 7.2. The best-fit width is very close to the width assumed in the simulation. The electronic noise Δ from the fit is slightly higher than the simulated value and the Fano factor from the fit is slightly lower. The linear term coefficient C is very small. Therefore, Eq. 7.1 is sufficient for

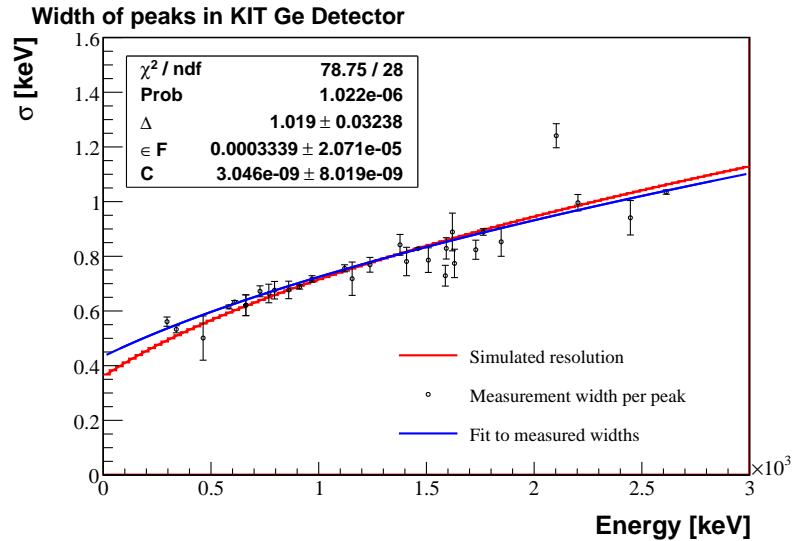


Figure 7.7: Width of peaks in unshielded KIT germanium detector measurements. The best fit to the peak widths is very close to the form assumed in the simulation. The outlier is the 2104 keV SEP of ^{208}Tl .

this detector. As discussed later, the energy resolution for the open-shield measurements is different than the unshielded and closed-shield measurements because the gain shifted during the open-shield measurement.

7.2.2 Calibration with ^{60}Co

Since we do not know the exact dimensions of the detector, we wish to compare the simulation to a measurement with a known source. In December of 1998, the manufacture calibrated this detector with a ^{60}Co source, following the IEEE standard test procedures [103]. Unfortunately, we do not have the measured spectrum from this calibration, but we do have the calculated relative efficiency and peak-to-Compton ratio. The relative efficiency depends on the detector volume; the peak-to-Compton ratio depends on the detector volume, the geometry of the cryostat, and the energy resolution. We simulated a ^{60}Co source and calculated the relative efficiency and peak-to-Compton ratio to compare to the measured values.

^{60}Co releases two photons, one at 1332.5 keV and the other at 1173.24 keV. Following the IEEE procedures, the source must be placed 25.0 cm from the center of the detector’s front end-cap for the calibration. The relative efficiency is defined as the area A of the 1332.5 keV peak normalized by the peak area A_{NaI} which would be measured by a “standard sodium-iodide scintillation crystal.”

$$E_{\text{Rel}} = \frac{A}{A_{\text{NaI}}} \quad (7.3)$$

A standard NaI crystal is a 76 mm by 76 mm cylindrical crystal. For a given number of source decays, N_S , the standard NaI crystal would have a peak area of $A_{\text{NaI}} = 1.2 \times 10^{-3} N_S$ [103]. For a measurement, N_S is determined by the source activity; for a simulation, N_S is determined by the number of simulated photons.

The peak-to-Compton ratio is defined as the height of the 1332.5 keV peak, N_{1333} , divided by the average Compton continuum height in the 1040–1096 keV range, \bar{N}_C .

$$P/C = \frac{N_{1333}}{\bar{N}_C} \quad (7.4)$$

The peak height depends on the energy resolution, so we match the simulation resolution to the measurement. The energy resolution for this calibration was better than the environmental radioactivity measurements; the electronic noise Δ in the calibration was only 414 eV.

We simulate the ^{60}Co photons from a point in air outside of the germanium detector. Since the photons have energy greater than 1 MeV, we can neglect the source capsule and self-absorption within it. The photon opening angle is limited to a total of 20° to save computation time. The two photons are generated in separate events; therefore pile-up is not simulated but should be negligible for a source–detector spacing of 25 cm.

Figure 7.8 shows the simulated spectrum. The 1332 keV peak is visible, along with its Compton edge at 1120 keV. This edge is the maximum energy of an electron created in the germanium detector by Compton scattering of the photon. The 1173 keV peak and its Compton edge at 960 keV are also visible. The analysis window used to estimate the

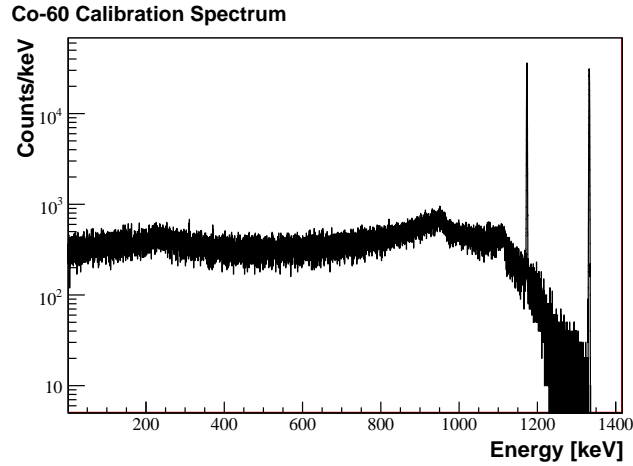


Figure 7.8: Simulation of a ^{60}Co calibration of the germanium detector used for measurements at KIT. The Compton continuum is defined as the region from 1040 keV to 1096 keV, below both peaks.

peak-to-Compton ratio, 1040 keV to 1096 keV, is between the two edges.

There are two mechanisms which contribute to the region between 1040 keV and 1096 keV: first, the 1332 keV photon Compton scattering in the detector; second, the small-angle Compton scattering of both the 1332 keV and 1173 keV photons from material in front of the detector. Other mechanisms which cannot contribute to the Compton continuum in the analysis window are: Compton scattering of the 1173 keV photon in the detector and large-angle Compton scattering of either photon in material behind the detector or behind the source.

The energy of a Compton-scattered photon depends on the scattering angle. A 1332 keV photon will emerge with 1040 keV of energy after scattering 26° ; a 1173 keV photon will emerge with 1040 keV after scattering 19° . Therefore, both photons can scatter in the aluminum window or cryostat and create counts in the analysis window. Scattering through larger angles will produce lower-energy photons, so the material behind the detector will not affect the peak-to-Compton ratio. The peak-to-Compton ratio verifies the detector volume and cryostat window thickness. The peak-to-Compton ratio cannot test how much material is missing behind the detector.

Table 7.5: Relative efficiency and peak-to-Compton ratio measured in 1998 compared to the simulation of the KIT detector. This assumes a detector volume of 125.6 cm³.

	Rel. Efficiency	FWHM keV	Peak/Compton
Measurement	34.3%	1.73	66.9:1
Simulation	33.9%	1.73	70.6:1
Difference	-1.2%	0%	5.2%

To determine the peak height and area, we fit the 1332.5 keV peak to a normalized gaussian:

$$\frac{P}{\sqrt{2\pi\sigma^2}} e^{-(x-\mu)^2/2\sigma^2}. \quad (7.5)$$

This fit also determines the FWHM of the peak. The peak area for the relative efficiency is the value P from the fit divided by the bin width. The peak height for the peak-to-Compton ratio is $\frac{P}{\sqrt{2\pi\sigma^2}}$. The average Compton continuum height \bar{N}_C is the sum of the counts between 1040 keV and 1096 keV divided by the number of bins in the same range.

Tab. 7.5 shows the values measured with this detector in 1998 and the simulated values. The relative efficiency of the simulation is within 1.2% of the measurement, indicating we are simulating a detector of the correct size. We set the energy resolution of the simulation to be the same as the measurement, so we can compare the peak-to-Compton ratio. The simulation is within 5.2%. Therefore, the detector volume and thickness of the entrance window should be accurate.

7.2.3 Environmental Radioactivity Measurements

With confidence that the germanium detector simulation is an adequate representation of the real detector, we used the simulation to characterize the environmental radioactivity in the KATRIN detector laboratory. Based on the germanium detector measurements, there are clearly large sources of uranium, thorium, and potassium external to the detector. As discussed in Section 6.2.2, this radioactivity may be embedded in the earth or build-

ing materials. We determined the environmental radioactivity's energy spectrum, angular distribution, and intensity from the measurements. Using the intensity measured with a germanium detector discussed in this section, we simulated the environmental radiation incident on the shielded KATRIN detector to estimate the background for KATRIN, discussed in Chapter 8.

Determining the Energy Spectrum

To determine the initial energy spectrum, we simulated the unshielded germanium detector and matched the energy spectrum to the measurements. The sources of environmental radioactivity are embedded in some material. The photons released in the decays will scatter within the material, altering the spectrum from that of the direct radioactive decay. The location of the radioactivity within a material can affect the energy spectrum; the impurities may not be evenly distributed through the material, or there may be other cleaner materials between the source and detector. To model the source with scattering, we assumed the radioactivity is evenly distributed in concrete of various thicknesses.

In concrete, photoelectric absorption dominates the scattering cross section for photons below 50 keV. Between 50 keV and 10 MeV, Compton scattering dominates and the cross section slowly decreases. Pair production becomes the most probable energy-loss mechanism above 10 MeV, above the highest-energy ^{208}Tl photon at 2.61 MeV. The mean free path of a 675 keV photon is 30 cm, increasing to 60 cm for the 2.61 MeV photon. Therefore, layers of concrete up to 60 cm thick could affect the energy spectrum.

To simulate the scattering, the simplified detector in Fig. 7.6a was surrounded by a sphere of concrete, with its inner radius at 9 cm and thickness set to 5, 10, 30 and 60 cm. Using Geant4's GPS and the custom `CalibrationGenerator`, we spread photons evenly through the concrete and emit them in all directions. We assumed the chains are in equilibrium and normalized the simulation by matching the area of one peak in each chain to the measurements. We fit the ^{214}Bi peak at 1.76 MeV, the ^{208}Tl peak at 2.61 MeV, and the ^{40}K peak at 1.46 MeV to gaussians to find the area in each peak. When the peak areas match, the simulation underestimates the continuum for thin layers of concrete. For layers

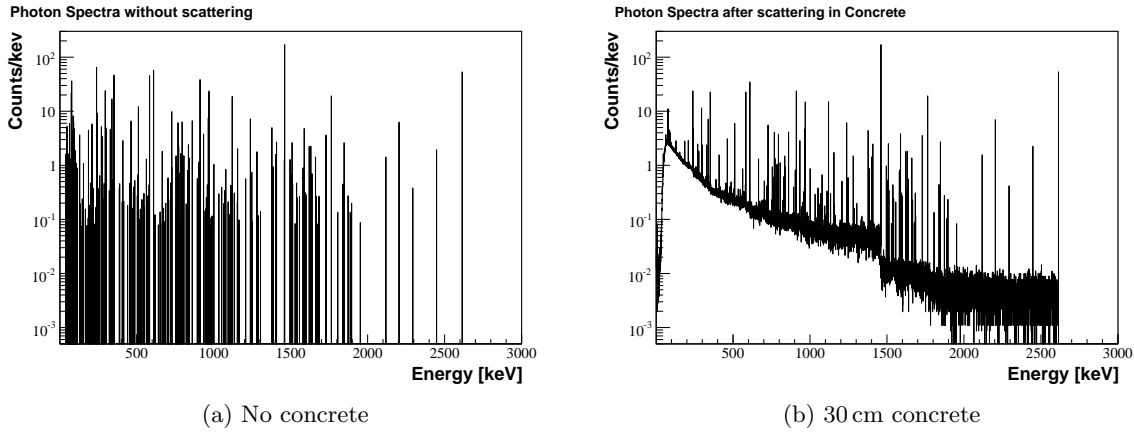


Figure 7.9: Effect of scattering in the concrete on the spectrum of photons. The photon spectrum emitted by potassium and the uranium and thorium chains as implemented in the `CalibrationGenerator` is shown in (a). The spectrum of photons emerging from 30 cm of concrete after scattering is shown in (b).

of concrete thicker than 30 cm, there is very little difference in the energy spectrum. Since the simulation of 30 cm of concrete had the best statistics and gave the best agreement for the continuum, we used 30 cm to generate the energy spectrum.

To save computation time, scattering in the concrete was not simulated again. Instead, we recorded the energy spectrum of photons emerging from the concrete and used this as the initial spectrum in the `RoomRadiationGun` described in Section 6.2.2. Figure 7.9 shows the photons emitted by potassium and the uranium and thorium chains compared with the calculated energy spectrum of the environmental radiation including scattering. When scattering is included, the average energy of the photons decreases from 875 keV to 534 keV.

Using this energy spectrum and the angular distribution and intensities determined later in this section, we simulated environmental radiation incident on the unshielded germanium detector. In addition, we simulated cosmic-ray muons and photons incident on the unshielded germanium detector. The combined simulation of environmental radiation and cosmic rays is compared to the measurement in Fig. 7.10. In the simulation, less than 1% of all counts come from cosmic rays, the majority of counts are from the environmental radiation. The agreement between the simulation and measurement is fairly good in the peaks

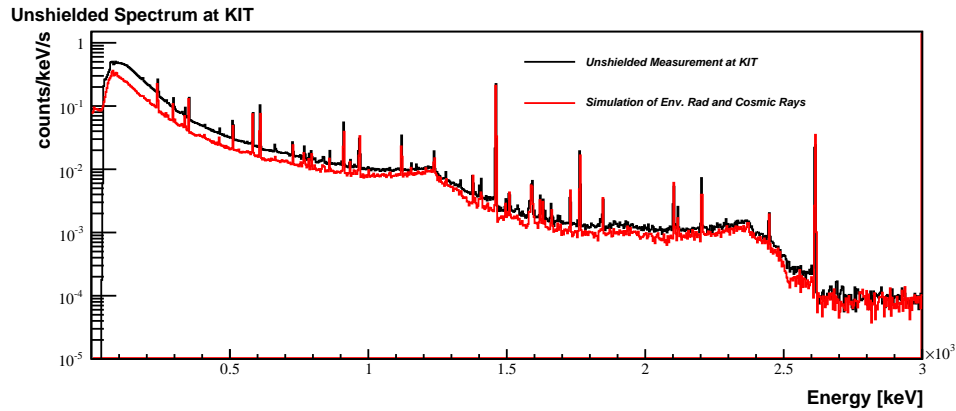


Figure 7.10: Comparison of the unshielded germanium detector measurements at KIT with the simulation. The simulation is normalized by the peak areas as discussed later in this section. The shape of the continuum matches very well and was not tuned in the simulation.

and in the continuum. Although, in reality, the environmental radiation may come from a complicated assortment of sources, a simulation of 30 cm of concrete produces a reasonable energy spectrum.

Determining the Angular Distribution

After determining the energy spectrum, we estimated the angular distribution of the environmental radiation. The source of the environmental radiation is unknown, but is likely distributed throughout the earth and the building materials. The radiation is released isotropically at the source; the angular distribution at the detector is determined by the source–detector separation. Inside the KATRIN shield, the KATRIN detector is most sensitive to photons coming through the shield openings. Since the angular distribution is unknown, we assume it is isotropic at the detector within three regions; photons that come from the beam direction, photons incident on the walls of the KATRIN shield, and photons that come from the readout direction.

Figure 7.11 shows the KATRIN shield and the three angular regions. We define the shield opening regions as photons making an angle less than 26° with the shield axis for a total angle of 52° . Therefore, each opening is 5% of the total solid angle. We used an angle

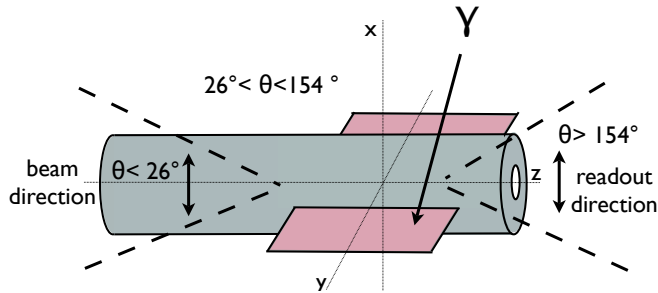


Figure 7.11: The three angular regions used to simulate environmental radiation are shown with the KATRIN shield. The shield has two openings; one on the beam side, the other on the readout side. The environmental radiation photons are simulated separately in each of these regions using the `RoomRadiationGun`, which aims photons at an area surrounding the detector, shown in pink.

more than twice the total shield opening of 25° to include all the photons that could enter through the shield opening.

We assume that within each of the three regions the radiation is isotropic. In reality, the angular distribution will be a smoothly varying function between the three regions. The shield openings cause the largest angular dependence of the KATRIN detector's response. In addition, the attenuation of photons through the shield is somewhat angular dependent, as the angle determines the path length of the photon through the shield. Since the detector is very thin, it covers a much smaller solid angle for radiation parallel to it, which is the radiation with the shortest path length through the shield. Both effects should be smaller than the dependence on the shield openings. Averaging the angular distribution over the three angular regions where the detector response has the greatest angular dependence is a first-order approximation.

The intensity through the shield opening in the beam direction I_B is measured with the 15 cm shield opening facing the beam direction. The intensity through the shield opening in the readout direction I_{RO} is measured with the 15 cm shield opening facing the readout direction. The unshielded germanium detector measurement determines the total intensity I_{Tot} . Using the intensity through the openings, we calculated the intensity incident on the

walls of the KATRIN shield, I_W .

$$I_W = I_{Tot} - I_{RO} - I_B \quad (7.6)$$

If the intensity were isotropic, I_{RO} and I_B would each be 5% of the total intensity, as they represent 5% of the total solid angle.

We simulated photons with the custom `RoomRadiationGun` described in Section 6.2.2. This particle gun aims the photons at a plane that surrounds the detector, as shown in red in Fig. 7.11. The area of this plane is used to normalize the simulation.

Intensity Through the KATRIN Shield Openings

To measure the intensity through each of the shield openings, we used the measurements with an opening in the 15 cm shield: one facing the beam direction and the other facing the readout direction. These measure the radiation through the shield opening—the signal—and a background of neutrons and photons that pass through or originate within the 15 cm lead shield. The background is determined by the closed-shield measurement, when the detector was completely surrounded by lead. The background includes environmental radiation that passes through the 15 cm shield, radioactive contamination in the lead or detector, radon gas in the air, and cosmic rays—including neutrons—interacting in the lead shield and detector. The small additional background introduced by the extra lead blocking the shield opening can be neglected because the shield opening is less than 5% of the total solid angle. No precautions were taken to prevent radon gas from entering the shield. If the amount of radon in the air varies with time, the radon background could be time-dependent.

We repeated the procedure for both the beam and readout directions. In all equations that follow we use a general subscript O to indicate the shield was open. This subscript could be replaced with the specific direction subscript, for example R_B for the beam-side measurement. The signal rate through each opening direction equals the measured total open-shield rate R_O minus the closed-shield background rate R_C .

$$R_\Delta = R_O - R_C \quad (7.7)$$

A simulation of the signal photons coming through the shield opening is compared with the measurements. We simulated the shielded germanium detector in Fig. 7.6b with the `RoomRadiationGun`, generating photons from within 26° of the shield axis. The same simulation is used for both directions, as there is no change in the germanium detector geometry.

To determine the simulation normalization and the intensity of the environmental radiation, we fit peaks in the measurements and simulation and match the peak areas. We assume the simulation peak areas should be correct because the simulated relative efficiency of the ^{60}Co calibration is within 5% of the measurement. The continuum shape may depend somewhat on the energy spectrum, which is approximated by simulating scattering in concrete. Peaks were fit to a normalized gaussian plus linear background as in Eq. 7.8.

$$\frac{P}{\sqrt{2\pi\sigma^2}}e^{-(x-\mu)^2/2\sigma^2} + B + Cx \quad (7.8)$$

The area of the peak was calculated from the parameter P normalized by the bin width w , and the rate for each peak is the area divided by the time duration, as shown in Eq. 7.9.

$$R = \frac{P}{wT} \quad \sigma_R = \frac{\sigma_P}{wT} \quad (7.9)$$

The same binning was used for all simulations and measurements, so the bin width cancels in a ratio of peak areas or a ratio of rates.

Peaks were fit using ROOT's log likelihood method with the "L" option. This assumes a Poisson probability density function for the contents of each bin and includes empty bins in the fit. The fitter is MINUIT and uncertainties are calculated by MIGRAD from the curvature of the negative likelihood function at the minimum. The uncertainty from the fit on P automatically includes correlations with the background and can be interpreted as one standard deviation assuming the likelihood function is parabolic. More accurate error estimates can be obtained using ROOT's "E" option, which calls MINOS.

An alternate method is to calculate the peak area or number of signal counts N_S from the total counts N_{Tot} and the expected background N_B . In the alternate method correlations

are neglected, and since these are all Poisson variables, the uncertainty on N_S would be $\sqrt{N_{Tot} + N_B}$. Instead, we calculated the peak area from the fit by normalizing P with the bin width. Using values from the fit, the uncertainty on the peak area or N_S is some number between $\sqrt{N_S}$ and $\sqrt{N_{Tot} + N_B}$ and depends on the height of the background, width of the background fit, and correlations between the peak and background. All rates and uncertainties listed in this section are from the fit.

Certain peaks were fit to double gaussian instead of the single gaussian in Eq. 7.8. The gain shifted in the two open-shield measurements, causing single peaks to appear as double peaks. Some peaks from different sources are naturally close together and must be fit simultaneously. In these cases, peaks were fit to double gaussians with independent parameters:

$$\frac{P_1}{\sqrt{2\pi\sigma_1^2}}e^{-(x-\mu_1)^2/2\sigma_1^2} + \frac{P_2}{\sqrt{2\pi\sigma_2^2}}e^{-(x-\mu_2)^2/2\sigma_2^2} + B + Cx. \quad (7.10)$$

For double peaks caused by the gain shift, the peak area is the sum of the two peaks and the uncertainty on the total area was calculated from the covariance matrix, as in Eq. 7.11.

$$P_{Tot} = P_1 + P_2 \quad (7.11)$$

$$\sigma_{P_{Tot}}^2 = \sigma_{P_1}^2 + \sigma_{P_2}^2 + 2 * Cov_{12}$$

For closely-spaced peaks from different sources, we fit both peaks simultaneously, using the gaussian area for each peak separately. In this case, the uncertainty on the single-peak area was taken from the fit.

Tables 7.6, 7.7 and 7.8 list the source of all peaks in the open- and closed-shield measurements facing the beam direction. We show the rates in each peak facing the beam direction, but the measurements facing the readout direction are similar. The p-values of the fits are also listed in the tables. In addition to photons from environmental radioactivity, neutron interactions and ^{235}U create peaks in the spectrum. The energies of ^{235}U peaks are very low, and the natural abundance is less than 1%, so we expect the source of ^{235}U is within the shield. Peaks from neutrons and ^{235}U are not included in the simulation and will not necessarily change between the two measurements. Therefore, any environmental radiation

Table 7.6: Energy and source of peaks in the thorium chain in the shielded germanium measurements in the KATRIN detector laboratory. The rates in each peak and the probability of the fits are shown for the two measurements, with open and closed shield facing the beam direction. The readout direction rates are similar.

Energy keV	Thorium Peaks	Rate [mHz]		p-value	
		Open	Closed	Open	Closed
2614.5	$^{208}\text{Tl}+^{208}\text{Pb}(\text{n}, \text{n}'\text{g})$	0.83 ± 0.06	0.65 ± 0.05	0.36	0.67
968.8	^{228}Ac	0.49 ± 0.12	0.41 ± 0.05	0.25	0.11
911.2	^{228}Ac	1.12 ± 0.09	0.79 ± 0.06	0.08	0.17
795	^{228}Ac	0.46 ± 0.15	0.20 ± 0.05	0.16	0.04
727.3	^{212}Bi	0.43 ± 0.12	0.18 ± 0.06	0.67	0.46
583.1	$^{208}\text{Tl}+^{208}\text{Pb}(\text{n}, \text{n}'\text{g})$	1.45 ± 0.10	1.01 ± 0.07	0.29	0.92
509.3 and 510.7 and 510.9	$^{208}\text{Tl}+^{207}\text{Pb}(\text{n}, \text{n}'\text{g})$ +annih	10.91 ± 0.20	9.44 ± 0.17	0.15	0.14
338.7	^{228}Ac	1.00 ± 0.13	0.75 ± 0.07	0.50	0.01
238.6	^{212}Pb	4.52 ± 0.11	3.47 ± 0.12	0.03	0.21

Table 7.7: Energy and source of peaks in the uranium chain in the shielded germanium measurements in the KATRIN detector laboratory. The rates in each peak and the probability of the fits are shown for the two measurements, with open and closed shield facing the beam direction. The readout direction rates are similar.

Energy keV	Uranium Peaks	Rate [mHz]		p-value	
		Open	Closed	Open	Closed
1764.7	^{214}Bi	0.37 ± 0.07	0.17 ± 0.04	0.09	0.01
1120.6	^{214}Bi	0.48 ± 0.08	0.14 ± 0.04	0.60	0.02
1001.5	$^{234\text{m}}\text{Pa}$	0.83 ± 0.08	0.95 ± 0.06	0.05	0.11
766.6 and 768.4	$^{234\text{m}}\text{Pa}+^{214}\text{Bi}$	0.35 ± 0.11	0.41 ± 0.08	0.11	0.13
609.2	^{214}Bi	1.87 ± 0.11	0.86 ± 0.08	0.65	0.60
351.9	^{214}Pb	2.14 ± 0.12	1.23 ± 0.09	0.01	0.01
295.2	^{214}Pb	1.26 ± 0.14	0.48 ± 0.09	0.67	0.72
186.1 and 186.2	$^{226}\text{Ra}+^{115}\text{In}(\text{n},\text{g})+^{235}\text{U}$	10.13 ± 0.21	10.67 ± 0.18	0.34	0.55

Table 7.8: Energy and source of peaks from potassium and other sources in the shielded germanium spectrum measured in the KATRIN detector laboratory. The rates in each peak and probability of the fits are shown for the two measurements, with open and closed shield facing the beam direction. The readout direction rates are similar.

Energy keV	Potassium and Other Peaks	Rate [mHz]		p-value	
		Open	Closed	Open	Closed
1460.8	^{40}K	1.69 ± 0.08	0.58 ± 0.05	0.46	0.18
897.3	$^{207}\text{Pb}(\text{n},\text{n}'\text{g})$	0.35 ± 0.10	0.27 ± 0.05	0.88	0.32
834.1	$^{72}\text{Ge}(\text{n},\text{n}'\text{g})$				
803.1	$^{206}\text{Pb}(\text{n},\text{n}'\text{g})$	1.08 ± 0.12	0.78 ± 0.07	0.16	0.05
692.4	$^{72}\text{G}(\text{n},\text{n}'\text{e}^-)$				
595.9	$^{74}\text{Ge}(\text{n},\text{n}'\text{g})$				
569.7	$^{207}\text{Pb}(\text{n},\text{n}'\text{g})$	0.53 ± 0.13	0.57 ± 0.08	0.68	0.15
563	$^{76}\text{Ge}(\text{n},\text{n}'\text{g})$				
205.2	^{235}U	0.64 ± 0.13	0.82 ± 0.09	0.02	0.80
197.1 and 198.4	$^{19}\text{F}(\text{n},\text{n}'\text{g}) + ^{71}\text{Ge}$ sum	1.37 ± 0.20	1.33 ± 0.16	0.05	0.00
162.4	$^{235}\text{U} + ^{115}\text{In}(\text{n},\text{g})$	1.22 ± 0.17	0.89 ± 0.09	0.35	0.38
143.9	^{235}U	2.17 ± 0.18	2.14 ± 0.10	0.78	0.13
139.7	$^{74}\text{Ge}(\text{n},\text{g})$	1.18 ± 0.19	1.10 ± 0.11	0.78	0.13

Table 7.9: Requirements for including peaks from the shielded spectra in the weighted average.

Peak Separation	$\Delta E > 1.5 \text{ FWHM}$
Peak Rate	$R > 5\sigma_R$
Peak Energy	$E > 150 \text{ keV}$
Peak Fit	p-value > 0.01

peak that overlaps with neutron-related or ^{235}U peaks should not be used to calculate the intensity. When a neutron interacts in the germanium detector, the germanium nuclear recoil will be detected. All peaks labeled Ge(n,n'x) in Tab. 7.8 create sawtooth nuclear recoil peaks, which were not fit to gaussians.

Typical γ -ray peaks of uranium, thorium, and potassium used in γ -ray counting are: the 583, 911 and 2614 keV peaks in the ^{232}Th series; the 186, 609, 1001 and 1764 keV peaks in the ^{238}U series; and in ^{40}K , the peak at 1461 keV [104]. We fit all of these peaks, but did not necessarily use them to calculate the intensity.

Only peaks that pass certain requirements were used to calculate the intensity. We only considered peaks produced solely by environmental radioactivity. Therefore, peaks must be separated by more than 1.5 FWHM from peaks from other sources. We did not consider any peaks with a measured rate less than 5σ from zero, as these peaks will not improve the intensity determination. Since the uncertainty includes correlations with the background, this requirement depends on the continuum background level as well as the rate in the peak. We did not fit any peaks under 150 keV for two reasons; the background continuum grows at low energy, and the FWHM of a low-energy peak is less than 0.888 keV, an ADC bin. Some low energy peaks are not listed in Tab. 7.6, 7.7 and 7.8. Peaks with poor fits, or p-values less than 0.01, were not included. In the 15 cm shield measurement, no peaks were excluded due to a low p-value. Table 7.9 lists these requirements.

After identifying which peaks to use, we calculated the intensity I_O of photons coming through each of the shield openings from the difference in the measured rates $R_\Delta = R_O - R_C$, the simulation peak areas and bin width P_S/w , the number of simulated events N , and the

area of the starting plane A in the `RoomRadiationGun`:

$$I_O = \frac{wR_\Delta N}{P_S A} \frac{\gamma}{\text{cm}^2\text{s}} (\theta < 26^\circ). \quad (7.12)$$

When calculating the uncertainty on I_O , we considered the uncertainty on the peak areas as determined from the fits. This also depends on the time duration of the measurements, T_O and T_C . The total uncertainty on I_O is:

$$\frac{\sigma_{I_O}^2}{I_O^2} = \frac{\sigma_{P_O}^2}{(wT_O R_\Delta)^2} + \frac{\sigma_{P_C}^2}{(wT_C R_\Delta)^2} + \frac{\sigma_{P_S}^2}{P_S^2} \quad (7.13)$$

Peaks that pass all requirements were used to calculate the weighted average intensity for the uranium and thorium chains. The weighted average $\overline{I_O}$ and uncertainty on the average $\sigma_{\overline{I_O}}$ are:

$$\begin{aligned} \overline{I_O} &= \frac{\sum_{i=1}^n (I_{O_i} / \sigma_i^2)}{\sum_{i=1}^n (1 / \sigma_i^2)} \\ \sigma_{\overline{I_O}}^2 &= \frac{1}{\sum_{i=1}^n (1 / \sigma_i^2)} \end{aligned} \quad (7.14)$$

Tables 7.10, 7.11 and 7.12 list the changes in rate between the two measurements, R_Δ , and intensity for each peak in the beam direction and the weighted average intensity in both directions. The changes in rate and intensity for each peak in the readout direction are similar. Since neutrons and ^{235}U have not been simulated, we could not calculate an intensity for peaks coming only from these sources. As expected, the change in rate from these sources is small. The peaks in bold were included in the intensity weighted average. The non-bold peaks are left out due to high uncertainty in the rate in one of the measurements.

In the thorium average, three peaks were included: two early-chain ^{228}Ac peaks and a late-chain peak of ^{212}Pb . The three peaks are in agreement, indicating the chain is in equilibrium as we assumed when calculating the energy spectrum. Figure 7.12 shows the two fits for the 238 keV ^{212}Pb peak, the peak with the smallest uncertainty on the intensity in the thorium chain.

Table 7.10: Intensity of environmental radioactivity coming through the beam-side shield opening. Peaks in bold were included in the weighted average. Results facing the readout direction are similar.

Energy keV	Thorium Peaks	R_{Δ} mHz	Intensity I_O $10^{-3}\gamma/\text{cm}^2/\text{s}$	σ_{I_O}
2614.5	$^{208}\text{Tl}+^{208}\text{Pb}(\text{n}, \text{n}'\text{g})$	0.18 ± 0.07	0.76	0.32
968.8	^{228}Ac	0.08 ± 0.13	0.49	0.79
911.2	^{228}Ac	0.33 ± 0.11	1.43	0.49
795	^{228}Ac	0.26 ± 0.16	6.91	4.26
727.3	^{212}Bi	0.26 ± 0.13	4.89	2.62
583.1	$^{208}\text{Tl}+^{208}\text{Pb}(\text{n}, \text{n}'\text{g})$	0.44 ± 0.13	1.41	0.42
509.3 and 510.7 and 510.9	$^{208}\text{Tl}+^{207}\text{Pb}(\text{n}, \text{n}'\text{g})$ +annih	1.47 ± 0.26	9.09	1.77
338.7	^{228}Ac	0.25 ± 0.15	1.33	0.77
238.6	^{212}Pb	1.05 ± 0.16	1.39	0.22
Beam-side Weighted Average at KIT			1.37	0.19
Readout-side Weighted Average at KIT			1.39	0.20

Table 7.11: Intensity of environmental radioactivity coming through the beam-side shield opening. Peaks in bold were included in the weighted average. Results facing the readout direction are similar.

Energy keV	Uranium Peaks	R_{Δ} mHz	Intensity I_O $10^{-3}\gamma/\text{cm}^2/\text{s}$	σ_{I_O}
1764.7	^{214}Bi	0.20 ± 0.08	1.24	0.51
1120.6	^{214}Bi	0.34 ± 0.09	2.15	0.59
1001.5	^{234m}Pa	-0.12 ± 0.10	-7.99	7.06
766.6 and 768.4	$^{234m}\text{Pa}+^{214}\text{Bi}$	-0.06 ± 0.14	-1.13	2.44
609.2	^{214}Bi	1.00 ± 0.14	1.48	0.21
351.9	^{214}Pb	0.91 ± 0.15	1.46	0.25
295.2	^{214}Pb	0.78 ± 0.17	1.87	0.41
186.1 and 186.2	$^{226}\text{Ra}+^{115}\text{In}(\text{n},\text{g})+^{235}\text{U}$	0.72 ± 0.29	7.19	3.20
Beam-side Weighted Average at KIT			1.53	0.14
Readout-side Weighted Average at KIT			1.54	0.15

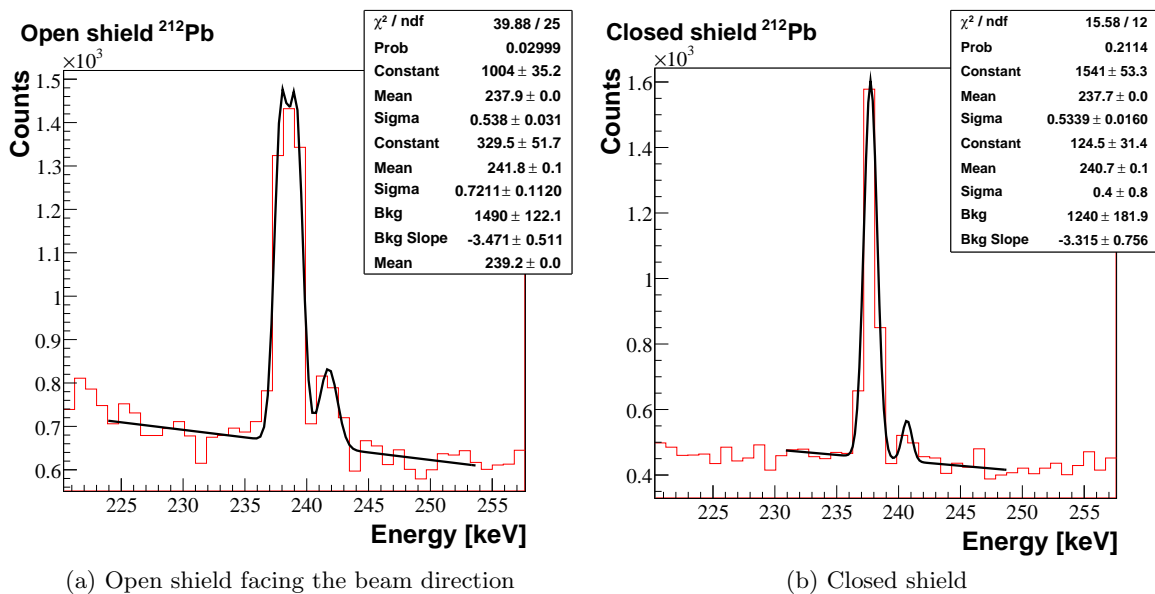


Figure 7.12: Fits to the beam-side measured ²¹²Pb peak in the thorium chain. The small peak at 241 keV is from ²¹⁴Pb, so its area is excluded from the 238 keV peak area. The double peak in the open-shield measurement is caused by the gain shifting during the run.

Table 7.12: Intensity of environmental radioactivity from potassium coming through the beam-side shield openings. Results facing the readout direction are similar.

Energy keV	Potassium and Other Peaks	R_{Δ} mHz	Intensity I_O $10^{-3}\gamma/\text{cm}^2/\text{s}$	σ_{I_O}
1460.8	^{40}K Beam-side	1.12 ± 0.10	0.63	0.06
1460.8	^{40}K Readout-side at KIT		0.64	0.10
897.3	$^{207}\text{Pb}(\text{n},\text{n}'\text{g})$	0.08 ± 0.11		
834.1	$^{72}\text{Ge}(\text{n},\text{n}'\text{g})$			
803.1	$^{206}\text{Pb}(\text{n},\text{n}'\text{g})$	0.30 ± 0.14		
692.4	$^{72}\text{G}(\text{n},\text{n}'\text{e}^-)$			
595.9	$^{74}\text{Ge}(\text{n},\text{n}'\text{g})$			
569.7	$^{207}\text{Pb}(\text{n},\text{n}'\text{g})$	-0.04 ± 0.15		
563	$^{76}\text{Ge}(\text{n},\text{n}'\text{g})$			
205.2	^{235}U	-0.18 ± 0.16		
197.1 and 198.4	$^{19}\text{F}(\text{n},\text{n}'\text{g}) + ^{71}\text{Ge}$ sum	0.03 ± 0.26		
162.4	$^{235}\text{U} + ^{115}\text{In}(\text{n},\text{g})$	0.33 ± 0.19		
143.9	^{235}U	0.03 ± 0.21		
139.7	$^{74}\text{Ge}(\text{n},\text{g})$	0.09 ± 0.22		

In the ^{238}U chain, three late-chain peaks of ^{214}Bi and ^{214}Pb and one early-chain ^{234}Pa were included in the intensity average. Other than the ^{234}Pa peaks, no early-chain uranium peaks have been fit. Since ^{222}Rn , which is radon gas, is in the uranium chain, some of the late-chain peaks could be caused by radon gas. Subtracting the closed-shield measurement will remove the contribution from radon gas assuming the contribution is stable in time. The rates in the ^{234}Pa peaks in both open and closed measurements, shown in Tab. 7.7, are abnormally large compared to other peaks in the uranium chain, indicating that peak may be out of equilibrium or may come from an unidentified source. However, the difference between the open and closed measurements is not statistically different from zero, indicating the environmental radiation coming through the shield opening is not causing the large ^{234}Pa peaks. There may be additional ^{234}Pa contamination of the shielding material or another unidentified peak at the same energy. Disequilibrium of the external environmental radiation is an unlikely explanation for the large ^{234}Pa peak, so we assume the uranium chain is in equilibrium and that the late-chain peaks come from environmental radiation

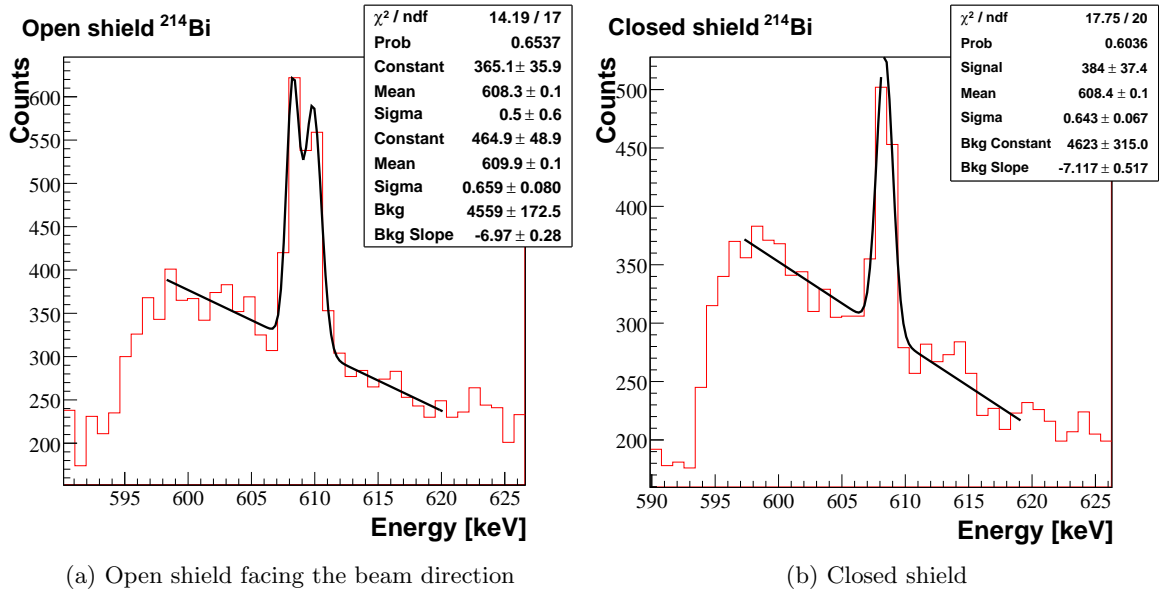


Figure 7.13: Fits to the beam-side measured ^{214}Bi peak in the uranium chain. This peak sits on top of a sawtooth recoil peak from neutron interactions. The double peak in the open-shield measurement is caused by the gain shifting during the run.

instead of radon gas. The peak with the smallest uncertainty on the intensity is the 609 keV ^{214}Bi peak, which is shown in Fig. 7.13.

The ^{40}K peak at 1.46 MeV passes all cuts and is used to determine the potassium intensity. The measurement fits are shown in Fig. 7.14.

Tables 7.10, 7.11 and 7.12 also list the weighted average intensity for both the beam-side and readout-side directions. The results in both directions agree. Since we took a weighted average, the averages are dominated by the peaks with the smallest uncertainty. Therefore, the intensities in both directions are in agreement because the 238 keV ^{212}Pb , the 609 keV ^{214}Bi , and the 1.46 MeV ^{40}K peaks are in agreement in both directions. Other than potassium, the intensity through the shield openings was determined from peaks under 1 MeV. Since ^{214}Bi is a radon daughter, the fact that the intensities in both directions, which were measured at different times, agree indicates that the radon gas contribution may not be varying in time or may not be large.

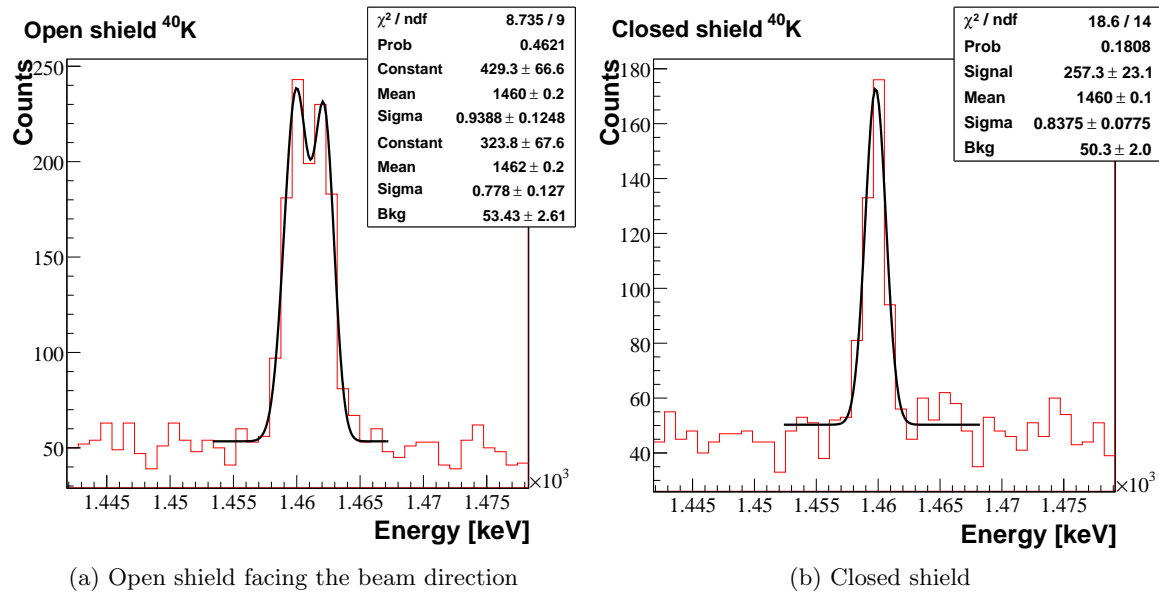


Figure 7.14: Fits to the beam-side measured ^{40}K peak. The double peak in the open-shield measurement is caused by the gain shifting during the run.

Using the weighted average intensity, we normalized the simulation of environmental radiation coming through the 15 cm shield opening and added it to the closed-shield measurement. This is compared with the open-shield measurement in Fig. 7.15 and 7.16. Since the gain shifted in the open-shield measurements, the energy resolution in the two measurements is different. This causes the simulation peaks to appear larger than the measurements, but the simulation was normalized based on the areas of the most-significant peaks.

The majority of the measured spectra is not caused by environmental radiation and does not change between measurements. Therefore, we also subtract the closed-shield measurement from the open-shield measurements and compare this to the simulation in Fig. 7.17. In this plot it is clear that the continuum below 500 keV in the simulation is lower than in the measurements.

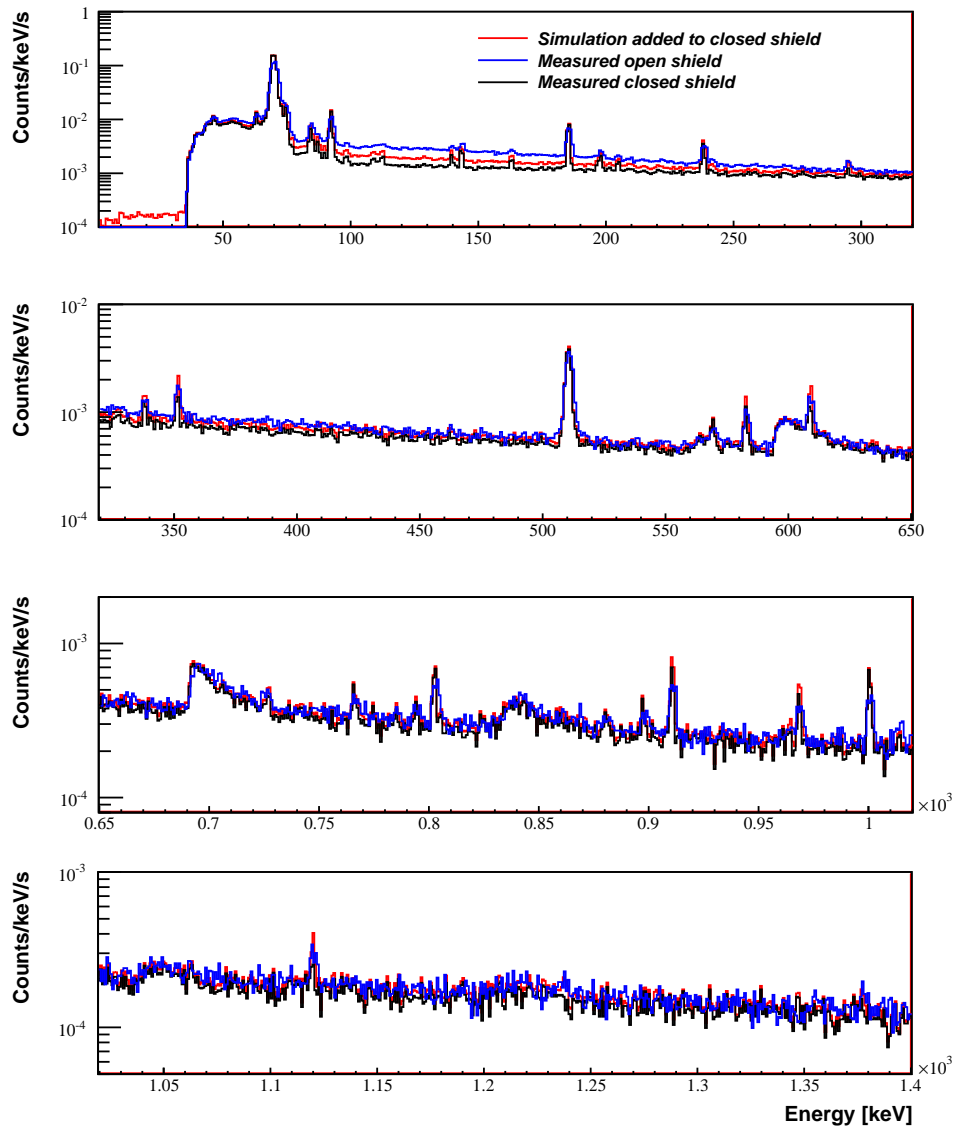


Figure 7.15: Final comparison of the shielded germanium detector measurements at KIT with the simulation (0–1.4 MeV). The source of the large peaks under 80 keV has not been identified, but the photons must originate close to the detector due to the low energy. The bin width is 0.89 keV.

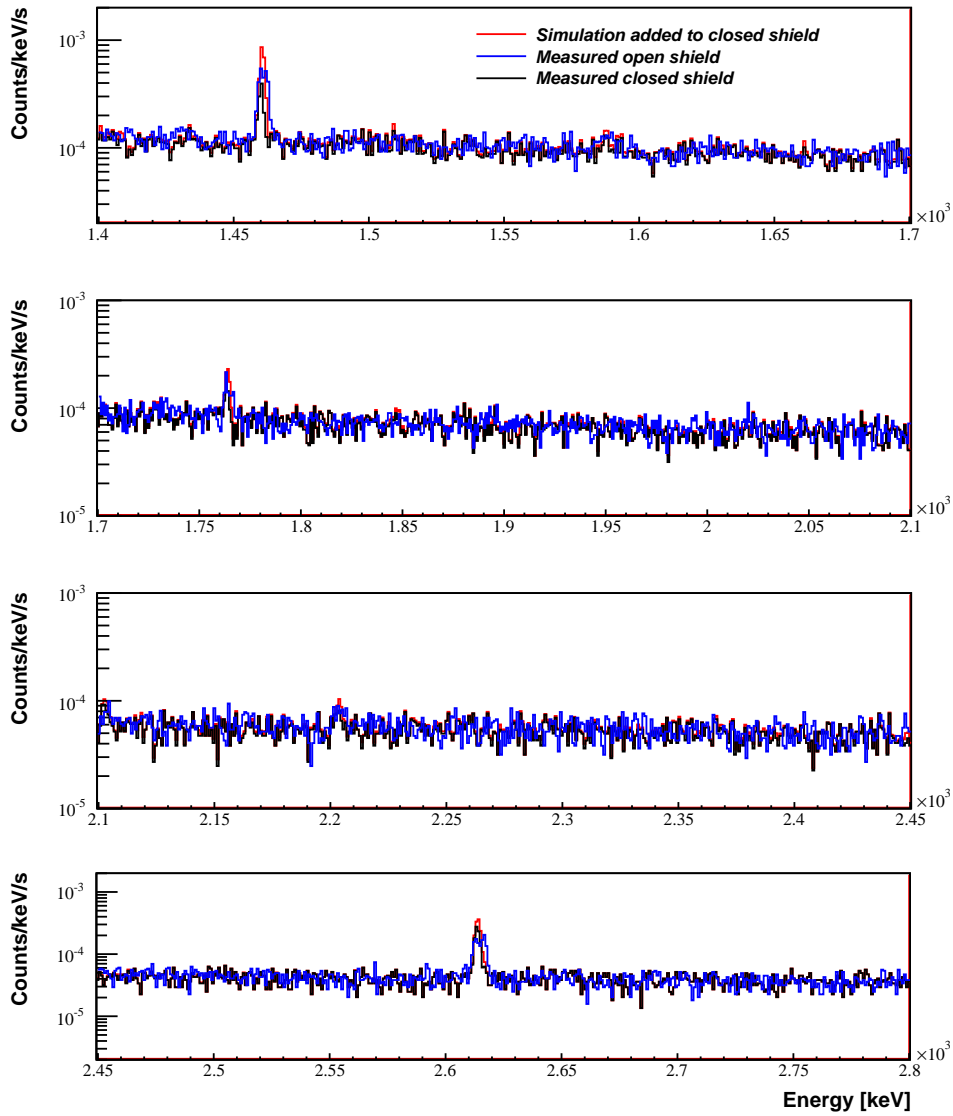


Figure 7.16: Final comparison of the shielded germanium detector measurements at KIT with the simulation (1.4–2.8 MeV). The spectrum is continuous across the 2.6 MeV ^{208}Tl peak, indicating the continuum is caused by sources other than the environmental radiation. The bin width is 0.89 keV.

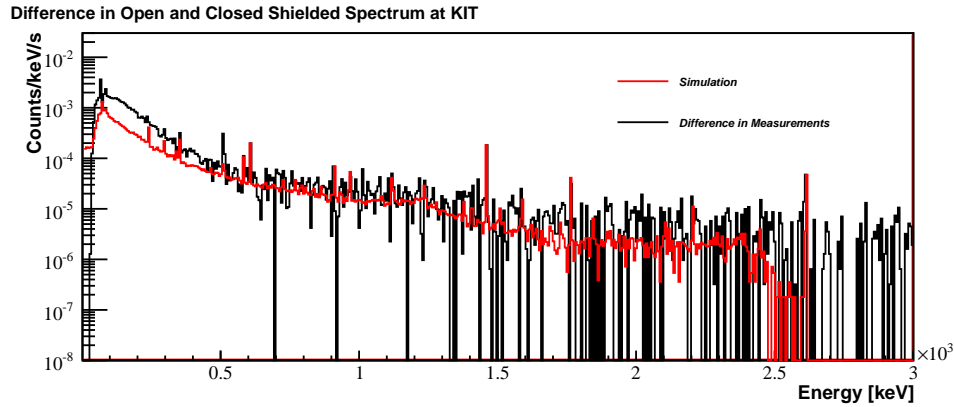


Figure 7.17: Difference of the open- and closed-shield measurements at KIT compared with the simulation of radiation coming through the shield opening. The bin width is 6.4 keV.

Intensity Incident on the Walls of the KATRIN Shield

In the previous section we determined the intensity which will come through the KATRIN shield openings. The final step is to determine the intensity which is incident on the walls of the KATRIN shield and the total intensity of each type of radiation. The unshielded germanium detector measurement includes photons from all directions and can be used to determine the total intensity. We simulated the unshielded germanium detector, dividing the environmental radiation into the three angular regions shown in Fig. 7.11. Using Eq. 7.6 and the intensities through the openings determined in the last section, we calculated the intensity incident on the walls of the shield I_W .

We fit all peaks in the unshielded spectrum to gaussians as in Eq. 7.5. Unlike the measurements with shielding, no neutron peaks are visible in this spectrum because the environmental radiation dominates. The energy resolution is better in the unshielded measurements since the gain did not shift. Some peaks sit on Compton edges. The Compton edges can be represented by the complementary error function, Erfc , which is a step-function background starting at the mean of the gaussian convolved with a gaussian noise. Peaks on

Table 7.13: Requirements for including unshielded peaks in the weighted average.

Peak Separation	$\Delta E > 1.5 \text{ FWHM}$
Peak Fit	p-value > 0.01
Peak Rate	$R > 10\sigma_R$
Peak Energy	$E > 200 \text{ keV}$

Compton edges were fit with:

$$\frac{P}{\sqrt{2\pi\sigma^2}} e^{-(x-\mu)^2/2\sigma^2} + B + C \times \text{Erfc}\left(\frac{x-\mu}{\sqrt{2\sigma^2}}\right) \quad (7.15)$$

$$\text{Erfc}(z) = \frac{2}{\sqrt{\pi}} \int_z^\infty e^{-t^2} dt.$$

More peaks are visible above the continuum in the unshielded spectrum. Tables 7.14, 7.15, and 7.16 list all peaks with a rate separated by more than 10σ from zero. All peaks in the uranium and thorium chains that appear in the measurement are also in the simulation. This is a strong indication that the simulation is correct. Three additional peaks appear in the measurement from ^{60}Co and ^{137}Cs which are not included in the simulation. Cobalt is a cosmogenic and may be produced in the materials surrounding the detector. Cesium is a product of nuclear fallout. Neither were observed in the shielded measurements, and therefore likely have an external source.

Just like the determination of the intensity through the openings I_O , we only calculated the intensity for peaks that fulfill certain requirements. These requirements are listed in Tab. 7.13. The peak must be produced solely by environmental radioactivity. It must be separated by more than 1.5 FWHM from any peaks from other sources. The p-value for the measured fit must be greater than 0.01. Two peaks were excluded due to this cut. Since there are more peaks in the unshielded spectrum, two requirements are more stringent for the unshielded measurements. The measured peak rate must be greater than 10σ from zero and the peak energy must be greater than 200 keV. Some low-energy peaks are not listed in Tab. 7.14, 7.15, and 7.16.

The total measured rate R_M equals the sum of the simulated rates in each angular

Table 7.14: Peaks from the thorium chain visible in the unshielded germanium detector measurements in the detector laboratory at KIT and the intensity of thorium incident on the walls of the shield. Peaks in bold were included in the weighted average.

Energy keV	Thorium Peaks	Meas. Rate mHz	p-value	Intensity I_W $\gamma/\text{cm}^2/\text{s}$	σ_{I_W}
2614.5	^{208}Tl	162.0 ± 1.7	0.22	0.398	0.007
2104.1	SEP of ^{208}Tl	20.6 ± 0.8	0.18	0.349	0.020
1630.7	^{228}Ac	7.8 ± 0.5	0.05	0.409	0.049
1620.5	^{212}Bi	8.0 ± 0.6	0.76	0.368	0.042
1592.5	DEP of ^{208}Tl	16.6 ± 0.8	0.26	0.317	0.022
1588.3	^{228}Ac	14.7 ± 0.8	0.26	0.320	0.023
968.8	^{228}Ac	98.1 ± 1.7	0.05	0.355	0.009
911.2	^{228}Ac	157.0 ± 1.9	0.19	0.337	0.006
860.4	^{208}Tl	25.9 ± 1.2	0.47	0.318	0.019
795.0	^{228}Ac	26.5 ± 1.3	0.35	0.340	0.022
727.3	^{212}Bi	46.7 ± 1.5	0.51	0.344	0.015
583.1	^{208}Tl	196.4 ± 2.3	0.06	0.310	0.005
509.3 and 510.9	$^{208}\text{Tl}+\text{annih}$	158.0 ± 2.9	0.00	0.643	0.018
463.3	^{228}Ac	28.8 ± 1.8	0.13	0.304	0.023
338.7	^{228}Ac	84.7 ± 2.4	0.31	0.274	0.010
238.6	^{212}Pb	366.4 ± 4.1	0.00	0.254	0.004
Weighted Average at KIT				0.335	0.003

Table 7.15: Peaks from the uranium chain visible in the unshielded germanium detector measurements in the detector laboratory at KIT and the intensity of uranium incident on the walls of the shield. Peaks in bold were included in the weighted average.

Energy keV	Uranium Peaks	Meas. Rate mHz	p-value	Intensity I_W $\gamma/\text{cm}^2/\text{s}$	σ_{I_W}
2448.5	^{214}Bi	6.8 ± 0.5	0.86	0.308	0.029
2204.0	^{214}Bi	23.1 ± 0.7	0.29	0.264	0.012
1846.9	^{214}Bi	9.3 ± 0.6	0.31	0.251	0.020
1764.7	^{214}Bi	79.8 ± 1.2	0.09	0.292	0.007
1729.6	^{214}Bi	13.7 ± 0.6	0.63	0.261	0.017
1508.9	^{214}Bi	11.7 ± 0.7	0.60	0.306	0.026
1408.6	^{214}Bi	12.5 ± 0.8	0.22	0.284	0.025
1378.0	^{214}Bi	21.8 ± 0.9	0.10	0.293	0.017
1238.4	^{214}Bi	33.6 ± 1.2	0.23	0.286	0.013
1155.2	^{214}Bi	10.3 ± 1.0	0.23	0.329	0.039
1120.6	^{214}Bi	88.4 ± 1.6	0.53	0.277	0.007
766.6 and 768.4	$^{214}\text{Bi} + ^{234m}\text{Pa}$	27.4 ± 1.5	0.53	0.232	0.015
609.2	^{214}Bi	292.9 ± 2.6	0.75	0.245	0.003
351.9	^{214}Pb	278.3 ± 3.1	0.00	0.222	0.003
295.2	^{214}Pb	149.6 ± 3.5	0.42	0.208	0.006
186.1	$^{226}\text{Ra} + ^{235}\text{U}$	76.6 ± 4.6	0.02	0.465	0.036
Weighted Average at KIT				0.252	0.002

Table 7.16: Peaks from potassium and other sources visible in the unshielded germanium detector measurements in the detector laboratory at KIT and the intensity of potassium incident on the walls of the shield.

Energy keV	Potassium and Other Peaks	Meas. Rate mHz	p-value	Intensity I_W $\gamma/\text{cm}^2/\text{s}$	σ_{I_W}
1460.8	^{40}K	845.9 ± 3.8	0.08	0.266	0.002
1332.5	^{60}Co	7.2 ± 0.9	0.57		
1173.2	^{60}Co	6.9 ± 1.0	0.21		
661.6	^{137}Cs	19.6 ± 1.4	0.26		

region.

$$R_M = R_{Tot} = R_W + R_{RO} + R_B \quad (7.16)$$

Since the intensity is the same through both openings, we can combine the beam and readout directions. In this section, the subscript $2O$ refers to the combination of both the beam and readout directions. The combined-opening intensity I_{2O} is twice the intensity through either opening $2I_O$. The combined peak areas P_{2O}/w of the readout- and beam-direction simulations are converted to a rate using the intensity through the openings $2I_O$, the number of events generated through the openings N_{2O} , and the area of the starting plane A , or the simulation time duration T_{2O} .

$$R_{2O} = \frac{P_{2O}2I_O A}{wN_{2O}} = \frac{P_{2O}}{wT_{2O}} \quad (7.17)$$

For each peak, the intensity incident on the walls of the shield I_W was calculated from the difference of the rates, the area of the shield-wall-direction simulation peaks P_W/w , the number of generated events N_W , and the area of the starting plane A .

$$I_W = \frac{w[R_M - R_{2O}]}{P_W} \frac{N_W}{A} \frac{\gamma}{\text{cm}^2\text{s}} (\theta > 26^\circ) \quad (7.18)$$

To calculate the uncertainty on the intensity, we considered the uncertainty on the peak areas from the fit and the uncertainty on the intensity through the openings. This also depends on the time duration of the measurement T_M and the time duration of the simulation T_{2O} .

$$\frac{\sigma_{I_W}^2}{I_W^2} = \frac{\sigma_{P_W}^2}{P_W^2} + \frac{1}{(R_M - R_{2O})^2} \left[\frac{\sigma_{P_M}^2}{(wT_M)^2} + \frac{4\sigma_{P_{2O}}^2}{(wT_{2O})^2} + \frac{4\sigma_{I_O}^2 P_{2O}^2}{(wT_{2O}I_O)^2} \right] \quad (7.19)$$

The peaks included in the weighted average for thorium are shown in bold in Tab. 7.14. We used fourteen thorium-chain peaks: seven early-chain ^{228}Ac peaks, five late-chain peaks of ^{208}Tl , and two late-chain peaks of ^{212}Bi . Figure 7.18a shows the intensity for the fourteen thorium-chain peaks as a function of peak energy. There is a systematic trend toward lower intensity for peaks at lower energy, but not a systematic difference between early-chain and late-chain peaks. Therefore, the chain appears to be in equilibrium as we assumed for the

energy spectrum. Although the ^{212}Pb peak at 238.6 keV is very significant and was used in the intensity determination with a shield, the fit has a low p-value in the unshielded measurement and was not included in the weighted average. The 2.61 MeV ^{208}Tl , 911 keV ^{228}Ac , and 583 keV ^{208}Tl peaks have the lowest uncertainty on the intensity and dominate the weighted average. The fit to the 2.61 MeV peak is shown in Fig. 7.19a.

The peaks included in the weighted average for uranium are shown in bold in Tab. 7.15. We used fourteen peaks, all late in the uranium chain. Thirteen peaks come from ^{214}Bi and one comes from ^{214}Pb . Unlike the shielded measurements, the early-chain 1.001 MeV ^{234m}Pa peak has a very small rate consistent with equilibrium and has not been fit. The early-chain 186 keV ^{226}Ra line has been fit and indicates a higher intensity, but is left out of the weighted average because it is low energy and overlaps with the most probable ^{235}U photon. Therefore, we assume the uranium chain is in equilibrium. Since essentially all photons of appreciable energy are late in the uranium chain, the assumption of equilibrium should not affect the background estimates. Similar to the thorium I_W , there is a systematic trend toward lower intensities for peaks at lower energy as shown in Fig. 7.18b. The ^{214}Pb peak at 351.9 keV was not included in the average due to a low p-value. The fit to the 609 keV ^{214}Bi peak, the peak with the lowest uncertainty on the intensity, is shown in Fig. 7.19b.

Table 7.16 shows the intensity for potassium. The fit to the 1.46 MeV peak is shown in Fig. 7.20.

The unshielded measured spectrum is compared with the final simulation including environmental radiation from all directions and cosmic-ray muons and photons in Fig. 7.21 and 7.22. We have not tuned any parameters to alter the shape of the continuum, but the shape of the continuum matches well above about 1 MeV. At low energy, the simulation continuum is lower than the measurement. All counts in the simulation above 2.6 MeV are from cosmic rays. The simulated contribution from cosmic-ray muons and photons is 0.68 Hz, or less than 1% of the counts.

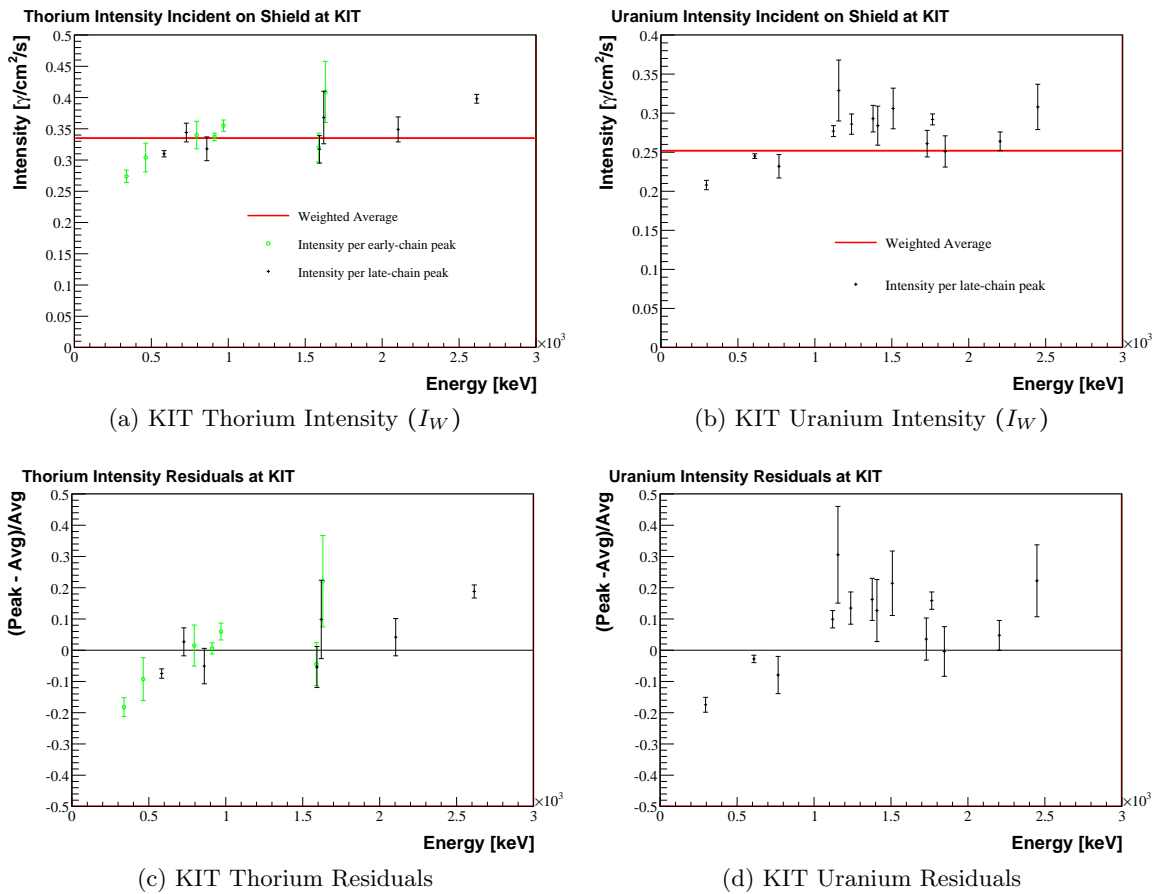


Figure 7.18: Intensity of radiation incident on the walls of the shield in KIT determined by fitting each peak in the uranium and thorium chains in the unshielded germanium detector spectrum. There is a systematic trend toward lower intensity at lower energy. The uncertainties shown are the statistical uncertainties listed in Tab. 7.15 and 7.14. The bottom plots are the residuals.

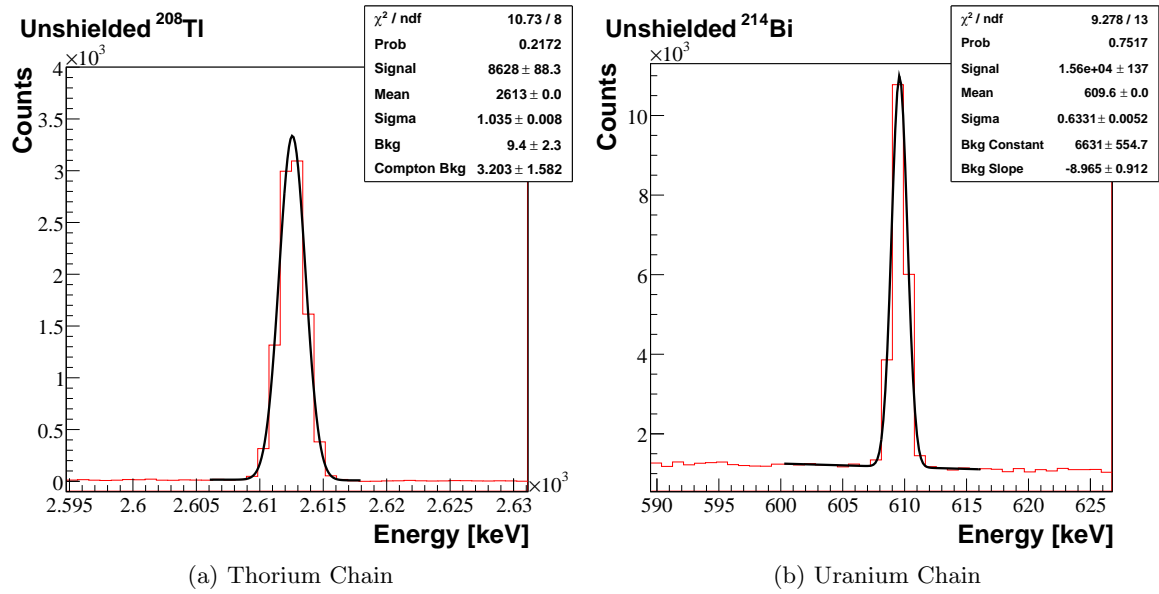


Figure 7.19: Fits to the unshielded measured ²⁰⁸Tl peak in the thorium chain and the ²¹⁴Bi peak in the uranium chain.

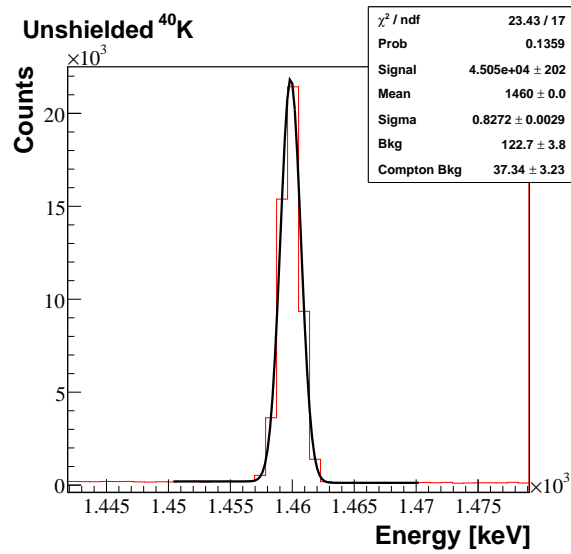


Figure 7.20: Fit to the unshielded measured ⁴⁰K peak.

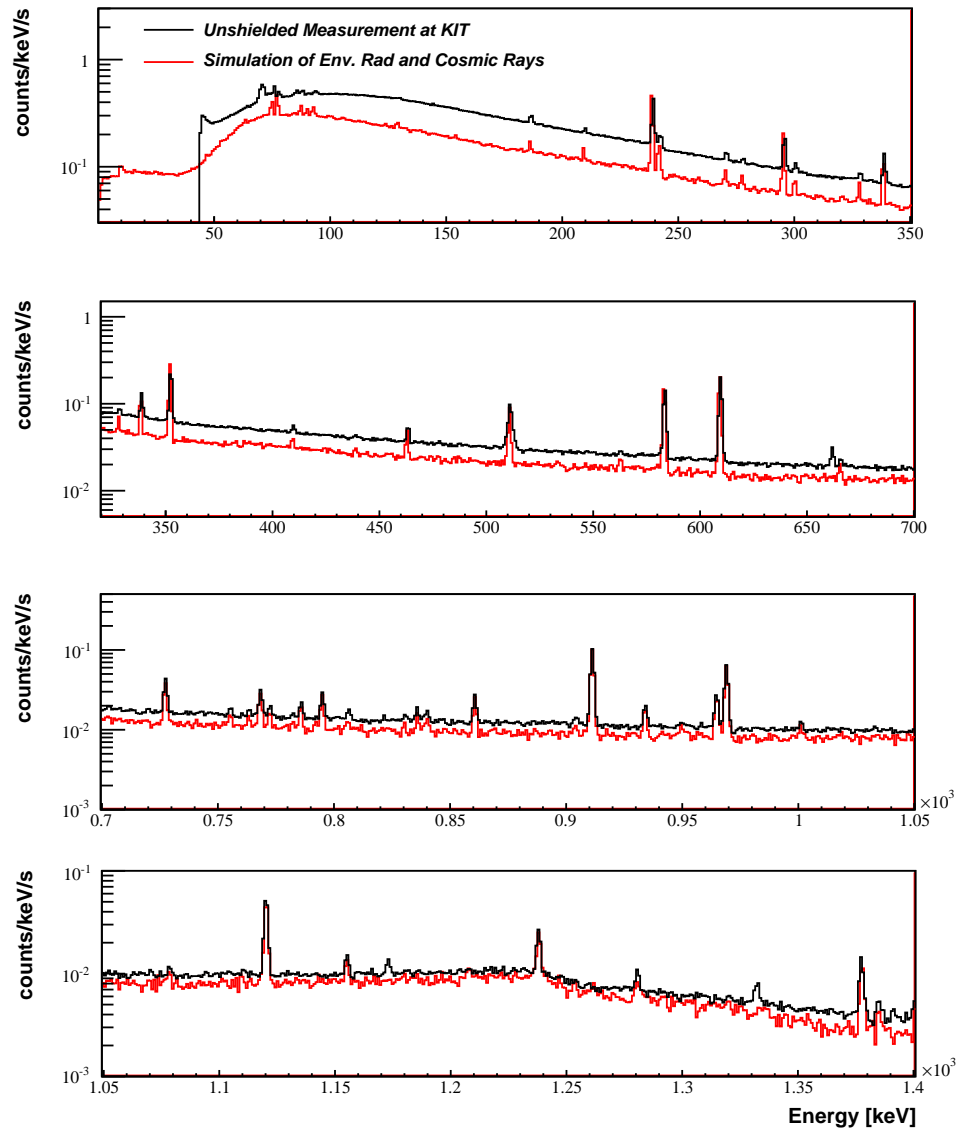


Figure 7.21: Comparison of the unshielded germanium detector measurements at KIT with the environmental radiation simulation (0–1.4 MeV). The shape of the continuum matches very well and was not tuned in the simulation. The bin width is 0.89 keV.

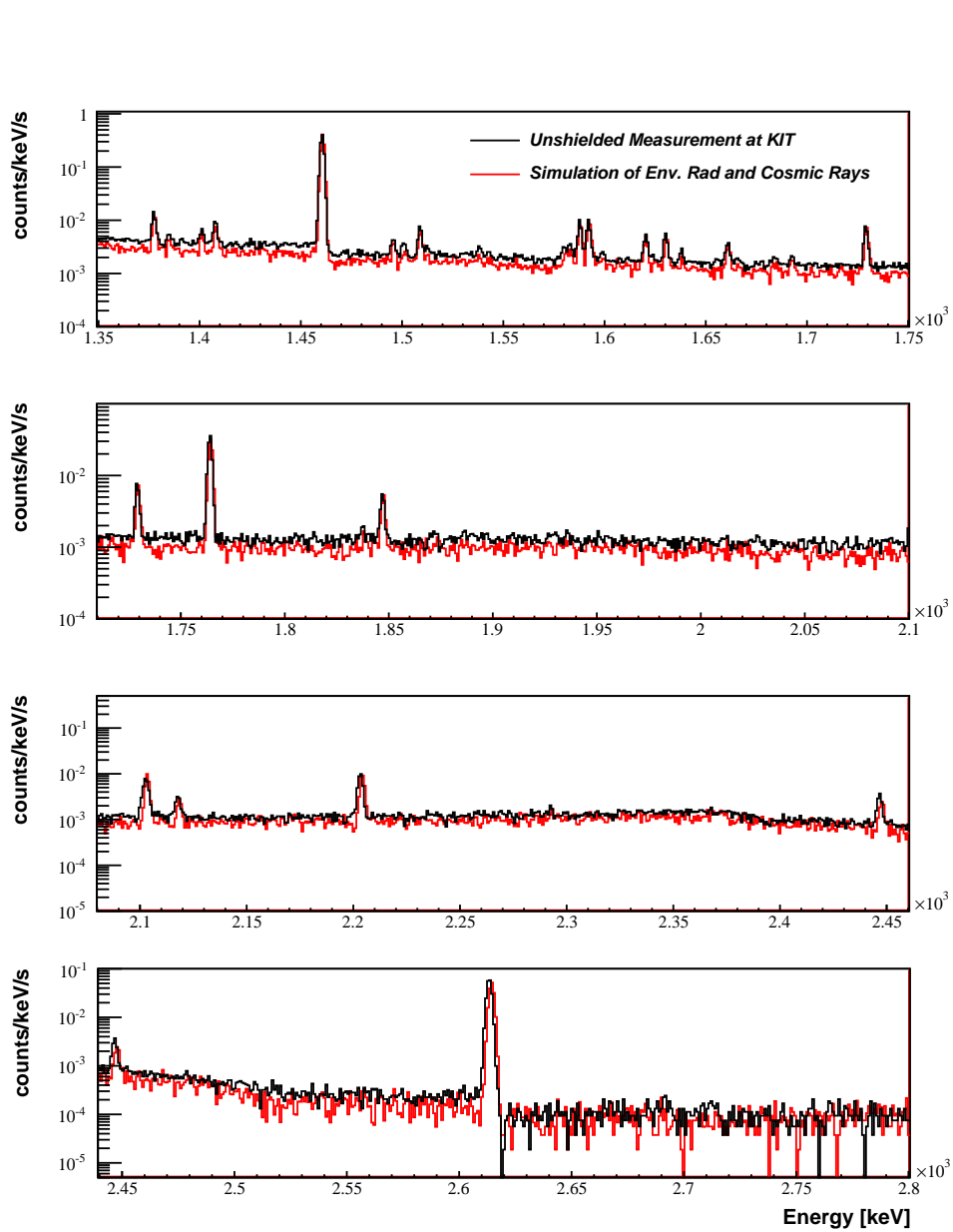


Figure 7.22: Comparison of the unshielded germanium detector measurements at KIT with the environmental radiation simulation (1.4–2.8 MeV). The shape of the continuum matches very well and was not tuned in the simulation. The bin width is 0.89 keV.

7.2.4 *Summary of KIT Environmental Radiation Measurements*

Using measurements and simulations with a germanium detector, we characterized the environmental radiation in the detector laboratory at KIT. The simulation depends on a number of free parameters determined in this section. First, the detector volume and exact geometry of the cryostat are unknown, so we compared the simulation to a ^{60}Co calibration. The relative efficiency depends on the detector volume, so we varied the inner-bore dimensions of the detector until the simulation produced the correct relative efficiency. The peak-to-Compton ratio depends on the front cryostat thickness, but not the geometry of the dewar behind the detector. The dewar may affect the background estimates as photons coming from other directions may scatter off the dewar. Second, we do not know the energy spectrum of the environmental radiation, so we assumed it would be the spectrum produced by photons from potassium and the uranium and thorium chains in equilibrium scattering in 30 cm of concrete. In reality, the radioactivity may not be evenly distributed, it may be embedded in a thicker source, or cleaner absorbing layers may separate the source from the detector. Third, we do not know the angular distribution of the environmental radiation, so we assumed it is isotropic within three angular regions to which the KATRIN silicon detector is most sensitive. The true angular distribution will depend on the location of the source of radioactivity with respect to the detector. The impact that the approximate angular distribution will have on the results depends on the detector; the germanium detector and the shielded KATRIN silicon detector have different angular responses to the radiation. This is investigated in Section 7.3.5.

To determine the intensity in each angular region—through the shield openings and incident on the walls of the shield—we fit the photon peaks to find the peak areas. Since the detector’s full-energy peak efficiency was validated with a ^{60}Co calibration and we know which peaks should appear in the energy spectrum, the simulated peak areas should match the measurement, at least near the calibration point. All peaks visible in the measurements have been identified, and all peaks from uranium, thorium, and potassium are also present in the simulation. The variance in the intensity determined from each peak within the uranium and thorium chains is less than 15% of the weighted average intensity, as shown

in Fig 7.18. The decay of ^{40}K produces only one peak so we cannot calculate a variance for the potassium intensity. Since all peaks are present in the simulation and the variance is small, we are confident we are correctly simulating the environmental radioactivity.

The variance of the intensity incident on the walls of the shield I_W is not random; it trends toward lower intensity for peaks of lower energy, as shown in Fig 7.18. This may be an indication that there are small errors in the detector efficiency or initial energy spectrum. Another calibration with a lower-energy peak would validate the detection efficiency over a broad energy range. The preference for lower intensity at lower energy indicates the simulation peaks are too large at low energy. In contrast, the simulated continuum is underestimated at low energy, as shown in Fig. 7.21 and 7.22. The initial energy spectrum could be altered by using a thicker layer of concrete—up to 60 cm—or a radio-pure, absorbing layer in front of the concrete to attenuate more of the low-energy peaks. The affect on the continuum from these changes is unknown. We take the systematic uncertainty on the environmental-radiation intensity incident on the shield walls to be 15% based on the variance of the intensity per peak within the uranium and thorium chains.

The environmental radiation properties, determined with the germanium detector, are used to simulate the background in the KATRIN silicon detector. The germanium detector and silicon detector are different; the silicon detector is surrounded by a 3 cm thick lead shield and has a much lower gamma detection efficiency. A germanium detector has an intrinsic efficiency of almost 100% for photons with energies up to about 800 keV, but a silicon detector's intrinsic efficiency drops significantly for photons above 50 keV. Without a shield, the photons incident on the germanium detector with energies under 800 keV dominate the spectrum. In contrast, since high-energy photons can pass through the KATRIN shield, then Compton scatter in the silicon detector and create counts in the low-energy region of interest, we are interested in the photons above 500 keV. Therefore, we compare the integral simulated rate in the germanium detector above 500 keV to the measurement.

The simulated unshielded-germanium-detector spectrum including cosmic rays is shown in Fig. 7.21 and 7.22. The integral rate in this simulation is lower than the measurement by 27.8% between 500 keV and 2.7 MeV. From the threshold of 40 keV up to 2.7 MeV, the simulation is 58.5% low. Since KATRIN employs a lead shield, photons under 500 keV

incident on the shield walls should not reach the detector and the low-energy discrepancy should not affect the KATRIN background estimate. The discrepancy is somewhat larger than the assigned systematic uncertainty and could be due to any of the assumptions we have made about the detector geometry, energy distribution, or angular dependence of the radiation.

The intensity through the shield openings I_O at KIT is less than 1% of the total, but may be an appreciable background in the shielded silicon detector. It was mostly determined from peaks under 1 MeV. If the trend toward lower intensity at lower energy observed in the intensity incident on the walls, shown in Fig 7.18, also occurs for the intensity through the shield openings, it may be systematically low. The difference in the 15 cm shield measurements, as in Fig. 7.17, and the simulation of radiation through the shield openings depend on I_O . Integrating the difference in rate between the open- and closed-shield measurements from 500 keV and 2.7 MeV and comparing to the integral simulation rate, the measurement is 31.5% higher than the simulation, comparable to the difference without a shield. The integral difference in the measurements between 40 keV and 2.7 MeV is 126% higher than the simulations. The disagreement is mostly in the low energy continuum, and could be due to the same assumptions which caused a low-energy discrepancy in the unshielded germanium detector simulation. An additional assumption for I_O is that the backgrounds to the environmental radiation signal were the same in the open- and closed-shield measurements. If some background is larger in the open-shield measurement, it could cause some of this discrepancy.

These photons come through the shield openings and are not attenuated by the shield, so the low-energy agreement may affect the estimated background in the KATRIN detector. Any discrepancy in photons incident on the germanium detector with energy less than 500 keV will be detected, but most of these will only have some probability of Compton-scattering in the silicon detector. Therefore, the simulation of radiation through the shield openings may include too few photons under 500 keV by about a factor of two, which is detected by the germanium detector. We take the systematic uncertainty on I_O to be 130% due to the difference in the total rate in the germanium detector measurements and simulations. The effect on the background in the silicon detector is likely much less than

this, so this is a very conservative uncertainty.

The agreement is very good in both the unshielded and shielded simulation above 500 keV where the photons will create backgrounds for KATRIN. We expect even better agreement if the germanium detector is enclosed in the KATRIN shield, as in the next section.

7.3 Measurements in the UW Commissioning Laboratory

The KATRIN detector will be commissioned at the University of Washington (UW), so we must characterize the UW laboratory environment to understand the detector backgrounds during commissioning. The environmental radiation's energy and angular distribution could be different in this laboratory than the detector laboratory at KIT. Since the laboratory is in a basement, the cosmic ray intensities may be affected by the overburden. To test these assumptions, we made another set of germanium detector measurements in the B037 laboratory of the UW physics building. In contrast to the KIT measurements, we did not measure the angular distribution using a funnel opening in the 15 cm shield. Therefore, the angular distribution in the B037 lab is not well known. The KATRIN shield was available, so we measured the attenuation by the shield and compared it to simulations. Four measurements were made, all with the detector facing the door.

Unshielded germanium detector: Measurements with the unshielded germanium detector to measure the total environmental radiation in the B037 laboratory.

KATRIN shield: Measurements with the germanium detector inside the KATRIN shield. Comparing this to the above measurement, we validated the simulated absorption by the shield and ensure the shield materials are radio-pure.

KATRIN shield with stainless steel cover: Measurements with the germanium detector inside the KATRIN shield with a stainless steel blank-off flange covering the beam-side shield opening. Comparing this to the previous measurement places limits on the amount of radiation coming through the shield opening.

15 cm closed shield: Measurements with the germanium detector inside a 15 cm lead

shield. A large reduction in the rate is observed with a 15 cm lead shield, ensuring the background in the other measurements originates outside the shield. Peaks from cosmic neutrons are visible in this spectrum. A different detector was used in this measurement than the others.

We placed the germanium detector close to the future position of the KATRIN detector. For commissioning at UW, the detector system support beams are 10 cm taller than in Karlsruhe, making the beam height 1.4 m. To position the germanium detector at a similar height, we built a 1 m tall wooden table covered with a 2.54 cm thick aluminum plate. Placed on the table, the actual detector height was 1.42 m for the first three measurements, and 1.26 m with a 15 cm shield. The measurements were made in B037 between April and August of 2009.

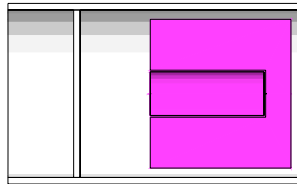
We used two ORTEC model GMX 55220-NDR n-type coaxial HPGe detectors with 50% relative efficiency. Both detectors were biased to -3.5 kV. Detector 1, used in the first three measurements, has serial number 30-N40037. Detector 2, used with the 15 cm shield, has serial number 30-N30479A. Both are mounted on a CFG: CG 1.2 portable dewar. The dewar capacity is small; the dewar must be refilled every six hours, including during data taking. No excess noise was observed during these auto-fills. Detector 1's volume is approximately 211.8 cm^2 , 69% larger than the detector used for measurements at KIT. Detector 2's volume is approximately 213.2 cm^2 .

The DAQ was a CAMAC-based system read out by ORCA. A trigger card, the LeCroy 4532 Majority Logic Unit (MALU), controlled the readout. The germanium detector signal was first shaped by an ORTEC 672 Spectroscopy Amplifier with time constant of $2 \mu\text{s}$, then it was recorded with an ORTEC AD413A ADC. We converted the recorded spectrum to energy by fitting the ^{40}K peak at 1460.8 keV and the ^{208}Tl peak at 2614.5 keV. Table 7.17 lists the time duration of each measurement.

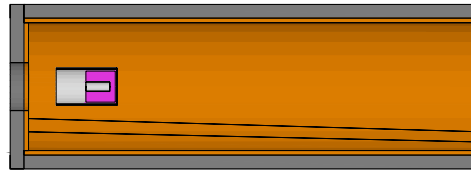
For measurements with the KATRIN shield, we slid the germanium detector cryostat through the hole on the readout side of the shield. This placed the center of the germanium detector 86 cm from the beam-side shield opening and 19 cm from the readout-side opening. The KATRIN detector will be centered 61.5 cm from the beam-direction opening and 43.5 cm

Table 7.17: Time duration of each of the measurements at UW.

Measurement	Time Duration s
Unshielded	86,400
KATRIN Shield	162,000
KATRIN Shield with Cover	133,200
15 cm Shield	1,504,500



(a) UW Coaxial germanium detector



(b) Lead and copper shield

Figure 7.23: Simulation geometry for the germanium detector measurements in the UW B037 laboratory. The germanium crystal is shown in purple. The copper shield is shown in orange and the lead shield is dark grey.

from the readout-direction hole. The KATRIN shield is described in detail in Section 5.1.2.

The 15 cm shield was built out of lead bricks. Since this detector's dewar is so small, we completely covered the dewar with bricks. A hole in the shield at the rear of the detector allowed the liquid nitrogen autofill lines to come out of the shield and connect to the larger dewar. Inevitably, some cracks between the bricks extended all the way through the shield, but should not allow much radiation to pass through the shield. The top layer of the shield cavity was supported by a 2.54 cm thick oxygen-free high thermal conductivity (OFHC) copper plate.

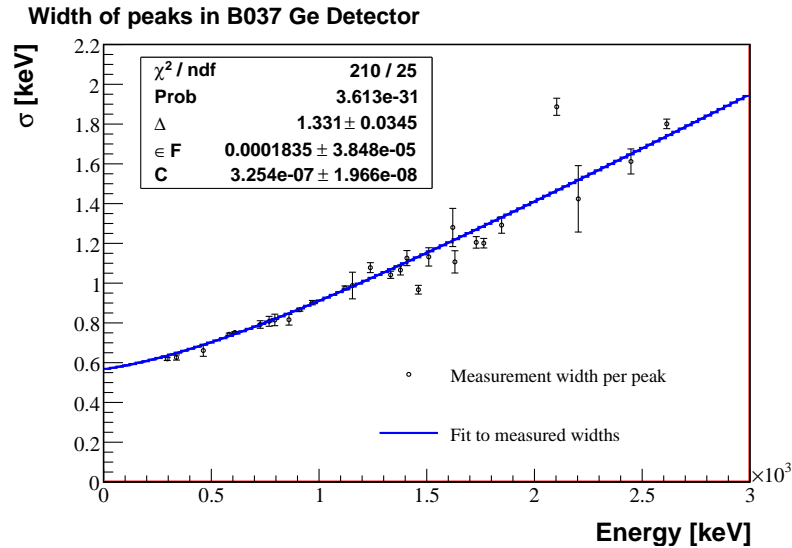


Figure 7.24: Width of peaks in the B037 germanium detector and best fit. The outlier is the 2104 keV SEP of ^{208}Tl .

7.3.1 Simulation Geometry and Response

Figure 7.23 shows the simple detector and the KATRIN shield in the simulation. The cryostat is aluminum, with a thin 1 mm front window. Just like the KIT detector, we do not know the dimensions of the inner bore or the dead layers. We used a ^{60}Co calibration to determine the dimensions. We assume the inner contact has a 750 μm dead layer and the outer contact has a 0.3 μm dead layer. Although not shown in the figure, the front corners of the crystal are rounded, or bulletized.

This detector is larger than the detector used for the measurements at KIT. Therefore, incomplete charge collection is a significant part of the energy resolution. To determine the energy resolution, we fit twenty-eight peaks in the unshielded spectrum to gaussians. These peaks were chosen because they pass the requirements listed in Tab. 7.13, as discussed in Section 7.3.3. The twenty-eight peaks include the 1332.5 keV ^{60}Co peak and all peaks listed in bold in Tab. 7.23 and 7.24. Figure 7.24 shows the width of the peaks as a function of energy and the best fit to Eq. 7.2. The parameters from the fit were used to add noise to the simulation. We used the unshielded measurement to determine the simulation

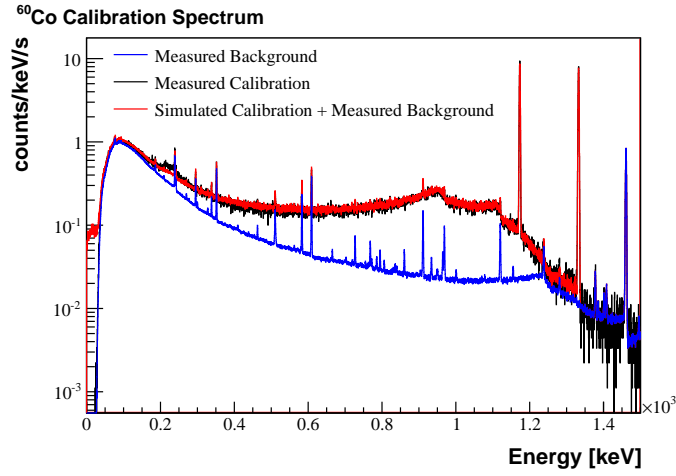


Figure 7.25: ^{60}Co calibration of the UW germanium detector. The region from 1040 keV to 1096 keV, below both peaks, was used to calculate the peak-to-Compton ratio.

resolution, but the resolution is similar in all measurements and should therefore agree with the simulation. In addition to affecting the energy resolution, the charge collection can cause asymmetric peaks. The measurement exhibits asymmetric peaks, which were fit to double gaussians, but the simulation peaks are purely symmetric.

7.3.2 Calibration with ^{60}Co

The relative efficiency and peak-to-Compton ratio were measured for this detector in 1998 by the manufacturer. We repeated the calibration for Detector 1 with a ^{60}Co source, which had an activity of 200 μCurie on May 21, 1968, or 7.40 MBq. On August 10, 2009, the source should have an activity of 32.6 kBq. Following the IEEE standard procedures [103], we placed the source 25 cm from the unshielded detector end cap.

Figure 7.25 shows the measured background, the measured calibration which includes a background, and the simulated ^{60}Co source added to the measured background. The simulation matches the measurement very well. The background is a small fraction of the counts between 1040 keV and 1096 keV, the region used to calculate the peak-to-Compton ratio.

Table 7.18: Relative efficiency and peak-to-Compton ratio for the ORTEC Detector 1 used at UW. The values measured in 1998 and 2009 are compared to the same simulation. The approximate volume of this detector is 211.8 cm^3 .

Measured in 1998			
	Rel. Efficiency	FWHM	Peak/Compton
Measurement	54.9%	2.13 keV	62.0:1
Simulation	54.7%	2.13 keV	63.1:1
Difference	-0.4%	0%	1.7%

Measured in 2009			
	Rel. Efficiency	FWHM	Peak/Compton
Measurement	55.8%	2.62 keV	46.8:1
Simulation	54.7%	2.62 keV	44.8:1
Difference	-2.0%	0%	-4.5%

For comparison to the values measured by the manufacturer in 1998, we calculated the peak-to-Compton ratio and the relative efficiency as described in Section 7.2.2. Our measurement includes a background, so we fit the measurement to a gaussian plus background and Compton edge, as in Eq. 7.15. The same simulation was used for both comparisons, except the background measured in B037 was added for that comparison. Table 7.18 compares the measured values to the simulation. The measurement in 1998 had better energy resolution than the UW measurement. Therefore, the peak-to-Compton ratio measured at UW is lower, since it depends on the peak height, not the peak area. The relative efficiency is consistent with the efficiency measured in 1998. Comparing the relative efficiency to the measurement ensures the simulated detector volume is correct. The peak-to-Compton ratio also depends on the window thickness and energy resolution. These values have not changed since 1998.

In addition to these values, we can compare the simulated and measured spectra in Fig. 7.25. The spectra match well, except the backscattering edge near 212 keV. This edge is caused by large-angle Compton scattering of photons in the material behind the detector

or behind the source. The 1.3 MeV photon scatters through a large angle in some other material, creating an electron of near-maximal energy, 1120 keV. The photon then returns to the detector with only 212 keV of energy. This feature is higher in the measurement, indicating that there is not enough material in the simulation behind either the detector or the source. Otherwise, we are very confident in the simulation geometry.

7.3.3 Environmental Radioactivity Measurements

The environmental radioactivity in B037 may not be the same as in the detector laboratory at KIT, so we determined the intensity of environmental radiation and angular distribution in this laboratory from the measurements. We simulated the same energy spectrum as the KIT detector laboratory, and the continuum in the unshielded measurements match even better in B037 than KIT. Just like the KIT lab, we divided the radiation into three angular regions: photons coming from the beam direction, photons incident on the walls of the KATRIN shield, and photons coming from the readout direction.

In B037, we did not make measurements with an opening in the 15 cm shield dedicated to determining the angular distribution of the radiation. Instead, we estimated how much radiation passes through the beam-side opening by comparing the measurements using the KATRIN shield with and without a stainless steel cover. We assumed the intensity through the readout-side opening is the same as the intensity through the beam-side opening. This method does not determine the intensity through the openings as accurately as the method used in KIT with the 15 cm shield. Finally, we determined the total intensity and the intensity incident on the walls of the KATRIN shield from the unshielded germanium detector measurements.

Intensity Through the KATRIN Shield Openings

We estimated the radiation through the beam side opening by comparing the KATRIN shield measurements with and without the beam-side covered. We simulated the signal, the photons coming from the beam side within 26° of the shield axis, using the `RoomRadiationGun` and the germanium detector enclosed in the KATRIN shield shown in Fig. 7.23b. Since

some photons will still pass through the 3 cm cover, we simulated the shield with and without a stainless steel cover. We calculated the intensity I_O through the beam-side shield opening by taking the difference in rate of the two measurements $R_{\Delta,M}$, and the difference of the simulation peak areas normalized by the number generated and the bin width $R_{\Delta,Sim} = \frac{P_{O,Sim}}{wN_O} - \frac{P_{C,Sim}}{wN_C}$. Note that $R_{\Delta,M}$ is the difference in rate of photons from all directions, but $R_{\Delta,Sim}$ is a difference in rate of photons coming from the beam-direction only. This intensity is modified from Eq. 7.12 to account for photons passing through the thin cover.

$$I_O = \frac{R_{\Delta,M}}{AR_{\Delta,Sim}} \frac{\gamma}{\text{cm}^2\text{s}} (\theta < 26^\circ) \quad (7.20)$$

When calculating the uncertainty on I_O , we considered the uncertainty on the peak areas as determined from the fits. This also depends on the time duration of the measurements, T_O and T_C , and the number generated for each simulation, N_O and N_C . Equation 7.21 shows the total uncertainty on I_O .

$$\frac{\sigma_{I_O}^2}{I_O^2} = \frac{\sigma_{P_{O,M}}^2}{(wT_O R_{\Delta,M})^2} + \frac{\sigma_{P_{C,M}}^2}{(wT_C R_{\Delta,M})^2} + \frac{\sigma_{P_{O,Sim}}^2}{(wN_O R_{\Delta,Sim})^2} + \frac{\sigma_{P_{C,Sim}}^2}{(wN_C R_{\Delta,Sim})^2} \quad (7.21)$$

The peak areas were calculated by fitting the peaks to gaussians. The largest measured peaks have an asymmetric shape due to incomplete charge collection and were difficult to fit with a single gaussian. A common method to account for the asymmetry is to add a skewed gaussian with exponential tail to the main peak. Instead, we fit to double gaussians as in Eq. 7.10. The second, smaller gaussian was not skewed, but we still obtained good fits. We added the areas of the two peaks together to get the total area and used the covariance matrix from the fit to calculate the uncertainty on the total area, as in Eq. 7.11.

Tables 7.19, 7.20 and 7.21 list all the peaks that have been fit in the measurements inside the KATRIN shield. Unlike the KIT measurement with a 15 cm shield, we assume all lines are caused exclusively by the environmental radiation because no neutron peaks are visible. Enough environmental radiation passes through the thin KATRIN shield that neutrons have not yet become a dominant background. The 509 keV peak is an exception, as it is also caused by positron annihilation.

Table 7.19: Intensity of environmental radioactivity through the beam-side shield opening in B037. Peaks in bold were included in the weighted average. We assume the readout direction intensity is the same.

Energy keV	Thorium Peaks	Rate [mHz]		Intensity I_O σ_{I_O}	
		Open	Covered	$10^{-3}\gamma/\text{cm}^2/\text{s}$	
2614.5	^{208}Tl	43.98 ± 0.54	42.95 ± 0.61	5.57	4.43
2104.1	SEP of ^{208}Tl	5.96 ± 0.32	5.42 ± 0.32	32.18	29.86
1630.7	^{228}Ac	1.37 ± 0.20	1.04 ± 0.26	36.89	38.42
1620.5	^{212}Bi	1.74 ± 0.24	1.61 ± 0.36	16.07	55.33
968.8	^{228}Ac	8.26 ± 0.63	6.27 ± 0.50	15.09	6.19
911.2	^{228}Ac	11.59 ± 0.50	10.17 ± 0.54	7.03	3.66
860.4	^{208}Tl	2.36 ± 0.54	1.33 ± 0.40	22.15	14.68
727.3	^{212}Bi	2.58 ± 0.50	1.87 ± 0.51	9.18	9.31
583.1	^{208}Tl	7.75 ± 0.59	4.20 ± 0.47	10.51	2.27
509.3 and 510.9	$^{208}\text{Tl}+\text{annih}$	57.04 ± 0.97	54.32 ± 1.04	20.28	10.74
238.6	^{212}Pb	10.44 ± 0.79	4.67 ± 0.69	8.11	1.58
Weighted Average at UW				8.73	1.16

The requirements to include a peak in the weighted average are listed in Tab. 7.13, the same requirements as for determining I_W from the KIT unshielded measurements. We included all peaks with rate greater than 10σ in the open-shield measurement. The included peaks are listed in bold in Tab. 7.19 and 7.20. In the thorium chain we included six peaks in the average. In the uranium chain we included ten peaks in the average. These are a subset of the peaks used from the KIT unshielded measurements. The 1588.3 keV ^{228}Ac peak and the 1592.5 keV double-escape peak were not fit since they are not separated by more than 1.5 FWHM. Some uranium and thorium peaks are not listed due to low rate.

Figure 7.26 shows the measurement with a cover on the shield subtracted from the measurement without a cover. The measurement of course includes photons from all directions. Also shown is the simulation of photons from the beam direction with a cover subtracted from the simulation of photons from the beam direction without a cover. The difference is larger at low energy in the measurement.

We assume the same intensity of radiation comes through the readout-side opening, but

Table 7.20: Intensity of environmental radioactivity through the beam-side shield opening in B037. Peaks in bold were included in the weighted average. We assume the readout direction intensity is the same.

Energy keV	Uranium Peaks	Rate [mHz]		Intensity I_O $10^{-3}\gamma/\text{cm}^2/\text{s}$	σ_{I_O}
		Open	Covered		
2448.5	^{214}Bi	2.29 ± 0.22	1.72 ± 0.22	155.11	154.13
2204.0	^{214}Bi	6.84 ± 0.30	6.49 ± 0.32	11.88	15.11
1846.9	^{214}Bi	2.46 ± 0.24	2.41 ± 0.25	2.81	21.15
1764.7	^{214}Bi	20.25 ± 0.41	18.94 ± 0.46	10.09	4.82
1729.6	^{214}Bi	3.91 ± 0.26	3.06 ± 0.30	27.57	13.64
1508.9	^{214}Bi	2.78 ± 0.36	1.78 ± 0.23	54.99	28.78
1408.6	^{214}Bi	2.47 ± 0.41	1.95 ± 0.39	22.92	25.46
1378.0	^{214}Bi	4.41 ± 0.39	3.27 ± 0.32	46.89	24.08
1238.4	^{214}Bi	5.50 ± 0.53	6.01 ± 0.53	-7.95	11.69
1120.6	^{214}Bi	10.29 ± 0.49	10.47 ± 0.54	-1.12	4.69
609.2	^{214}Bi	11.75 ± 0.54	6.37 ± 0.52	8.78	1.25
351.9	^{214}Pb	7.63 ± 0.59	1.77 ± 0.54	8.54	1.20
295.2	^{214}Pb	3.52 ± 0.57	0.62 ± 0.26	7.10	1.56
Weighted Average at UW				8.43	0.83

Table 7.21: Intensity of environmental radioactivity through the beam-side shield opening in B037. We assume the readout direction intensity is the same.

Energy keV	Potassium Peak	Rate [mHz]		Intensity I_O $10^{-3}\gamma/\text{cm}^2/\text{s}$	σ_{I_O}
		Open	Covered		
1460.5	^{40}K	205.72 ± 1.15	190.34 ± 1.35	10.08	1.19

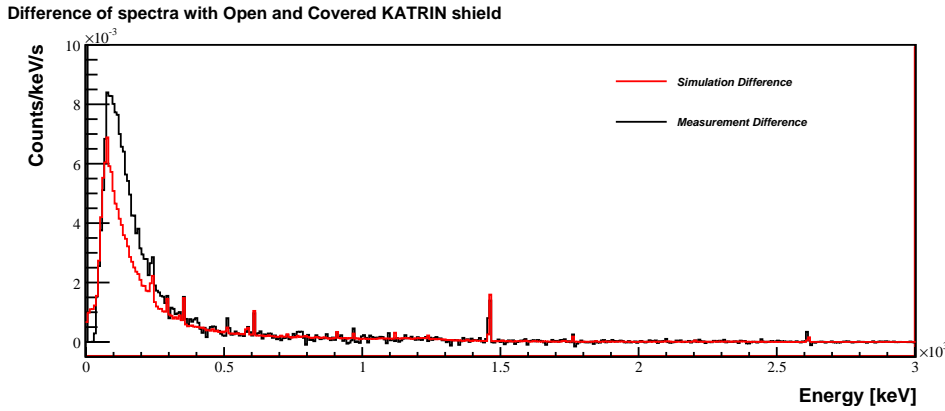


Figure 7.26: Spectra from environmental radiation measured by a germanium detector inside the KATRIN shield with a cover subtracted from the spectra without a cover. The measurement includes photons from all directions, but the simulation only includes photons from the beam direction. The measured difference is larger at low energy than the simulation. The bin width is 7.5 keV.

have not measured it. The intensity through the shield openings in B037 is more than five times higher than at KIT. Table 7.22 compares the intensities in both locations.

Intensity Incident on the Walls of the KATRIN Shield

To determine the intensity incident on the walls of the shield, we used the unshielded germanium detector measurement, which includes radiation coming from all directions. As in Eq. 7.6, the total intensity, as measured with the unshielded germanium detector, is the sum of the intensity through the shield openings measured in the previous section and the intensity incident on the walls of the shield. We simulated the environmental radiation divided into three regions incident upon the unshielded germanium detector shown in Fig. 7.23a. Then we calculated the intensity incident on the walls of the shield from Eq. 7.18.

Tables 7.23, 7.24 and 7.25 list all peaks in the unshielded measurements which have been fit. The requirements to include a peak in the weighted average are listed in Tab. 7.13, the same requirements as for determining I_W from the KIT unshielded measurements. Many peaks have been fit to double gaussians as in Eq. 7.10 because they have an asymmetric

Table 7.22: Intensity of environmental radioactivity through the shield openings ($\theta < 26^\circ$) in B037 compared to KIT. In B037, we measure the beam-direction intensity and assume the readout direction is the same. At KIT, both directions were measured to be the same.

Source	B037 I_O $10^{-3}\gamma/\text{cm}^2/\text{s}$	KIT I_O $10^{-3}\gamma/\text{cm}^2/\text{s}$	Increase
^{232}Th	8.73 ± 1.16	1.37 ± 0.19	537%
^{238}U	8.43 ± 0.83	1.53 ± 0.14	451%
^{40}K	10.08 ± 1.19	0.64 ± 0.06	1475%

shape due to incomplete charge collection. The areas of the two peaks were added together and the uncertainty came from the covariance matrix, as in Eq. 7.11.

In the thorium chain, the weighted average intensity excludes the annihilation peak at 509 keV. The 1588.3 keV ^{228}Ac peak and the 1592.5 keV double-escape peak were not fit and are not listed in Tab. 7.23 since they are closer than 1.5 FWHM. The 238.6 keV ^{212}Pb peak was also excluded due to a low p-value. Therefore, other than the two closely spaced peaks, we took weighted averages over the exact same peaks as in the detector laboratory at KIT measurements. Figure 7.27 shows the intensity calculated for each peak as a function of energy. Again, a lower intensity is preferred at lower energy.

In the uranium chain, we excluded the 351 keV ^{214}Pb and 186 keV ^{226}Ra peaks due to the low p-value and low energy. The weighted average is taken over the same fourteen peaks as the KIT measurements, which are all late in the chain. Again, ^{226}Ra is the only early-chain peak which has been fit since the 1.001 MeV ^{234m}Pa peak has a very low rate. Just like the KIT measurements, the intensity calculated from ^{226}Ra is higher than the other late-chain peaks. Fig. 7.27 shows the intensity as a function of energy with the same trend toward lower intensity at lower energy.

The 1.4 MeV ^{40}K peak was successfully fit and is used to calculate the potassium intensity.

Table 7.26 compares the B037 intensity incident on the walls of the shield to the KIT intensity. The total intensity in B037 is $1.10 \gamma/\text{cm}^2/\text{s}$, 30% higher than at KIT, where the

Table 7.23: Intensity of thorium incident on the walls of the shield in the B037 commissioning laboratory. Peaks in bold were included in the weighted average.

Energy keV	Thorium Peaks	Rate mHz	p-value	Intensity I_W $\gamma/\text{cm}^2/\text{s}$	σ_{I_W}
2614.5	^{208}Tl	324.5 ± 2.0	0.03	0.420	0.009
2104.1	SEP of ^{208}Tl	44.9 ± 1.1	0.93	0.425	0.026
1630.7	^{228}Ac	14.0 ± 0.8	0.89	0.376	0.058
1620.5	^{212}Bi	12.9 ± 1.0	0.24	0.369	0.065
968.8	^{228}Ac	170.6 ± 2.1	0.20	0.337	0.010
911.2	^{228}Ac	275.2 ± 2.4	0.05	0.322	0.008
860.4	^{208}Tl	48.4 ± 1.6	0.05	0.307	0.019
795.0	^{228}Ac	45.4 ± 1.7	0.80	0.345	0.024
727.3	^{212}Bi	81.1 ± 1.9	0.16	0.306	0.014
583.1	^{208}Tl	351.1 ± 2.8	0.14	0.313	0.007
509.3 and 510.9	$^{208}\text{Tl}+\text{annih}$	221.9 ± 3.2	0.00	0.504	0.016
463.3	^{228}Ac	51.8 ± 2.2	0.56	0.287	0.022
338.7	^{228}Ac	142.7 ± 3.0	0.10	0.298	0.012
238.6	^{212}Pb	610.1 ± 4.8	0.01	0.246	0.006
Weighted Average at UW				0.335	0.004

Table 7.24: Intensity of uranium incident on the walls of the shield in the B037 commissioning laboratory. Peaks in bold were included in the weighted average.

Energy keV	Uranium Peaks	Rate mHz	p-value	Intensity I_W $\gamma/\text{cm}^2/\text{s}$	σ_{I_W}
2448.5	^{214}Bi	17.8 ± 0.8	0.08	0.427	0.037
2204.0	^{214}Bi	59.5 ± 1.0	0.29	0.374	0.016
1846.9	^{214}Bi	24.7 ± 0.8	0.11	0.390	0.031
1764.7	^{214}Bi	197.5 ± 1.7	0.78	0.392	0.010
1729.6	^{214}Bi	35.5 ± 0.9	0.04	0.355	0.021
1508.9	^{214}Bi	25.3 ± 1.0	0.01	0.394	0.038
1408.6	^{214}Bi	32.6 ± 1.2	0.69	0.458	0.040
1378.0	^{214}Bi	51.4 ± 1.2	0.33	0.369	0.021
1238.4	^{214}Bi	83.4 ± 1.9	0.37	0.415	0.019
1155.2	^{214}Bi	23.3 ± 1.6	0.46	0.408	0.047
1120.6	^{214}Bi	199.3 ± 2.2	0.90	0.352	0.009
766.6 and 768.4	$^{214}\text{Bi} + ^{234m}\text{Pa}$	63.4 ± 1.9	0.39	0.292	0.016
609.2	^{214}Bi	653.0 ± 3.3	0.01	0.309	0.005
351.9	^{214}Pb	586.8 ± 3.7	0.00	0.275	0.005
295.2	^{214}Pb	301.8 ± 3.7	0.53	0.248	0.006
186.1	$^{226}\text{Ra} + ^{235}\text{U}$	130.9 ± 4.8	0.93	0.525	0.043
Weighted Average at UW				0.317	0.003

Table 7.25: Intensity of potassium incident on the walls of the shield in the B037 commissioning laboratory.

Energy keV	Potassium Peak	Rate mHz	p-value	Intensity I_W $\gamma/\text{cm}^2/\text{s}$	σ_{I_W}
1460.8	^{40}K	2377.1 ± 5.4	0.01	0.398	0.005

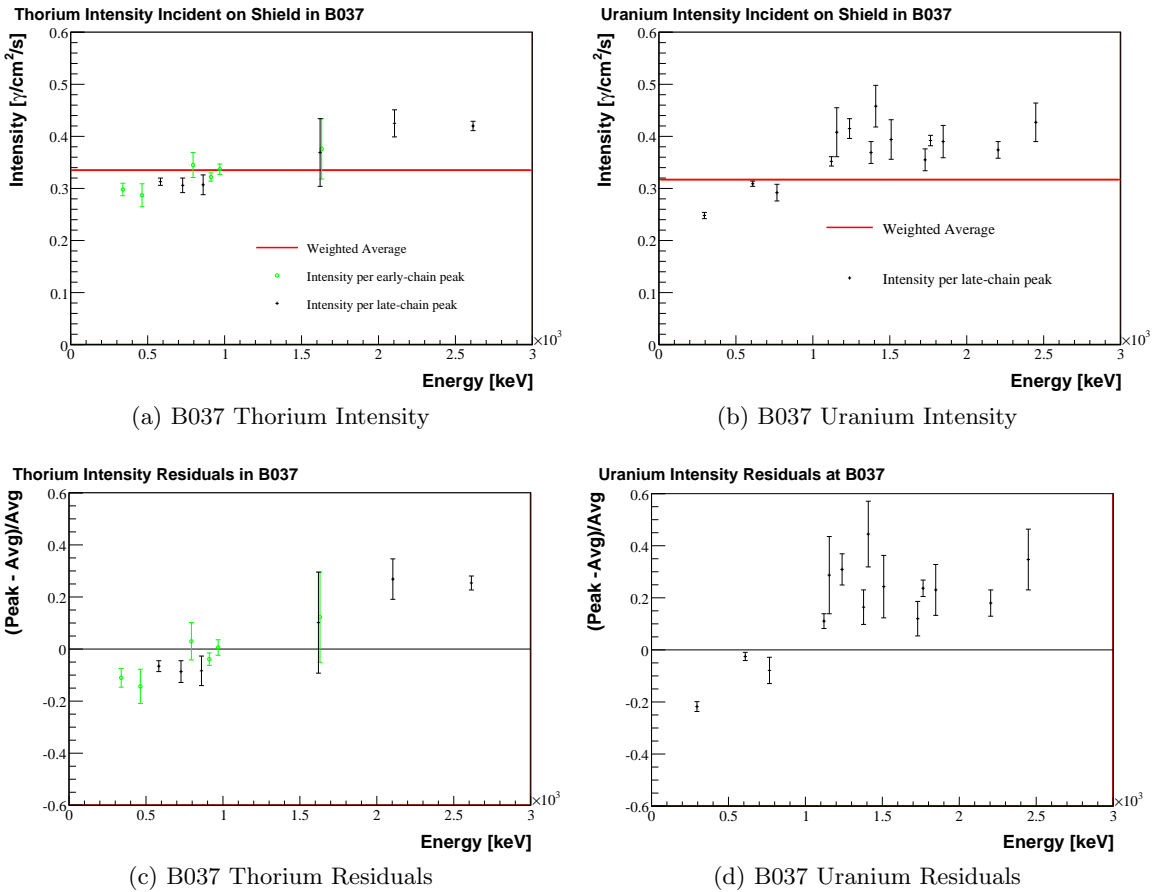


Figure 7.27: Intensity of radiation incident on the walls of the shield in B037 determined by fitting each peak in the uranium and thorium chains in the unshielded germanium detector spectrum. There is a trend toward lower intensity at lower energy. The uncertainties shown are the statistical uncertainties listed in Tab. 7.23, 7.24 and 7.25. The bottom plots are the residuals.

Table 7.26: Intensity of environmental radioactivity incident on the walls of the shield ($\theta > 26^\circ$) determined from measurements in B037 compared to the intensity measured at KIT.

Source	B037 I_W $\gamma/\text{cm}^2/\text{s}$	KIT I_W $\gamma/\text{cm}^2/\text{s}$	Increase
^{232}Th	0.335 ± 0.004	0.335 ± 0.003	0.0%
^{238}U	0.317 ± 0.003	0.252 ± 0.002	25.8%
^{40}K	0.398 ± 0.005	0.266 ± 0.002	49.6%

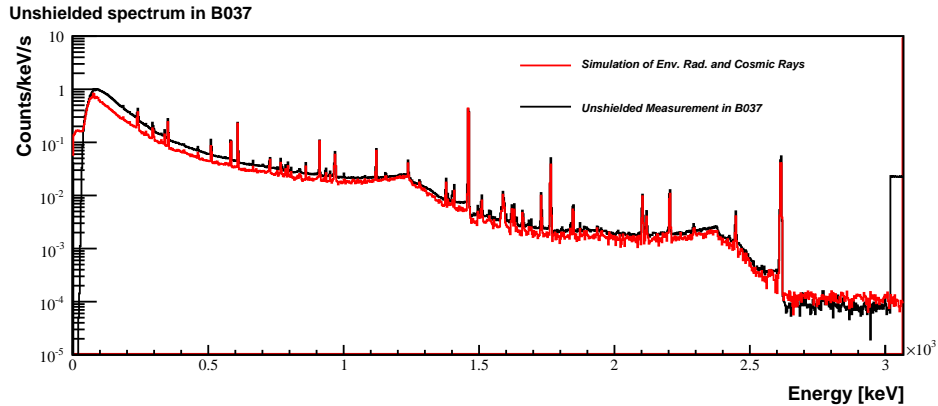


Figure 7.28: Unshielded background measurement in B037. The bin width is 3 keV. The agreement is within 41% at all energies.

total intensity is $0.860 \gamma/\text{cm}^2/\text{s}$. If the KIT thorium intensity is calculated from the exact same peaks as B037—excluding the 1588 keV, and 1592 keV peaks—the KIT intensity does not change from the values listed in Tab. 7.26.

Figure 7.28 shows the measured unshielded spectra compared with the simulation including cosmic-ray muons and photons. Essentially all of the spectrum, 99.5%, is from environmental radiation. The cosmic rays are visible above 2.6 MeV. Just like the KIT comparison, when the peak areas match, the simulation low-energy continuum is underestimated.

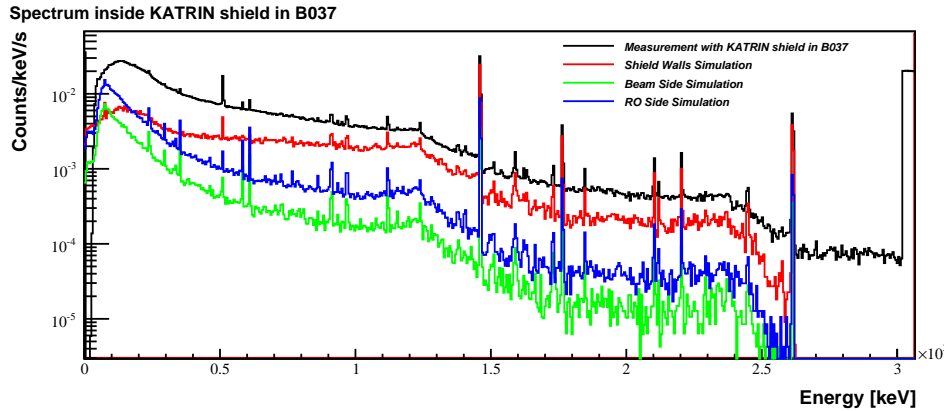


Figure 7.29: Contributions to the spectra inside the KATRIN shield. At high energy, the largest contribution is from photons incident on the shield walls. At low energy, the largest contribution is from the readout direction.

7.3.4 Comparison Inside the KATRIN Shield

After characterizing the radiation in the B037 lab, we can simulate the germanium detector enclosed in the KATRIN shield without any free parameters and compare it to the measured spectrum. The KATRIN shield reduces the measured rate by a factor of sixteen by blocking radiation incident on the shield walls. Therefore, the radiation through the shield openings and cosmic rays become a significant part of the spectrum.

Using the intensity of radiation determined in B037, we simulated the germanium detector enclosed by the KATRIN shield. Figure 7.29 shows the contribution to the simulated spectrum inside the shield from each angular region. The germanium detector was positioned closer to the readout side shield opening, making the detector even more sensitive to radiation coming from the readout direction. The largest contribution at low energy comes from the readout direction. We measured the intensity from the beam direction and assumed the intensity from the readout direction is the same, but that assumption may not be correct.

Adding all angular contributions together, we obtain a full simulation of the environmental radiation. Figure 7.30 compares the measured spectrum and the simulated environmental radiation without cosmic rays. Unlike the unshielded measurements, cosmic rays

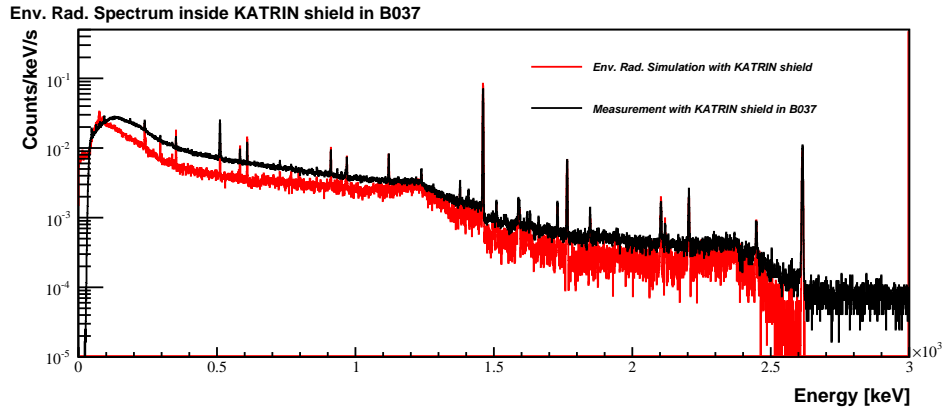


Figure 7.30: Simulated environmental radiation compared to the spectra measured with a germanium detector inside the KATRIN shield. The simulation does not include cosmic rays. The bin width is 0.75 keV.

are a significant part of the spectra.

We simulated cosmic-ray photons and muons incident on the germanium detector enclosed by the KATRIN shield. This is compared to the difference between the measurements and the environmental radiation simulation in Fig. 7.31. The negative peaks in the difference indicate the environmental radiation simulation is higher than the measurement. The simulated cosmic rays are higher than the difference in measured and simulated environmental radiation above 1 MeV, and lower under 1 MeV. Since this laboratory is in a basement, the actual intensity of cosmic rays may be lower than the intensity we used for the simulation. Cosmic rays account for much of the difference in Fig. 7.31, but the simulated spectrum may be too large.

Figure 7.32 shows the combined simulation including cosmic-ray muons, cosmic-ray photons, and environmental radiation inside the KATRIN shield compared with the measurement. Roughly one quarter of the simulated rate is from cosmic rays, and three-quarters of the simulated rate is from the environmental radiation. The combined simulation is larger than the measurement above 2 MeV, possibly because of an overestimation of the cosmic rays in the simulation. The combined simulation is larger than the measurement below 100 keV as well, possibly because the radiation coming through the shield openings is not

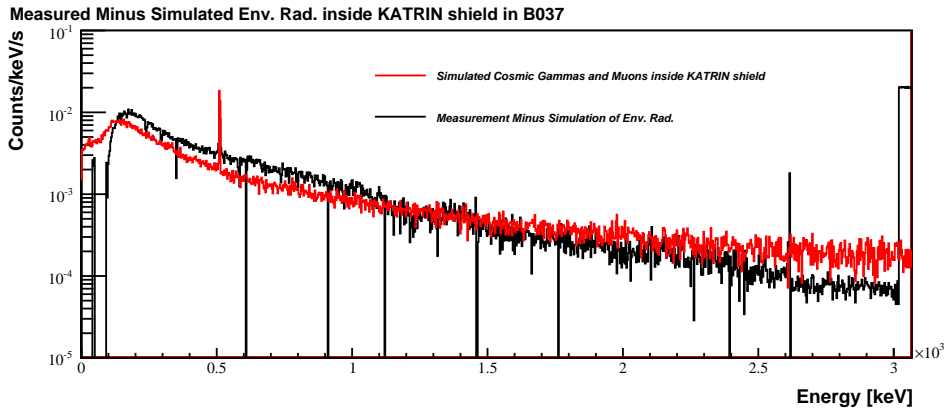


Figure 7.31: Comparison between the simulated cosmic-ray photon and muon spectrum in the germanium detector and the difference between the total measurement and simulated environmental radiation. The negative peaks indicate the simulated environmental radiation is large than the measurement. Cosmic rays account for much of the difference, but appear to be overestimated above 1 MeV.

well-determined. In between 100 keV and 2 MeV, the simulated rate is smaller than the measurement, but the shape of the spectra match well.

7.3.5 Effect of the Angular Distribution Inside the KATRIN Shield

The method we used to simulate the environmental radiation, described in Section 6.2.1, is the same method used for cosmic rays. Cosmic rays have a preferred direction since their momenta are distributed as $\cos^2\theta$, where θ is the zenith angle. Therefore, we simulate cosmic rays passing through a plane perpendicular to the zenith, and normalize the simulation to the cosmic-ray intensity through this plane. Most cosmic rays have a small zenith angle and are normal to this plane. In contrast, the exact angular distribution of the environmental radiation is unknown. We approximate it as isotropic in three regions, and simulate the measured intensity through a plane. A smaller amount of radiation comes through the shield openings, but, unlike cosmic rays, the radiation does not preferentially pass downward through this plane.

To investigate whether this method affects the results of the simulation, we also simu-

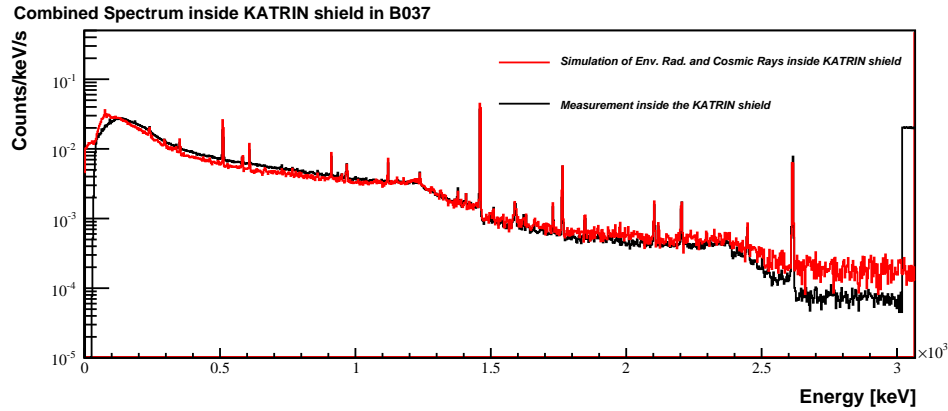


Figure 7.32: Combined simulation of cosmic-ray muons, photons, and environmental radiation compared with measurements using a germanium detector inside the KATRIN shield. The bin width is 3 keV.

late the environmental radiation with an alternate method. Instead of choosing positions randomly on a plane 60 cm in length and 60 cm in width and shooting the radiation toward this plane, we choose positions homogeneously in a spherical volume of radius 30 cm and shoot the radiation toward this volume. In both cases, the photons start with initial positions on a sphere of radius 100 cm; the choice of plane versus sphere just changes the angular distribution slightly. In the case of the sphere, there is no preferred direction. Both simulations are divided into two angular regions; photons coming within 26° of the shield axis, and photons which must pass through the shield walls.

This alternate angular distribution is simulated in the unshielded germanium detector in B037, the germanium detector inside the KATRIN shield, and the silicon detector inside the KATRIN shield. To normalize the alternate simulation, we integrate the rate in the unshielded germanium detector above 500 keV and match it to the original simulation for the radiation incident on the shield walls and through the shield openings. With this normalization, the spectra from the two simulations are indistinguishable; the total rate in the unshielded germanium detector from both simulations is within 2%. For better accuracy, the alternate simulation normalization should be determined with the same method as the original simulation; the radiation through the shield openings should be determined by the

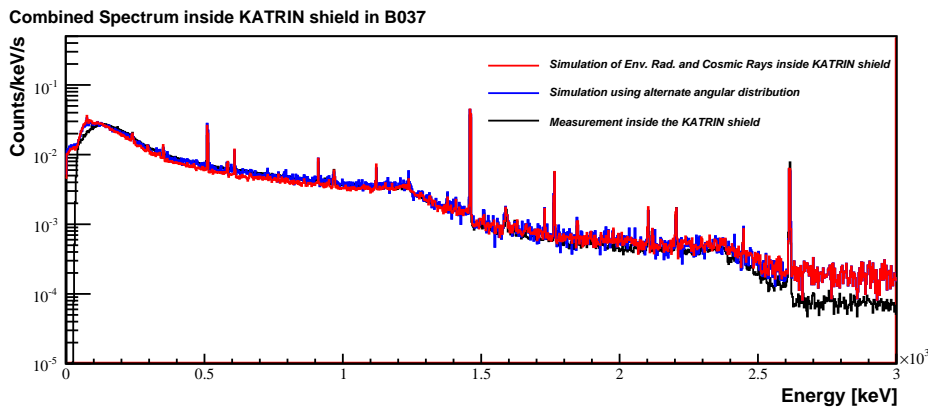


Figure 7.33: An alternate angular distribution increases the simulated rate of cosmic-ray muons, photons, and environmental radiation in the germanium detector inside the KATRIN shield by 7.8%. Both simulations are within 5% of the measurement.

difference in the open- and covered-shield measurements and simulations. The radiation incident on the shield walls should be normalized by the peak areas in the unshielded measurement. Although the spectra from the two simulations appear to match well, without fitting peaks in the alternate simulation we cannot compare the variance in the intensity per peak as in Fig 7.27. The angular distribution may affect this agreement.

Assuming the normalization is correct, we simulate the germanium detector surrounded by the KATRIN shield. With the shield in place, the detector is more sensitive to which directions the radiation is coming from. The two different simulations including cosmic rays are shown with the measurement in Fig. 7.33. The alternate simulation is 7.8% higher than the original simulation, with an increase of 29% through the shield walls and a decrease of 15% through the shield openings. Both simulations match the measurement well; the alternate simulation, including cosmic rays, has an integral rate above 40 keV 4.7% higher than the measurement, and the original simulation, including cosmic rays, has an integral rate above 40 keV 3.6% lower than the measurement.

The KATRIN silicon detector has a different detection efficiency and a different angular response than the germanium detector. The position of the silicon detector within the KATRIN shield is farther from the readout opening than the germanium detector. Therefore,

the effect in the silicon detector from the alternate angular distribution may be different than the effect in the germanium detector. We simulate the silicon detector with the alternate method. This simulation gives a rate 20% higher through the shield walls and 5% lower through the shield openings, similar to the changes in rate in the germanium detector.

Clearly, the angular distribution can have an effect on the simulated spectra in the germanium and silicon detectors. The direction the radiation comes from depends on where the radioactivity is located with respect to the detector. Both simulations are an approximation, but since the alternate simulation has no preferred direction, we take this as the more correct method. Therefore, we apply a correction of +30% to the intensity incident on the shield walls, and -15% to the intensity through the shield openings based on the change in the germanium detector rate inside the KATRIN shield. The correction is applied for environmental radiation in B037 as well as in KIT.

7.3.6 *Comparison of Cosmic Rays*

The intensity of cosmic rays also depends on location. For example, preliminary tests at UW conducted in a CENPA laboratory observed higher rates in a scintillator veto than in the B037 laboratory. Moving the scintillator veto from CENPA to B037 reduced the rate from 112 Hz to 81 Hz. This reduction is most likely due to the attenuation of cosmic-ray muons or photons by the overburden. The secondary-neutron-related backgrounds are also lower in the B037 laboratory. This reduction is evident in spectra measured with a germanium detector inside a 15 cm shield. Figure 7.34 shows the spectra measured in CENPA, B037 and KIT normalized by the detector volumes. The B037 measurements were taken with Ortec Detector 2. The CENPA measurements were taken by A. Schubert with Ortec Detector 1. The KIT measurements were taken with the smaller Canberra detector. The neutron peaks are smallest in B037. In the KIT data, the source of the peaks under 80 keV has not been identified, but most likely they originate in the shield or the detector cryostat or electronics because of the low energy.

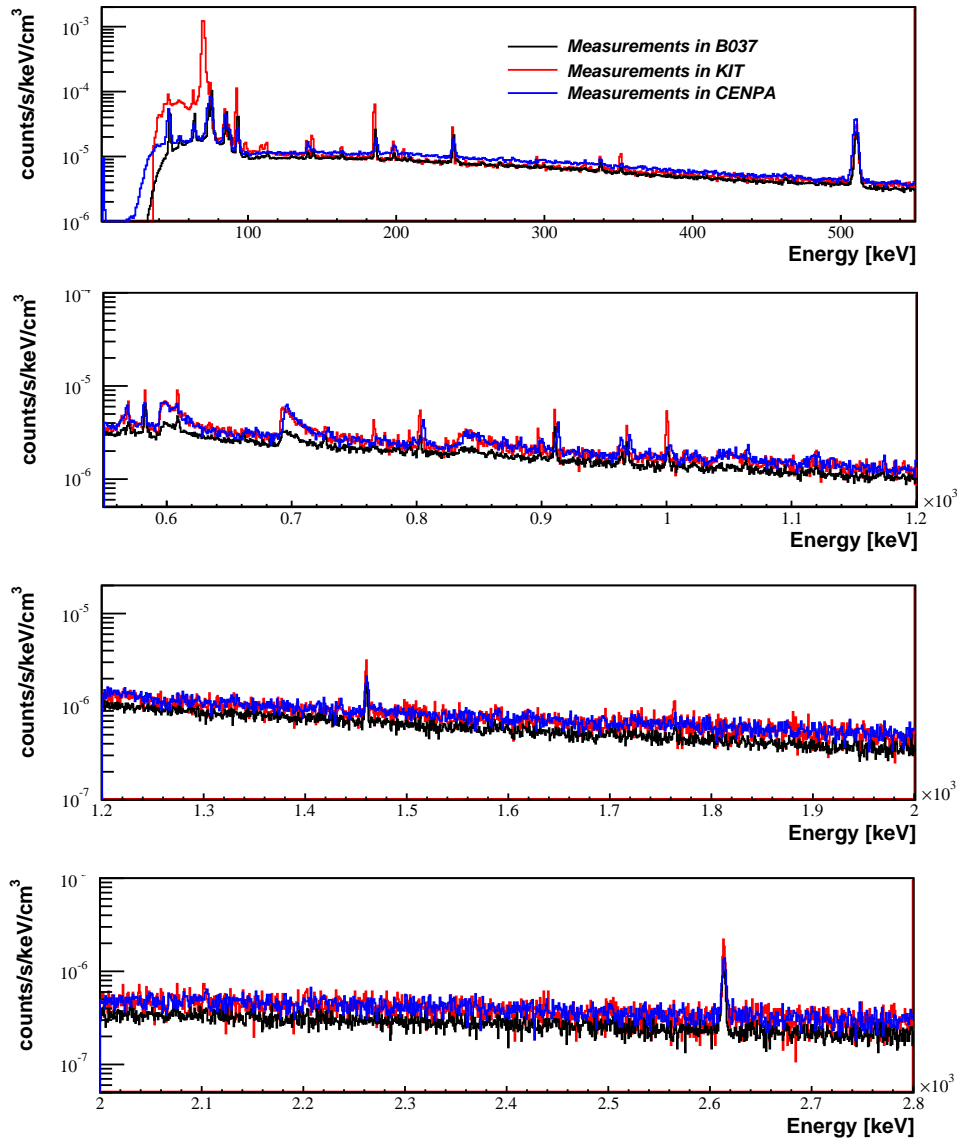


Figure 7.34: Comparison of the 15 cm-shield background measurements in B037 and KIT. Clearly, the neutron peaks are smallest in B037.

7.3.7 Summary of the UW Environmental Radiation Measurements

In summary, we have characterized the environmental radiation in the UW commissioning laboratory. Just like the KIT measurements, we calibrated the detector with a ^{60}Co source, ensuring that the simulation geometry is correct. The same initial energy spectrum as the KIT environmental radiation agrees with the measurements. Unlike KIT, the angular distribution was measured by placing a stainless steel cover on the beam side opening of the KATRIN shield and comparing the spectrum measured without a cover. We then assumed the same intensity through the readout opening. Therefore, the angular distribution in the B037 laboratory has not been determined as well as at KIT.

The detector and the radiation in B037 are different than in KIT. The detector used for the B037 measurements is 69% larger than the KIT detector. The total intensity in the B037 laboratory is 30% higher than in KIT, and more than six times more radiation comes through the shield openings. In particular, the potassium intensity increased the most for all directions.

We estimated the systematic uncertainty on the B037 environmental radiation intensity incident on the walls of the shield using the same method as KIT: by calculating the variance of the intensity incident on the walls of the shield for each peak in the uranium and thorium chains, shown in Fig. 7.27. The variance is 20%, slightly larger than the systematic uncertainty in KIT.

To test the agreement of the total environmental radiation simulation, we compared the unshielded germanium detector measurements and simulation, as shown in Fig. 7.28. The simulation rate is 21.0% lower than the measurement between 500 keV and 2.7 MeV and 40.9% lower than the measurement between the threshold of 40 keV and 2.7 MeV. This is in better agreement than at KIT and comparable to the 20% systematic uncertainty for B037.

To test the agreement of the radiation through the shield openings, we compared the germanium spectrum enclosed in the KATRIN shield minus the germanium spectrum enclosed in the KATRIN shield with the beam-side opening covered with a stainless steel cover to the simulation. This difference is plotted in Fig. 7.26. The integral difference between 500 keV and 2.7 MeV in the simulation is within 1% of the integral difference in the measurement.

Between 40 keV and 2.7 MeV, the integral difference in the simulation is 33% lower than the measurement. Therefore, the systematic uncertainty on the intensity through the shield openings is 33%. Again, this is better agreement than at KIT, although the method used at KIT should be more accurate.

In addition, at B037 we measured the background in a germanium detector inside the KATRIN shield. The simulation of environmental radiation and cosmic-ray muons and photons agrees well with the measurement, as shown in Fig. 7.32. The integral simulation rate of cosmic rays combined with environmental radiation is 4% lower than the measurement between 500 keV and 2.7 MeV. Between 40 keV and 2.7 MeV, the integral simulation rate is 3% lower than the measurement. We found the results of this simulation depend on the method we use to generate the radiation, as shown in Fig 7.33. Therefore, we apply a correction of +30% to the radiation incident on the shield walls, and a correction of -15% to the radiation through the shield openings.

Overall, the simulation of environmental radiation in B037 in a germanium detector agrees with measurements better than the simulation at KIT. As expected, the agreement between simulation and measurement improves when the detector is enclosed by the KATRIN shield.

7.4 Summary of the Validation

In this section we have extensively validated the KATRIN background simulations. The response of the silicon detector to calibration photons above 40 keV is within 7% of the measurement. The total rate of simulated cosmic-ray muons is 30% higher than the measurements, larger than the projected 10% systematic uncertainty listed in Section 6.2.1, but we maintain this is a conservative estimate. The silicon detector response to higher-energy photons has not been measured. This is likely a large contribution to the background, and should be investigated.

A measurement program using germanium detectors was undertaken to characterize the detector laboratory at KIT and the commissioning laboratory at UW. The germanium detector was calibrated in B037 with a ^{60}Co source, and the measured spectrum is within 5% of the calibration simulation, indicating the germanium detector simulation is accurate.

The intensity of the environmental radiation measured in both labs is used to estimate the background in the KATRIN detector. The variance of the intensity calculated per peak is 15% at KIT and 20% at B037, which we use as the systematic uncertainty on the intensity incident on the shield walls for each location. The discrepancy in the simulations versus open- minus closed-shield measurements is 126% at KIT and 33% at B037, which is the systematic uncertainty of the intensity through the shield openings in both locations. The unshielded germanium-detector measurements at KIT match the simulation within 30% above 500 keV, with most of the discrepancy at low energy. The KATRIN shield should block some of the low-energy photons, and we expect better agreement within the shield. The spectra measured by a germanium detector inside the KATRIN shield in the UW commissioning laboratory is within 5% of the simulation including environmental radiation and cosmic rays. Although the angular distribution of the environmental radiation in this laboratory is not well known, and the cosmic-ray spectrum has not been corrected for overburden, this is very good agreement.

The measurements confirm the results of the simulation. In the next section, we present predictions of the background rates in the KATRIN detector.

Chapter 8

**BACKGROUND ESTIMATES AND OPTIMIZATION OF THE
DETECTOR DESIGN**

Now that we have validated the KATRIN background model, we use it to estimate the background under the KATRIN signal. Each source is simulated separately to understand the individual background mechanisms. We investigate the dependence of the background on magnetic field and post-acceleration with the aim of achieving the greatest reduction. We optimize the veto and shield and identify which components contribute radioactivity backgrounds.

The electrons that emerge from the spectrometer have energies near the beta-decay endpoint. As discussed in Section 5.1, shifting the signal to a higher energy may improve the detection efficiency and lower the background. The detector design includes a post-acceleration electrode that can be elevated to +30 kV. We do not simulate these electric fields, but we evaluate the background rates in the region 15 to 50 keV.

Another tunable experimental parameter is the magnetic field. The area of the flux tube at the detector is determined by the magnitude of the magnetic field because the magnetic flux is conserved. The nominal field at the detector is 3.3 T, but can be raised to 5.0 T, decreasing the beam size and the number of radial pixels needed on the detector. If most background counts are uncharged particles, this will improve the signal to background ratio. The simulation assumes a constant 3 T magnetic field. First, we calculate the background in all twelve rings of the detector at 3 T. Then, based on the background mechanisms, we estimate the effect of a higher magnetic field after the simulation by calculating the background rate in the eight inner rings of the detector.

Because of these possible dependencies, when investigating the nature of KATRIN's backgrounds, these questions should be answered:

- What is the background shape between 15–50 keV? Are there X-ray lines to avoid or

an optimized point where the post-acceleration should shift the signal?

- How does a higher magnetic field affect the background rate?
- Does the scintillator cover an adequate solid angle and have a high enough efficiency?
- How thick must the passive shield be?
- What activities are allowed for the detector components?

8.1 Background Contributions From Each Source

We investigate the backgrounds in four regions of interest (ROI) with four different post-acceleration settings, 0 kV, 10 kV, 20 kV, and the maximum of 30 kV. The ROI must be wide enough to allow 90% detection efficiency of the signal electrons. Table 8.1 lists the ROI widths for a 3 T magnetic field as determined by P. Renschler using version 1.2 of KATRIN Electron Scattering in Silicon (KESS) [105]. The width of the ROI assuming no post-acceleration is 4.1 keV, much wider than the 2.4 keV width assumed in the Figure of Merit in Section 4.3.3. Post-acceleration decreases the width of the ROI because the differential energy loss in the dead layer decreases with energy. Also, post-acceleration decreases the angle of incidence of the electron and the probability of backscattering.

The KESS simulation assumes all backscattered electrons are reflected by the pinch magnet or main spectrometer and return within the same detector count. Therefore, backscattered electrons have a larger energy loss by passing through the dead layer multiple times, but 100% return to the detector. Dedicated tracking simulations are necessary to improve our estimate of the probability of detecting the reflected electrons within the same detector count.

Each source is simulated separately. We calculated the statistical uncertainty on each source from the number of events in the region of interest. Other uncertainties are discussed in Section 8.3. Some sources create small rates in the silicon detector; therefore, we generate only enough events to limit a single-source background to less than 5% of the goal, or 50 μ Hz. If there are 10 counts or less in the ROI, a 90% CL upper limit assuming Poisson statistics

Table 8.1: Regions of interest at 3 T assuming 600 eV FWHM noise, 110 nm deadlayer, and all backscattered electrons are reflected within the same count. The minimum field at the detector is slightly higher, 3.3 T, which will increase the maximum angle slightly.

Signal Energy keV	Post-Acceleration kV	Max Angle	ROI keV	ΔE keV
18.6	0	45°	15.58–19.68	4.10
28.6	10	34°	26.90–29.67	2.77
38.6	20	29°	37.42–39.81	2.39
48.6	30	25°	47.69–49.70	2.01

is listed in the tables. For higher-rate sources, the tables list central values and statistical uncertainties. We aim for a total statistical uncertainty of less than 10%. Therefore, once the statistical uncertainty on an individual source is less than 50 μ Hz, it will not make an appreciable contribution to the total statistical uncertainty.

8.1.1 Cosmic Rays

Cosmic rays are the highest-energy source of background that create counts in our low-energy region of interest. Since all cosmic rays originate outside the detector system, the cosmic-ray veto can tag coincidences between the plastic scintillator and the silicon detector.

The goal of the scintillator veto is better than 90% efficiency for cosmic-ray muons. Due to the simplistic scintillator response in the simulation, correcting for the scintillator efficiency is necessary. The loss of efficiency is due to loss of light as the photons enter the fiber optics, are transported by the fiber optics, and as the optics are coupled to the SiPMs. The efficiency loss may also depend on the veto threshold. We approximate the threshold as 1.2 MeV in the scintillator. In addition to applying this threshold cut, we assume only 90% of events tagged by the scintillator are removed with the veto cut. We investigate two scintillator veto cuts; we remove silicon-detector counts that are in coincidence with *two* scintillator-panel counts and in coincidence with a *single* scintillator-panel count. Correcting for the efficiency, 19% of the counts removed with the two-panel veto and 10% of the counts removed with the single-panel veto remain in our region of interest.

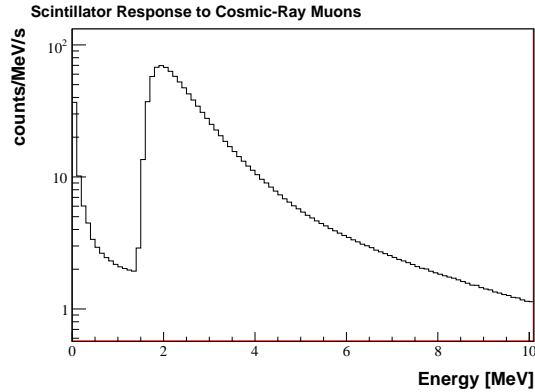


Figure 8.1: Energy depositions in the five scintillator sections with cosmic-ray muons incident. Counts above 1.2 MeV will be tagged to veto silicon-detector counts within $1 \mu\text{s}$.

Also, since the KATRIN detector is pixelated, we veto counts that are coincident in multiple silicon-detector pixels. If more than 15 keV is deposited in two silicon-detector pixels within 100 ns, both counts are removed. This low-energy limit is conservative; the detector threshold may be as low as 5 keV.

Cosmic-ray muons, photons, neutrons, and nucleons are investigated. We first discuss cosmic-ray muons and photons and the effect of various veto cuts. Cosmic neutrons and nucleons will not be removed with the veto, but need a correction for the pulse-height defect as described in Section 6.1.1. The neutrons and nucleons are discussed at the end of the section.

Cosmic-Ray Muons

Cosmic-ray muons are abundant, high-energy, and interact with high probability. Therefore, they create the largest cosmic-ray background but are easily tagged with a scintillator. Figure 8.1 shows the sum of the spectra produced by cosmic-ray muons in the five scintillator panels. The broad bump above 1.2 MeV is caused by muons passing through the 1 cm scintillator panels. Muons that deposit more than 1.2 MeV of energy in one or two panels of the scintillator within $1 \mu\text{s}$ of a detector count are tagged and removed. Figure 8.2 shows the background spectra in the silicon detector before and after the most aggressive cut, the

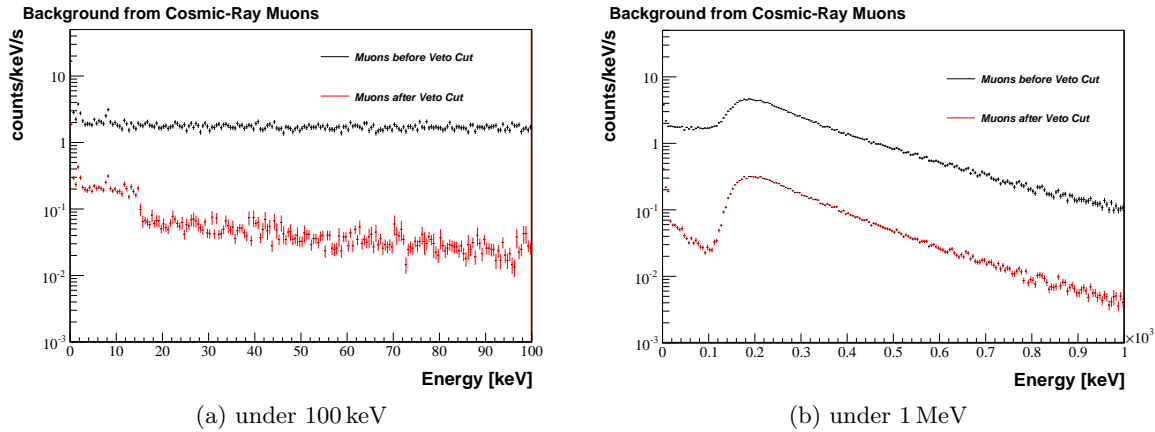


Figure 8.2: Background spectra in the silicon detector from cosmic-ray muons before and after a 90% efficiency veto cut. This veto cut requires that a single scintillator panel or multiple detector pixels are hit. In the spectrum after a veto cut, the drop in the rate at 15 keV is due to the threshold of the multi-pixel silicon detector cut.

90% efficiency single-panel and multi-pixel veto cut.

The cosmic-muon-induced background spectrum in the silicon detector has two distinct energy regions. The most dominant feature is a broad bump above 100 keV. This is caused by high-energy muons passing completely through a silicon-detector pixel and depositing a fraction of their total energy. The position of this minimum-ionizing-particle bump depends on the path length of the particle in the detector and therefore the detector thickness. The second region includes the range of energies that the KATRIN signal can reach with post-acceleration, 15 keV to 50 keV. Two background mechanisms dominate this region: a small fraction of the muons hit multiple detector pixels and share energy depositions between pixels, ending up in our region of interest; also, high-energy photons—produced after muons interact in the surrounding materials—Compton scatter in the detector.

The muons are very effectively tagged by the veto; the two-panel veto cut tags 96% of counts at all energies, reduced down to 77.8% of counts when corrected for the 90% efficiency. Figure 8.3 shows the spectra using other veto cuts. The multi-pixel veto cut removes counts coincident in multiple silicon-detector pixels. Using the multi-pixel cut, we

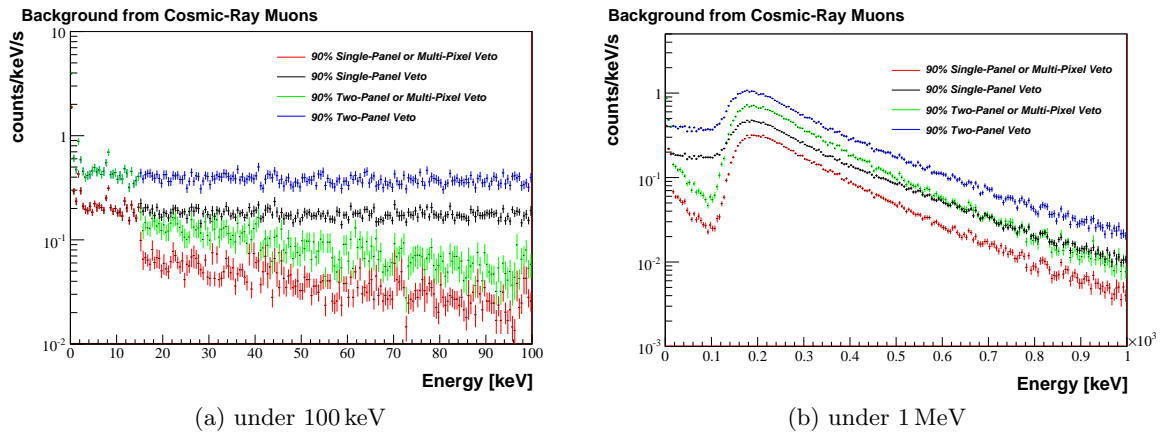


Figure 8.3: Various veto cuts reduce the background in the silicon detector from cosmic-ray muons. The lowest rates are achieved with the multi-pixel cut.

achieve the lowest rates between 15 keV and 50 keV.

Table 8.13 shows the background rates for various veto cuts. Combining the two-panel veto, multi-pixel cut and post-acceleration, the cosmic-muon background is reduced to an acceptable level. Further reductions occur with a single-panel veto. The counts remaining after the veto cuts are mostly photons or muons depositing less than the typical energy for a minimum-ionizing particle. Although muons are charged particles, their energy is large enough that an increase in the magnetic field will not affect the background spectrum from cosmic-ray muons.

Cosmic-Ray Photons

Cosmic-ray photons are lower-energy but more abundant than cosmic-ray muons. The photons are not as effectively detected by either the plastic scintillator or the silicon detector. The photons do interact and deposit energy in the scintillator, but the probability of a photon interacting in both the scintillator and the detector is smaller than for muons. Figure 8.4 shows the energy depositions in the scintillator. A small bump is visible above 1.2 MeV, caused by minimum-ionizing particles, most likely pair-produced electrons. Since there are many more counts below 1.2 MeV, the amount of photons removed with the veto

Table 8.2: The effect of various veto cuts on the background rates from cosmic-ray muons assuming 90% veto efficiency. The uncertainties are purely statistical.

Source	18.6 keV	28.6 keV	38.6 keV	48.6 keV
Cosmic-Ray Muons	mHz	mHz	mHz	mHz
Before Veto	7.604 ± 0.207	4.893 ± 0.166	4.176 ± 0.153	3.215 ± 0.134
90% Two-Panel Veto	1.708 ± 0.057	1.048 ± 0.042	0.939 ± 0.043	0.679 ± 0.033
90% Two-Panel and Multi-Pixel Veto	0.585 ± 0.036	0.325 ± 0.026	0.287 ± 0.028	0.150 ± 0.016
90% Single-Panel Veto	0.786 ± 0.024	0.504 ± 0.019	0.438 ± 0.019	0.327 ± 0.015
90% Single-Panel and Multi-Pixel Veto	0.268 ± 0.016	0.153 ± 0.012	0.126 ± 0.014	0.075 ± 0.008

is sensitive to the position of the cut threshold. We are conservative in using 1.2 MeV.

Figure 8.5 shows the energy depositions in the silicon detector before and after removing counts with the most aggressive cut, the single-panel, multi-pixel veto cut. The dominant mechanism for background counts in the silicon detector is a secondary photon Compton scattering. The secondary photons are created by the cosmic-ray photon interacting in other materials. The majority have energy under 1 MeV, but can extend up to hundreds of MeV. A magnetic field increase should not change the background spectrum from cosmic-ray photons.

Figure 8.6 shows the silicon-detector spectra after other veto cuts. Each causes a small reduction of the background. The most aggressive veto, a single-panel and multi-pixel veto, reduces the background rate by almost a factor of two. Table 8.3 shows the background rates after each veto cut. Post-acceleration reduces the cosmic-ray photon background more than the veto. Assuming the most aggressive veto cuts, cosmic-ray photons are the largest cosmic-ray background due to the inability to efficiently veto photons.

Primary Nucleons and Secondary Neutrons

Primary nucleons have the lowest intensity of the simulated cosmic rays and produce the lowest background rates. The secondary neutrons are more abundant, have a lower energy,

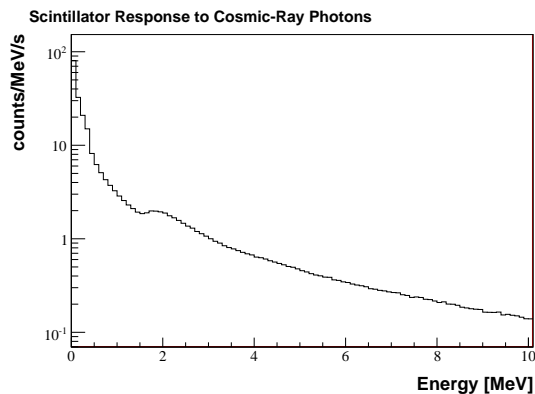


Figure 8.4: Energy depositions in the five scintillator sections with cosmic-ray photons incident. Counts above 1.2 MeV will be tagged to veto silicon-detector counts within $1 \mu\text{s}$.

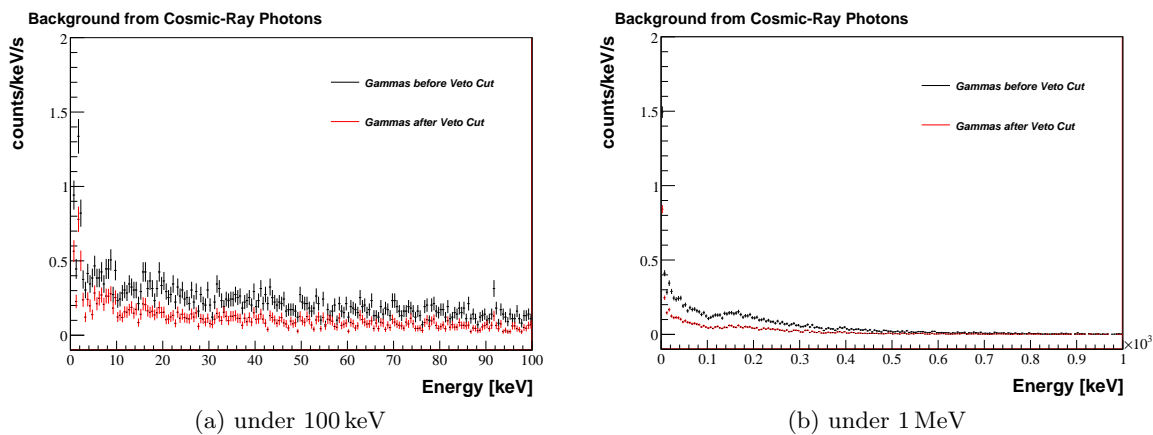


Figure 8.5: Background spectra in the silicon detector from cosmic-ray photons before and after the single-panel, multi-pixel veto cut (90% efficiency) has been applied.

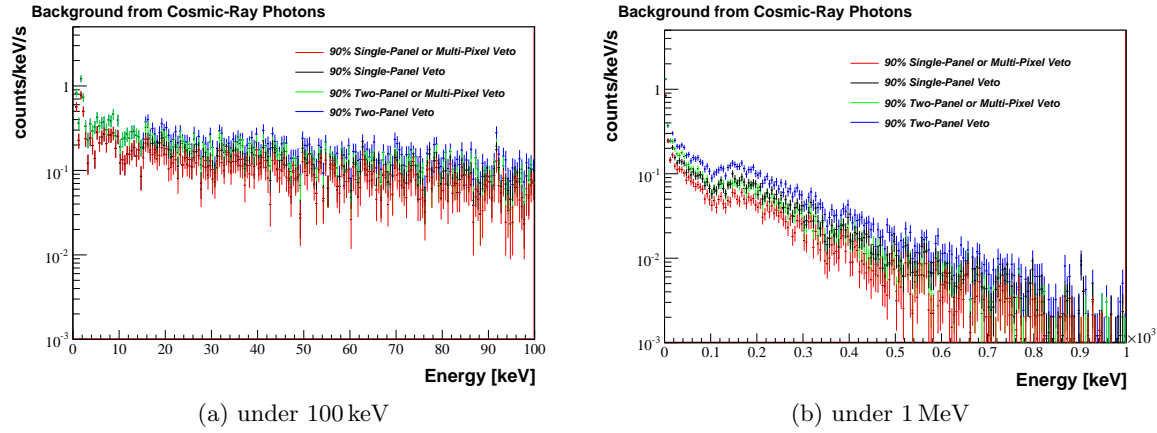


Figure 8.6: Various veto cuts reduce the background in the silicon detector from cosmic-ray photons.

Table 8.3: The effect of various veto cuts on the background rates from cosmic-ray photons assuming 90% veto efficiency. The uncertainties are purely statistical.

Source	18.6 keV	28.6 keV	38.6 keV	48.6 keV
Cosmic-Ray Photons	mHz	mHz	mHz	mHz
Before Veto	1.448 ± 0.086	0.638 ± 0.057	0.593 ± 0.055	0.365 ± 0.043
90%Two-Panel Veto	1.270 ± 0.079	0.547 ± 0.052	0.535 ± 0.052	0.303 ± 0.038
90%Two-Panel and Multi-Pixel Veto	1.014 ± 0.071	0.443 ± 0.047	0.420 ± 0.046	0.225 ± 0.033
90%Single-Panel Veto	0.857 ± 0.064	0.350 ± 0.040	0.337 ± 0.040	0.191 ± 0.030
90%Single-Panel and Multi-Pixel Veto	0.705 ± 0.058	0.287 ± 0.037	0.272 ± 0.036	0.153 ± 0.027

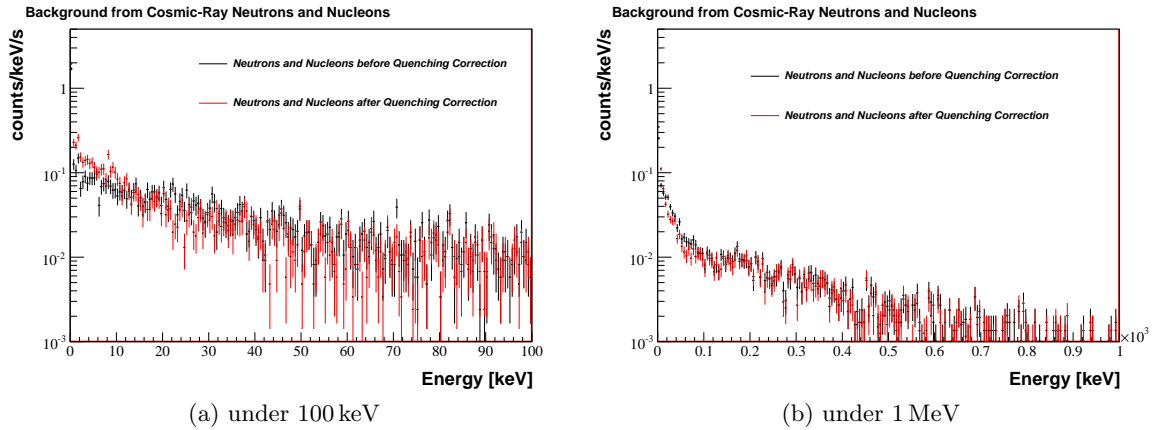


Figure 8.7: Background spectra in the silicon detector from cosmic neutrons and nucleons before and after the pulse-height-defect correction has been applied. The correction shifts counts to lower energy.

and create a larger background. Neutrons under 10 MeV elastic scatter off silicon nuclei in the detector and require a correction for the pulse-height defect. Therefore, both have been corrected for the pulse-height defect, but neither are effectively removed with a scintillator veto.

Figure 8.7 shows the spectra before and after the pulse-height-defect correction. The correction shifts neutron counts to lower energy. Table 8.4 shows the rates before and after correction. The background from neutrons and nucleons is the smallest of all the cosmic rays.

The primary nucleons interact in the materials around the detector and create secondary photons. Most background counts following a primary nucleon are caused by the photon interactions. Conversely, the lower-energy secondary neutrons interact in the detector creating nuclear recoils. Therefore, the pulse-height correction is larger for the secondary neutrons than for the primary nucleons. In addition, materials around the detector can capture thermal neutrons and emit photons. Copper has a high capture cross section for neutrons, but we estimate the background from this mechanism to be less than $25 \mu\text{Hz}$ per ROI. None of the neutron-related sources of background will be affected by a larger magnetic field.

Table 8.4: Cosmic neutron rates corrected for the pulse-height defect. The uncertainties are purely statistical.

Source	18.6 keV mHz	28.6 keV mHz	38.6 keV mHz	48.6 keV mHz
Neutrons	0.142 ± 0.013	0.067 ± 0.009	0.036 ± 0.007	0.024 ± 0.005
Neutrons Corrected	0.112 ± 0.012	0.045 ± 0.007	0.036 ± 0.007	< 0.014
Nucleons	0.074 ± 0.011	0.036 ± 0.008	0.025 ± 0.007	< 0.026
Nucleons Corrected	0.071 ± 0.011	0.032 ± 0.007	0.030 ± 0.007	0.019 ± 0.006

8.1.2 Natural Radioactivity

Natural radioactivity produces photons and electrons under a few MeV. Photons can reach the detector from considerable distances, but electrons have a very short range. Radiation coming from components far from the detector can be shielded; components close to the detector must be low in radioactive impurities. We first discuss impurities in the detector components, then the environmental radiation.

Radioactivity in the Detector Components

All materials contain trace amounts of primordial radioactivity. Uranium and thorium produce X rays with energy in our region of interest but the X rays have a very short range. Electrons can only reach the detector from very short distances but are easily detected. Therefore, as discussed in Section 6.2.2, seven components close to the detector are simulated with Geant4's Radioactive Decay Module (GRDM). The GRDM includes beta-decay electrons and has been corrected for low-energy X rays. The thirteen components that are farther from the detector are simulated with the `CalibrationGenerator`, which only generates photons, not beta electrons.

Figure 8.8 shows the background spectra from both types of simulation. The detector is most sensitive to components close to it, so we have chosen cleaner materials for the components closest to the detector, as listed in Appendix B.1. Because of the lower activities, components simulated with the GRDM contribute a smaller background. In the

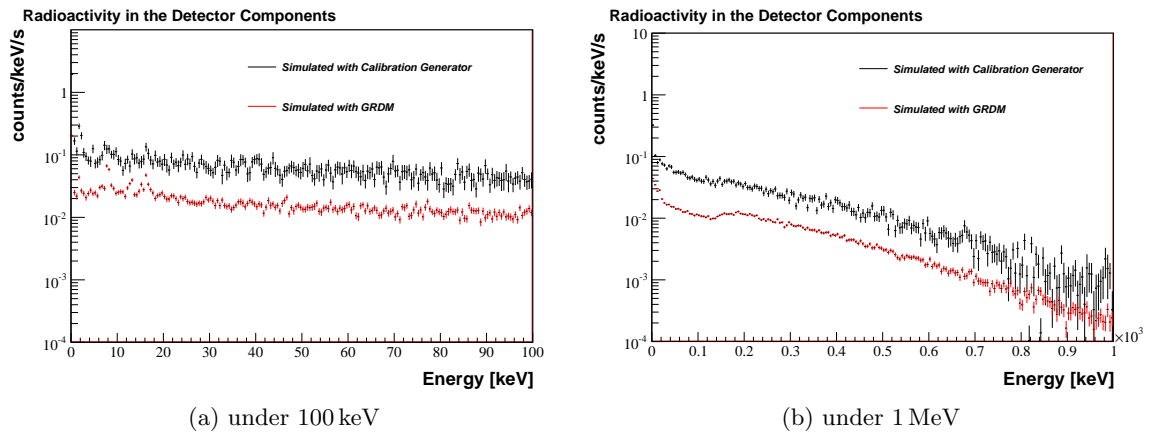


Figure 8.8: Background spectra from primordial radioactivity in the detector components. Components closest to the detector are simulated with the GRDM, which includes beta-decay electrons. Components farther away are simulated with the `CalibrationGenerator` which only produces photons.

GRDM spectra, X rays are visible below 20 keV. Beta-decay electrons which pass through the detector cause a minimum-ionizing-particle bump above 100 keV. Beta-decay electrons are also a large part of the continuum in the GRDM simulation. This background will be focused onto the detector by the magnetic field and could change with an increasing magnetic field. Of the components simulated with the GRDM, the pogo pins contribute the largest background. Table 8.5 lists the total background from these seven components. The background from the individual components are listed in Appendix B.2.

The radioactivity backgrounds simulated with the `CalibrationGenerator` are caused by higher-energy photons Compton scattering in the detector. The spectrum has a slight decrease at higher energy, but no X rays or minimum-ionizing-particle bump. The magnetic field will not focus this photon background onto the detector. The largest contributors are the large ceramic insulator, the preamps, and the telescoping quartz insulators. The quartz insulator and the distribution board have not been assayed, so the uncertainty on their activity may be larger than than listed in the activity tables. All of these components are inside the lead shield. Table 8.6 lists the total background rates from these thirteen

Table 8.5: Background rates from primordial radioactivity simulated with the GRDM. The uncertainties are purely statistical.

Source GRDM	18.6 keV mHz	28.6 keV mHz	38.6 keV mHz	48.6 keV mHz
Thorium	0.011 ± 0.001	0.004 ± 0.001	0.004 ± 0.001	0.003 ± 0.001
Uranium	0.099 ± 0.003	0.041 ± 0.002	0.034 ± 0.002	0.025 ± 0.002
Potassium	0.007 ± 0.001	0.004 ± 0.001	0.002 ± 0.000	0.002 ± 0.000
Total	0.117 ± 0.003	0.050 ± 0.002	0.040 ± 0.002	0.030 ± 0.002

Table 8.6: Background rates from primordial radioactivity simulated with the CalibrationGenerator. The uncertainties are purely statistical.

Source CalibrationGenerator	18.6 keV mHz	28.6 keV mHz	38.6 keV mHz	48.6 keV mHz
Thorium	0.099 ± 0.010	0.043 ± 0.006	0.031 ± 0.005	0.029 ± 0.005
Uranium	0.239 ± 0.021	0.119 ± 0.013	0.112 ± 0.014	0.069 ± 0.011
Potassium	0.045 ± 0.008	0.031 ± 0.007	0.029 ± 0.006	0.022 ± 0.006
Total	0.383 ± 0.025	0.193 ± 0.016	0.172 ± 0.016	0.120 ± 0.013

components. The backgrounds from the individual components are listed in Appendix B.2.

The detector components also contain the cosmogenic activities listed in Appendix B.3. Early simulations showed that cosmogenics contribute less than 0.01 mHz [106], or less than 1% of the background goal. Schwamm estimated the cosmogenics ^{60}Co and ^{32}Si would contribute less than 0.03 mHz [57]. Therefore, we assume the contribution from cosmogenics is negligible and do not simulate it here.

Environmental Radiation

The environmental radiation in the KATRIN detector laboratory is caused by uranium, thorium, and potassium outside the detector components and is discussed at length in Section 7.2. The simulation is divided into photons coming through the openings of the

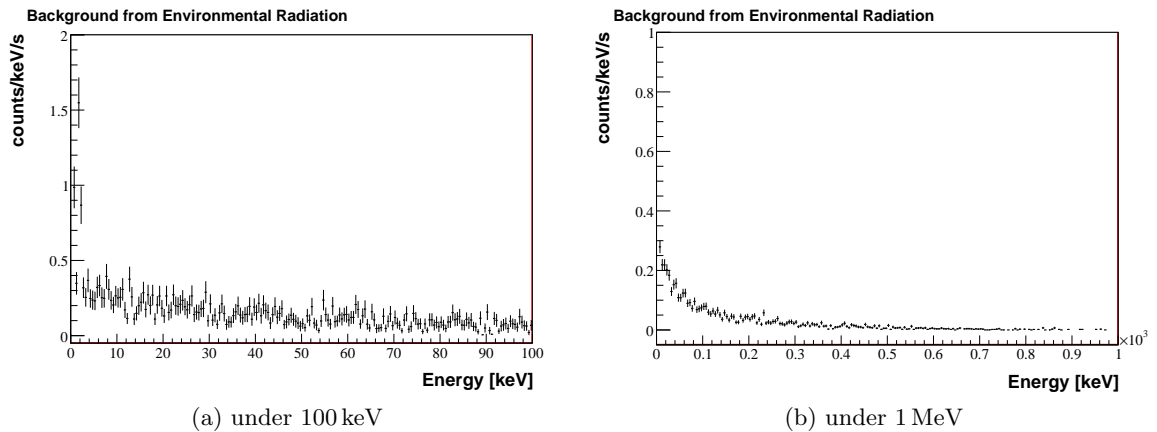


Figure 8.9: Background spectrum in the silicon detector from environmental radiation in the KATRIN detector laboratory.

shield and photons that must pass through the shield walls. Table 8.7 lists the backgrounds from both of these sources in the KATRIN detector laboratory. The largest component of the environmental radiation background comes from photons that pass through the passive shield. A thicker shield would reduce this background. Figure 8.9 shows the background spectrum. The photons Compton-scatter in our detector so the spectrum will not change with a magnetic field increase.

For commissioning studies at the University of Washington, it is useful to estimate the

Table 8.7: Environmental radiation background rates in the KATRIN detector laboratory. Most of the background comes through the shield walls. The uncertainties are purely statistical.

Source	18.6 keV	28.6 keV	38.6 keV	48.6 keV
KIT Radiation	mHz	mHz	mHz	mHz
Through Shield Walls	0.736 ± 0.087	0.459 ± 0.068	0.291 ± 0.055	0.139 ± 0.039
Through Openings	0.150 ± 0.009	0.063 ± 0.006	0.041 ± 0.005	0.036 ± 0.004
Total	0.885 ± 0.088	0.522 ± 0.068	0.332 ± 0.055	0.175 ± 0.039

Table 8.8: Environmental radiation background rates in the UW commissioning laboratory. Most of the background comes through the shield openings. The uncertainties are purely statistical.

Source	18.6 keV	28.6 keV	38.6 keV	48.6 keV
B037 Radiation	mHz	mHz	mHz	mHz
Through Shield Walls	0.917 ± 0.107	0.582 ± 0.085	0.361 ± 0.068	0.163 ± 0.046
Through Openings	1.135 ± 0.065	0.458 ± 0.042	0.310 ± 0.034	0.264 ± 0.031
Total	2.051 ± 0.125	1.041 ± 0.094	0.672 ± 0.076	0.427 ± 0.055

background in this laboratory. The environmental radiation in the UW commissioning laboratory (B037) was discussed in Section 7.3. The background in the UW commissioning laboratory is shown in Tab. 8.8. Due to a different angular distribution, this background is dominated by photons that come through the shield openings and cannot be reduced with a thicker shield.

8.2 Background Reductions

We calculate the total background rates assuming the most aggressive cosmic-ray veto, a single-panel veto and multi-pixel cut with 100% veto efficiency. The total background spectrum is shown in Fig. 8.10 and the rates in each ROI are listed in Tab. 8.9. The dominant feature in the background spectrum is the minimum-ionizing-particle bump from cosmic-ray muons.

The single largest background source is the environmental radiation. Cosmic-ray photons are also a large contribution. Many detector components inside the shield add up to a large contribution as well. Most of the backgrounds are created by high-energy photons Compton-scattering in the detector. A thorough comparison of these simulations with early background estimates is given in Appendix C.

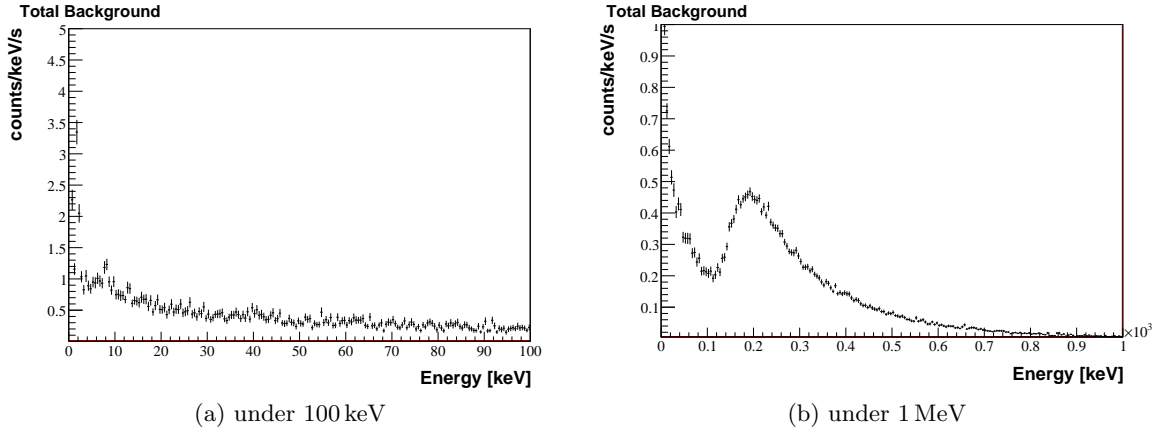


Figure 8.10: Total background spectrum. The slope in the continuum indicates that post-acceleration will improve the background.

Table 8.9: Total background rates assuming a 3 T field at the detector, the single-panel veto with 90% efficiency and a multi-pixel cut. The uncertainties are purely statistical.

Source with 3 T field	18.6 keV mHz	28.6 keV mHz	38.6 keV mHz	48.6 keV mHz
Cosmic Rays	1.157 ± 0.062	0.516 ± 0.040	0.464 ± 0.040	0.255 ± 0.029
Environmental Radiation	0.885 ± 0.088	0.522 ± 0.068	0.332 ± 0.055	0.175 ± 0.039
Rad in Components	0.500 ± 0.025	0.243 ± 0.016	0.212 ± 0.016	0.150 ± 0.013
Total	2.542 ± 0.110	1.281 ± 0.080	1.008 ± 0.070	0.580 ± 0.050

Table 8.10: Regions of interest at 5 T assuming 600 eV FWHM noise, 110 nm deadlayer, and all backscattered electrons are reflected into the same count.

Signal Energy keV	Post-Acceleration kV	Max Angle	ROI keV	ΔE keV
18.6	0	65°	14.91–19.65	4.74
28.6	10	46°	26.71–29.68	2.97
38.6	20	38°	37.35–39.69	2.34
48.6	30	33°	47.64–49.68	2.04

8.2.1 Post-acceleration Setting

Post-acceleration clearly improves the background, as shown in Tab. 8.9. The simulated background spectrum is a continuum without lines from photons. The copper X ray at 8.0 keV is barely visible. Although niobium, uranium, and thorium produce X rays near the tritium endpoint, these are not visible above the continuum. Therefore, post-acceleration is not necessary to avoid an X ray. But the background spectrum does have a negative slope, so post-acceleration will move the signal to a region of lower background. In addition, post-acceleration reduces the width of the ROI, the dominant effect of post-acceleration. Therefore, the optimal post-acceleration setting is the largest possible voltage. With at least 20 kV of post-acceleration, we will meet our background goal.

8.2.2 Magnetic Field Setting

A higher magnetic field reduces the area of the detector needed for the signal electrons. A higher magnetic field also affects the detection efficiency because it increases the electron angle of incidence. The necessary ROI widths to achieve 90% detection efficiency at 5 T have been calculated by P. Renschler using version 1.2 of KESS [105]. Table 8.10 shows the width of ROIs assuming a 5 T field at the detector. With no post-acceleration, the ROI is wider, but even with only 10 kV of post-acceleration, the ROI width at 5 T is comparable to the 3 T width.

Higher magnetic fields will not change the photon background distribution in the detec-

Table 8.11: Total background rates assuming a 5 T field at the detector, the single-panel veto with 90% efficiency and a multi-pixel cut. The uncertainties are purely statistical.

Source with 5 T field	18.6 keV mHz	28.6 keV mHz	38.6 keV mHz	48.6 keV mHz
Cosmic Rays	0.806 ± 0.040	0.332 ± 0.025	0.265 ± 0.023	0.153 ± 0.017
Environmental Radiation	0.631 ± 0.057	0.321 ± 0.041	0.207 ± 0.034	0.119 ± 0.025
Rad in Components	0.397 ± 0.016	0.171 ± 0.009	0.133 ± 0.009	0.101 ± 0.008
Total	1.834 ± 0.072	0.824 ± 0.049	0.606 ± 0.042	0.373 ± 0.032

tor pixels. But all beta-particles originating from within the area of the flux tube at the feed-through flange will focus onto the same detector pixels as the signal. Since we simulate a constant 3 T field, the flux tube does not expand at the feed-through flange. This simulation images an area of the flange equal to the area of the detector onto the detector. A more realistic field map will be necessary to improve simulations of the charged-particle backgrounds. The current estimates indicate this is a small portion of the total background.

To estimate the reduction of the background due to a higher magnetic field, we calculate the background in the inner eight rings of the detector in the ROIs listed in Tab. 8.10. As a conservative estimate, we assume the radioactive backgrounds simulated with the GRDM will be focused into the inner eight rings. Since the GRDM background is a small fraction of the total, the magnetic field should reduce the background by the ratio of the fields, 3.0/5.0 or 0.6. Table 8.11 shows the reduced background with a 5 T field. With a higher magnetic field we can reach the background goal with very little post-acceleration.

8.2.3 *Passive Shield*

The passive shield reduces the external photon backgrounds, especially the environmental radiation and radioactivity in components outside the shield. Radioactivity creates photons up to 2.6 MeV. The other external photon background, cosmic-ray photons, has energy up to 10 GeV. Is the KATRIN shield the optimal thickness to reduce these backgrounds?

To answer this, we look at the intensity remaining of a beam of photons that pass

Table 8.12: Transmission of various-energy photons through 3 cm of lead. Mass attenuation coefficients taken from XCOM: The photon cross sections database [69].

Energy MeV	μ/ρ cm ² /g	I/I₀
0.5	0.161	0.42%
1.0	0.0710	8.9%
2.6	0.0432	23%
10	0.0497	18.4%
100	0.0931	4.2%
10 ³	0.115	2.0%

through the shield, as in Eq. 8.1.

$$I = I_0 e^{-x\rho\left(\frac{\mu}{\rho}\right)} \quad (8.1)$$

The fraction of transmitted photons depends on the material density ρ , the path length x of the photon in the material, and the energy-dependent mass attenuation coefficient μ/ρ . We use the density of lead, 11.35 g/cm³, and the shield thickness of 3 cm as the path length. Table 8.12 shows the transmission for various-energy photons. A maximum in the transmission, or minimum in the attenuation, occurs just above 1 MeV near the ²⁰⁸Tl peak. Below 1 MeV, the shield reduces the intensity by more than 90%.

Figure 8.11 shows the cross section in lead. The shallow minimum near the ²⁰⁸Tl peak is due to pair production turning on just above 1 MeV. Below 1 MeV, most photons are absorbed through the photoelectric effect. For a small energy region around 1 MeV, the Compton effect dominates the cross section in lead. Above 1 MeV the scattered photons may still pass through the shield since incoherent scattering or pair production can create lower-energy photons or electron-positron pairs. Therefore, although a large fraction of gammas above 10 MeV scatter in the shield, the shield may not reduce this background.

A thicker shield would reduce the environmental radioactivity background, which is about 30% of the background. Radioactivity in detector components outside the shield is not a large contribution. A slightly thicker shield most likely will not reduce the cosmic-ray photon background. Since we expect to reach our background goal with the existing shield,

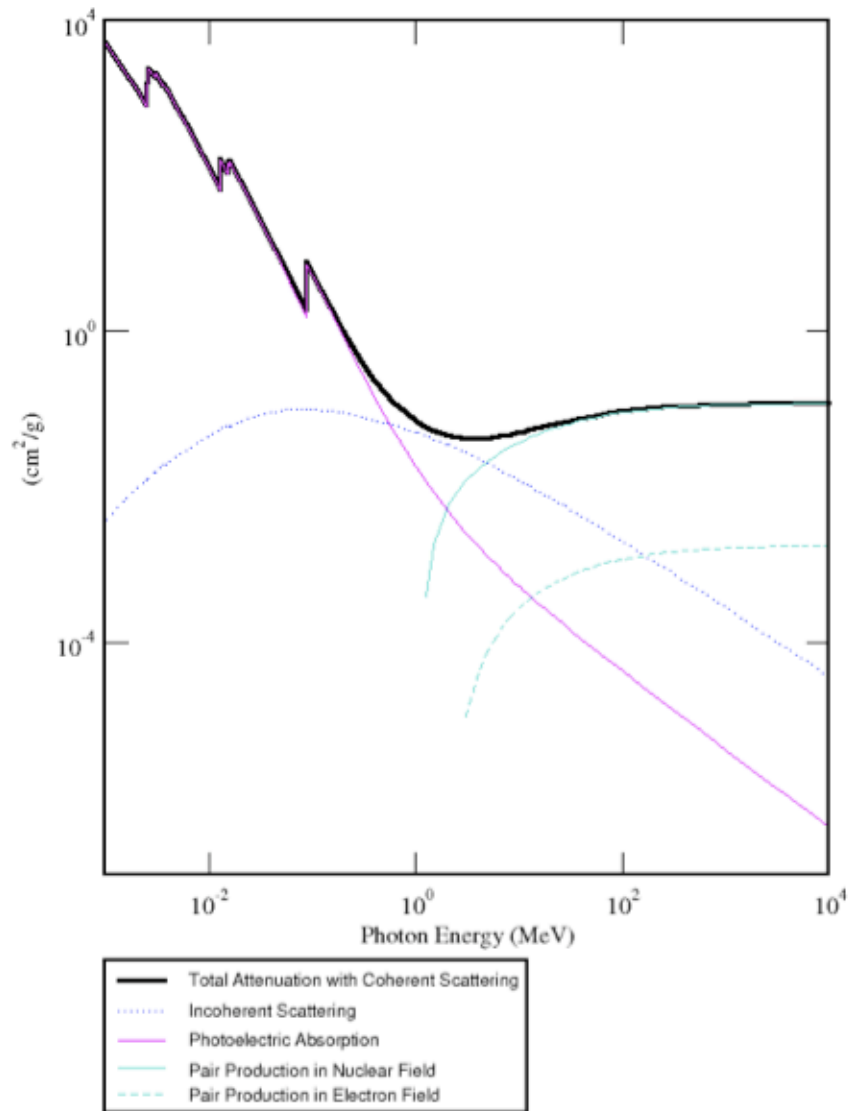


Figure 8.11: Photon interaction cross section in lead. Figure from XCOM: The photon cross sections database [69].

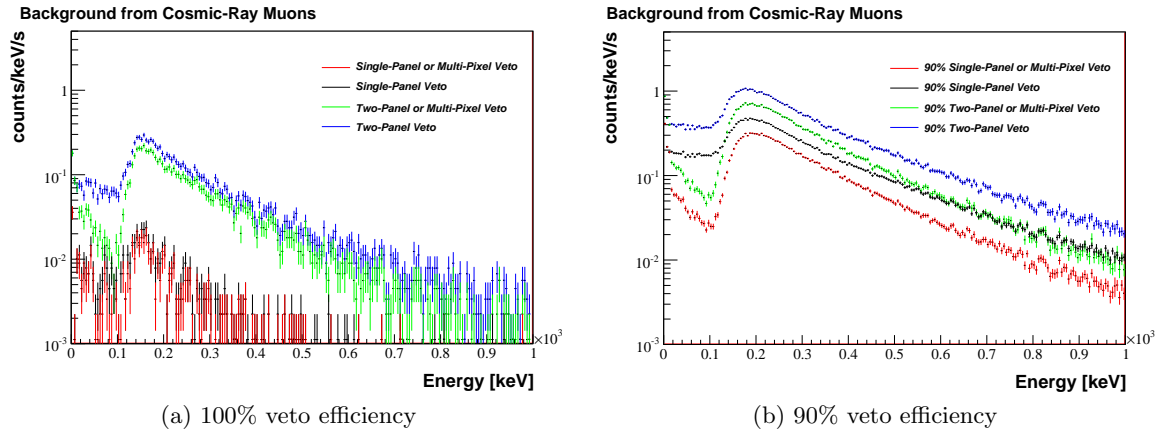


Figure 8.12: The veto cut with 100% efficiency reduces the background in the silicon detector from cosmic-ray muons even more.

we conclude a thicker shield is not necessary.

8.2.4 Scintillator Veto

The scintillator veto drastically reduces the background from cosmic-ray muons, but only reduces the cosmic-ray photon background by about half. Would more complete solid-angle coverage or higher efficiency improve the background? Figure 8.12 shows the cosmic-ray muon background improvement with 100% veto efficiency. The minimum-ionizing-particle bump is essentially removed with the single-panel veto cut. Clearly, the scintillator covers an adequate solid angle, the muon background is due to the efficiency correction of the scintillator veto. Table 8.13 shows the cosmic-muon background rate which could be reached with 100% veto efficiency. Because there are so many counts from cosmic-ray muons, an improvement in the veto efficiency will improve the background. But the 90% efficiency is adequate, we expect to reach our background goal.

8.2.5 Allowed Activities

The background rates estimated in this section are based on a novel method to mount and make electrical connections to the detector. The largest background sources are much

Table 8.13: Effect of 100% efficient veto cuts on cosmic-ray muons. The uncertainties are purely statistical.

Source	18.6 keV	28.6 keV	38.6 keV	48.6 keV
Cosmic-Ray Muons	mHz	mHz	mHz	mHz
Before Veto	7.604 ± 0.207	4.893 ± 0.166	4.176 ± 0.153	3.215 ± 0.134
Two-Panel Veto	0.326 ± 0.043	0.146 ± 0.029	0.180 ± 0.032	0.084 ± 0.022
Two-Panel and Multi-Pixel Veto	0.140 ± 0.028	0.067 ± 0.019	0.107 ± 0.024	< 0.045
Single-Panel Veto	< 0.052	< 0.038	< 0.045	< 0.022
Single-Panel and Multi-Pixel Veto	< 0.045	< 0.030	< 0.045	< 0.022

different than the early estimates discussed in Section 4.3.2. Most importantly, the novel connection scheme reduces the radioactivity coming from the flux tube behind the detector. For the initial design of mounting the detector on ceramic, Schwamm estimated 6.0 mHz from the ceramic detector mount alone [57]. The background rate from the current mounting structure is less than 0.12 mHz without post-acceleration. The entire mounting structure is simulated with the GRDM. Most of the background comes from the pogo pins.

Sapphire insulators are a crucial part of the novel connection scheme. Other materials considered for this purpose had unacceptably high activities. One early candidate, Kryoflex, could cause a background of 5.6 mHz, barely an improvement over the ceramic mount. Glass beads were also investigated, and contributed 0.26 mHz in addition to the pogo pins. If the sapphire feedthrough solution does not work, we may need to use materials with higher activity and we can expect a larger background. Radioactivity inside the flux tube behind the detector will be focused by the magnetic field. Therefore, all materials in the Conflat flange feedthrough must meet strict activity requirements.

8.3 Uncertainty Estimates and Discussion

All background rates presented so far include only statistical uncertainties. The overall accuracy of the simulation introduces a systematic shift, as well as uncertainties on individual background sources. In this section, we investigate each uncertainty.

Overall Monte Carlo Accuracy: We estimated the overall accuracy of the Monte Carlo with calibration sources. Since calibration sources release photons with well-known energy and intensity, using a calibration source separates the overall simulation accuracy from ambiguity about the source. Calibrations of a silicon detector with ^{109}Cd and ^{241}Am are presented in Section 7.1.2. A germanium detector calibration with ^{60}Co is discussed in Section 7.3.2. Simulations of both detectors agree within 7% of the measurements. Since we have not calibrated the silicon detector at 18.6 keV, the nominal region of interest, and have not calibrated the germanium detector at multiple energies, we assume the overall uncertainty is 10%. This uncertainty affects all background mechanisms; the overall Monte Carlo uncertainty in a given region of interest is 10% of the total rate in that ROI because the uncertainty is completely correlated for each background mechanism. Multiplying each background by 10% and adding in quadrature would assume the uncertainties are uncorrelated.

Cosmic-Ray Intensity: The estimated systematic uncertainty on the cosmic-ray intensity, discussed in Section 6.2.1, is $^{+10\%}_{-15\%}$. The theoretical intensity of cosmic-ray muons used in the simulation is 15% higher than a measurement in Karlsruhe. Solar and geomagnetic effects are expected to cause a variation of 10%. Measurements of cosmic-ray muons in a silicon detector, presented in Section 7.1.3, agree with the simulation within 30%. Although we base the uncertainty on measurements of muons, we assume it is the same for all sources of cosmic rays. This uncertainty should only be applied to cosmic-ray backgrounds; to estimate the uncertainty from the cosmic-ray intensity in a given region of interest, multiply the cosmic-ray background rate by 10% for the upper uncertainty and by 15% for the lower uncertainty.

Environmental-Radiation Intensity: The uncertainty on the environmental-radiation intensity is based on measurements with a germanium detector in the KATRIN detector laboratory, described in Section 7.2. We calculated the intensity incident on the walls of the KATRIN shield I_W for each peak in the uranium and thorium chain using an unshielded germanium detector measurement. The variance of the intensity for

each peak is 15%, so we take this as the systematic uncertainty on I_W , the intensity incident on the shield walls at KIT. In addition, we compared the integral rate in the unshielded germanium detector above 500 keV to the simulation. The germanium detector simulation is within 30% of the measurement, but the KATRIN shield should improve this difference by blocking the low-energy photons. To estimate the uncertainty from I_W , multiply the background from radiation through the shield walls in Tab. 8.7 by 15%.

The intensity through the shield openings I_O was calculated from measurements with a germanium detector enclosed in a 15 cm shield. The difference in the measured spectra with the shield open and closed was 126% higher than the simulation over all energies. Therefore, we take the systematic uncertainty on the intensity through the shield openings I_O to be $^{+130\%}_{-15\%}$. To estimate the uncertainty from I_O , multiply the background from radiation through the shield openings in Tab. 8.7 by $^{+130\%}_{-15\%}$.

Measurements in the UW commissioning laboratory described in Section 7.3 included the KATRIN shield. A simulation of a germanium detector enclosed in the KATRIN shield, including cosmic-ray muons and photons, produced an integral rate within 5% of the integral measured rate. Therefore, we expect the simulation of a shielded silicon detector should agree with measurements better than a simulation of an germanium detector. Also, the systematic uncertainties in B037 are different than at KIT.

Estimated Activities: Not all materials used in the detector construction have been assayed; the activities of eleven components are based on values found in the literature. Different samples of the same materials can vary by large amounts, but we have chosen to use high activities. For example, lead, copper, and steel may have impurities as low as a few $\mu\text{Bq/kg}$ [107], but we use values of a few mBq/kg . Plastic scintillator and quartz insulators can also be much cleaner than the estimated activities. The distribution board, made of Rogers 4000 circuit board, was chosen for low-activity. Many circuit board materials have higher activity than we assume, so this material has the highest probability of being under-estimated. For estimated components, we assume

an uncertainty of $\begin{smallmatrix} +30\% \\ -100\% \end{smallmatrix}$ regardless of whether it is an upper limit or measurement. This uncertainty is only applied to a subset of the detector components. To calculate the uncertainty in a given ROI, sum up the backgrounds from estimated components, and multiply by 30% for the upper uncertainty and 100% for the lower uncertainty. Appendix B.1 lists the activities, including indicating those which are estimated, and lists backgrounds from individual components.

Measured Activities: The nine components that have been assayed have a statistical uncertainty on the activity. The uncertainties, listed in Appendix B.1, are different for each material. The largest is 50%. If an upper limit is given, we assume an uncertainty of $\begin{smallmatrix} +0\% \\ -100\% \end{smallmatrix}$. To calculate the uncertainty in a given ROI, multiply the background rate from each component by the fractional uncertainty on the activity, then sum up the uncertainties in quadrature. Appendix B.1 lists the activities, including indicating those which have been measured, and lists backgrounds from individual components.

Table 8.14 summarizes the uncertainties from the identified sources of uncertainty. The uncertainty in two regions of interest are also given. The total uncertainty in one ROI depends on the relative size of each background in that ROI. The total uncertainty is less than 15% for most ROI. The largest uncertainty comes from the overall Monte Carlo accuracy, followed closely by the environmental-radiation intensity and the cosmic-ray intensity.

8.4 Summary

We utilize multiple methods to reduce the detector-related backgrounds for KATRIN: post-acceleration, magnetic field, scintillator veto, passive shield, and a novel, radio-pure connection scheme. Combining these methods, we expect to reach the design goal of 1 mHz in the region of interest.

Table 8.14: Total estimated uncertainties for two regions of interest with a 3 T magnetic field. The fractional uncertainties associated with the intensity of cosmic rays and environmental radiation and the activity of components are only applied to the background rate from that source, not the total rate in the ROI.

Source	Fractional Uncertainty	0 kV PA mHz	20 kV PA mHz
Systematic Uncertainties			
Overall MC Accuracy	10%	0.254	0.101
Cosmic-Ray Intensity	+10% -15%	+0.116 -0.174	+0.046 -0.070
Env.-Rad. Intensity I_W	15%	0.110	0.044
Env.-Rad. Intensity I_O	+130% -15%	+0.195 -0.023	+0.053 -0.006
Estimated Activities	+30% -100%	+0.034 -0.113	+0.014 -0.047
Total Systematic		+0.360 -0.347	+0.131 -0.138
Statistical Uncertainties			
MC Statistics	< 10%	0.110	0.070
Measured Activities	+<50% -<100%	+0.022 -0.023	+0.013 -0.013
Total Statistical		0.112	0.071
Total	$\approx 16\%$	+0.377 -0.364	+0.149 -0.156

Chapter 9

CONCLUSION

In this dissertation, we present estimates of the detector-related backgrounds for the Karlsruhe Tritium Neutrino Experiment. Limiting the intrinsic backgrounds in the detector to 1 mHz should allow KATRIN to achieve sensitivity to neutrino mass as low as 0.2 eV (90% CL).

We validated the simulations by measuring spectra from calibration photon sources using a silicon *p-i-n* diode detector. The simulated rates in the calibration peaks and backscattering edges are within 7% of the measured rates. The simulation accounts for radiation associated with the local laboratory environment, as measured using a germanium detector and shield. The environmental radiation simulated in an unshielded germanium detector is within 30% of the measured radiation, and simulated in a germanium detector enclosed by the KATRIN shield is within 5%. The intensity of cosmic rays depends on location, but we use average spectra from the literature, introducing the second-largest systematic uncertainty.

The estimated total background rate in the silicon detector with a 3 T magnetic field and no post acceleration is $[2.54 \pm 0.11(\text{stat.}) \pm_{-0.35}^{+0.36}(\text{sys.})]\text{mHz}$. This could be reduced with 20 kV of post-acceleration to $[1.01 \pm 0.07(\text{stat.}) \pm_{-0.14}^{+0.13}(\text{sys.})]\text{mHz}$. Additional reductions can be achieved with a magnetic field larger than 3 T by decreasing the beam size and the area at the detector.

The simulations in this dissertation agree reasonably well with measurements, but a few upgrades to the simulation could improve the backgrounds estimates. In particular, a realistic magnetic field will be necessary to investigate fully the background improvement with a higher magnetic field. Simulations in this dissertation do not use an electric field to investigate the effect of post-acceleration. The effects of an electric field should also be simulated. The geometry of the detector in this simulation is based on design drawings; if

the as-built dimensions differ from the drawings, the geometry code should be upgraded. In the simulation, the scintillator veto readout is assumed to have 90% efficiency. The simulation does not produce scintillation light or propagate photons along the fiber optics. A full simulation of the scintillator veto combined with measurements of the efficiency should improve our estimates of the backgrounds from cosmic rays.

In the coming months it should be possible to compare the simulation predictions to measurements with the actual KATRIN silicon detector, as it becomes operational in the B037 laboratory at the University of Washington. Based on germanium detector measurements presented here, in the B037 laboratory the largest background will be the environmental radiation, in particular the radiation through the shield openings. Correcting the background rates for the B037 environmental radiation, we predict the background during commissioning will be $[3.71 \pm 0.14(\text{stat.}) \pm_{-0.52}^{+0.55}(\text{sys.})]\text{mHz}$ at 3 T and no post-acceleration. To check that the environmental radiation is the dominant background, a background spectra could be measured without the passive shield, and again with the passive shield in place. We have seen evidence that the background from cosmic rays is smaller in the B037 laboratory, but we do not correct the background estimates for a reduction in the cosmic rays.

The background rates from radioactivity in the detector components will be the same in B037 as at KIT. Therefore, the background spectra should be inspected for signatures of radioactivity in each detector component. Initially, we may mount the detector on a feed-through flange that is not made of radio-pure components. Once the sapphire feed-through is in place, we should see a large decrease in the background. If the measured background spectrum includes visible X rays, a material close to the detector has a larger activity than assumed. If the background increases when the magnetic field is turned on, the background could be from beta-decays in the flux tube behind the detector. We expect high-energy cosmic rays to penetrate the magnetic field and create a minimum-ionizing-particle bump. If the magnetic field decreases the minimum-ionizing bump, it may indicate there is natural radioactivity outside the flux tube. Using the planned calibration sources will provide another opportunity to validate the simulations.

Other than the overall Monte Carlo accuracy, the two largest systematic uncertainties are associated with backgrounds that depend on location: cosmic rays and the environ-

mental radiation. Additional measurements in the Karlsruhe laboratory with a germanium detector could reduce the systematic uncertainties. We have estimated the uncertainty on the environmental radiation based on measurements with an unshielded germanium detector. Measuring the radiation inside the KATRIN shield on site in Karlsruhe could reduce this uncertainty. Simulations indicate that three-quarters of the background spectrum measured by a germanium detector enclosed in the KATRIN shield will come from environmental radiation and one-quarter will come from cosmic rays. Adding the scintillator veto to a measurement with a germanium detector would help separate these background sources, and should improve the uncertainty on both the cosmic-ray intensity and the environmental-radiation intensity.

In conclusion, the background rates estimated for KATRIN in this dissertation are within the target limits. Based on the work presented in this dissertation, we are optimistic that KATRIN will reach its sensitivity goal and measure or limit the neutrino mass, which is important for cosmology and particle physics. Including an external neutrino mass measurement in cosmological models can break parameter degeneracies. A neutrino mass measurement will restrict extensions to the Standard Model.

BIBLIOGRAPHY

- [1] W. Pauli, “Letter to the physical institute of Tübingen,” December 1930. Reproduced in [2].
- [2] L. Brown, “The idea of the neutrino,” *Phys. Today*, vol. 31, pp. 23–28, September 1987.
- [3] E. Fermi, “Trends to a theory of beta radiation,” *Nuovo Cim.*, vol. 11, pp. 1–19, 1934.
- [4] C. Cowan *et al.*, “Detection of the free neutrino: a confirmation,” *Science*, vol. 124, no. 103, p. 3212, 1956.
- [5] R. Davis, “An attempt to observe the capture of reactor neutrinos in chlorine-37,” in *UNESCO Conf.*, vol. 1, p. 728, 1958.
- [6] T. D. Lee and C. N. Yang, “Question of parity conservation in weak interaction,” *Phys. Rev.*, vol. 104, pp. 254–258, 1956.
- [7] C. S. Wu *et al.*, “Experimental test of parity conservation in beta decay,” *Phys. Rev.*, vol. 105, no. 1413–1415, 1957.
- [8] T. D. Lee and C. N. Yang, “Parity nonconservation and a two component theory of the neutrino,” *Phys. Rev.*, vol. 105, no. 1671–1675, 1957.
- [9] M. Goldhaber, L. Grodzins, and A. Sunyar, “Helicity of neutrinos,” *Phys. Rev.*, vol. 109, pp. 1015–1017, 1958.
- [10] S. L. Glashow, “Partial symmetries of weak interactions,” *Nucl Phys*, vol. 22, no. 579, 1961.
- [11] S. Weinberg, “A model of leptons,” *Phys. Rev. Lett.*, vol. 19, p. 1264, 1967.
- [12] A. Salam in *Proc. 8th Nobel Symp.* (N. Svartholm, ed.), (Stockholm), p. 367, Almqvist and Wiksell, 1968.
- [13] C. Amsler, (Particle Data Group), *et al.*, “Electroweak model and constraints on new physics,” *Phys. Lett.*, vol. B667, no. 1, 2008.
- [14] N. Cabibbo, “Unitary symmetry and leptonic decays,” *Phys. Rev. Lett.*, vol. 10, pp. 531–533, 1963.

- [15] M. Kobayashi and T. Maskawa, “CP-violation in the renormalizable theory of weak interaction,” *Prog. Theor. Phys.*, vol. 49, pp. 652–657, 1973.
- [16] R. Davis, D. S. Harmer, and K. C. Hoffman, “Search for neutrinos from the sun,” *Phys. Rev. Lett.*, vol. 20, pp. 1205–1209, 1968.
- [17] V. Gribov and B. Pontecorvo, “Neutrino astronomy and lepton charge,” *Phys. Lett. B*, vol. 28, no. 7, pp. 493–496, 1969.
- [18] Y. Fukuda *et al.*, “Evidence for oscillation of atmospheric neutrinos,” *Phys. Rev. Lett.*, vol. 81, pp. 1562–1567, 1998.
- [19] E. Aliu *et al.*, “Evidence for muon neutrino oscillation in an accelerator-based experiment,” *Phys. Rev. Lett.*, vol. 94, p. 081802, 2005.
- [20] Q. R. Ahmad *et al.*, “Measurement of the rate of $\nu_e + d \rightarrow p + p + e^-$ interactions produced by ^8B solar neutrinos at the Sudbury Neutrino Observatory,” *Phys. Rev. Lett.*, vol. 87, p. 071301, 2001.
- [21] Q. R. Ahmad *et al.*, “Measurement of day and night neutrino energy spectra at SNO and constraints on neutrino mixing parameters,” *Phys. Rev. Lett.*, vol. 89, p. 011301, 2002.
- [22] B. Aharmim *et al.*, “Electron energy spectra, fluxes, and day-night asymmetries of ^8B solar neutrinos from the 391-day salt phase SNO data set,” *Phys. Rev. C*, vol. 72, p. 055502, 2005.
- [23] L. Wolfenstein, “Neutrino oscillations in matter,” *Phys. Rev.*, vol. 17, pp. 958–960, 1978.
- [24] S. P. Mikheyev and A. Y. Smirnov, “Resonance amplification of oscillations in matter and spectroscopy of solar neutrinos,” *Sov. J. Nucl. Phys.*, vol. 42, pp. 913–917, 1985.
- [25] M. Gell-Mann, P. Ramond, and R. Slansky in *Supergravity* (P. van Nieuwenhuizen and D. Freedman, eds.), p. 315, North Holland, 1979.
- [26] T. Yanagida in *Proc. of the Workshop on Unified Theory and the Baryon Number of the Universe* (O. Sawada and A. Sugamoto, eds.), 1979.
- [27] K. Zuber, *Neutrino Physics*. Institute of Physics, 2004.
- [28] B. Pontecorvo *Zh. Eksp. Teor. Fiz.*, vol. 53, p. 1717, 1967. translated in [29].

- [29] B. Pontecorvo, “Neutrino experiments and the question of leptonic-charge conservation,” *Sov. Phys. JETP*, vol. 26, pp. 984–988, 1968.
- [30] Z. Maki, M. Nakagawa, and S. Sakata, “Remarks on the unified model of elementary particles,” *Prog. Theor. Phys.*, vol. 28, p. 870, 1962.
- [31] E. Otten, J. Bonn, and C. Weinheimer, “The Q-value of tritium β -decay and the neutrino mass,” *Int. J. Mass Spectrom.*, vol. 251, no. 2-3, pp. 173–178, 2006.
- [32] C. Kraus *et al.*, “Final results from phase II of the Mainz neutrino mass search in tritium β decay,” *Eur. Phys. J. C*, vol. 40, pp. 447–468, Apr. 2005.
- [33] V. M. Lobashev *et al.*, “Direct search for neutrino mass and anomaly in the tritium beta-spectrum: Status of “Troitsk neutrino mass experiment”,” *Nucl. Phys. B (Proc. Suppl.)*, vol. 91, no. 1-3, pp. 280–286, 2001.
- [34] R. G. H. Robertson *et al.*, “Limit on $\bar{\nu}_e$ mass from observation of the β decay of molecular tritium,” *Phys. Rev. Lett.*, vol. 67, pp. 957–960, Aug 1991.
- [35] C. Amsler, (Particle Data Group), *et al.*, “The cosmological parameters,” *Phys. Lett.*, vol. B667, no. 1, 2008.
- [36] J. Dunkley *et al.*, “Five-year Wilkinson Microwave Anisotropy Probe (WMAP) observations: Likelihoods and parameters from the WMAP data,” *Astrophys. J. Suppl.*, vol. 180, pp. 306–376, 2009.
- [37] J. Lesgourgues and S. Pastor, “Massive neutrinos and cosmology,” *Physics Reports*, vol. 429, no. 6, pp. 307–379, 2006.
- [38] E. Komatsu *et al.*, “Five-year Wilkinson Microwave Anisotropy Probe (WMAP) observations: Cosmological interpretation,” *Astrophys. J. Suppl.*, vol. 180, pp. 330–376, 2009.
- [39] F. T. Avignone, S. R. Elliott, and J. Engel, “Double Beta Decay, Majorana Neutrinos, and Neutrino Mass,” *Rev. Mod. Phys.*, vol. 80, pp. 481–516, 2008.
- [40] The 2007 Nuclear Science Advisory Committee, “The frontiers of nuclear sciences: A long range plan,” tech. rep., Department of Energy Office of Nuclear Physics, 2007.
- [41] C. Arnaboldi *et al.*, “Results from the Cuoricino $0\nu\beta\beta$ -decay experiment,” *Phys. Rev. C*, p. 035502, 2008.
- [42] R. Gornea *et al.*, “Double beta decay in liquid xenon,” *J. Phys. Conf. Ser.*, vol. 179, p. 012004, 2009.

- [43] J. Angrik *et al.*, “KATRIN design report 2004,” tech. rep., Forschungszentrum Karlsruhe, 2005. FZKA-7090.
- [44] R. Janev *et al.*, *Elementary Processes in Hydrogen-Helium Plasmas: Cross Sections and Reaction Rate Coefficients*. Springer, 1987.
- [45] A. Saenz, S. Jonsell, and P. Froehlich, “Improved molecular final-state distribution of HeT⁺ for the β -decay process of T₂,” *Phys. Rev. Lett.*, vol. 84, p. 242, 2000.
- [46] J. Beamson, H. Q. Porter, and D. W. Turner, “The collimating and magnifying properties of a superconducting field photoelectron spectrometer,” *J. Phys. E*, vol. 13, pp. 64–66, Jan. 1980.
- [47] A. Picard *et al.*, “A solenoid retarding spectrometer with high resolution and transmission for keV electrons,” *Nucl. Instrum. Meth. B*, vol. 63, p. 345, 1992.
- [48] V. M. Lobashev and P. E. Spivak, “A method for measuring the electron antineutrino rest mass,” *Nucl. Instrum. Meth. A*, vol. 240, p. 305, 1985.
- [49] V. M. Lobashev, A. I. Fedoseyev, O. V. Serdyuk, and A. P. Solodukhin, “Numerical simulation of a low-energy electron electrostatic integral spectrometer with adiabatic magnetic collimation,” *Nucl. Instrum. Meth. A*, vol. 238, p. 496, 1985.
- [50] P. Doe *et al.*, “Optimization criterion for the signal and background in the KATRIN focal-plane detector,” tech. rep., University of Washington, 2008.
- [51] A. Osipowicz *et al.*, “KATRIN: A next generation tritium beta decay experiment with sub-eV sensitivity for the electron neutrino mass,” Tech. Rep. FZKA-6691, Forschungszentrum Karlsruhe, 2001.
- [52] E. W. Otten, “The Mainz neutrino mass experiment,” *Prog. Part. Nucl. Phys.*, vol. 32, pp. 153–171, 1994.
- [53] S. Nagy *et al.*, “On the Q-value of the tritium β -decay,” *Europhys. Lett.*, vol. 74, pp. 404–410, 2006.
- [54] E. Otten and C. Weinheimer, “Neutrino mass limits from tritium beta decay,” *Reports on Progress in Physics*, 2008.
- [55] R. G. H. Robertson and D. A. Knapp, “Direct measurements of neutrino mass,” *Ann. Rev. Nucl. Part. Sci.*, vol. 38, pp. 185–215, 1988.
- [56] M. Steidl, “KATRIN sensitivity in dependence of detector performance,” tech. rep., Forschungszentrum Karlsruhe, 2005.

- [57] F. Schwamm, *Untergrunduntersuchungen für das KATRIN experiment*. PhD thesis, University of Karlsruhe, 2004.
- [58] M. Steidl *et al.*, “KATRIN detector design document,” tech. rep., University of Washington, 2007.
- [59] J. Dunmore, “Pixelation-dependence of transmission function,” tech. rep., Center for Experimental Nuclear Physics and Astrophysics, July 2007.
- [60] B. A. VanDevender *et al.*, “Performance of a monolithic silicon pin-diode array under mechanical stress.” to be submitted to *Nucl. Instrum. Meth. A*, 2009.
- [61] J. Formaggio, “Test plans for the KATRIN active and passive shield,” tech. rep., Massachusetts Institute of Technology, 2009.
- [62] A. Kopmann *et al.*, “FPGA-based DAQ system for multi-channel detectors,” in *Nuclear Science Symposium Conference Record*, May 2008.
- [63] M. A. Howe *et al.*, “Sudbury Neutrino Observatory neutral current detector acquisition software overview,” *IEEE Trans. Nucl. Sci.*, vol. 51, no. 3, pp. 878–83, 2004.
- [64] V. T. Jordanov and G. F. Knoll, “Digital synthesis of pulse shapes in real time for high resolution radiation spectroscopy,” *Nucl. Instrum. Meth. A*, vol. 345, pp. 337–345, 1994.
- [65] G. F. Knoll, *Radiation Detection and Measurement*. John Wiley & Sons, Inc., 3rd ed., 2000.
- [66] S. Agostinelli *et al.*, “Geant4— a simulation toolkit,” *Nucl. Instrum. Meth. A*, vol. 506, pp. 250–303, 2003.
- [67] J. Allison *et al.*, “Geant4 developments and applications,” *IEEE Trans. Nucl. Sci.*, vol. 53, pp. 270–278, Feb. 2006.
- [68] R. Brun and F. Rademakers, “ROOT – an object oriented data analysis framework,” *Nucl. Instrum. Meth. A*, vol. 389, pp. 81 – 86, 1997.
- [69] M. J. Berger *et al.*, “XCOM: Photon cross sections database (version 1.4).” Web site, Feb. 2009. <http://physics.nist.gov/PhysRefData/Xcom/Text/XCOM.html>.
- [70] J. M. Palms, P. V. Rao, and R. E. Wood, “Fano factor measurement for silicon using low energy photons,” *Nucl. Instrum. Meth.*, vol. 76, no. 59, 1969.

- [71] J. Lindhard, V. Nielsen, M. Scharff, and P. V. Thomsen, "Integral equations governing radiation effects," *Mat. Fys. Medd. Dan. Vid. Selsk.*, vol. 33, no. 10, pp. 2–42, 1963.
- [72] A. R. Sattler, "Ionization produced by energetic silicon atoms within a silicon lattice," *Phys. Rev.*, vol. 138, no. 6A, 1965.
- [73] B. L. Dougherty, "Measurements of ionization produced in silicon crystals by low-energy silicon atoms," *Phys. Rev. A*, vol. 45, pp. 2104–2107, Feb 1992.
- [74] G. Gerbier *et al.*, "Measurement of the ionization of slow silicon nuclei in silicon for the calibration of a silicon dark-matter detector," *Phys. Rev. D*, vol. 42, pp. 3211–3214, Nov 1990.
- [75] P. Zecher *et al.*, "Energy deposition of energetic silicon atoms within a silicon lattice," *Phys. Rev. A*, vol. 41, pp. 4058–4061, Apr 1990.
- [76] P. K. F. Grieder, *Cosmic Rays at Earth: Researcher's Reference Manual and Data Book*. Elsevier Science Ltd., 2001.
- [77] T. Antoni *et al.*, "Geometric structures in hadronic cores of extensive air showers observed by KASCADE," *Phys. Rev. D*, vol. 71, p. 072002, Apr 2005.
- [78] C. AMSLER, (Particle Data Group), *et al.*, "Cosmic rays," *Phys. Lett.*, vol. B667, no. 1, 2008.
- [79] S. Miyake, "Rapporteur paper on muons and neutrinos," in *Proc. of the 13th Int. Cosmic Ray Conf.*, vol. 5, pp. 3638–3655, 1973.
- [80] P. Lipari, "Lepton spectra in the earth's atmosphere," *Astropart. Phys.*, vol. 1, no. 2, pp. 195–227, 1993.
- [81] M. P. de Pascale *et al.*, "Absolute spectrum and charge ratio of cosmic ray muons in the energy region from 0.2 GeV to 100 GeV at 600 m above sea level," *J. Geophys. Res.*, vol. 98, no. 3501, 1993.
- [82] O. C. Allkofer, K. Carstensen, W. D. Dau, and H. Jokisch, "The absolute cosmic ray flux at sea level," *J. Phys. G: Nucl Phys*, vol. 1, no. 6, 1975.
- [83] B.C. Rastin, "A study of the muon charge ratio at sea level within the momentum range 4 to 2000 GeV/c," *J. Phys. G: Nucl Phys*, vol. 10, pp. 1629–1638, 1984.
- [84] C. A. Ayre *et al.*, "Precise measurement of the vertical muon spectrum in the range 20-500 GeV/c," *J. Phys.*, vol. G1, p. 584, 1975.

- [85] J. Kremer *et al.*, “Measurements of ground-level muons at two geomagnetic locations,” *Phys. Rev. Lett.*, vol. 83, pp. 4241–4244, Nov 1999.
- [86] S. Haino *et al.*, “Measurements of primary and atmospheric cosmic-ray spectra with the BESS-TeV spectrometer,” *Phys. Lett. B*, vol. 594, no. 1-2, pp. 35–46, 2004.
- [87] P. Archard *et al.*, “Measurement of the atmospheric muon spectrum from 20 to 3000 GeV,” *Phys. Lett. B*, vol. 598, pp. 15–32, 2004.
- [88] H. Jokisch *et al.*, “Cosmic-ray muon spectrum up to 1 TeV at 75° zenith angle,” *Phys. Rev. D*, vol. 19, p. 1368, 1979.
- [89] J. Wentz *et al.*, “Delayed muons and their relation to primary cosmic rays,” in *24th International Cosmic Ray Conference*, pp. 520–523, 1995.
- [90] R. R. Daniel and S. A. Stephens, “Cosmic-ray-produced electrons and gammas in the atmosphere,” *Rev. Geophys. Space Phys.*, vol. 12, pp. 233–258, May 1974.
- [91] M. Yamashita, “Cosmic-ray produced neutrons at ground level: Neutron production rate and flux distribution,” *J. Geophys. Res.*, vol. 71, no. 16, pp. 3817–3834, 1969.
- [92] J. Farine. PhD thesis, Neuchatel University, 1996.
- [93] National Council on Radiation Protection and Measurements No. 94, “Exposure of the population in the United States and Canada from natural background radiation,” Bethesda, MD, 1987.
- [94] A. R. Smith Private communication.
- [95] ENDF/B-VI: Cross Section Evaluation Working Group, “ENDF/B-VI Summary Document, Report BNL-NCS-17541,” Tech. Rep. ENDF-201, National Nuclear Data Center, Brookhaven National Laboratory, Upton, NY, USA, 1991.
- [96] L. Ekström and R. Firestone, “WWW Table of Radioactive Isotopes, database version 2.1.” Web site, January 2004. <http://ie.lbl.gov/toi/index.asp>.
- [97] J. A. S. Adams, W. M. Lowder, and T. F. Gesell, eds., *The physics of environmental radiation fields*, vol. 1, (Oak Ridge, Tennessee), United States Atomic Energy Commission, 1975.
- [98] C. J. Martoff, “COSMO- a program to estimate spallation radioactivity produced in a pure substance by exposure to cosmic radiation on the earth,” *Comput. Phys. Commun.*, vol. 72, pp. 96–103, 1992.

- [99] J. F. Wilkerson Private communication.
- [100] K. Rielage, “KATRIN electron gun testing of detector dead layers,” annual report, University of Washington Center for Experimental Nuclear Physics and Astrophysics, 2004.
- [101] M. C. Lepy *et al.*, “Comparison of experimental and theoretical L X-ray emission probabilities of ^{241}Am , ^{239}Pu and ^{240}Pu ,” *Nucl. Instrum. Meth. A*, vol. 353, pp. 10–15, 1994.
- [102] H. R. Bilger, “Fano factor in germanium at 77°K ,” *Phys. Rev.*, vol. 163, p. 238, 1967.
- [103] Nuclear Instruments and Detectors Committee, “IEEE standard test procedures for germanium gamma-ray detectors,” Tech. Rep. ANSI/IEEE Std 325-1986, The Institute of Electrical and Electronics Engineers, 1987.
- [104] P. Jagam and J. J. Simpson, “Measurements of Th, U and K concentrations in a variety of materials,” *Nucl. Instrum. Meth.*, vol. A324, pp. 389–398, 1993.
- [105] P. Renschler, “KESS user manual,” tech. rep., Karlsruhe Institute of Technology, 2009.
- [106] M. Leber, “Detector background simulations for the KATRIN experiment,” tech. rep., University of Washington, 2006.
- [107] D. S. Leonard *et al.*, “Systematic study of trace radioactive impurities in candidate construction materials for EXO-200,” *Nucl. Instrum. Meth. A*, vol. 591, pp. 490–509, 2008.
- [108] M. Howe, “Data acquisition system design document KATRIN experiment,” tech. rep., University of Washington, 2007.
- [109] A. Kopmann, “DAQ and slow control for KATRIN.” KATRIN Collaboration Meeting Presentation, October 2008.
- [110] F. Hubert *et al.*, “Ultra low radioactivity measurements in the Fréjus underground laboratory,” *Nucl. Phys. B (Proc. Suppl.)*, vol. 28A, pp. 425–429, 1992.
- [111] M. Steidl *et al.*, “Activity of rubalit samples.” Private communication.

Appendix A

IPE DAQ CHARACTERISTICS

This chapter gives a detailed description of the custom IPE DAQ hardware, data format, and user controls. Upgrades for the Mark IV version are listed at the end of the chapter.

A.1 Hardware

The custom IPE DAQ relies on field-programmable gate arrays FPGAs for flexibility and versatility. It is designed with a hierarchical trigger system using two custom cards, the First-Level Trigger (FLT) board and the Second-Level Trigger (SLT) board. Figure A.1 shows the flow of data through the IPE DAQ. The first-level trigger provides the pixel trigger and tags inter-board coincidences. The SLT tags coincidences across FLT boards and even across crates. The veto logic requiring a signal on both ends of a scintillator fiber can be programmed into the FLTs and SLTs. The status of the KATRIN veto can be associated with silicon detector events using the FLTs and SLTs.

The Mark III system consists of a 9u crate containing twenty custom Front-End Boards (FEB), one custom Second-Level-Trigger Interface Board (SIB), and a custom backplane. Each FEB is divided into an analog board which prepares the detector signals for digitization and a FLT board which digitizes and provides the pixel trigger and first-level trigger algorithms. The SIB board controls communication between the FEB boards and the DAQ computer and contains the SLT board.

A Mark III crate with ten Front-End Boards was tested at UW. The FEB input is a positive polarity signal through a ninety-six-pin ribbon cable connector. We invert the signal with a LEMO-to-ribbon-cable conversion board. Therefore, all tests were done with negative signals, mostly using an Agilent 33220 pulse generator. Each FEB card has twenty-two channels plus two specialized “sum” channels designed for the Auger experiment. The sum channels are not useable for KATRIN. Also, there is not adequate space in the FPGAs

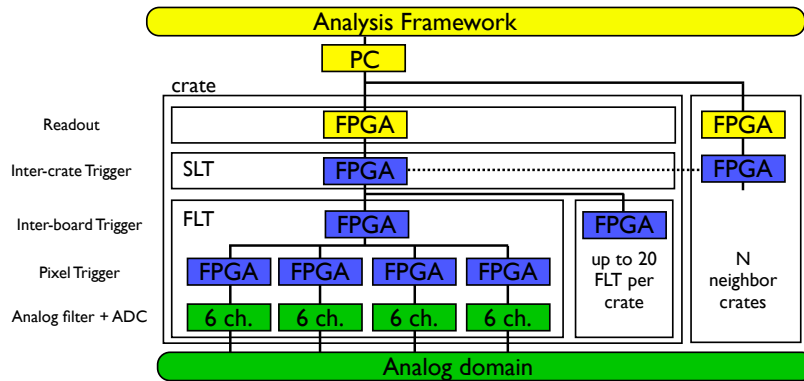


Figure A.1: Flow of signals through the IPE DAQ. The hierarchical trigger concept allows the tagging of coincidences within a First Level Trigger (FLT) board, across boards, and even across crates. Each crate contains up to twenty FLT's and one Second Level Trigger (SLT) board. Each FLT contains twenty-four ADCs, four peripheral FPGAs for filtering, and one central FPGA, which acts as a circular event buffer for the card.

to process all channels, so channels 10 and 11 are not filtered. Therefore, channels zero to nine and twelve to twenty-one are useable for KATRIN. In total, we had two hundred channels available.

A.1.1 Analog Boards

Input signals plug into the analog boards. An anti-aliasing filter removes high frequency components of the signal, preparing them for digitization.

A.1.2 First-Level Trigger Boards

The FLT's contain twenty-four ADCs, one for each channel, although only twenty channels are processed. The input is amplified with a programmable gain. The allowed range of input voltage to the ADC depends on the gain. The ADCs continuously digitize with 12-bit precision at a sampling rate of 10 MHz. Then, the ADC values are stored in 16 bit words in external SRAM memory.

Each channel has an external 16 bit×64K SRAM chip to store ADC values. The memory is organized into pages of 1024 ADC words, so the 64K external SRAM can store up to 64

Table A.1: Each peripheral FPGA is connected to a six-channel group, but due to space constraints only filters five channels. Only the filtered channels, shown in bold, are useable for KATRIN.

FPGA	Channel Group
FPGA6-A	0, 2, 4, 6, 8, 10
FPGA6-B	1, 3, 5, 7, 9, 11
FPGA6-C	12, 14, 16, 18, 20, 22
FPGA6-D	13, 15, 17, 19, 21, 23

pages. After a pixel trigger, the ADC values are read out in pages. The full set of ADC values for a single pixel trigger is called a waveform; the waveform can be a single page, 1024 words, or any number up to the maximum of 64 pages.

The ADC values are analyzed by four peripheral FPGAs. Each peripheral FPGA is programmed with a trapezoidal filter to find the peak height from the ADC values. The trapezoidal filter and pixel trigger algorithm are discussed in Section 5.2.1. Since four peripheral FPGAs analyze twenty channels, the filter values are not independent for each channel. Table A.1 shows which channels are filtered by the same peripheral FPGA, or are in the same channel group. The peripheral FPGAs are often labeled FPGA6, as in the table.

A fifth FPGA on the FLT is the central FPGA which handles the communication with the SLT and can be programmed with an inter-board trigger. Possibly the most important job of the the central FPGA is to act as a circular buffer in event mode, allowing 100% of events to be recorded. In both waveform and event mode, the central FPGA stores the “trigger data” in its internal 512×88 RAM for all channels on the FLT card. The trigger data includes the event time stamp, channel map, and event ID. The trigger data is 88 bits, so the central FPGA has a capacity for 512 events for the entire FLT card. When this buffer fills, event-mode events will be lost.

A.1.3 Second-Level Trigger Interface Boards

The control FPGAs on the SLT Interface Board (SIB) communicate with the DAQ computer via IEEE 1394, commonly known as Firewire. All FPGAs on the crate are programmed through the SIB. When necessary, this card provides an absolute time stamp to sync events with an external calibration source. An FPGA on the SIB can be programmed with a second-level trigger.

A.2 Data Acquisition Modes

This section describes the structure of data and readout rates in the three data acquisition modes: waveform, event, and histogram mode. The structure of the data as stored in an ORCA file is slightly different than the structure of the data read out from the IPE DAQ. In the Mark III design, all channels on the same card must acquire data in the same mode. The FPGAs can only be programmed with the code for a single mode due to memory constraints. Therefore, in Mark III, the FPGAs must be re-programmed to switch between event and histogram modes.

A.2.1 Debugging: Waveform Mode

In waveform mode, when an event passes the pixel trigger requirements, the entire waveform of ADC values are read out. As discussed in Section A.1.2, the ADC values are stored in the external SRAM in pages of 1024 values. The ADCs digitize at 10 MHz, so each time bin is 100 ns and a page is 102.4 μ s wide. A maximum of 64 pages can be stored in the external SRAM per pixel trigger, which creates a waveform 6.5 ms wide. The number of pages read out per waveform is set by the user, from 1 to 64. The users also sets the position of the step rise within the waveform with the “post trigger time.” With a post trigger time of 511, the trigger bit, explained below, falls 51.1 μ s before the end of the waveform, regardless of how many pages the waveform contains.

The ADC has a precision of 12 bits, but each ADC word contains 16 bits. As shown in Tab. A.2, the first 12 bits are the ADC values, ranging from 0 to 4095. Bit 12 indicates the input is out of range. If the input is below the allowed range, bit 12 will be set and bits 0

Table A.2: Structure of an ADC record for Mark III. The ADC values are sampled at 10 MHz. The trigger bit is set $3L/2$ bins after the input-pulse step rise.

Bit	Information
15	Trigger
14	Inhibit
13	Unused
12	Out of range
11	
.	
.	ADC values
.	
0	

to 11 will usually be zero, so the ADC value will usually be 4096. If the input voltage is too high, usually bits 0 to 11 will be set in addition to bit 12, so the ADC value will usually be 8191. The trigger bit is bit 15, set by the FPGAs when the pixel trigger conditions are met. This gives the waveform a large negative value—or positive for unsigned displays—at the bin $3L/2$ shaping lengths after the step rise.

In waveform mode, the ADC values are written to external SRAM, the trigger data is stored in the central FPGA, and peak heights are stored in the “energy registers.” The energy registers prevent 100% of events from being read out since there are twenty-four energy registers per card, one for each channel. When one channel passes the pixel trigger requirements, logging of ADC values stops for all channels on the FLT card until the waveform is read out and the software resets the FPGA. If the rate is high enough for pile-up to occur and two events pass the trigger requirement within one waveform, the second peak height overwrites the first in the energy register. In the Mark III design, two triggers in one waveform cause the waveform and peak heights to be read out twice, but both the peak-height values will correspond to the second trigger.

In addition to the waveforms, seven variables are read out and stored. Tab. A.3 shows the structure of a waveform-mode data record in ORCA. The first two rows are information from the ORCA software. The next four rows are the trigger data, stored in the central

Table A.3: ORCA data structure in the Waveform Mode. Chart length is 32 bits. The number of ADC values depends on the number of pages n , set by the user to be a number between 1 and 64. Chart taken from M. Howe [108] and ORCA code.

0	data ID (14 bits)	length (# longs) (17 bits)			
spare (7 bits)	crate (4 bits)	card (5 bits)	channel (8 bits)	spare (8 bits)	
second counter (32 bits)					
spare (8 bits)	sub-second counter (24 bits)				
channel (10 bits)	channel map (22 bits)				
spare (22 bits)	event ID (10 bits)				
spare (16 bits)			peak height (16 bits)		
reset second (32 bits)					
reset sub-second (32 bits)					
1st ADC value of $n \times 1024$			2nd ADC value of $n \times 1024$		
...					
2nd last ADC value (16 bits)			last ADC value (16 bits)		

FPGA. The second and sub-second counters are the time stamps of the events. The event ID is an integer from 0 to 1023 assigned to the event by the central FPGA. The channel map is a bit mask indicating how many channels trigger at one time. After the trigger data, the peak height, called “energy” in the ORCA code, is stored. In waveform mode, data taking stops on all channels after one trigger until ORCA resets the FLT card. The reset second and reset sub-second variables are the time stamp of the reset command, or the time data taking starts again. The next entries are the ADC values. The waveforms contain 1024 16 bit words per page, up to 64 pages. If a single page is read out, 512 words of ADC values follow the other variables. If 64 pages are read out, 32768 words follow.

A.2.2 Neutrino-Mass Data: Event Mode

In event mode, the ADC values are no longer written to the external SRAM. Instead, when a channel triggers, the peak height is written to the external SRAM. The external SRAM has room for many peak heights, unlike the single energy register used in waveform mode. The “trigger data” is stored in the central FPGA’s internal RAM. The central FPGA acts as a circular buffer for the entire card, allowing events to be read out as other events are

Table A.4: ORCA data structure in the Event Mode. Chart length is 32 bits. The first two rows are information from the ORCA software, the last read from hardware. Chart taken from M. Howe [108] and ORCA code.

0	data ID (14 bits)	length (# longs) (17 bits)			
spare (7 bits)	crate (4 bits)	card (5 bits)	channel (8 bits)	spare (8 bits)	
second counter (32 bits)					
spare (8 bits)	sub-second counter (24 bits)				
spare (10 bits)	channel map (22 bits)				
spare (7 bits)	page number (9 bits)		spare (6 bits)	event ID (10 bits)	
spare (16 bits)			peak height (16 bits)		

added. It prevents any dead time until the buffer reaches capacity at 512 events. The peripheral FPGAs continue to filter the ADC values as data is read out.

Tab. A.4 shows the data structure in the event mode. In this mode, no waveforms are read out. There are no reset time stamps, since data taking does not stop after events. The trigger data and peak heights are read out and have the same meaning as in waveform mode. In addition, the “page number” or “stored pages” variable is read out. This is not the same as the number of pages of a waveform. It is the number of pages recorded by the hardware when reading the actual event and is a type of load indicator.

A.2.3 Calibration: Histogram Mode

Histogram mode was designed to handle the highest rates. In this mode, the peak heights are stored in a histogram in the peripheral FPGA’s internal memory instead of being read out after each event. In Mark III, only one channel per channel group can take data in histogram mode. There is no time stamp associated with the peak height. The histograms have 512 bins, each 24 bits. The value of each bin indicates how many counts occurred with that peak height. Since the peak-height variable is a 16 bit variable, storing it in a 512 bin histogram loses information. The user can determine how this information is lost by setting the range of peak heights the histogram spans. The user defines the peak height of the first histogram bin and the peak-height width of each histogram bin. The user also sets the recording time for each histogram. There are always two histograms in memory: one that

Table A.5: ORCA data structure in the Histogram Mode. Chart length is 32 bits. The first two rows are information from the ORCA software, the last read from hardware. Chart taken from M. Howe [108] and ORCA code.

0	data ID (14 bits)	length (# longs) (17 bits)			
spare (7 bits)	crate (4 bits)	card (5 bits)	channel (8 bits)	spare (8 bits)	
readout second counter (32 bits)					
refresh time second counter (32 bits)					
first bin (32 bits)					
last bin (32 bits)					
histogram length (32 bits)					
max histogram length (32 bits)					
bin size of (32 bits)					
energy offset (32 bits)					
spare (8 bits)	1st bin content of 512 bins (24 bits)				
...					
spare (8 bits)	last bin content (24 bits)				

is actively being filled, the other to be read out.

Tab. A.5 shows the data structure in the histogram mode. Rows three through ten describe the histogram settings. Then, 512 words containing the histogram bin contents follow. In this mode, individual events do not have time stamps, but the time stamp of the histogram readout is recorded.

A.2.4 Data Transfer Rates

The amount of data and the transfer method across the IEEE 1394 or Firewire is different in each mode. Blocks of data up to 2KB can be transferred faster across Firewire than single access reads. The block transfer rate is 2.5 MB/s as opposed to 0.03 MB/s for single access. Waveforms, histograms, and blocks of “trigger data” in event mode can be transferred in blocks. All other data is transferred through single access. Table A.6 shows the total time it takes to read out data in each mode.

In waveform mode, the amount of data transferred depends on the number of pages n . Each page can be transferred in a block read, since a page is the block maximum of 2KB.

Table A.6: The time it takes to read out data in various modes. Rates from A. Kopmann [109].

Mode	Amount of data B	Data transfer rate MB/s	Readout duration ms
Waveform	ADCs: $n \times 2$ KB	2.5	$0.8 \times n + 1$
	Trigger data: 16	0.03	
	Peak heights: 4	0.03	
	Other: 12	0.03	
Single Event	Trigger data: 16	0.03	0.64
	Peak heights: 4	0.03	
Block Event (128 events)	Trigger data: 128×16	2.5	1.72
	Peak heights: 128×4	0.03	
	Other: 4	0.03	
Histogram	Histograms: 2 KB	2.5	0.8

Other variables are transferred in single access mode. Reading out the maximum number of pages, 64, takes 52 ms, but reading out a single page only takes 1.8 ms. Since data-taking stops on all channels during readout of a single channel, events that come within the readout time duration of the last event will be lost. The fraction of events lost in waveform mode depends on the total rate per FLT card and affects all channels on an FLT card. This is a non-paralyzable system, so the fraction of recorded events F_R depends on the true rate in the card R_T and the readout time duration ΔT , as in Eq. A.1.

$$F_R = \frac{1}{R_T \Delta T + 1} \quad (\text{A.1})$$

To read out 99% of events from a random signal, the rate in the entire card must stay below 5.6 Hz per page.

In event mode, “trigger data” can be read from the central FPGA’s RAM through single access or in a block transfer. A single event’s trigger data is 16 B, so a maximum of 128 events can be transferred in a block. Other data must be transferred in single access mode. Since the central FPGA serves as the circular buffer for an entire FLT card, events will

be lost from all channels when the central FPGA fills up. This happens when the rate of incoming events across the card is higher than the rate that events are read out. In block mode, the maximum data transfer rate is 128 events/1.72 ms, or 7.7 kHz. Due to the circular buffer, the system should not lose any events if the event rate is lower than the maximum data transfer rate.

In histogram mode, the rate that histograms are read out is set by the user, from once per second to once every ten seconds. Histograms are transferred in block mode, which is fast enough to transfer a histogram every second without a loss of events. Events can only be lost if a histogram bin fills up before the histogram is read out. If the 24 bit bins are read out every second, this would occur at a rate of $(2^{24} - 1)$ events/bin/second, or 16.8 MHz. Event rates will not be this high even during calibrations.

A.3 User Controls

As mentioned in Section 5.2, digital signal processing gives the user control over the filter parameters. This subsection lists the variables the user can control in the Mark III system.

A.3.1 Gain

The gain is applied at the ADC and can be changed independently for each channel. Increasing the gain increases the input pulse step and noise fluctuations, but does not shift the baseline, which is consistently offset to 110. The input range of the ADC depends on the gain. The gain settings are integers ranging from 0 to 255. The ADC values increase a factor of 10 with a gain increase from 0 to 255. At a gain of one hundred, the input voltage range is 0 to 250 mV.

If the input exceeds the ADC range, no error is generated, so the user must check that the input is within the ADC range for every gain setting. There are two ways for the user to check that the input is within the ADC range. The best method is to look for the out-of-range bit in the ADC values in waveform mode. If the input is too high, the ADC value will usually be 8191. If the input is too low, the ADC value will usually be 4096. The second method is to check that the peak heights are within the maximum range. The peak-height

range also depends on the shaping length and gap as discussed in the next section, so the user should set the gain in waveform mode to observe the ADC values.

A.3.2 Shaping Length

The shaping length determines the number of bins that are summed in the trapezoidal filter. A longer shaping length averages over more noise, lengthens the trapezoidal pulse, and increases the peak height. The peak height is not normalized by the shaping length, so increasing the shaping length appears to increase the gain. The shaping length must be the same for each channel in a six-channel group analyzed by one peripheral FPGA. The user can select the length in bins ranging from 1 to 128 in powers of 2. Each bin is 100 ns, so a shaping setting of 32 corresponds to $3.2 \mu\text{s}$. For a silicon detector pulse, we expect to use shaping times of $3.2 \mu\text{s}$ or $6.4 \mu\text{s}$.

The maximum calculable peak-height value is 128×4095 , the longest shaping setting times the ADC maximum. Therefore, the peak-height values can span 19 bits, but only 16 bits are read out and the peak height is truncated. In the Mark III crate, bits 3 to 18 of the peak-height values are read out. This means the peak height is shifted 3 bits, or divided by 8. In very early versions of the Mark III crate, bits 4 to 19 were read out, so the peak height was shifted by 4 bits, or divided by 16.

A 16 bit peak height can range from 0 to 65,535, but the maximum calculable peak height is less than this for shorter shaping lengths. Table A.7 shows the maximum peak-height value $L \times 4095$ for each shaping length L . Due to the ADC baseline offset of 110, calculated peak heights are about $L \times 110$ less than the maximum. The IPE DAQ does not flag an error if the ADC out-of-range bit is set, so the user must check that the peak heights are well within the expected range for the shaping setting or check the waveforms. Note that a shaping length setting of one appears to be the same as a shaping length setting of two.

A.3.3 Gap

The gap setting affects an entire FLT card. The user can choose a gap setting of 0 to 3. As described in Section 5.2.1, the current implementation subtracts the number of bins equal

Table A.7: The range of calculable peak heights is different for each shaping length and gap. This table shows the maximum peak height for each shaping length with a gap of zero. The observable peak heights are about $110 \times L$ less than this due to the ADC baseline of about 110.

Shaping Length	Max Peak Height
1	1023
2	1023
4	2047
8	4095
16	8190
32	16380
64	32760
128	65520

to the gap setting from each side of the trapezoidal filter. Therefore, if the gap setting is 2, the trapezoid has a flat top 4 bins wide. The gap implementation in the Mark IV version will be different.

A.3.4 Threshold Settings

The threshold is set independently for every channel. The threshold setting is compared to the peak height, so it defines the lowest peak-height value that will be read out, independent of gain or shaping length setting. The thresholds are 16 bits, but the calculated peak height is 19 bits shifted by 3 bits. Therefore, bits 3 to 18 of the calculated peak height must be greater than bits 0 to 15 of the threshold to satisfy the pixel trigger condition.

A.4 Recursive Trapezoidal Filter

In contrast to the discussion in Section 5.2.1, filtering is usually done recursively in the FPGAs. The simple trapezoidal filter can be implemented recursively as:

$$T[i] = T[i-1] + ADC[i] - ADC[i-L+G] - ADC[i-L-G] + ADC[i-2L];$$

Where $T[i]$ is the i -th value of the trapezoidal filter, $ADC[i]$ is the i -th digitized value in the waveform, L is the shaping length, and G is the gap and half the total flat top length.

A pole zero correction, described in Section 5.3.3, can be added by filtering the simple trapezoidal values $T[i]$:

$$PZ[i] = PZ[i-1] + T[i] + \tau \times (T[i] - T[i-1]);$$

Here, τ is the fall time of the pulse and $PZ[i]$ is the i -th value of the pole-zero corrected trapezoidal filter.

The correction can be done all at once as well:

$$d[i] = ADC[i] - ADC[i-L+G] - ADC[i-G-L] + ADC[i-2L];$$

$$T[i] = T[i-1] + d[i];$$

$$PZ[i] = PZ[i-1] + T[i] + \tau \times d[i];$$

In this case, $PZ[i]$ is the i -th value of the pole-zero corrected trapezoidal filter, $T[i]$ is the i -th value of the simple trapezoidal filter, and $d[i]$ is the change to the simple filter value at each step.

A.5 Upgrades for Mark IV

The Mark IV DAQ system will be available for testing in 2009. It uses a 6u crate because the custom cards have been reduced in size. The SIB cards are upgraded to contain a single-board computer running Linux, replacing the control FPGA. The connection to the DAQ computer is via gigabit ethernet instead of IEEE 1394 Firewire. The FPGAs on the FLT board have a larger memory, so all DAQ modes will be available without reprogramming the FPGAs. Also, different DAQ modes can run on the same card. There will be twenty-four channels filtered by three FPGAs per FLT card. The ADC sample rate will increase to 20 MHz with an increased precision of 14 bits. The histogram mode histograms will increase from 512 bins to 2048 bins, and each bin will be 32 bits, up from 24 bits. The veto will first be tested with Mark IV. A pole-zero correction will be implemented in the trapezoidal filter. The upgrades should reduce the dead time in waveform mode, so it will be used for taking neutrino-mass data.

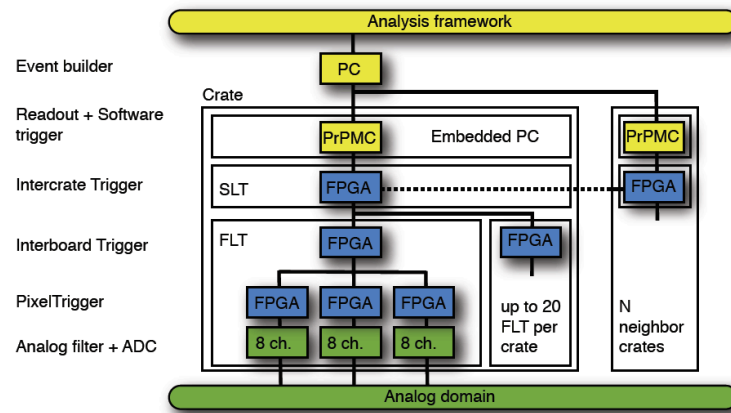


Figure A.2: Flow of signals through the Mark IV IPE DAQ. In this design, there are 3 FPGAs per FLT and a single-board computer communicates with the DAQ computer. Figure from A. Kopmann [62].

Appendix B

RADIOACTIVITY IN THE DETECTOR COMPONENTS

Specific activity, the number of decays per second, is measured in Bq/kg. Impurity is often measured in part-per-billion (ppb), or nanograms of impurity per gram of material (ng/g). The conversion for each isotope is different, and depends on the isotope half-life λ , the element's atomic weight A , and the isotope's natural abundance C :

$$1 \text{ Bq/kg} \hat{=} \frac{A}{C\lambda N_A} 10^6 \text{ ng/g}. \quad (\text{B.1})$$

The natural abundances of ^{238}U and ^{232}Th are close to one, but the abundance of ^{40}K is 0.012%, which accounts for the very different conversion from ^{40}K specific activity to concentration of K. The conversion factors for each isotope are:

$$\begin{aligned} 1 \text{ Bq } ^{238}\text{U} / \text{kg} &\hat{=} 81 \text{ ng U} / \text{g} \text{ (81 ppb U)}, & (\text{B.2}) \\ 1 \text{ Bq } ^{232}\text{Th} / \text{kg} &\hat{=} 246 \text{ ng Th} / \text{g} \text{ (246 ppb Th)}, \\ 1 \text{ Bq } ^{40}\text{K} / \text{kg} &\hat{=} 32 \mu\text{g K} / \text{g} \text{ (32 ppm K)}. \end{aligned}$$

B.1 Component Masses and Activities

All sources that are separated from the detector by more than a few mm of material were simulated with the `CalibrationGenerator`. Components with direct sight of the detector were simulated with the `GRDM`. All tables in this section are divided between the two types of simulation.

To convert from specific activity to total activity, we multiply by the component mass. Table B.1 lists the mass of each component as calculated by the `Geant4` simulation. To check that the simulation geometry was correctly defined, these masses were compared with engineering drawings.

Table B.1: Mass of each component in the simulation.

Component	Material	Mass [kg]
<hr/> GRDM <hr/>		
Pogo Pins (196)	Copper/Beryllium	0.011
Readout Pins (196)	Niobium	0.0094
Readout Sleeves for Insulators (196)	Niobium	0.0042
Feed-through Insulators (196)	Sapphire	0.014
Detector Stand	Copper	0.073
Conflat Flange	Stainless Steel	4.1
Post-acceleration Electrode	Copper	9.1
<hr/> CalibrationGenerator <hr/>		
Preamp Boards (24)	Rubalit 710	0.40
Distribution and Cable Boards	Rogers 4000	0.17
Preamp Cooling Structure	Copper	3.2
Large Telescoping Insulator	Quartz	5.5
Medium Telescoping Insulator	Quartz	1.9
Large Ceramic Insulator	Ceramic	12.3
Small Ceramic Insulator	Ceramic	1.4
Vacuum Tube	Stainless Steel	22
Copper Shield	Copper	88
Lead Shield	Lead	392
Plastic Scintillator	Plastic	13.7
Magnet Coils	Copper/Titanium/Niobium	126
Magnet Coil Banding	Aluminum	60

Table B.2: Measured and estimated uranium impurities. All measurements were made by Al Smith except as noted [94].

Material	Specific Activity ^{238}U [Bq kg ⁻¹]	Impurity [ng/g]	Meas. Date
GRDM			
Pogo Pins (Copper/Beryllium)	0.86 ± 0.12 (early) < 0.04 (late)	70 ± 10 < 3	5/28/08
Readout Pins and Sleeves (Niobium)	0.74 ± 0.12 (early) < 0.06 (late)	60 ± 10 < 5	4/28/2008 4/28/2008
Feed-through Insulators (Sapphire)	0.74 ± 0.12 (early) < 0.06 (late)	60 ± 10 < 5	4/28/2008 4/28/2008
Detector Stand (Copper)	< 0.005	< 0.4	est. [110]
Conflat Flange (Stainless Steel)	< 0.004	< 0.3	2/19/08
Post-Acceleration Electrode (Copper)	< 0.005	< 0.4	est. [110]
CalibrationGenerator			
Preamp Boards (Rubalit 710)	3.85 ± 1.31	312 ± 106	3/6/08 [111]
Distribution and Cable Boards (Rogers 4000)	2.5 ± 0.5	200 ± 43	est. [104]
Preamp Cooling (Copper)	< 0.005	< 0.4	est. [110]
Telescoping Insulators (Quartz)	0.47 ± 0.05	38 ± 4	est. [104]
Ceramic Insulators	3.3 ± 0.12	270 ± 10	6/7/08
Vacuum Tube (Stainless Steel)	< 0.004	< 0.3	est. [94]
Copper Shield	< 0.005	< 0.4	est. [110]
Lead Shield	< 0.004	< 0.3	est. [110]
Plastic Scintillator	0.033	2.7	est. [110]
Magnet Coil (Cu/Ti/Nb)	0.25 ± 0.12	20 ± 10	3/12/07
Magnet Coil Banding (Aluminum)	10 ± 1.2 (early) < 0.25 (late)	800 ± 100 < 20	3/24/09 3/24/09

Table B.3: Measured and estimated thorium impurities. All measurements were made by Al Smith [94] except as noted.

Material	Specific Activity ^{232}Th [Bq kg ⁻¹]	Impurity [ng/g]	Meas. Date
GRDM			
Pogo Pins (Copper/Beryllium)	< 0.041	< 10	5/28/08
Readout Pins and Sleeves (Niobium)	< 0.041	< 10	4/28/2008
Feed-through Insulators (Sapphire)	< 0.041	< 10	4/28/2008
Detector Stand (Copper)	< 0.0057	< 1.4	est. [110]
Conflat Flange (Stainless Steel)	< 0.004	< 1	2/19/08
Post-Acceleration Electrode (Copper)	< 0.0057	< 1.4	est. [110]
CalibrationGenerator			
Preamp Boards (Rubalit 710)	0.7 ± 0.3	172 ± 74	3/6/08 [111]
Distribution and Cable Boards (Rogers 4000)	2.8 ± 0.4	690 ± 90	est. [104]
Preamp Cooling (Copper)	< 0.0057	< 1.4	est. [110]
Telescoping Insulators (Quartz)	0.07 ± 0.03	18 ± 6	est. [104]
Ceramic Insulators	1.2 ± 0.1	300 ± 30	6/7/08
Vacuum Tube (Stainless Steel)	< 0.004	< 1	est. [94]
Copper Shield	< 0.0057	< 1.4	est. [110]
Lead Shield	< 0.005	< 1.2	est. [110]
Plastic Scintillator	< 0.02	< 5	est. [110]
Magnet Coil (Cu/Ti/Nb)	0.20 ± 0.041	50 ± 10	3/12/07
Magnet Coil Banding (Aluminum)	1.0 ± 0.3	250 ± 70	3/24/09

Table B.4: Measured and estimated potassium impurities. All measurements were made by Al Smith [94] except as noted.

Material	Specific Activity ^{40}K [Bq kg $^{-1}$]	Impurity [$\mu\text{g/g}$]	Meas. Date
GRDM			
Pogo Pins (Copper/Beryllium)	< 0.125	< 4	5/28/08
Readout Pins and Sleeves (Niobium)	0.84 ± 0.28	27 ± 9	4/28/2008
Feed-through Insulators (Sapphire)	0.84 ± 0.28	27 ± 9	4/28/2008
Detector Stand (Copper)	< 0.05	< 1.6	est. [110]
Conflat flange (Stainless Steel)	< 0.013	< 0.4	2/19/08
Post-Acceleration Electrode (Copper)	< 0.05	< 1.6	est. [110]
CalibrationGenerator			
Preamp Boards (Rubalit 710)	< 2.2	< 70	3/6/08 [111]
Distribution and Cable Boards (Rogers 4000)	2.8 ± 0.9	90 ± 30	est. [104]
Preamp Cooling (Copper)	< 0.05	< 1.6	est. [110]
Telescoping Insulators (Quartz)	0.31 ± 0.16	10 ± 5	est. [104]
Ceramic Insulators	28 ± 3.1	900 ± 100	6/7/08
Vacuum Tube (Stainless Steel)	< 0.013	< 0.4	est. [94]
Copper Shield	< 0.05	< 1.6	est. [110]
Lead Shield	< 0.03	< 1.1	est. [110]
Plastic Scintillator	< 0.17	< 5.5	est. [110]
Magnet Coil (Cu/Ti/Nb)	0.56 ± 0.28	18 ± 9	3/12/07
Magnet Coil Banding (Aluminum)	< 0.6	< 20	3/24/09

The activity of each component was either measured or estimated based on activities listed in the literature. Samples were most often assayed individually by Al Smith [94]. The niobium pins, sleeves, and sapphire feed-through insulators were assayed together, so we assume the same activity for all three components. All chains are assumed to be in equilibrium. The measurements of multiple components indicated the uranium chain was out of equilibrium. In these cases, we assumed the higher impurity level and equilibrium. The copper-clad samples of the Rubalit alumina used for the preamp boards were measured by our colleagues in KIT [111], not by Al Smith.

Not all components have been assayed. For components made of the same material as an assayed component, we assumed the same activity for both components. For example, we assume all steel parts have the same activity as the steel conflat flange. Other component activities were taken from the literature. Tables B.2, B.3 and B.4 list the measured and estimated activities for all components.

Table B.5: Background rates from uranium simulated with the GRDM.

Source	18.6 keV	28.6 keV	38.6 keV	48.6 keV
Uranium	μHz	μHz	μHz	μHz
Pogo Pins	63.6 ± 2.5	28.9 ± 1.7	23.8 ± 1.5	17.2 ± 1.3
Nb Readout Pins	9.9 ± 0.8	3.2 ± 0.5	2.9 ± 0.5	1.9 ± 0.4
Nb Readout Sleeves	10.6 ± 0.6	3.7 ± 0.3	3.1 ± 0.3	1.8 ± 0.2
Feed-through Insulators	10.5 ± 1.0	3.9 ± 0.6	2.6 ± 0.5	2.2 ± 0.5
Detector Stand	0.2 ± 0.0	0.1 ± 0.0	0.1 ± 0.0	0.0 ± 0.0
Post-Acc. Electrode	< 3.0	< 1.8	< 1.8	< 1.8
Conflat Flange	2.6 ± 0.7	< 1.9	< 2.1	1.8 ± 0.5

Table B.6: Background rates from thorium simulated with the GRDM.

Source	18.6 keV	28.6 keV	38.6 keV	48.6 keV
Thorium	μHz	μHz	μHz	
Pogo Pins	2.7 ± 0.1	1.1 ± 0.1	0.7 ± 0.1	0.5 ± 0.0
Nb Readout Pins	0.5 ± 0.0	0.2 ± 0.0	0.1 ± 0.0	0.1 ± 0.0
Nb Readout Sleeves	0.5 ± 0.0	0.2 ± 0.0	0.1 ± 0.0	0.1 ± 0.0
Feed-through Insulators	0.6 ± 0.1	0.2 ± 0.0	0.2 ± 0.0	0.1 ± 0.0
Detector Stand	0.1 ± 0.0	0.1 ± 0.0	< 0.0	0.0 ± 0.0
Post-Acc. Electrode	< 4.1	< 2.0	< 2.0	< 2.0
Conflat Flange	4.3 ± 0.8	2.1 ± 0.6	2.0 ± 0.6	< 2.1

B.2 Background Rates from Radioactivity in the Components

The background rate from individual components simulated with the GRDM are listed in Tab. B.5, B.6, and B.7. The uranium in the pogo pins is the largest contribution to the GRDM background.

Components simulated with the `CalibrationGenerator` are listed in Tab. B.8, B.9, and B.10. The large ceramic insulator and the preamp boards contribute the largest background rate.

Table B.7: Background rates from potassium simulated with the GRDM.

Source	18.6 keV	28.6 keV	38.6 keV	48.6 keV
Potassium	μHz	μHz	μHz	μHz
Pogo Pins	1.6 ± 0.3	0.9 ± 0.2	< 0.7	< 0.6
Nb Readout Pins	0.9 ± 0.3	0.9 ± 0.3	< 0.7	< 0.6
Nb Readout Sleeves	1.7 ± 0.2	0.7 ± 0.2	< 0.5	0.8 ± 0.2
Feed-through Insulators	< 1.8	< 1.1	< 1.2	< 0.5
Detector Stand	0.1 ± 0.0	< 0.0	< 0.0	< 0.0
Post-Acc. Electrode	< 1.5	< 1.8	< 0.9	< 0.9
Conflat Flange	1.1 ± 0.2	< 0.6	< 0.5	< 0.4

Table B.8: Background rates from uranium simulated with the CalibrationGenerator.

Source	18.6 keV	28.6 keV	38.6 keV	48.6 keV
Uranium	μHz	μHz	μHz	μHz
Dist. and Cable Boards	6.8 ± 1.1	4.3 ± 0.8	2.3 ± 0.6	2.0 ± 0.6
Preamp Boards	49.3 ± 7.7	39.7 ± 6.9	34.8 ± 6.5	20.4 ± 5.0
Preamp Cooling	< 0.5	< 0.4	< 0.6	< 0.2
Copper Shield	< 4.6	< 2.7	< 2.7	< 2.7
Lead Shield	1.6 ± 0.4	1.2 ± 0.3	< 1.0	< 1.1
Med. Tel. Quartz	22.8 ± 2.4	15.5 ± 2.0	11.4 ± 1.7	6.1 ± 1.2
Lar. Tel. Quartz	30.7 ± 3.4	11.9 ± 2.1	11.9 ± 2.1	11.9 ± 2.1
Sm. Ceramic Ins.	< 12.2	< 5.1	< 8.8	< 5.1
Magnet Coils	< 12.7	< 12.7	< 12.7	< 12.7
Magnet Banding	< 74.0	< 25.5	< 32.1	< 25.5
Lar. Ceramic Ins.	67.0 ± 11.0	30.8 ± 7.5	27.1 ± 7.0	< 21.3
Vacuum Tube	< 1.2	< 1.2	< 1.0	< 0.7
Scintillator	< 1.8	< 1.8	< 1.8	< 1.8

Table B.9: Background rates from thorium simulated with the CalibrationGenerator.

Source	18.6 keV	28.6 keV	38.6 keV	48.6 keV
Thorium	μHz	μHz	μHz	μHz
Dist. and Cable Boards	9.4 ± 0.7	5.4 ± 0.6	3.5 ± 0.4	2.8 ± 0.4
Preamp Boards	16.1 ± 4.1	< 5.7	< 7.2	< 11.3
Preamp Cooling	< 0.5	< 0.7	< 0.5	< 0.4
Copper Shield	4.2 ± 1.2	< 3.4	< 2.1	< 2.6
Lead Shield	< 6.0	< 6.0	< 2.9	< 2.9
Med. Tel. Quartz	3.6 ± 0.7	1.7 ± 0.5	< 1.8	< 1.8
Lar. Tel. Quartz	5.9 ± 1.2	2.9 ± 0.8	< 3.2	< 1.0
Sm. Ceramic Ins.	< 6.0	< 3.4	< 2.5	< 2.5
Magnet Coils	< 14.0	< 6.3	< 4.6	< 6.3
Magnet Banding	< 23.4	< 9.8	< 9.8	< 9.8
Lar. Ceramic Ins.	31.0 ± 5.4	18.8 ± 4.2	14.1 ± 3.6	< 14.5
Vacuum Tube	0.9 ± 0.1	0.5 ± 0.1	0.3 ± 0.1	0.4 ± 0.1
Scintillator	< 1.4	< 1.4	< 1.4	< 1.4

Table B.10: Background rates from potassium simulated with the CalibrationGenerator.

Source	18.6 keV	28.6 keV	38.6 keV	48.6 keV
Potassium	μHz	μHz	μHz	μHz
Dist. and Cable Boards	< 0.6	< 0.3	< 0.4	< 0.2
Preamp Boards	1.1 ± 0.3	< 1.3	< 1.1	< 1.0
Preamp Cooling	0.2 ± 0.1	< 0.2	< 0.2	< 0.1
Copper Shield	< 1.7	< 2.3	< 1.7	< 1.7
Lead Shield	< 4.6	< 4.6	< 4.6	< 4.6
Med. Tel. Quartz	< 0.8	< 0.9	< 0.4	< 0.7
Lar. Tel. Quartz	< 2.2	< 1.6	< 1.1	< 0.9
Sm. Ceramic Ins.	< 5.2	< 2.5	< 2.5	< 2.5
Magnet Coils	< 3.1	< 3.1	< 3.1	< 3.1
Magnet Banding	< 4.9	< 4.9	< 4.9	< 4.9
Lar. Ceramic Ins.	34.4 ± 7.5	23.0 ± 6.1	23.0 ± 6.1	< 25.3
Vacuum Tube	< 0.3	< 0.3	< 0.3	< 0.2
Scintillator	< 1.2	< 0.9	< 0.9	< 0.9

Table B.11: Cosmogenic activity calculated for copper and steel assuming a 5-year exposure and no cooldown. The activities are calculated using the COSMO code [98].

Copper		Steel (Ni-Fe-Cr)	
Nuclide	Activity [Bq kg ⁻¹]	Nuclide	Activity [Bq kg ⁻¹]
⁸ Li	9.11×10^{-5}	⁷ Be	3.41×10^{-5}
¹² B	1.58×10^{-4}	⁴⁶ Sc	1.02×10^{-4}
⁴⁹ V	1.04×10^{-4}	⁴⁹ V	5.32×10^{-4}
⁵⁴ Mn	2.02×10^{-4}	⁵⁴ Mn	7.99×10^{-4}
⁵⁵ Fe	2.22×10^{-4}	⁵⁵ Fe	4.22×10^{-4}
⁵⁷ Co	3.76×10^{-4}	⁵⁶ Co	2.81×10^{-5}
⁵⁸ Co	7.97×10^{-4}	⁵⁷ Co	1.22×10^{-4}
⁶⁰ Co	6.19×10^{-4}	⁵⁸ Co	5.48×10^{-5}

B.3 Cosmogenic Activities

The produced activity of cosmogenic isotopes was estimated with the COSMO code [98]. Tables B.11 and B.12 list the estimated activities. Since early prediction indicate cosmogenics do not contribute a large background rate, these have not been included in the background estimates in this dissertation.

Table B.12: Cosmogenic activity for silicon and ceramic assuming a 5-year exposure and no cooldown. The activities were calculated using the COSMO code [98].

Silicon		Ceramic (Al₂O₃)	
Nuclide	Activity [Bq kg⁻¹]	Nuclide	Activity [Bq kg⁻¹]
²⁶ Si	3.36×10^{-3}	⁷ Be	3.71×10^{-4}
²⁷ Si	3.47×10^{-3}	¹⁵ C	8.13×10^{-4}
²⁷ Mg	9.3×10^{-4}	¹⁴ O	2.86×10^{-3}
²⁸ Al	1.13×10^{-3}	¹⁵ O	2.94×10^{-3}
		²² Na	3.73×10^{-4}
		²⁶ Na	5.43×10^{-4}
		²⁷ Mg	5.51×10^{-4}
		²⁵ Al	1.90×10^{-3}

Appendix C

COMPARISON WITH PREVIOUS SIMULATIONS

The first background estimates for KATRIN of Schwamm [57] are very different than the results of this dissertation. As discussed in Section 4.3.2, Schwamm predicted visible X rays and a large minimum ionizing particle bump in the total background spectrum from radioactivity. We have optimized the KATRIN detector region design based on predictions of both simulations to reduce the backgrounds. The novel pogo-pin connections and radio-pure sapphire feed-throughs of the current design minimize the radioactivity behind the detector, significantly reducing the contribution from electrons and X rays. Therefore, the current KATRIN detector region design should have a different background than the preliminary design used by Schwamm.

To ensure that the background estimates from the two simulations are different only due to the design changes, two of Schwamm's results are reproduced here. Using the detector geometry of Schwamm, natural radioactivity in the detector mount—replaced by the pogo-pins in the current design—and cosmic-ray muons have been simulated and the rates are directly compared in the three ROI. This compares the assumptions of the two simulations, including the initial energy spectra, the choice of physics list which determines how particles interact, and assumptions about the detector and scintillator response. Outside the ROI, the cosmic-ray muon spectrum of Schwamm can be directly compared to this work. Conversely, the background spectra from the ceramic mount cannot be directly compared; the plots of Schwamm show all sources of uranium and thorium combined together. Therefore, Schwamm's total spectra from uranium and thorium have been scaled to estimate the contribution from the ceramic mount.

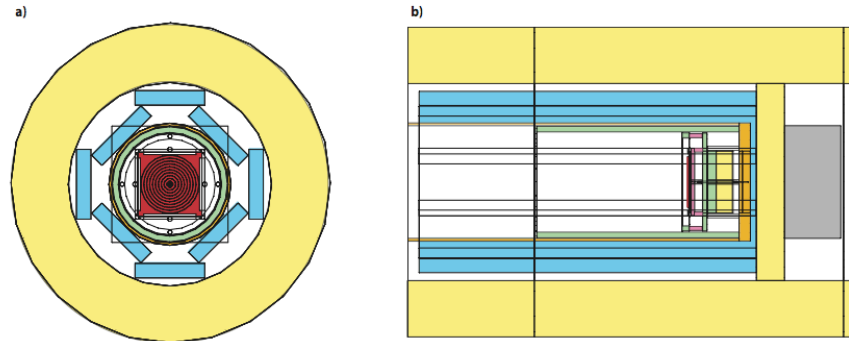


Figure C.1: The detector region of Schwamm. The silicon detector is shown in red, the scintillator panels in cyan, and the lead shield in yellow.

C.1 Detector Geometry and Response

The preliminary design of the KATRIN detector region used by Schwamm is shown in Fig. C.1. For this comparison, the code defining the detector geometry is copied from Schwamm, but the response of the detectors is similar to the response outlined in Sections 6.1.1 and 6.1.1. The silicon diode detector, shown in red, is $300\ \mu\text{m}$ thick. The active area of the detector is 10 cm in diameter and is divided into ten concentric circular pixels. Each of the ten circular pixels acts independently. Schwamm did not include noise, so no electronic or statistical noise is added to the silicon detector. Although the ceramic mount is a large source of background, it is a small piece of ceramic; it is 0.65 mm thick and has a mass of 61.9 g. The ceramic mount is separated from the detector by a thin layer of vespel or polyimide, 0.125 mm thick.

Outside the detector are eight plastic scintillator panels shown in cyan in Fig. C.1. The panels are shorter and thicker than the current design—60 cm long and 2.5 cm thick—and there is no end-cap panel. To veto a count, one scintillator panel must have greater than 3 MeV deposited energy within $1\ \mu\text{s}$ of a count in the detector. This energy threshold is just below the minimum ionizing particle bump in the plastic scintillator; the threshold is

Table C.1: Direct comparison of background rates from ^{232}Th chain decays in the ceramic detector mount. Rates calculated by Schwamm are taken from Schwamm’s Tab. B.3, B.4, and 6.3.

^{232}Th Region of Interest	Schwamm Rate (mHz) R_S	This work Rate (mHz) R_T	Difference $\frac{R_T - R_S}{R_T}$
15.9-19.4 keV	2.599	2.73 ± 0.10	4.8%
36.9-39.5 keV	0.198	0.183 ± 0.017	-8.2%
47.1-49.5 keV	0.145	0.180 ± 0.017	19.4%

higher than for the KATRIN design because Schwamm’s scintillator panels are thicker.

A 10 cm thick lead shield surrounds the scintillators, shown in yellow. The shield is also shorter than the current shield at 80 cm long. No magnetic fields are included in either Schwamm’s simulation or this reproduction.

C.2 Natural Radioactivity in the Ceramic Mount

To model ^{238}U and ^{232}Th decays, Schwamm used a custom tool to generate the alphas, betas, and photons. Each particle was generated in a separate event preventing the possibility of summation of particles. This work utilizes the GRDM, corrected for low-energy photons as described in Section 6.2.2. Both Schwamm and this work assumed 13.46 Bq/kg of uranium and 4.91 Bq/kg of thorium spread evenly throughout the ceramic mount.

Schwamm used different regions of interest (ROI) than are used in this dissertation. The Lowest ROI (LROI) assumes no post-acceleration and falls between 15.9–19.4 keV. The Middle Region of Interest (MROI), 36.9–39.5 keV, is above the X rays of thorium and uranium. The Highest Region of Interest (HROI), 47.1–49.5 keV, is just above the 45 keV photon released by ^{210}Pb .

Table C.1 compares the calculated backgrounds for thorium; the rates agree. Table C.2 shows the calculated rates for uranium. This work calculates a higher rate for uranium by almost a factor of two in all ROIs. The reason for the difference is not known.

Comparing the rates in the ROI does not yield any information about the agreement

Table C.2: Direct comparison of background rates from ^{238}U chain decays in the ceramic detector mount. Rates calculated by Schwamm are taken from Schwamm’s Tab. B.1, B.2, and 6.2.

^{238}U Region of Interest	Schwamm Rate (mHz) R_S	This work Rate (mHz) R_T	Difference $\frac{R_T - R_S}{R_T}$
15.9-19.4 keV	3.369	5.68 ± 0.22	40.7%
36.9-39.5 keV	0.451	0.688 ± 0.054	34.4%
47.1-49.5 keV	0.387	0.742 ± 0.056	47.8%

outside the ROI; the spectra need to be compared. Schwamm shows the combined background spectra from uranium and thorium in all materials—not just the ceramic mount—in his Fig. 6.6. Each component creates a background spectrum of a different shape. Since the ceramic mount is a large part of the total background from radioactivity, we expect it to dominate the background shape. Therefore, this figure has been digitized and scaled to approximate the spectrum from the ceramic mount only.

Schwamm estimated that the ceramic contributes 85%, 55%, and 54% of the total uranium rate in the LROI, MROI, and HROI respectively. For thorium, Schwamm estimated the ceramic contributes 82%, 62%, and 56% of the total background in the LROI, MROI, and HROI respectively. This energy dependence is expected; proximity to the detector will determine the amount of X rays and minimum ionizing electrons a material contributes, but all components may contribute higher-energy photons to the continuum. Schwamm’s total background spectrum is therefore scaled by 0.55 to approximate the ceramic’s contribution to the continuum. The same scale factor is appropriate for both uranium and thorium, but this is not required since materials can vary in the ratio of uranium to thorium impurities.

Figure C.2 compares the background spectra from thorium. In the HROI and above, the shapes of the two spectra are similar. The X rays in this work are more intense, which is most likely due to the energy-dependence of the proper scaling factor, indicating the ceramic mount contributes more X rays than other materials. Figure C.3 compares the background spectra from uranium. At all energies this work has a larger background from uranium

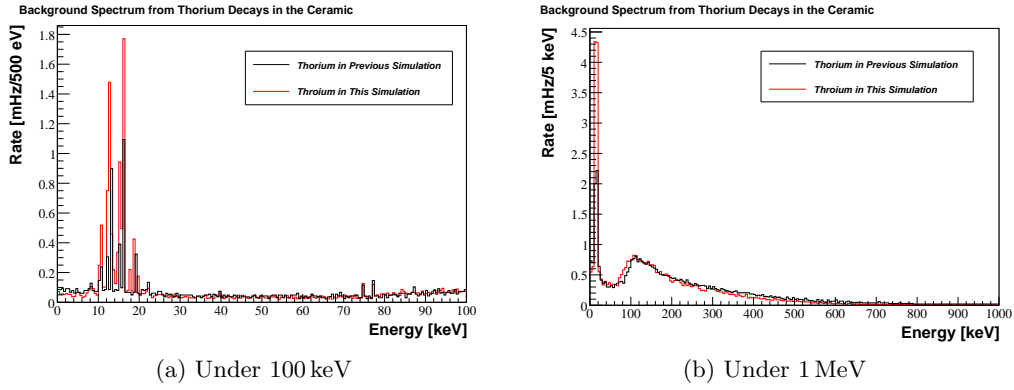


Figure C.2: Schwamm’s background spectrum from thorium decays in all materials scaled by 0.55 (black) compared with this work’s background spectrum from thorium decays in the ceramic mount only (red).

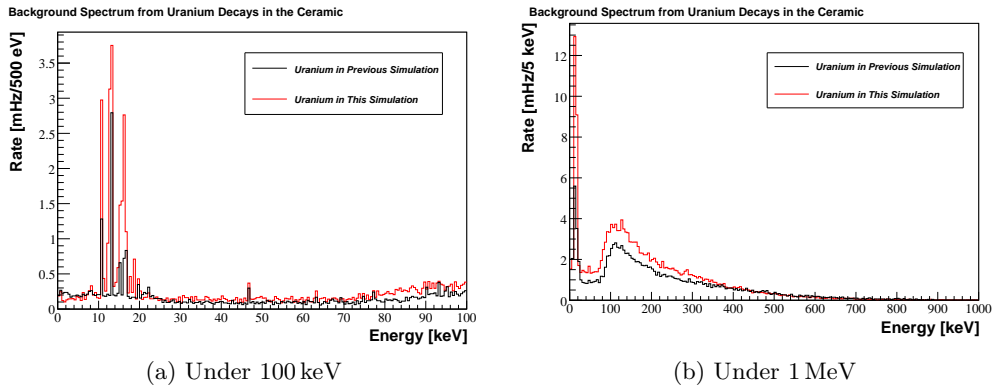


Figure C.3: Schwamm’s background spectrum from uranium decays in all materials scaled by 0.55 (black) compared with this work’s background spectrum from uranium decays in the ceramic mount only (red).

Table C.3: Direct comparison of background rates from cosmic-ray muons in the regions of interest before applying the veto cut. Rates calculated by Schwamm are taken from Tab. B.15, B.16, and 6.9

Muons before Veto ROI	Schwamm Rate (mHz)	This work Rate (mHz)
15.9-19.4 keV	0.253	5.71 ± 0.49
36.9-39.5 keV	0.180	3.43 ± 0.38
47.1-49.5 keV	0.172	2.86 ± 0.35
Total	124	1,480

in the ceramic mount, as predicted by Tab. C.2. It is unclear what causes the difference. Apart from the normalization, the shape of the two spectra match.

Although the total spectra of Schwamm require complicated scalings to compare to this work, it is clear both estimations include X rays and a minimum ionizing bump. The difference in uranium indicates this work estimates higher backgrounds from uranium. The current KATRIN design has mitigated these features in the current background prediction.

C.3 Cosmic-Ray Muons

To simulate cosmic-ray muons, Schwamm assumed a $\cos^2\theta$ distribution and the energy spectrum from O. C. Allkofer, K. Carstensen, W. D. Dau, and H. Jokisch [82]. This is a total intensity of $190 \mu's/m^2/s$. This work uses the muon spectrum given in Section 6.2.1 and a total intensity of $251 \mu's/m^2/s$. Although the two initial spectra come from different sources, since the total intensities are within 30%, the simulation results should be within 30%. These muons rain down on Schwamm's geometry and plastic scintillators.

Before removing any counts with the scintillator veto, the calculated background rates can be compared. As shown in Tab. C.3, this work estimates rates twenty times higher than Schwamm at all energies. It is unclear what causes the difference since the intensity of muons in this work is only 30% higher. Using a common estimate of the muon intensity—1 vertical muon above $1 \text{ GeV}/\text{cm}^2/\text{min}$ —we would expect a rate of 1.3 Hz. This work calculates 1.5 Hz, somewhat high, especially for a vertical detector. Schwamm's calculation

Table C.4: Direct comparison of background rates from cosmic-ray muons in the regions of interest after applying the veto cut. Rates calculated by Schwamm are taken from B.15, B.16, 6.9, and C.5.

Muons After Veto ROI	Schwamm Rate (mHz)	This work Rate (mHz)
15.9-19.4 keV	0.176	0.495 ± 0.143
36.9-39.5 keV	0.026	0.090 ± 0.063
47.1-49.5 keV	0.018	0.084 ± 0.060
Total	9.207	89.6

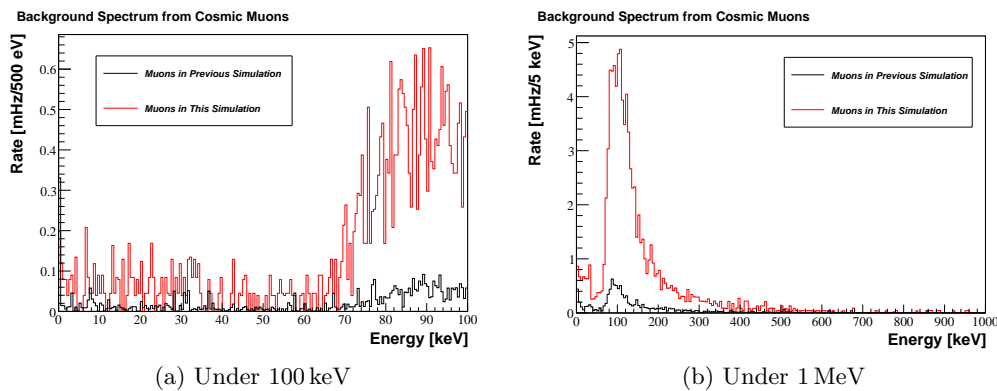


Figure C.4: Schwamm's background spectrum from cosmic rays after a veto but without any scaling (black) compared with this work (red).

is a factor of ten too low, so he may be underestimating the background from cosmic-ray muons. We cannot compare the background spectra because Schwamm does not include a plot.

After applying a veto cut, we can compare the rates in the ROI, as shown in Tab. C.4. Statistics in the ROI are still low, but the total rate is clearly much higher in this work. Schwamm's Fig. 6.10 shows the background spectrum from cosmic-ray muons independent of other sources, after a veto cut. After digitizing Schwamm's spectrum, it is shown with this work in Fig. C.4. Clearly this work estimates a higher rate. The LROI rate quoted by

Schwamm—0.176 mHz—does not agree with his plot and may be a typo.

Over the entire spectrum, Schwamm estimated a reduction to the background by 13.5 by using a veto. Using Schwamm's geometry, this work estimates a reduction of 16.5 with the veto. Although the veto reduction and initial spectra are within 30%, the calculated rates are drastically different in the two simulations. The simulations in this dissertation predict higher background rates than previous simulations; there is no indication that the background for KATRIN has been under-estimated.

VITA

Michelle L. Leber is originally from the east coast of the United States. In high school she developed an interest in science fiction and disassembling cars. After a very short career as an automechanic, she decided to attend the University of Pittsburgh in 1998 to pursue her other interest, science. Michelle was invited to work with Professor James Mueller and Professor Steven Dytman on the Jefferson Lab CLAS experiment. In 2002 she participated in the Research Experience for Undergraduates program and received the Halliday Award for Excellence in Undergraduate Research for her work investigating systematic uncertainties for CLAS. In addition to her research advisors, her inspiring teacher Professor Chandralekha Singh encouraged her to apply for graduate school. She completed her degree in Physics and Astronomy in 2003.

Shortly after, Michelle started graduate school at the University of Washington Department of Physics. She spent two quarters teaching undergraduate physics labs, then joined the Electroweak Interactions group at CENPA. Working with Professor John Wilkerson on the Karlsruhe Tritium Neutrino Experiment (KATRIN), she began testing silicon detectors before switching to simulations of the detector backgrounds. In addition, she led the commissioning studies of the data acquisition hardware for KATRIN. After completing her Ph.D. in Physics in 2009, Michelle moved to Santa Barbara to continue neutrino research at the University of California.